Manipulation of graphitic microparticles in solution with magnetic and electric fields

By

Johnny Nhat Linh Nguyen

A thesis submitted to

University College London

in partial fulfilment of the requirements for the

degree of Doctor of Philosophy

Department of Physics and Astronomy

University College London

I, Johnny Nhat Linh Nguyen, confirm that the work presented in this thesis is my own. Where information has been derived from other sources, I confirm that this has been indicated in the thesis.

Signed .... Date ....

Abstract

Contactless manipulation methods for individual microparticles in solution are essential for the controlled study on the microscopic scale. Microparticles derived from graphitic materials, in particular, are of great interest due to their unique material properties. However to date, the manipulation methods for such particles remain widely unexplored. This thesis presents the first research on the particle manipulation of graphitic microparticles in a diamagnetic solution with electric and magnetic fields. The results show that the particles can be rotationally trapped on a well-defined plane with a combination of an alternating current electric field and a static magnetic field. Furthermore, particle transport and three-dimensional particle trapping can be achieved with static magnetic fields. This research shows that the unique electrical and magnetic properties of graphitic microparticles can lead to novel particle manipulation methods in solution which can be attractive for applications in many areas of research.

Contents

List of Figures

List of Tables

Chapter 1

Introduction

Microparticles is a term most of us have encountered in our daily lives, be it in association with cosmetic and pharmaceutical products, medical applications or air pollution. It is commonly used to describe particles with sizes in the range $10^{-7} - 10^{-4}$ m. Barely visible to the eye, microparticles play an essential role in today's research and technology. They can consist of many different materials, ranging from organic solids to artificially generated highly specialised components. In recent years, there has been an increasing interest in them due to their vast application spectrum. To name a few examples: polyethylene microspheres serve as an exfoliation agent in skin care products; fluorescent latex microspheres are used to determine the resolution of a confocal microscope [1]; graphite microparticles can be used as a coating to improve gas sensors [2]; galactose microparticles are used as a contrast agent in ultrasound imaging [3]; polymeric microparticles are used for controlled engineering of cell aggregates [4]; biodegradable microparticles serve as vessels for controlled and targeted drug delivery to cells [5, 6]; and polystyrene microspheres are used as a transducer to measure forces on biological systems [7].

A substantial factor that led to the versatile use of microparticles was the development of technologies that enabled particle manipulation. The latter term summarizes methods derived from the ability to control the particle movement and orientation in an environment (e.g. in solution or in gas). These particle manipulation methods include: particle-sorting, particle-orientation, particle-trapping and particle-transportation. In principle, particle manipulation relies on the application of external forces on the particle by means of acoustic, optical, electric and magnetic fields. The integration of particle manipulation techniques into experiments must cover two key aspects: first, the chosen technique must be selective (i.e. material specific); and second, it must not damage the microparticle and its environment over the course of the experiment. Today, particle manipulation is used in many areas of research: in biology,

focussed laser fields are used to fix cells in position; in material science, electric fields align graphite oxide microparticles for the production of novel materials; and in particle engineering, electric and magnetic fields are integrated in lab-on-a-chip devices where they serve as particle filters for sample preparation.

Whilst various tools for particle manipulation are broadly available at present, the demand for novel techniques is continuously growing. One of the greatest challenges in the development of manipulation techniques is the balance between advantages and disadvantages depending on the specific utilisation of the microparticles. For example, optical tweezers rely on the use of focussed laser fields which raise concerns over sample heating in biological experiments.

Particle manipulation with electric and magnetic forces

To achieve particle manipulation, the external force applied on the microparticle must be dominant compared to other forces present. For example, for particle trapping in solution the external force must be larger than the gravitational force and the random forces that cause Brownian motion. For particle manipulation with electric and magnetic fields, which is the focus of this thesis, the force magnitude depends on the following parameters: the material properties of the particle and its environment, the particle volume, the field strength and the field gradient. Due to the small volume that comes with the use of microparticles, it is necessary to generate strong external fields with large field gradients to control the microparticle in its environment. Thanks to recent technological advances, it is possible to generate such fields on the micrometre scale. As a result, the success of new application possibilities depends mainly on the material properties of the microparticle itself and its immediate environment (i.e. the solution and additional treatments like lipid-coatings on the microparticle).

Graphite as a candidate for particle manipulation

In the context of electrical and magnetic properties, graphite stands out owing to its unique molecular structure. Graphite is a single-crystal structure made of carbon which consists of many individual layers called graphene. Each layer is a one-atom-thick, two-dimensional structure where the carbon atoms are arranged on a hexagonal lattice as illustrated in Figure 1.1. Two neighbouring layers are displaced as shown on the right hand side of the figure. Within one hexagonal structure only every other atom is located directly above an atom on the subjacent layer (orange circles), while the atoms in between (blue circles) are located on top of the empty center of one of the hexagons in the layer below. Carbon has a total of four valence electrons of which three form covalent bonds to create the two-dimensional lattice. The forth one is delocalized over the entire graphene plane. Van der Waals bonds are formed between

the layers which hold the structure together. These bonds are the result of temporary uneven electron distributions on each graphene layer that results in temporary dipoles and lead to attractive forces between the layers. This structural arrangement makes the material anisotropic with different electrical and magnetic properties in the directions parallel (in-plane) and perpendicular (out-of-plane) to the graphene planes. Because of this molecular structure, the material properties of graphite are exceptional: it has a large in-plane electrical and thermal conductivity and it is the strongest diamagnetic material known to date.
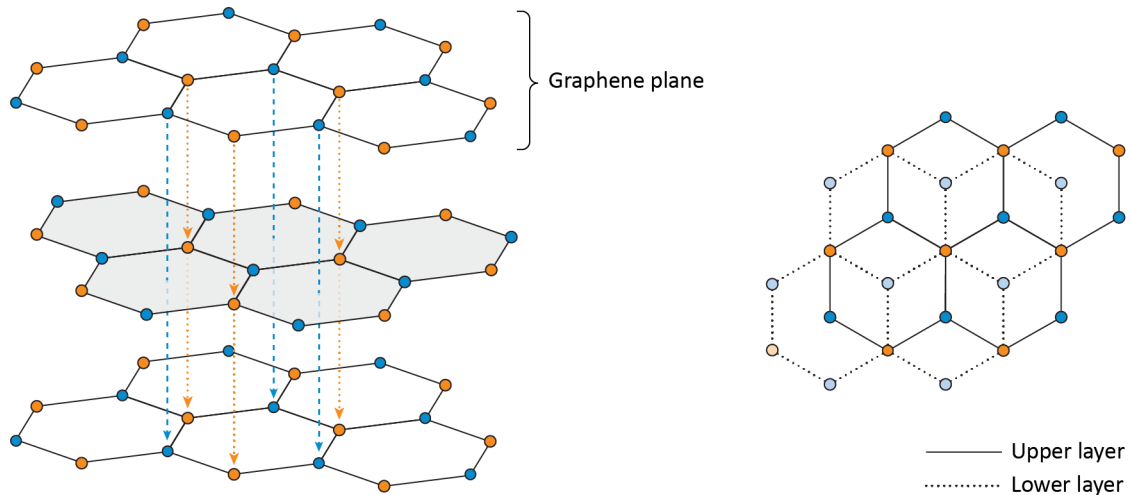
Figure 1.1: Molecular structure of graphite. Left hand side: Three-dimensional illustration of graphite with three graphene planes. Right hand side: Top view of the graphite structure to illustrate the displacement between two neighbouring graphene planes. Within one hexagonal structure only every other atom is located directly above an atom on the subjacent layer (orange circles), while the atoms in between (blue circles) are located on top of the empty center of one of the hexagons in the layer below.

Application possibilities for graphitic microparticles

Today, we find a vast spectrum of application possibilities with graphitic microparticles, i.e. particles with a similar molecular structure to graphite such as graphene or graphite oxide. The majority of those applications focus on the material's electrical, thermal and chemical properties. Here, we list a few of these research fields to illustrate the versatility of graphitic particles.

In material engineering, graphitic particles are mixed with composite materials (a material made from at least two different materials with different physical and chemical properties) to improve existing material properties. For example, Sengupta *et al.* presented in their review numerous studies demonstrating that the addition of graphite to polymer composites can improve its mechanical and electrical properties [8]; Yasmin *et al.* showed that polymers reinforced with 250 nm-thick graphite platelets can improve its thermal stability [9]. The

generation of composites with new properties leads to the development of novel applications. For example, Ponnamma *et al.* reviewed the potential of using graphitic particles in polymer composites for the development of novel sensors [10].

In electrical engineering, the anisotropic electric property of graphite oxide liquid crystals is used for electro-optical switching which can be used in liquid-crystal displays [11, 12]. Only recently, magneto-optical switching of graphene-based liquid crystals has been reported by Niu *et al.* [13]. For energy storage devices, aligned graphite particles can generate batteries with faster charge-up times as reported by Billaud *et al.* [14] or even produce novel batteries as shown by Wang *et al.* [15].

In biomedicine, the majority of current applications is centred around graphene nanoparticles due to their large surface-to-volume ratio and the resulting sensitivity towards biochemical reactions. Because of this property, the surface can be functionalised for several applications: M. Pumera reviewed graphene-based nanoparticles as biosensors for biomolecules such as glucose [16]; Servant *et al.* reviewed graphene particles as potential carriers for drug delivery and gene therapy [17]; Sun *et al.* showed that graphene oxide nanoparticles can be functionalised for cellular uptake and then used for cell imaging in the near-infrared [18]; Liu *et al.* cited several studies, that use graphene to improve the mechanical properties of hydrogels for tissue engineering [19]; Jung *et al.* took advantage of the optical properties of graphene oxide nanoparticles for photothermal therapy of skin cancer [20]; Vincent *et al.* showed that the electrical conductivity on the surface of graphite microparticles can be used for enzymatic catalysis [21]; and only recently, Yoshimi *et al.* generated new electrodes made from graphite particles that can be used to monitor the heparin (a blood thinner) level in blood [22]. The vast number of application possibilities underlines that the full potential of graphitic particles is yet to be discovered and the importance of further research.

Particle manipulation of individual graphitic microparticles

Amongst the many studies we have seen so far, not one has looked into the manipulation of individual graphitic microparticles. Furthermore, the use of the magnetic properties of graphite for particle manipulation remains widely unexplored. Many experiments related to the above-mentioned applications of graphitic microparticles could benefit from particle manipulation techniques as they allow to conduct controlled experiments in gas or solution.

In this thesis, we aim to close this gap by looking into the manipulation of individual graphitic microparticles. We focus on the particle manipulation in solution as this is the environment where most of the experiments reviewed earlier are conducted, and specifically on using electric and magnetic fields to control and measure the orientation and position of

the particle in solution. As a representative graphitic particle, we chose microparticles made from highly oriented pyrolytic graphite (HOPG). The present work comprises of three different types of experiments: the control of the orientation of individual HOPG microparticles with electric and magnetic fields; the transport of an individual HOPG microparticle in solution with magnetic fields; and the magnetic trapping in three dimensions of an individual HOPG microparticle.

Thesis structure

The structure of this thesis is as follows:

Chapter 2 serves as an introduction to HOPG. The electrical and magnetic properties of HOPG are described and our protocol to fabricate (I) lipid-coated HOPG microparticles in a saline aqueous solution and (II) uncoated HOPG microparticles in a mixture of acetone and water, is presented.

Chapter 3 introduces the mathematical background used to theoretically describe the interaction of HOPG microparticles in solution with external electric and magnetic fields.

Chapter 4 focusses on the image acquisition and analysis part in our experiments. Here, we present our imaging system and the tools to acquire and analyse the data.

Chapter 5 presents our research on the orientation manipulation of HOPG microparticles in solution with AC electric fields and static magnetic fields.

Chapter 6 presents our experimental results on the magnetic transport of a HOPG microparticle in solution.

Chapter 7 looks at the three-dimensional magnetic trapping of individual HOPG microparticles in solution with static magnetic fields.

Chapter 8 gives a summary of our research and outlines potential developments for the future.

Chapter 2

Highly oriented pyrolytic graphite (HOPG): properties and characterisation

2.1 Structural properties of HOPG

Graphite is available in various forms which vary in purity and in the amount of defects within them. In its natural form, graphite is a polycrystal, i.e. an ensemble of many single graphite crystals with different sizes and orientations. The angular distribution of the graphene planes in the polycrystal is quantified by the mosaic spread which describes the angular dispersion of the out-of-plane axes of the individual crystals (Figure 2.1a). Therefore, the lower the mosaic spread value, the higher the degree of parallelism between the single crystals. Highly oriented pyrolytic graphite (HOPG) is a synthetic form of graphite with the lowest degree of mosaic spread available (Figure 2.1b). The processes involved in the production of HOPG are pyrolysis (thermal decomposition at high temperatures in an inert atmosphere) and the application of tensile stress in the direction of the graphene planes. Commercially bought HOPG has a known mosaic spread with values less than 4° and the best grade of HOPG corresponding to $\approx 0.4°$. In the present work, we use HOPG due to its electrical and magnetic properties which are presented in the following sections.

2.2 Electrical properties of HOPG

The electrical properties of HOPG are anisotropic, due to the delocalised electrons that move freely throughout the graphene planes. Because of these electrons, the properties in the in-
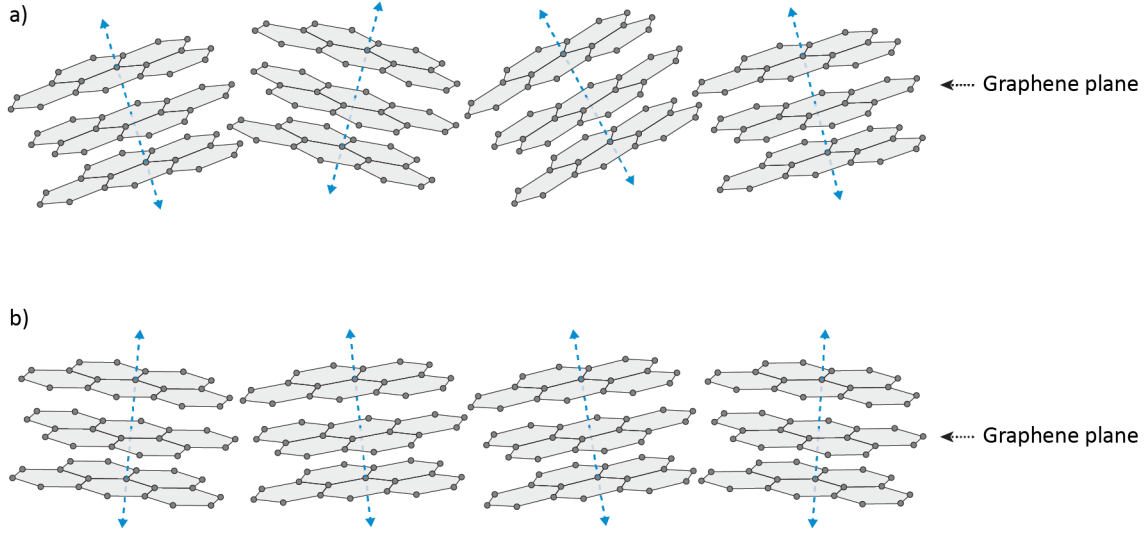
Figure 2.1: Illustration of the mosaic spread for two different forms of graphite. The mosaic spread describes the angular dispersion of the out-of-plane axes (dashed blue axes) of the individual single graphite crystals. a) Orientation of the crystals in natural graphite samples. b) Orientation of the crystals in HOPG.

plane ($\parallel$) and out-of-plane ($\perp$) directions are different. The interaction of HOPG with external electric fields is described by two physical quantities, namely the electrical conductivity ($\sigma_\parallel$, $\sigma_\perp$) and the relative permittivity ($\varepsilon_\parallel, \varepsilon_\perp$). The latter accounts for the reorganisation of electric charges inside the material in the presence of an external electric field. This interaction results in an internal electric field that is weaker than the external one.

The latest measurements for the relative permittivity of HOPG were published by Jellison *et al.* who used ellipsometry experiments to determine the optical function in the visible light range ($400 - 750\,\text{nm}$) [23]. The relative permittivity values, averaged over all visible-light wavelengths and the corresponding standard deviations, are $\varepsilon_\parallel = 2.54 \pm 0.25$ and $\varepsilon_\perp = 1.85 \pm 0.03$ in the in-plane and out-of-plane directions, respectively. Measurements for the electrical conductivity of HOPG have been reported by Matsubara *et al.* [24]. In their study, they used the four-terminal sensing method to measure the electrical resistivity, $\rho = 1/\sigma$, of three HOPG samples with varying defects and impurities in the temperature range $4.2 - 300\,\text{K}$. Following their report, the electrical conductivities at $300\,\text{K}$ in the in-plane and out-of-plane directions are in the range $(2 - 2.2) \times 10^6\,\text{S/m}$ and $100 - 1000\,\text{S/m}$, respectively. The values for the relative permittivity and electrical conductivity of HOPG in the in-plane and out-of-plane directions are summarised in Table 2.1.

$\sigma_\parallel$ (S/m)	$\sigma_\perp$ (S/m)	$\varepsilon_\parallel$	$\varepsilon_\perp$	Reference
-	-	(2.54 ± 0.25)	(1.85 ± 0.03)	[23]*
$(2 - 2.2) \times 10^6$	$100 - 1000$	-	-	[24]

Table 2.1: Electrical conductivity σ and relative permittivity ε for HOPG as reported in the literature. $\parallel$: Component in the in-plane direction. $\perp$: Component in the out-of-plane direction. * Values for the relative permittivity are obtained by averaging over all frequencies in the visible light range.

2.3 Magnetic properties of HOPG

The magnetic properties of HOPG can be quantified with the dimensionless volume magnetic susceptibility, χ (herein referred to as magnetic susceptibility), that relates the magnetisation, M, of HOPG to the external magnetic field, H, as $M = \chi H$. We can use χ to distinguish between three classes of magnetism, namely diamagnetism ($\chi < 0$), paramagnetism ($\chi > 0$) and collective magnetism ($\chi(H) \gg 0$). Diamagnetism arises from the orbiting electrons around the nuclei which generate electric currents that interact with the external magnetic field. This type of magnetism is only relevant in the absence of paramagnetism or collective magnetism in the material. Diamagnetic and paramagnetic materials have two important characteristics: at a fixed temperature, the magnetic susceptibility is constant with the external magnetic field strength; and their magnetisation is zero when the external magnetic field is turned off. Because of the latter characteristic, diamagnetic and paramagnetic materials are not permanent magnets.

HOPG has anisotropic magnetic properties with different magnetic susceptibilities in the in-plane direction, $\chi_\parallel$, and in the out-of-plane direction, $\chi_\perp$. Pristine HOPG is a purely diamagnetic material with $\chi_\perp < \chi_\parallel < 0$. The magnetic susceptibilities have been measured by numerous studies [25–28], which reported values for $\chi_\parallel$ and $\chi_\perp$ of order 10^{-5} and 10^{-4}, respectively. The value for $\chi_\perp$ makes HOPG special as it is the largest (absolute) value found for any diamagnetic material known to date. This remarkable property of HOPG originates from the delocalized electrons between the graphene layers.

Table 2.2 summarises the $\chi_\parallel$ and $\chi_\perp$ values for HOPG as reported in the literature. These values were initially published as mass magnetic susceptibilities in cgs units (χ_m^{cgs}). To convert them to SI units we use $\chi_V^{\text{SI}} = 4\pi \rho_{\text{HOPG}} \chi_m^{\text{cgs}}$, where χ_V^{SI} is the volume magnetic susceptibility in SI units and $\rho_{\text{HOPG}} = 2.26 \, \text{g/cm}^3$ is the density of HOPG [29]. The variations in the literature values indicate possible differences from one HOPG sample to another owing to the possible presence of impurities in the samples and to different levels of order in the structure. Since the values for $\chi_\parallel$ and $\chi_\perp$ are essential for our analysis, we decided to measure $\chi_\parallel$ and $\chi_\perp$ for the HOPG samples used in our experiments.

$\chi_{\parallel}/10^{-5}$	$\chi_{\perp}/10^{-5}$	Reference
-1.1	-56.9	[25]
-8.5	-45	[26]
-0.5	-68.3	[27]
-1.1	-81.7	[28]

Table 2.2: Volume magnetic susceptibility values for HOPG from the literature as shown in the last column. $\chi_{\parallel}$: In-plane magnetic susceptibility. $\chi_{\perp}$: Out-of-plane magnetic susceptibility.

2.3.1 Measuring the magnetic susceptibility

Our research uses two different bulk HOPG samples that were purchased as $10\,\text{mm} \times 10\,\text{mm} \times 1\,\text{mm}$ blocks. Both samples come from different manufacturers and have different mosaic spread values: the sample specified as 'HOPG-3.5' has a mosaic spread of $3.5 \pm 1.5\,°$ and was manufactured by μmasch; the sample 'HOPG-0.4' has a mosaic spread of $0.4 \pm 0.1\,°$ and was sold by Agar Scientific. To measure the magnetic susceptibilities for both HOPG samples, we use a superconducting quantum interference device (SQUID). The instrument is a highly sensitive magnetometer that applies a homogeneous magnetic field on the sample and measures the changes in the field due to the sample's presence. This allows us to measure the sample magnetisation at different magnetic field strengths and fit the data to $M = \chi H$ to extract the magnetic susceptibility. The experiments are conducted on the Quantum Design MPMS-5S with the assistance of Dr. Laura Bovo at the UCL London Centre for Nanotechnology. We take the data at $295\,\text{K}$ and set the sequence of the magnetic field from $H = 2.4 \times 10^6\,\text{A/m}$ to $H = -2.4 \times 10^6\,\text{A/m}$. This magnetic field is equivalent to $3\,\text{T}$ to $-3\,\text{T}$ using $B = \mu_0 H$, where B is the magnetic flux density (often referred to as magnetic field) and $\mu_0 = 4\pi \times 10^{-7}\,\text{H/m}$ is the permeability of free space.

For measurements with a SQUID, the sample of interest must fit in a plastic tube with a circular cross section and a diameter of $4\,\text{mm}$. To prepare the sample, we use a razor blade to cut out a $3\,\text{mm} \times 2\,\text{mm} \times 1\,\text{mm}$ block from each bulk HOPG sample. We then proceed to determine $\chi_{\parallel}$ and $\chi_{\perp}$ for the two smaller blocks as follows:

- To measure $\chi_{\parallel}$, we need to make sure that the graphene planes in the sample are aligned parallel to the external magnetic field direction. For this purpose, we build a small container to keep the sample aligned to the magnetic field as shown in Figure 2.2a. That way, the HOPG sample is fixed over the course of the experiment as shown in Figure 2.2b. We measure the sample magnetisation M as a function of H and then fit the data to $M = \chi_{\parallel} H$ to get $\chi_{\parallel}$.
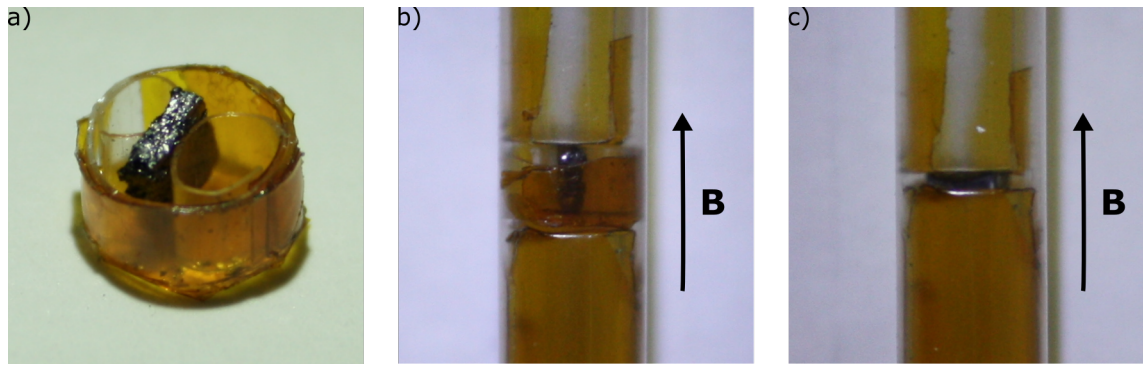
Figure 2.2: Sample mounting for cut-out HOPG blocks to measure the magnetic susceptibilities of HOPG in the in-plane and out-of-plane direction. a) Container made from plastic straws and polyimide tape to align the graphene planes in the sample parallel to the magnetic field. b) Container fixed in a tube to measure the in-plane magnetic susceptibility of HOPG. c) Fixation of HOPG in the tube to measure the out-of-plane magnetic susceptibility of HOPG. **B** specifies the direction of the applied external magnetic field.

- To measure $\chi_\perp$, the graphene planes in the sample must be aligned perpendicular to the external magnetic field. To realize this, we fix the sample inside the tube as shown in Figure 2.2c. We then use the same procedure described for $\chi_\parallel$ to acquire the data and determine the out-of-plane magnetic susceptibility $\chi_\perp$ from the fit.

To keep the samples aligned in the measurement, we use plastic straws and polyimide tape. Measurements conducted by Dr. Bovo showed that the magnetisation of both materials are orders of magnitude lower than of HOPG. Following her advise, we neglect the magnetic contribution of the sample holder in our data analysis.

Figure 2.3 shows the measured sample magnetisation in the in-plane and out-of-plane direction as a function of the magnetic field strength for HOPG-3.5 and HOPG-0.4. For both samples, the sample magnetisation decreases linearly with the increasing magnetic field strength. This magnetic response is expected, since HOPG is diamagnetic as we mentioned earlier. The fitted values along with the standard deviation from the fit for $\chi_\parallel$ and $\chi_\perp$ are summarized in Table 2.3. We can see that the measured values between the samples are slightly different from each other. Potential reasons for this are the sample specific mosaic spread, angular misalignments between the graphene planes and the external magnetic field in the sample holder and possible sample impurities. Our measured values are within the range of those reported in the literature (see Table 2.2).
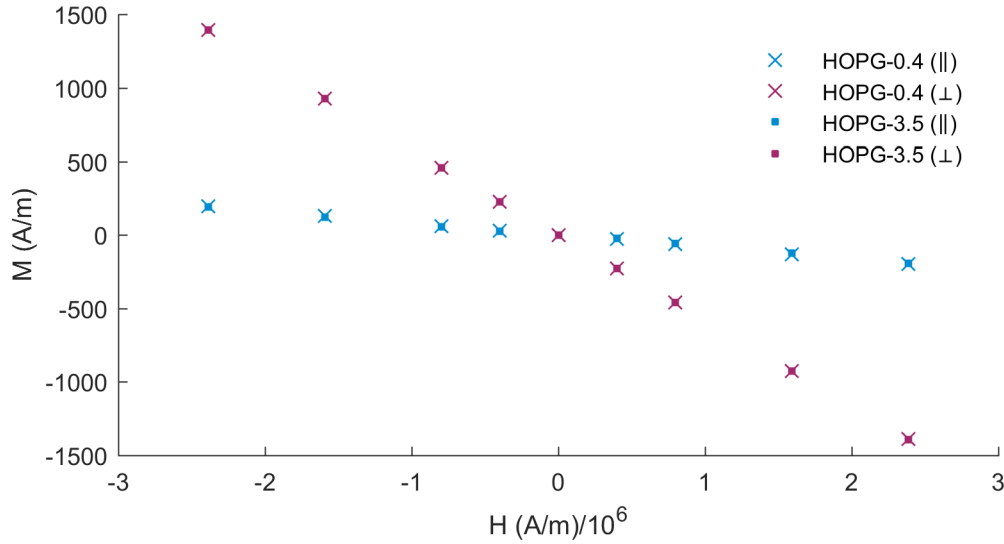
Figure 2.3: Measured sample magnetisation for HOPG as a function of magnetic field strength. The magnetisation data is acquired for the samples HOPG-3.5 (Marker symbol: □) and HOPG-0.4 (Marker symbol: ×). For each sample, the magnetisation is measured in the in-plane (∥) and out-of-plane (⊥) direction. The error bars (included in the figure) are two orders of magnitude smaller than the measured sample magnetisation.

Sample	$\chi_\parallel/10^{-5}$	$\chi_\perp/10^{-5}$
HOPG-0.4	-8.16 ± 0.07	-58.15 ± 0.09
HOPG-3.5	-7.8 ± 0.1	-58.3 ± 0.1

Table 2.3: Measured volume magnetic susceptibilities and corresponding standard deviations along the in-plane ($\chi_\parallel$) and out-of-plane ($\chi_\perp$) directions for the HOPG samples 'HOPG-3.5' and 'HOPG-0.4'. 'HOPG-3.5' has a mosaic spread of 3.5° and 'HOPG-0.4' has a mosaic spread of 0.4°.

2.4 Aqueous dispersions of HOPG microparticles for experiments at room temperature

In our research, we focus on the interaction of individual graphitic microparticles made from HOPG with electric and magnetic fields in an aqueous solution. HOPG is a hydrophobic material from which follows that the produced microparticles cannot be simply mixed in an aqueous solution as they immediately form clumps (agglomerates) that prevent experiments on single graphitic microparticles. In this thesis, we use two different dilute HOPG-microparticle solutions: one consists of lipid-coated HOPG microparticles in a saline aqueous solution and the other contains HOPG microparticles in a mixture of acetone and water with volume fractions 40 % and 60 %, respectively. In the following two subsections, we present the protocols to generate both dispersions.

2.4.1 Protocol for lipid-coated HOPG microparticles

One way to prevent agglomeration is to coat the particle with a thin bilayer of the phospholipid 1-palmitoyl-2-oleoyl-sn-glycero-3-phosphocholine (POPC, Avanti Polar Lipids). The hydrophobic tails of the lipid molecules form a non-covalent bond with the HOPG microparticle surface while the hydrophilic heads are in contact with the solution. That way, particles cannot form agglomerates as the hydrophilic part on one particle is repelled by the hydrophobic part of another particle. Consequently, particles stay dispersed in solution. The possibility of applying stable lipid bilayers around the particles has been demonstrated both theoretically for graphene [30] and experimentally for graphene oxide [31, 32] and graphene sheets [33]. At room temperature, pure POPC is in liquid phase (gel-to-liquid phase transition temperature: 271 K) and can form stable layers around sharp edges which is an important feature for our experiments because the particles produced for our research have flake-like shapes.

We use a protocol developed in collaboration with Prof. Sonia Contera from the University of Oxford, that allows us to quickly prepare lipid-coated HOPG microparticles in a 20 mM NaCl aqueous solution. The preparation starts with drying 1 ml of POPC dissolved in chloroform at 0.6 mg/ml in a N_2 gas flow for 30 min. This produces a dried POPC film which we then rehydrate with 1 ml of 20 mM NaCl aqueous solution. During the re-suspension process, the hydrated lipid sheets start to swell and detach to form multilamellar vesicles. As a result, the solution gets cloudy. Next, we reduce the size of the vesicles by sonicating the solution for 2 min with a probe sonicator (MSE Soniprep 150) at 60 °C and an amplitude of 5 μm. Probe-type sonication is necessary for this step as they are more powerful compared to a sonic bath. This sonication process turns the solution clear again. The sonication probe is made from titanium alloy which introduces compounds to the solution during sonication that need to be removed for further processing. For this purpose, we centrifuge the solution for 30 min at 8000 revolutions per minute (rpm) and transfer the supernatant into another bottle. We then extract HOPG flakes from the bulk HOPG sample by exfoliating thin layers with tweezers and immerse them in solution. To break up the HOPG flakes into micrometre-sized particles and induce the formation of lipid bilayers around them, we place the solution with the particles in a sonic bath (James Sonic 3MX) for one to four hours. The temperature during the sonication process is kept below 30 °C following a report by M. Sepioni showing that the process of breaking up the graphite flakes is attenuated in excess of 30 °C [34].

The shape and surface of uncoated HOPG microparticles can be appreciated in Figure 2.4a. The images were taken with a scanning electron microscope at the Rutherford Appleton Laboratory. Figure 2.4b shows a larger image of the HOPG microparticle encircled in Figure 2.4a.
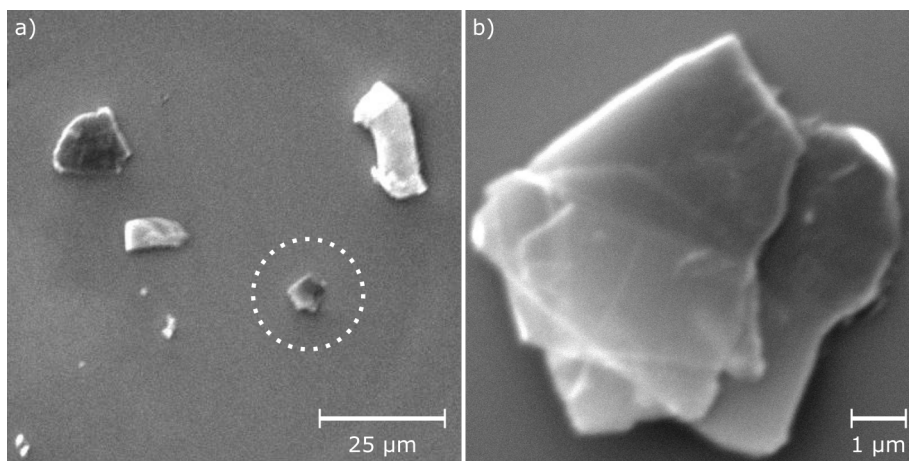
Figure 2.4: Images of HOPG microparticles taken with a scanning electron microscope. a) Image taken at 450× magnification. b) Image taken at 10000× magnification of the particle encircled in a).

Our protocol produces HOPG microparticles with sizes ranging from less than a micrometre to several tens of micrometres. The average size can be adjusted by varying the sonication time in the sonic bath when we break up the HOPG sheets into micrometre-sized flakes. For our experiments we choose micrometre-sized flakes that are less than 10 μm wide and about 2 μm thick. These sizes are suitable for potential applications in biology which are typically on the μm scale. Furthermore, the sizes are sufficient to apply biologically relevant forces and torques on the particle with external electric and magnetic fields (details are presented later in Chapter 3).

Figure 2.5 shows images and measurements for lipid-coated HOPG microparticles that were taken with an atomic force microscope (AFM) by Prof. Contera. Figure 2.5a shows an AFM image of lipid-coated HOPG microparticles in solution. We can clearly see round particle shapes which are due to the applied lipid-layer that covers the entire HOPG core. Figure 2.5b shows an AFM image of a dried lipid-coated HOPG microparticle where the surface is rough owing to the dehydrated lipid-layer. The thickness of the lipid-layer on the HOPG microparticles can directly be measured with an AFM. Figure 2.5c shows force versus indentation depth curves for two HOPG microparticles. The origin on the indentation axis specifies the initial position of the AFM probe. Each curve shows four to five distinct steps that are separated by a constant region over an indentation of $3 - 5\,\text{nm}$. The steps appear in the curves when the AFM probe penetrates a lipid bilayer around the particle which is typically $3 - 5\,\text{nm}$ thick. Therefore, the measurement suggests that the examined particles are coated with four to five lipid bilayers.

2.4.2 Protocol for HOPG microparticles in an acetone and water mixture

The generation of graphitic microparticle dispersions with an acetone and water mixture was first reported by Nonomura *et al.* [35]. According to their study, graphitic microparticles can be

28
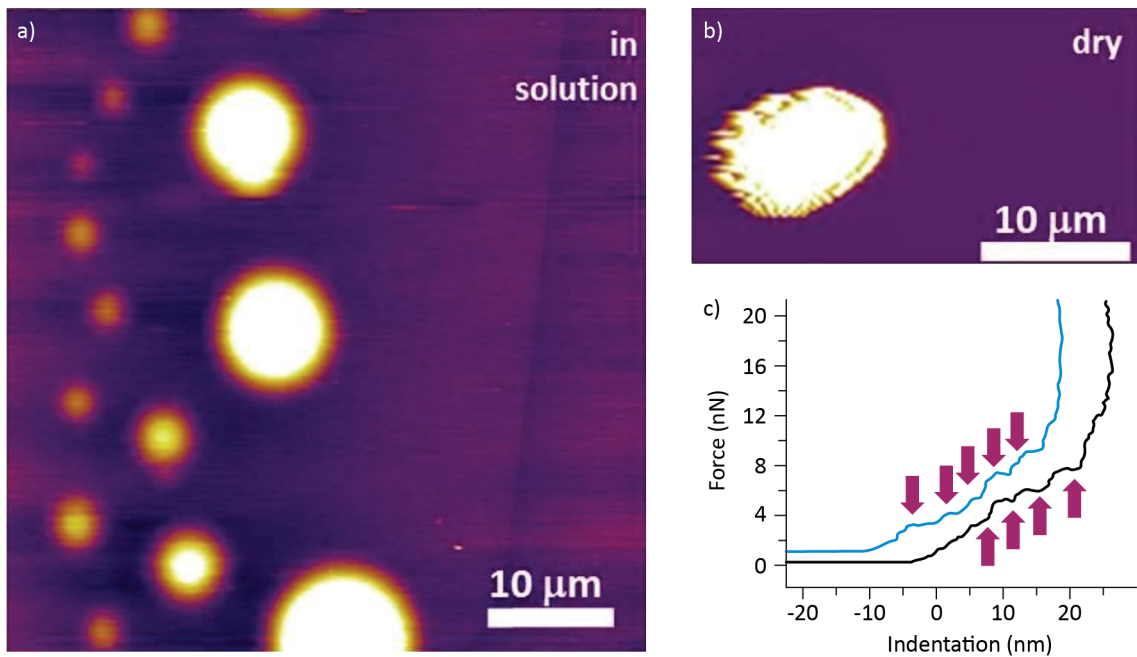
Figure 2.5: Atomic force microscope (AFM) measurements for HOPG microparticles. a) AFM image of lipid-coated HOPG microparticles in solution. b) AFM image of a dried lipid-coated HOPG microparticle. c) Force vs. indentation depth of two lipid-coated HOPG microparticles.

stably dispersed if the volume fractions of acetone and water are 40 % and 60 %, respectively. To produce the dispersion, we follow the same protocol described in their report: first, we place HOPG sheets exfoliated from a bulk HOPG block into a glass vial containing the acetone and water mixture; and then, we place the vial in a sonic bath for one to four hours. As before, we keep the temperature in the sonic bath below 30 °C to maximise the breaking up process of the large HOPG sheets into HOPG microparticles. The advantage of this solution is that the particles stay dispersed without the application of a lipid coating. Therefore, we use the solution to evaluate the effect of lipid-bilayers on the particle manipulation with external fields.

Chapter 3

The effective moment method for submerged coated particles

In this chapter, we provide the fundamental theory to describe the interaction of coated particles in solution with external electric and magnetic fields. For this purpose, we derive expressions for the induced electric and magnetic dipole moment in the coated particle. In our research, these solutions are used to describe the forces and torques exerted on lipid-coated HOPG microparticles in solution by electric and magnetic fields.

As a first approximation, we model the lipid-coated HOPG microparticle as an ellipsoid with a confocal shell. An illustration of our model is presented in Figure 3.1. The inner ellipsoid represents the HOPG core with semi-axes a_2, b_2 and c_2. The outer ellipsoid describes the shape of the entire lipid-coated HOPG microparticle. It has semi-axes $a_1 = \sqrt{a_2{}^2 + \delta}$, $b_1 = \sqrt{b_2{}^2 + \delta}$ and $c_1 = \sqrt{c_2{}^2 + \delta}$, where δ is a parameter that defines a set of confocal ellipsoids. The illustration shows that in our model the thickness lipid layer is not uniform over the HOPG core. To correct for this effect, we developed a two-ellipsoid model which we analysed and discussed in [36].

We define the particle frame of reference such that its origin is located in the ellipsoid's centre of mass and the semi-axes of both ellipsoids are parallel to the x-, y- and z-axes of the particle frame of reference. The electrical and magnetic properties in our model are described by the relative permittivity $\varepsilon_{j,k}$, the electrical conductivity $\sigma_{j,k}$ and the magnetic permeability $\mu_{j,k}$. Similar to the relative permittivity, the magnetic permeability describes the response of a material to an external magnetic field. The sub-index j associates the properties to the different components in the model: $j = 1$ refers to the properties of the solution that surrounds the particle, $j = 2$ refers to the properties of the lipid-shell and $j = 3$ refers to the properties of

Properties

Solution: $\varepsilon_1, \sigma_1, \mu_1$

Lipid layer: $\varepsilon_{2,k}, \sigma_{2,k}, \mu_{2,k}$

HOPG core: $\varepsilon_{3,k}, \sigma_{3,k}, \mu_{3,k}$

Semi-axes

Outer ellipsoid: a_1, b_1, c_1

Inner ellipsoid: a_2, b_2, c_2
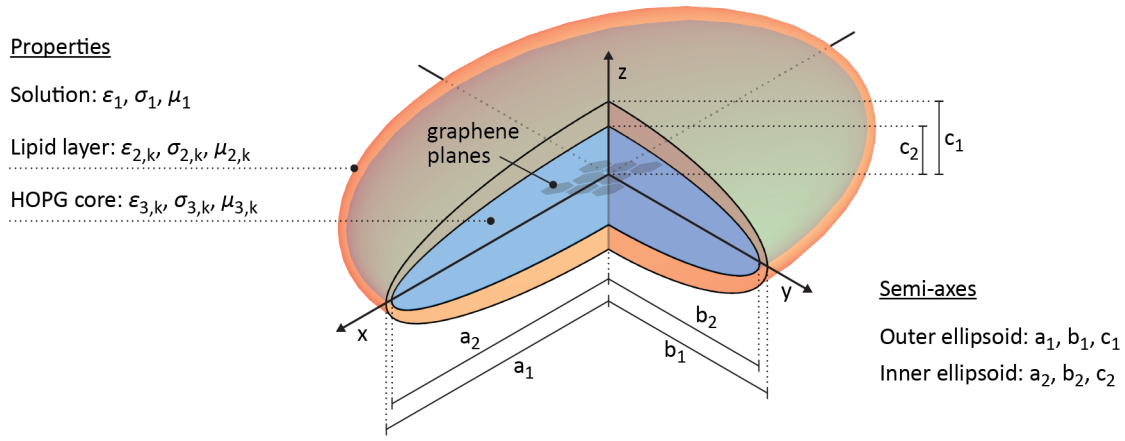
Figure 3.1: Ellipsoidal model for a HOPG microparticle with a single lipid layer. The inner ellipsoid describes the HOPG core of the particle with semi-axes a_2, b_2 and c_2. The outer ellipsoid with semi-axes a_1, b_1 and c_1 describes the entire particle including the HOPG core and the lipid-layer. The particle is assumed to be submerged in solution. The electric and magnetic properties for each component in the model (solution, lipid-layer, HOPG core) are described by the relative permittivity (ε), the electrical conductivity (σ) and the magnetic permeability μ. The sub-index $k \in [x, y, z]$ specifies the properties along the x, y and z directions in the particle frame of reference. The graphene planes of the particle are assumed to be on the x-y plane.

the HOPG core. The other sub-index, $k \in [x, y, z]$, specifies the properties along the x, y and z directions. For HOPG microparticles fabricated by means of sonication the layered structure remains unchanged (see Figure 2.4). Therefore, we set the properties in the x and y directions equal to the in-plane ($\parallel$) properties of HOPG (e.g. $\varepsilon_{3,x} = \varepsilon_{3,y} = \varepsilon_\parallel$) and the properties in the z direction equal to the out-of-plane ($\perp$) properties (e.g. $\varepsilon_{3,z} = \varepsilon_\perp$).

To derive the force and torque on the particle induced by the external field, we use the effective moment method for submerged coated ellipsoids as described in T. B. Jones's book 'Electromechanics of Particles' [37]. The idea behind this method is to substitute the particle with a point dipole with effective electric dipole moment $\mathbf{p}_{\text{eff}}$ and effective magnetic dipole moment $\mathbf{m}_{\text{eff}}$ such that when we place it in the exact same location and solution as the particle, it produces the same electric and magnetic potential energy. Two assumptions are employed in this method: first, the multipolar interactions of higher order, e.g. quadrupole interactions, and particle-particle interactions, can be neglected; and second, the external field across the particle volume is uniform. In our experiment, both assumptions are valid as we use dilute particle solutions and the external electric and magnetic field gradient are of order $10^{-3}\,\text{V}/\mu\text{m}^2$ and $10^{-3}\,\text{T}/\mu\text{m}$, respectively. By applying the effective moment method, the electric and magnetic force as well as the electric and magnetic torque exerted on the particle are equivalent to those on a representative point dipole. In the presence of a time-varying electric field $\mathbf{E}(t)$, the electric force on the particle is [38]:

$$\mathbf{F}_{\text{el}}(t) = \mathbf{p}_{\text{eff}}(t) \cdot \nabla \mathbf{E}(t), \tag{3.1}$$

32

and the electric torque is:

$$\mathcal{T}_{\text{el}}(t) = \mathbf{p}_{\text{eff}}(t) \times \mathbf{E}(t). \tag{3.2}$$

Similarly, in a static magnetic field $\mathbf{B}$, the magnetic force on the particle is given by [38]:

$$\mathbf{F}_{\text{mag}} = \mathbf{m}_{\text{eff}} \cdot \nabla \mathbf{B}, \tag{3.3}$$

and the magnetic torque is formulated as:

$$\mathcal{T}_{\text{mag}} = \mathbf{m}_{\text{eff}} \times \mathbf{B}. \tag{3.4}$$

The general derivation of the effective moment consists of two steps. First, Laplace's equation ($\Delta\psi = 0$, where ψ is the electric or magnetic scalar potential) is solved with the corresponding boundary conditions at each interface of two consecutive materials (here: the HOPG-to-lipid interface and the lipid-to-solution interface). Next, the potential is formulated at large distances from the particle's centre of mass and compared to the potential of a point dipole. This comparison allows to identify the expressions for the effective electric and magnetic dipole moments. In the next two subsections, we summarise the main results of the effective moment method applied to lipid-coated HOPG microparticles in solution as modelled in Figure 3.1. We start with the effective electric dipole moment from which we can then directly derive the effective magnetic dipole moment due to the similar mathematical formulation of electric and magnetic fields.

3.1 Effective electric dipole moment of lipid-coated HOPG microparticles

In our experiments, we study the electrical interaction for lipid-coated HOPG microparticles in alternating current (AC) electric fields with MHz frequencies (10^6 Hz). For the theoretical description of the effective electric dipole moment, we assume isotropic electrical properties for the lipid layer. In general, the latter can have anisotropic electrical properties that can arise due to the presence of mobile surface charges on the lipid shell. With respect to our experiments, such charges could possibly be present due to the absorption of Na^+ ions in the NaCl aqueous solution into the polar head groups (the head group has an electric dipole moment because the charge distribution is uneven but it is overall neutral) of POPC as shown in simulations by Knecht *et al.* [39]. However, Sukhorukov *et al.* showed that for microparticles with thin lipid layers (few nanometres thick), those effects are only relevant at electric field frequencies

less than 10^4 Hz [40]. Consequently, we can neglect the anisotropic electrical properties of the lipid layer in our experiments. For a dielectric object with finite conductivity in an oscillating electric field it is convenient to introduce the complex permittivity defined as [37]:

$$\epsilon = \varepsilon - i\frac{\sigma}{\varepsilon_0 \omega},$$ (3.5)

where $\omega = 2\pi f$ is the angular frequency of the AC electric field with frequency f, ε_0 is the permittivity of free space and $i = \sqrt{-1}$.

The effective electric dipole moment for a submerged coated ellipsoid has already been derived by Asami *et al.* to study the electrical behaviour of biological cells in solution [41]. The components of the effective electric dipole moment, $p_{\text{eff},k}$, are given by:

$$p_{\text{eff},k} = V_1 \varepsilon_1 \varepsilon_0 K_k E_k(t),$$ (3.6)

where $V_1 = \frac{4}{3}\pi a_1 b_1 c_1$ is the volume of the outer ellipsoid and K_k are the effective complex polarisation factors of the layered ellipsoid, given by:

$$K_k = \frac{\epsilon'_{2,k} - \epsilon_1}{\epsilon_1 + \left(\epsilon'_{2,k} - \epsilon_1\right) L_{1,k}}.$$ (3.7)

$\epsilon'_{2,k}$ in Equation (3.7) are the equivalent complex permittivity components of the layered ellipsoid, defined as:

$$\epsilon'_{2,k} = \epsilon_2 \frac{\epsilon_2 + (\epsilon_{3,k} - \epsilon_2)\left[L_{2,k} + \nu\left(1 - L_{1,k}\right)\right]}{\epsilon_2 + (\epsilon_{3,k} - \epsilon_2)\left(L_{2,k} - \nu L_{1,k}\right)},$$ (3.8)

where:

$$\nu = \frac{a_2 b_2 c_2}{a_1 b_1 c_1},$$ (3.9)

and $L_{1,k}$, $L_{2,k}$ are geometrical depolarisation factors given by:

$$L_{1,k} = \frac{a_1 b_1 c_1}{2} \int_0^\infty \frac{ds}{\left(p_{1,k}^2 + s\right)\sqrt{(a_1{}^2 + s)(b_1{}^2 + s)(c_1{}^2 + s)}},$$ (3.10)

and:

$$L_{2,k} = \frac{a_2 b_2 c_2}{2} \int_0^\infty \frac{ds}{\left(p_{2,k}^2 + s\right)\sqrt{(a_2{}^2 + s)(b_2{}^2 + s)(c_2{}^2 + s)}},$$ (3.11)

with $p_{1,k} = a_1, b_1, c_1$ and $p_{2,k} = a_2, b_2, c_2$ for $k = x, y, z$, respectively. Both depolarisation

34

factors account for the different particle shapes and satisfy the relations:

$$\sum_{k=x,y,z} L_{1,k} = 1,$$

$$\sum_{k=x,y,z} L_{2,k} = 1, \qquad (3.12)$$

$$0 \leq L_{1,k}, L_{2,k} \leq 1.$$

Once the effective electric dipole moment of the coated particle in solution is known, we can calculate the electric force and torque on the particle with Equations (3.1) and (3.2), respectively.

3.2 Effective magnetic dipole moment of lipid-coated HOPG microparticles

We can derive the effective magnetic dipole moment directly from Equation (3.6) by replacing the complex permittivity ϵ with the magnetic permeability μ and the factor $\varepsilon_1 \varepsilon_0$ with $1/\mu_1$. Then, the effective magnetic dipole moment becomes:

$$m_{\text{eff},k} = \frac{V_1}{\mu_1} \frac{\mu'_{2,k} - \mu_1}{\mu_1 + \left(\mu'_{2,k} - \mu_1\right) L_{1,k}} B_k, \qquad (3.13)$$

where $\mu'_{2,k}$ are the effective magnetic permeability components of the layered ellipsoid.

Equation (3.13) can be further simplified by comparing the magnetic properties of the lipid layer with the properties of HOPG. For this purpose, we look at the magnetic susceptibility, χ, that is related to μ as $\mu = (1 + \chi)\mu_0$ where $\mu_0 = 4\pi \times 10^{-7}$ H/m is the permeability of free space [38]. Phospholipids are one of the major components of cell membranes. In a previous study, Azanza $et\ al.$ used a SQUID to measure the magnetic susceptibility of red blood cell plasma membranes [42]. They reported a value of order 10^{-6} which is less than the in-plane and the out-of-plane magnetic susceptibilities of HOPG ($\chi_\parallel \propto 10^{-5}$, $\chi_\perp \propto 10^{-4}$). Therefore, the contribution of phospholipids to the magnetic interaction of lipid-coated HOPG microparticles is negligible, i.e. $|\chi_{2,k}| \ll |\chi_\parallel| < |\chi_\perp|$. It follows that the effective magnetic dipole moment can be expressed as:

$$m_{\text{eff},k} = \frac{V_1}{\mu_0} \left(\chi_{3,k} - \chi_1\right) B_k. \qquad (3.14)$$

In the final expression, we can see that the magnetic interaction is determined by the magnetic susceptibilities of HOPG and the solution. Furthermore, it does not depend on the particle

shape since the factors $L_{1,k}$ and $L_{2,k}$ are not present in Equation (3.14). The latter feature is an important difference to the electrical case, where the particle shape cannot be neglected. This can be advantageous as it allows the manipulation of particles with identical volumes but with different shapes. In the following experiments, we can now use the effective magnetic dipole moment to calculate the magnetic force and torque on the particle with Equations (3.3) and (3.4), respectively.

Chapter 4

Imaging HOPG microparticles in solution

As mentioned in the beginning, our research on the manipulation of HOPG microparticles in solution focusses on the control of the particle position and orientation with electric and magnetic fields. We study the particle manipulation by monitoring the particle with a purpose-built upright microscope and use our image analysis code to extract the particle size, position and orientation from the acquired videos. In this section, we describe our video acquisition setup and the image analysis code which we use in all our experiments. We first present the microscope and our software to control the video acquisition. Then, we describe our image analysis code to extract the data (i.e. particle size, position and orientation) from the recorded videos.

4.1   The video acquisition setup

4.1.1   The microscope

For all experiments presented in this thesis, we built an upright microscope with optical components from Thorlabs. A photograph and a schematic of the microscope are shown in Figure 4.1 which consists of four different components, namely an infinity-corrected microscope objective, a tube lens with focal length $f = 200\,\text{mm}$ (Thorlabs, part no. TTL200), a monochrome CMOS camera (Thorlabs, part no. DCC1545M) and a LED. The latter acts as a visible light source where the wavelengths are in the range $400 - 700\,\text{nm}$. To produce an image, the LED illuminates the sample from below and the light transmitted by the sample propagates through the objective producing collimated light which is focussed by the tube lens onto the camera sensor. In this configuration, opaque objects such as HOPG microparticles appear as dark spots on a bright background. The specifications of the microscope objectives used in our experiments are summarized in Table 4.1.
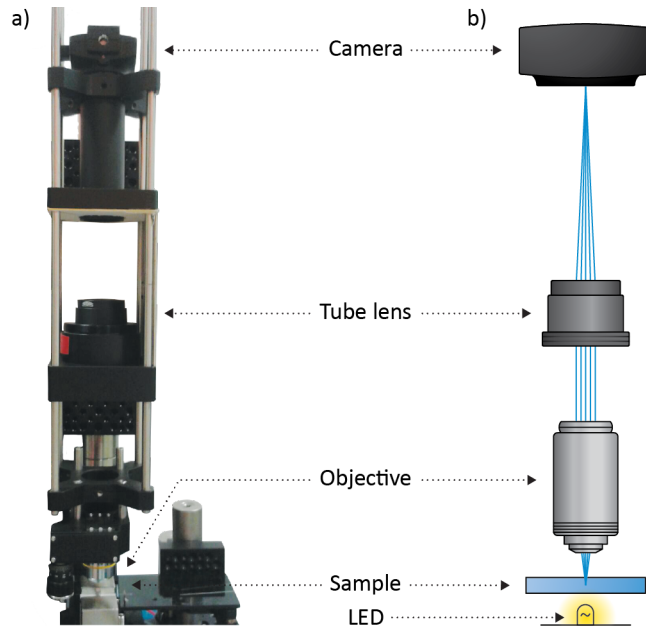
Figure 4.1: The purpose-built upright microscope used in all experiments to analyse the particle manipulation of HOPG microparticles with electric and magnetic fields. a) Photograph of the microscope. b) Schematic of the microscope. The microscope consists of four optical components: a LED, a microscope objective, an infinity-corrected tube lens (focal length $f = 200\,\text{mm}$) and a CMOS camera. The LED illuminates the sample from below and the light transmitted by the sample propagates through the objective producing collimated light which is then focussed by the tube lens onto the camera sensor.

Model	Olympus, PLN 10×	Olympus, PLN 40×
Magnification	10×	40×
Working distance (mm)	10.6	0.6
Numerical aperture	0.25	0.65
Type	achromatic, ∞	achromatic, ∞

Table 4.1: Specifications of the microscope objectives used to image HOPG microparticles in solution. ∞: Infinity-corrected.

4.1.2 The software

All electronic components in our experimental setups except the camera are controlled through a data acquisition device (National Instruments, part no. NI USB-6229) which is connected to a computer via USB. For our analysis it is crucial that both the camera and the data acquisition device can be controlled simultaneously. In Chapter 5, for example, we analyse the electric torque on the HOPG microparticle exerted by an AC electric field. To analyse the potential time-delayed response from the particle to the field, it is important to turn on the video acquisition and the field at the same time. For this purpose, we wrote our own Labview program using the software development kit delivered with the camera and the tool
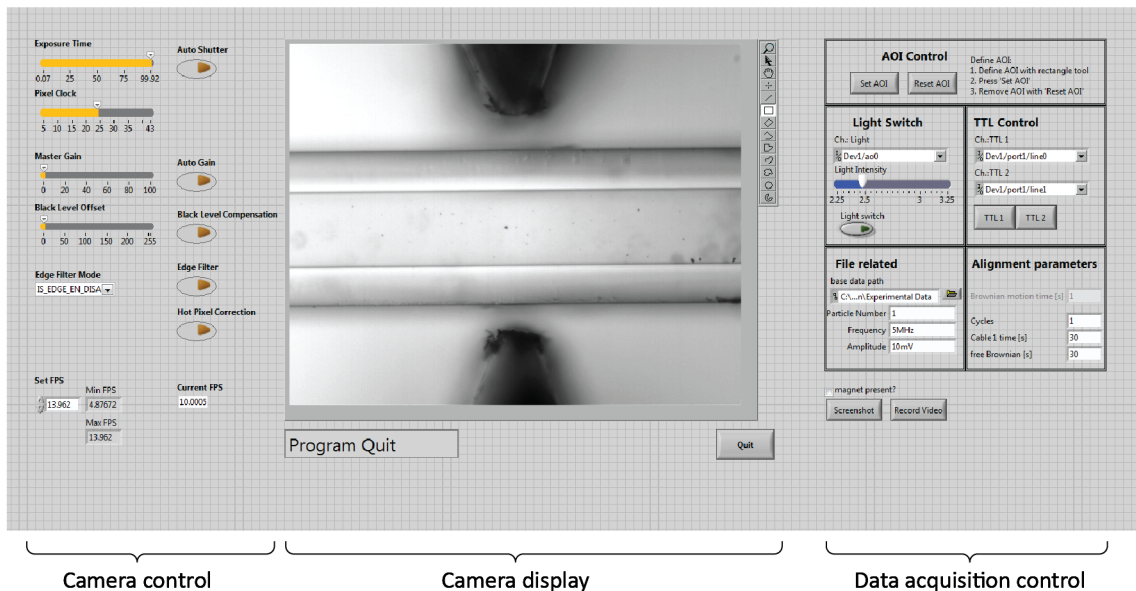
Figure 4.2: Labview program to control the camera and all electronic components connected to the data acquisition board. Left hand side: Camera related controls. Middle: Camera display. Right hand side: Controls for all electronic components connected to the data acquisition board and controls to set the region of interest on the image as well as to start and stop the video acquisition.

packages from National Instruments to control the data acquisition device. The interface of the software is presented in Figure 4.2. On the left hand side, we can control all settings related to the camera, for example the exposure time, the gain and the frame rate. In the middle part of the software, we have the camera display where we can put markers or select a region of interest (ROI) on the image. On the right hand side, we can control all electronic components connected to the data acquisition device (e.g. LED and voltage signal generator). Furthermore, we can set the ROI to image a reduced region at higher frame rates and we can turn the video acquisition on and off.

4.2 From pixels to micrometres

The particle position and size extracted from the video are initially measured in units of pixels and need to be converted to micrometres for further evaluation. This conversion is done by multiplying the position data and the size in pixels with a constant factor c_{px}. We determine this factor with the help of a reference slide that contains laser engraved 15 μm-diameter circles from the National Physical Laboratory. We start by taking an image of the reference slide with our microscope for each objective in Table 4.1. An image of the laser engraved circles is shown in Figure 4.3 which was taken with the $10\times$ objective. We measure the diameter of five circles with the software Inkscape which gives us the diameter for each circle in units of pixels. The conversion factor is then calculated as $c_{px} = \frac{d_{\mu m}}{d_{px}}$, where $d_{\mu m}$ is the known diameter of the

circle in micrometres and d_{px} is the corresponding diameter in pixels. Table 4.2 summarises the conversion factor averaged over all circles and the standard deviation for both microscope objectives. The main contribution to the error is the uncertainty when measuring the circle diameter manually with the software.
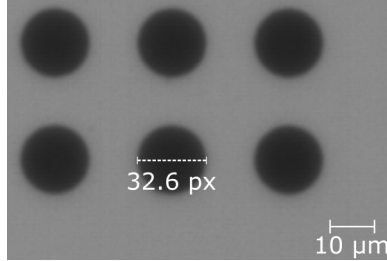
Figure 4.3: Image of laser engraved $5\,\mu$m-diameter circles taken with a $10\times$ microscope objective.

Objective Magnification	c_{px} $\left(\frac{\mu m}{pixels}\right)$
$10\times$	0.457 ± 0.006
$40\times$	0.1142 ± 0.0009

Table 4.2: Measured conversion factors and corresponding standard deviation for the $10\times$ and $40\times$ microscope objectives used in this thesis.

4.3 Assessing the minimum detectable particle size

In order to analyse the particle manipulation with external electric and magnetic fields, it is essential to measure the particle size and its volume. All optical imaging systems have a limited spatial resolution that can depend on many factors such as the quality of the lenses or the alignment of individual optical components. Theoretically, the resolution limit d_{min} of an optical imaging system is given by the diffraction limit:

$$d_{min} = \frac{0.61\lambda}{NA},\tag{4.1}$$

where λ is the wavelength of the light and NA is the numerical aperture. It follows that a particle with sizes below d_{min}, appears under the microscope as a blurred spot which can lead to an overestimation of the particle size and volume. For the microscope objectives in Table 4.1, the range of d_{min} in the visible light range is $1 - 1.7\,\mu$m for the $10\times$ objective and $0.4 - 0.7\,\mu$m for the $40\times$ objective.

Since we are interested in particles that are a few μm wide, it is crucial to determine the minimum detectable size for the 10× objective. For this purpose, we measure the limit of our microscope by using 1 μm-diameter and 0.8 μm-diameter polystyrene beads (Kisker Biotech, part no. PSI-1.0 and PSI-0.8) and measure their sizes on images with Inkscape. The measurement shows that both beads appear as blurred spots with a diameter of 1.5 μm. This value is within the range of the theoretical limit calculated for the visible light spectrum and is larger than the actual particle size. Consequently, for particle imaging with the 10× objective, we choose particles that have sizes larger than 1.5 μm.

4.4   Detecting the particle location and orientation

We determine the position and orientation of HOPG microparticles from images as shown in Figure 4.4. Those images were taken with the 40× microscope objective in Table 4.1.

Figures 4.4a − c show typical images of horizontally aligned HOPG microparticles. These images are processed to obtain the centre-of-mass particle position as detailed in Chapters 6 and 7. Figures 4.4d − f show typical images used for the determination of the particle orientation in Chapter 5. The images show HOPG microparticles where the graphene planes are aligned parallel to the magnetic field **B**.
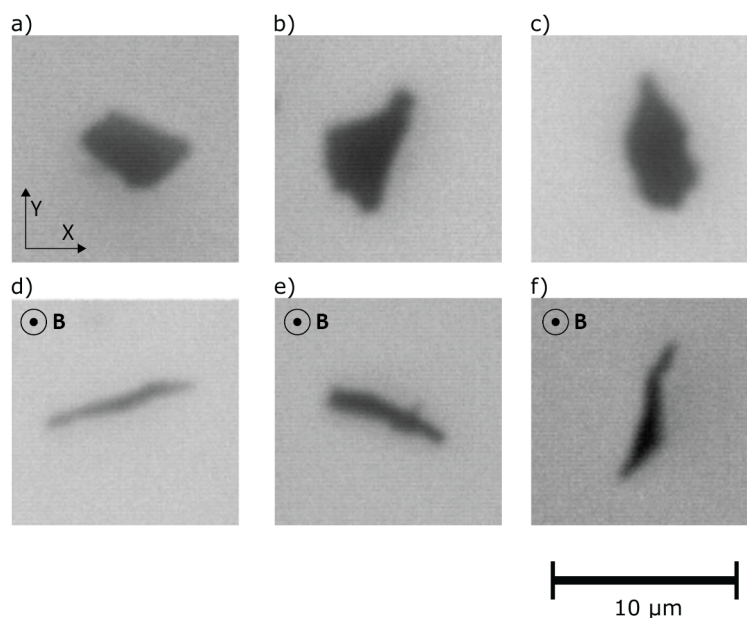
Figure 4.4: Microscope images of lipid-coated HOPG microparticles in a 20 mM NaCl aqueous solution. a − c) Images of typical particle shapes used to localise the particle. d − f) Images of typical particle shapes used for the determination of the particle orientation. The graphene planes in the particle are parallel to the magnetic field **B**. All images were taken with a 40× microscope objective.
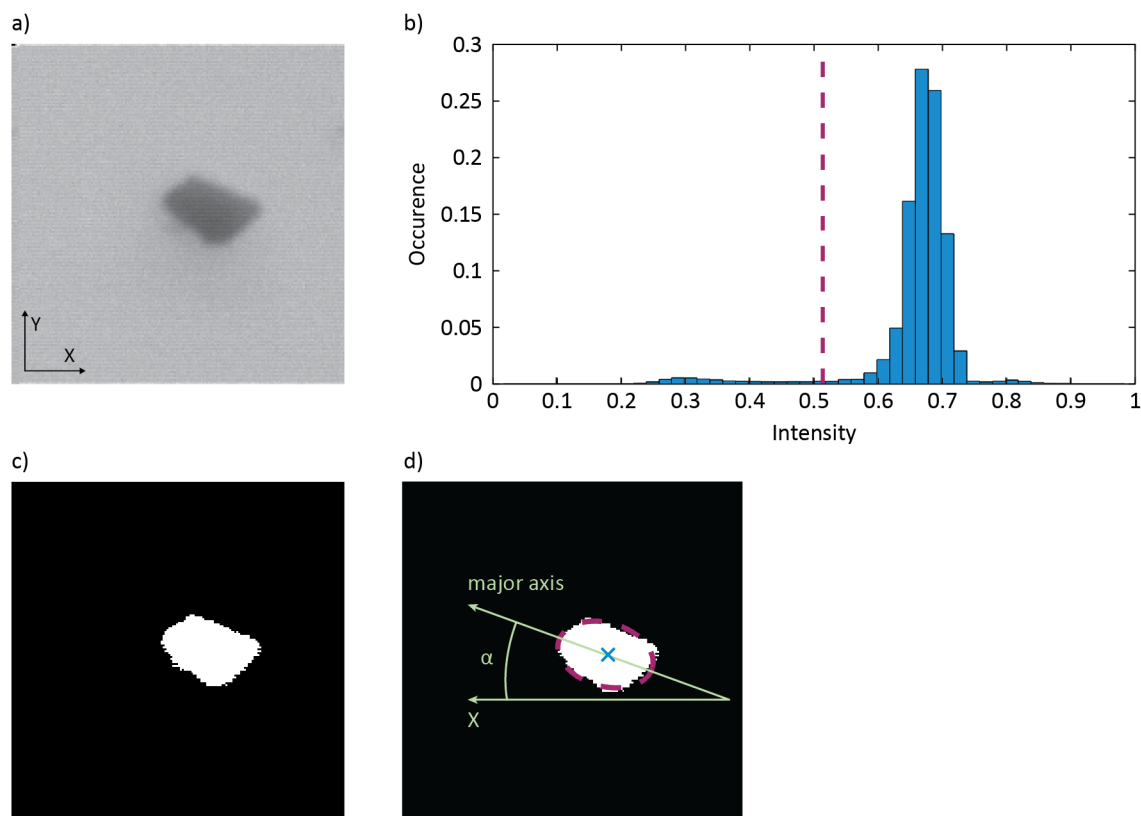
Figure 4.5: Illustration of the particle localisation and orientation detection process. a) Microscope image of an HOPG microparticle. b) Intensity histogram of the image in a). The histogram shows the intensity distribution of the image. The purple dashed line shows the threshold level calculated in Matlab. c) Binary image of a) by setting the pixel intensity values below threshold to 1 (white) and those above to 0 (black). d) Particle position and orientation detected by the image analysis code. The position is defined as the centre of mass of the particle (marked as $\times$). To determine the orientation, the particle area is fitted to an ellipse and from the fit result we extract the angle, α, between the X-axis and the major axis of the ellipse (shown as a purple dashed line).

We track the location and orientation of the particle in every video frame by processing them in Matlab using our own written image analysis code. In Figure 4.5a, we see the particle as imaged with our microscope. Figure 4.5b shows the corresponding distribution of the pixel intensity values. We can see two distributions: one at low intensities centred around 0.3, which corresponds to the pixels representing the particle; and one at high intensities centred around 0.68, which corresponds to the pixels representing the background. To extract the data from the recorded video, we apply image thresholding on each frame which divides the histogram of the image into two regions, namely the particle and the background. We use the function *greythresh* in Matlab which applies a common image thresholding method (Otsu's method [43]) to determine the image thresholding level. In Figure 4.5a the calculated thresholding level is highlighted as a purple dashed line in Figure 4.5b. We use the calculated threshold intensity level to generate a binary image where the pixel intensity values below threshold are

set to one (white, particle) and those above are set to zero (black, background) as shown in Figure 4.5c. To determine the particle position, we use the Matlab function *regionprops* which calculates the centre of mass in the particle region and is highlighted by the marker × in Figure 4.5d. To determine the particle orientation, we use the same Matlab function which fits the particle region to an ellipse and calculates the angle,α, between the major axis of the ellipse and the X-axis of the image. The fit result for the particle is shown as a dashed line in Figure 4.5d.

4.5   Quantifying the uncertainties in particle tracking

The videos acquired with the microscope are subject to background intensity noise which makes two consecutive video frames stochastically different. Its presence can affect the precision of our image-based analysis as it is more difficult to determine particle edges with image thresholding. Therefore, it is necessary to quantify the precision of our method and account for it in the analysis.

In this section, we use synthetic particle images with known position and orientation (the truth) to quantify the errors in our image-based analysis. For this purpose, we superimpose those images with background noise and apply our image analysis code on them to compare the results with the truth. We start this section with a description of the particle model which we use to approximate the particle shape. Then, we describe our method to generate the synthetic particle images for the error analysis. Finally, we present and discuss the results of our method with respect to our experiments.

4.5.1   Modelling HOPG microparticles for the image analysis

We approximate the particle shape as an ellipse, described by the following four parameters: major axis length, eccentricity, orientation and roughness at the edges. This approximation allows us to analyse the error as a function of the parameter values for the ellipse. Our HOPG microparticles are typically a few micrometres wide (see Figure 4.4). We therefore choose an ellipse with a major axis length of 5 µm as a representative size for the HOPG microparticle. The orientation of the ellipse is defined as the angle between the major axis and the X-axis of the image and is set to 45°. To test our image analysis code, we vary the eccentricity of the ellipse and the degree of roughness at the edges. The former is defined as $e = \sqrt{1 - \frac{b^2}{a^2}}$, where a and b are half the length of the major axis and the minor axis, respectively. This quantity describes the circularity of the ellipse where $e = 0$ implies a circular shape whereas $e = 1$ indicates a line. To introduce roughness at the edges of the ellipse, we proceed as illustrated in Figure 4.6. Figure 4.6a shows a synthetic image of an ellipse with a major axis length of 5 µm
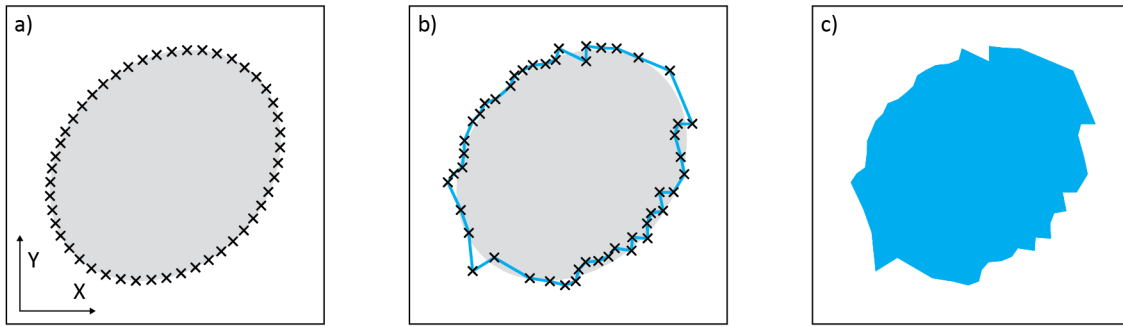
Figure 4.6: Illustration for the generation of rough edges for an ellipse with a major axis length of 5 μm and an eccentricity of 0.6. a) Synthetic image of an ellipse with a smooth edge. The points on the edge of the ellipse are highlighted with the marker symbol 'x'. b) Illustration of the random displacement of each point on the edge along the X and Y directions. The displacement length is normally distributed with zero mean and standard deviation σ_{XY} (here: $\sigma_{XY} = 0.1$ μm). The original shape of the ellipse is highlighted in gray in the background. c) Synthetic image of an ellipse with rough edges after connecting the displaced points in b).

and an eccentricity of 0.6. In the first step, we write a function extract the coordinates of 50 points on the edge of the ellipse which are highlighted with the marker 'x' in Figure 4.6a. Each point is displaced by a random amount along the X and Y directions as shown in Figure 4.6b. The displacement length for each point along both directions is normally distributed with zero mean and standard deviation σ_{XY}. The latter quantity determines the roughness of the edge: a large value σ_{XY} implies larger displacements which produces a rougher edge. For the image in Figure 4.6b, we set $\sigma_{XY} = 0.1$ μm. In the last step, we connect the displaced points to get a synthetic image of an ellipse with rough edges as shown in Figure 4.6c.

4.5.2   Generation of synthetic particle images

For the analysis, we first generate noise-free, high resolution (HighRes) synthetic particle images that have a size of 10000 pixels × 10000 pixels and where 1 μm corresponds to 1000 pixels. It follows that the HighRes image presents an area of size 10 μm × 10 μm and the pixel-to-μm conversion factor is $c_{HighRes} = 10^{-3} \frac{\mu m}{pixel}$. In order to quantify the particle localisation and orientation detection errors in our experiments, we must account for two effects: first, the image resolution is lower than the one of the HighRes image when we use the 10× and 40× objectives for imaging; and second, the acquired images in our experiments are subject to background intensity noise. In the following two subsections, we describe the integration of both effects into the synthetic particle image generation process.

Reducing the image resolution

Our goal is to reduce the resolution of the HighRes image to the one in images acquired with the microscope and the objectives in Table 4.1. To calculate the low resolution (LowRes) image, we determine the amount of pixels needed to cover the 10 μm × 10 μm area on the HighRes image with our microscope. By using the measured conversion factors in Table 4.2, we find that the area on the HighRes image is equivalent to 22 pixels × 22 pixels with the 10× objective and 85 pixels × 85 pixels with the 40× objective. The resolution reduction is illustrated in Figure 4.7. First, we divide HighRes synthetic particle image (Figure 4.7a) into equal rectangular sections along the X- and Y-axes. Then, we integrate over each rectangular section to get the average pixel intensity value and set it equal to the intensity of a pixel on the LowRes image. The resulting images for the 10× and 40× objective are presented in Figure 4.7b and Figure 4.7c, respectively.
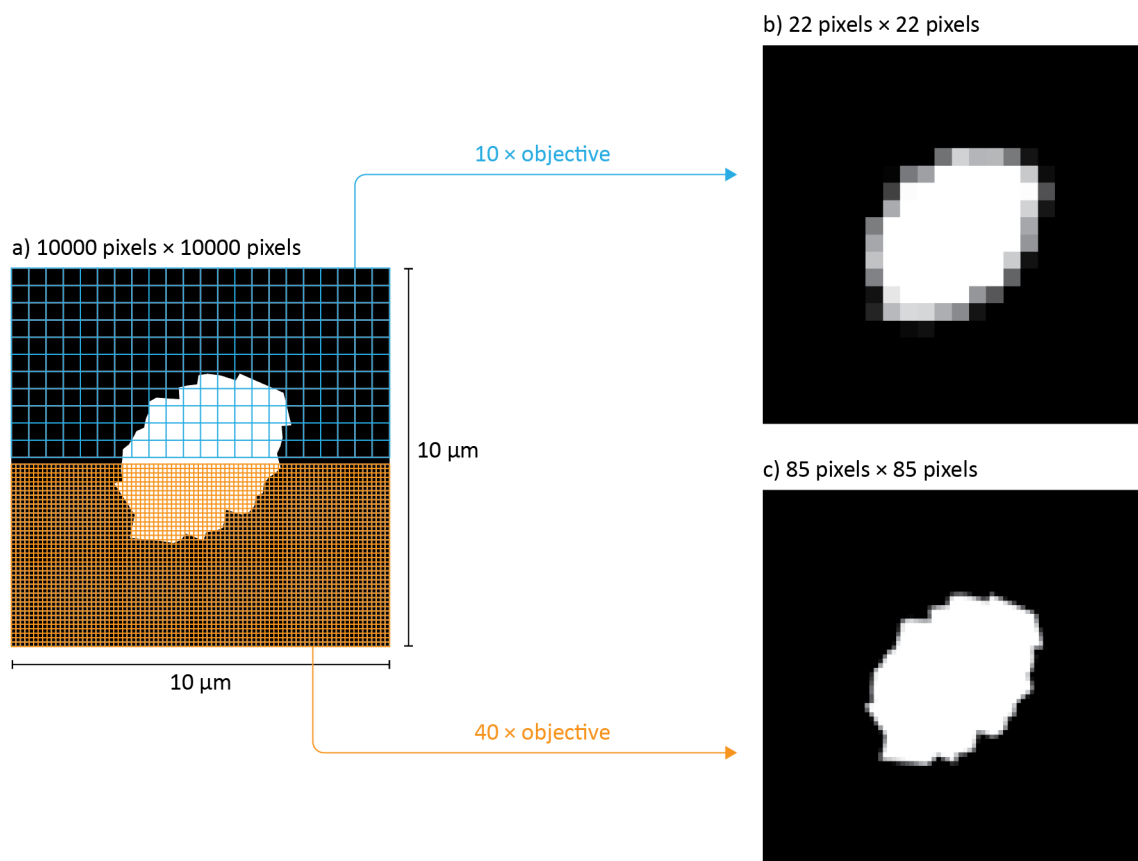
Figure 4.7: Generation of low resolution synthetic particle images corresponding to images acquired with a 10× and 40× microscope objective. a) High resolution synthetic particle image. The image size is 10000 pixels × 10000 pixels which is equivalent to 10 μm × 10 μm. b) Low resolution synthetic particle image corresponding to the image taken with a 10× objective. c) Low resolution synthetic particle image corresponding to the image taken with a 40× objective.

Adding background intensity noise to the synthetic particle image

In order to add background intensity noise to the synthetic particle image, we assume this noise to be normally distributed with zero mean and standard deviation σ_{noise}. To describe the particle intensity with respect to the background noise, we use the signal-to-noise ratio (SNR), defined as:

$$\text{SNR} = \frac{\mathcal{I}_{\text{noise}} - \mathcal{I}_{\text{particle}}}{\sigma_{\text{noise}}}, \tag{4.2}$$

where $\mathcal{I}_{\text{particle}}$ is the particle intensity and $\mathcal{I}_{\text{noise}}$ is the average background intensity. The SNR values in our experiments vary as we use different microscope objectives and camera settings to record the videos in each of them. Therefore, for each of the experiments described in Chapters 5 to 7, we measure the values for $\mathcal{I}_{\text{particle}}$, $\mathcal{I}_{\text{noise}}$, σ_{noise} from our acquired videos. To determine $\mathcal{I}_{\text{particle}}$ we choose the maximum particle intensity value in the videos. To determine $\mathcal{I}_{\text{noise}}$ and σ_{noise}, we select a region in our experimental videos where no objects are present and fit the pixel intensity distribution to a Gaussian function. From the fit, we extract the mean background intensity for $\mathcal{I}_{\text{noise}}$ and the standard deviation for σ_{noise}. The extracted variables, the SNR and the microscope objective used in the corresponding experiments are summarised in Table 4.3. We can see that the SNR values are between 12 and 47, which is sufficient to enable an easy automatic detection of the HOPG microparticles. For our uncertainty analysis, we use these SNR values to generate the background noise and add them to our synthetic images. The generation and addition of noise to our image is realised with the standard Matlab function *imnoise*.

Experiment	$\mathcal{I}_{\text{particle}}$	$\mathcal{I}_{\text{noise}}$	σ_{noise}	SNR	Obj. mag.	Ref. name
Chapter 5	0.1	0.58	0.04	12	$40\times$	40xLowSNR
Chapter 6	0.35	0.82	0.01	47	$10\times$	10xHighSNR
Chapter 7	0.1	0.70	0.03	20	$10\times$	10xLowSNR

Table 4.3: Measured values of $\mathcal{I}_{\text{particle}}$, $\mathcal{I}_{\text{noise}}$, σ_{noise} and the SNR for the experiments in Chapters 5 to 7. Obj. mag.: Magnification of the objective used in the corresponding experiment. Ref. name: reference name for the error discussions in the particle localisation and orientation detection.
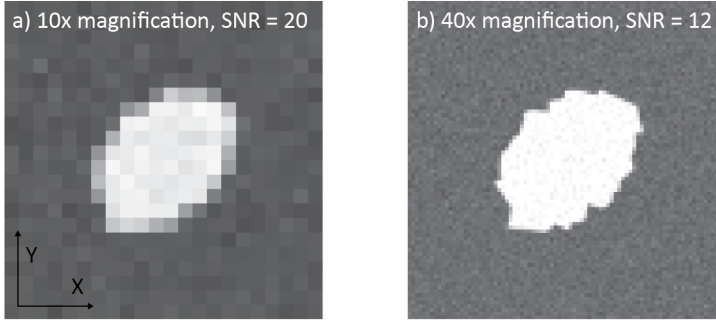
Figure 4.8: Examples of synthetic particle images with Gaussian background intensity noise. a) Synthetic particle image with a resolution of the $10 \times$ objective and a SNR of 20. b) Synthetic particle image with a resolution of the $40 \times$ objective and a SNR of 12.

To illustrate the noise generation, in Figure 4.8 we show the synthetic particle image with background noise. Figure 4.8a shows the synthetic particle image in Figure 4.7b with background intensity noise corresponding to a SNR value of 20. Figure 4.8b shows the image in Figure 4.7c with background intensity noise corresponding to a SNR value of 12.

4.5.3 Extracting the particle localisation and orientation detection errors from the synthetic particle images

To calculate the error, we do a total of 100 iterations where for each iteration, i, we add noise to the image and determine the positions X_i and Y_i and orientation α_i of the ellipse. The corresponding values of the truth are X_0, Y_0 and α_0. The discrepancy between the measurement and the truth is evaluated by calculating the root mean squared error (RMSE) defined as $\text{RMSE}_X = \sqrt{\langle (X_i - X_0)^2 \rangle}$, $\text{RMSE}_Y = \sqrt{\langle (Y_i - Y_0)^2 \rangle}$ for the position on the X- and Y-axes and $\text{RMSE}_\alpha = \sqrt{\langle (\alpha_i - \alpha_0)^2 \rangle}$ for the orientation. The angle brackets specify the average for all iterations. The RMSE for the particle position is converted from pixels into micrometres using the conversion factors listed in Table 4.2.

We analyse the particle orientation in Chapter 5 with a $40 \times$ objective. The particle location is analysed in the experiments presented in Chapters 6 and 7 using a $10 \times$ objective. For that reason, we evaluate the orientation detection errors for synthetic particle images generated with the parameters specified by '40xLowSNR' in Table 4.3. As for the particle localisation errors, we analyse synthetic particle images generated with the parameters specified by '10xLowSNR' and '10xHighSNR' in Table 4.3.

4.5.4 Errors for elliptical shaped particles

We evaluate the RMSE for the particle position and orientation as a function of eccentricity, e, and roughness parameter, σ_{XY}. For e, we select values between 0.4 and 0.9 and for σ_{XY}, we chose values between 0 and 0.25 µm. As an illustration, in Figure 4.9 we show three synthetic particle images of a smooth ellipse ($\sigma_{XY} = 0$) for different values of e: 0.4, 0.6 and 0.9. Figure 4.10 shows three images of an ellipse with e = 0.9 for three different values of σ_{XY}: 0, 0.05 µm and 0.1 µm.
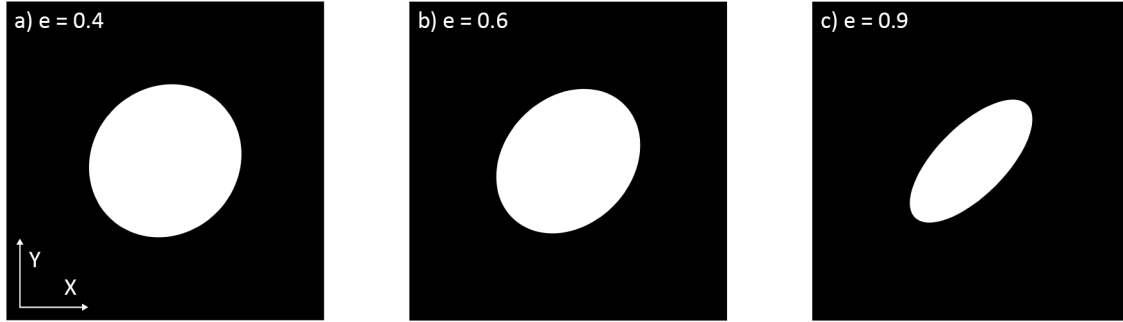
Figure 4.9: Synthetic images of an ellipse with σ_{XY} =0 for different eccentricities. a) e=0.4. b) e=0.6. c) e=0.9.
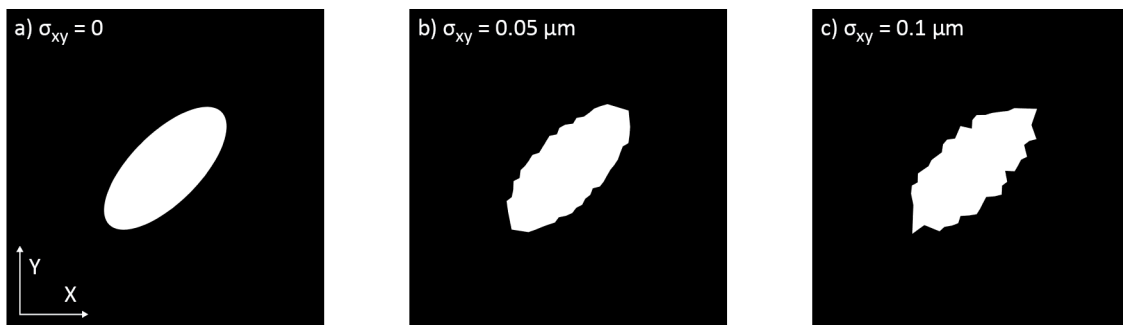
Figure 4.10: Synthetic images of an ellipse with e = 0.9 for different roughness parameter values. a) $\sigma_{XY} = 0$. b) σ_{XY} =0.05 µm. c) $\sigma_{XY} = 0.1$ µm.

Since the edge roughness of the ellipse is generated randomly, the RMSE values of two synthetic particle images constructed with the same e and σ_{XY} values are different. To account for this variation for each combination of e and σ_{XY}, we proceed as follows: first, we generate 100 synthetic particle images and calculate the RMSE for each of them; then, for the uncertainty analysis we take the mean and standard deviation of these values. That way, the standard deviation of the RMSE represents the variation due to the edge roughness.

Particle localisation error

For synthetic particle images with no edge roughness ($\sigma_{XY} = 0$), the localisation errors in the X and Y directions are close to zero. Figure 4.11a shows the average values and standard deviations for RMSE$_X$ and RMSE$_Y$ as a function of eccentricity for $\sigma_{XY} = 0.1\,\mu$m. We can see that the overall localisation error is in the range $0.01 - 0.02\,\mu$m.

Figure 4.11b shows the localisation error as a function of σ_{XY} for e $= 0.4$. Initially, the error increases with σ_{XY} and then saturates for $\sigma_{XY} > 0.1\,\mu$m at around $0.02\,\mu$m and $0.01\,\mu$m for low and high SNR values, respectively.

From the particle localisation error analysis, we can see that the overall error is below $0.03\,\mu$m. As expected, the particle localisation error is low if the SNR in the image is high. With respect to our particle localisation experiments in Chapters 6 and 7, the calculated error is low as the range of linear displacements is between $1\,\mu$m and $100\,\mu$m.
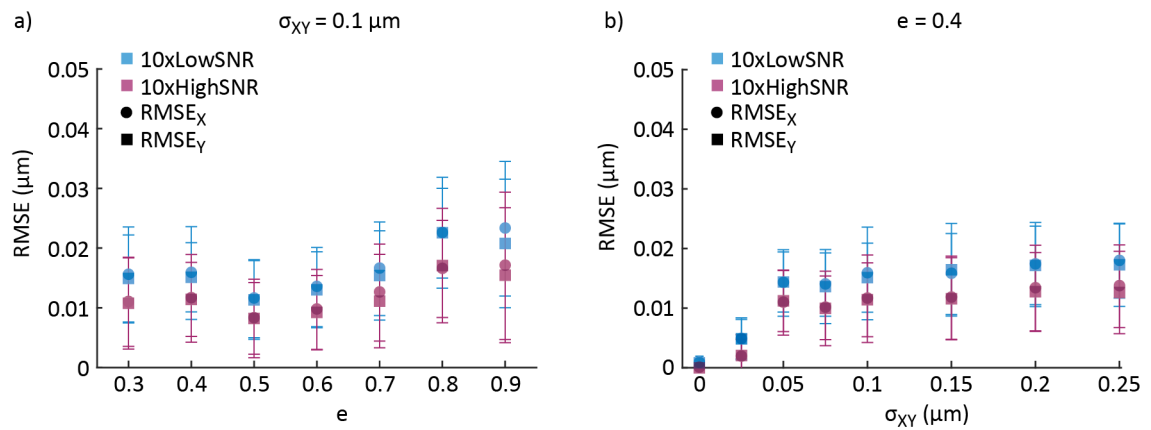
Figure 4.11: Calculated average root mean squared error and standard deviation for the particle localisation in the X and Y directions. a) Error as a function of eccentricity, e, for an ellipse with $\sigma_{XY} = 0.1\,\mu$m. b) Error as a function of roughness parameter, σ_{XY}, for an ellipse with e $= 0.4$. The average error and corresponding standard deviation are calculated from 100 synthetic particle images with the same values for e and σ_{XY}. The particle in each of these images has a different shape due to the generated edge roughness. '10xHighSNR': Error calculated for the experiment in Chapter 6. '10xLowSNR': Error calculated for the experiment in Chapter 7.

Orientation detection error

Figure 4.12a shows a plot of the RMSE_α as a function of eccentricity for ellipses with $\sigma_{XY} = 0$. We can see that the error decreases with increasing eccentricity: at $\mathrm{e} = 0.4$, the error is roughly at $0.6\,°$ which continuously decreases to $0.1\,°$ at $\mathrm{e} = 0.9$. This behaviour is expected since ellipses with a low eccentricity are more circular which makes it more difficult to identify the major axis and extract the particle orientation from the fit.

Figure 4.12b shows the RMSE_α as a function of σ_{XY} for $\mathrm{e} = 0.9$. We can see that the average value for RMSE_α is consistently around $0.1°$ for all values of σ_{XY}. This shows that our image analysis code can reliably determine the orientation of particles with rough edges as long as the particle shape is elongated.

In our experiments, particles have eccentricity values around 0.9 and the angular displacements are in the range $5° - 90°$. The corresponding error in our detection is around $0.2\,°$ which is small compared to the angular displacement range.
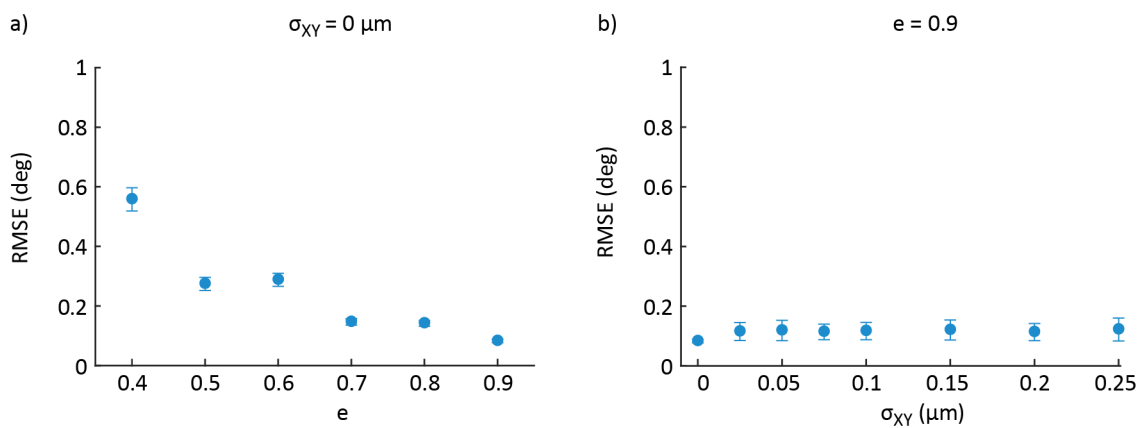
Figure 4.12: Calculated average root mean squared error and standard deviation for the particle orientation detection in Chapter 5. a) Error as a function of eccentricity, e, for an ellipse with $\sigma_{XY} = 0$. b) Error as a function of roughness parameter, σ_{XY}, for an ellipse with $\mathrm{e} = 0.9$. The average error and corresponding standard deviation are calculated from 100 synthetic particle images with different background intensity noise. The particle in each of these images has a different shape due to the generated edge roughness.

4.5.5 Errors for non-elliptical shaped particles

In addition to the elliptical particle shape, we test our image analysis code on shapes that have a closer resemblance to our HOPG microparticles in the experiments (see Figure 4.4). For this purpose, we generate synthetic images of randomly shaped polygons with three to five edges.

The synthetic particle images and the calculated errors are shown in Figures 4.13 to 4.15. We can see that the errors for the particle localisation and orientation detection are in the range $0.01 - 0.03\,\mu$m and $0.05 - 0.22°$, respectively. Therefore, these errors are in the same range as calculated for elliptical shaped particles.
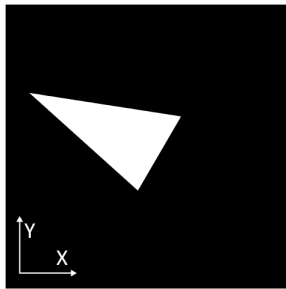
Reference Name	RMSE$_X$ (μm)	RMSE$_Y$ (μm)	RMSE$_\alpha$ (deg)
10xLowSNR	0.03	0.02	-
10xHighSNR	0.01	0.01	-
40xLowSNR	-	-	0.14

Figure 4.13: Left hand side: Synthetic particle image of a polygon with three edges. Right hand side: Calculated root mean squared errors for the particle localisation on the X- and Y-axes and for the orientation detection.
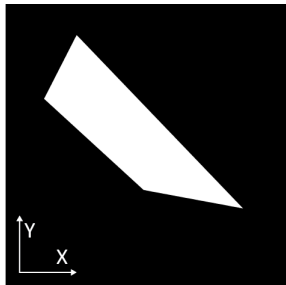
Reference Name	RMSE$_X$ (μm)	RMSE$_Y$ (μm)	RMSE$_\alpha$ (deg)
10xLowSNR	0.01	0.02	-
10xHighSNR	0.01	0.02	-
40xLowSNR	-	-	0.05

Figure 4.14: Left hand side: Synthetic particle image of a polygon with four edges. Right hand side: Calculated root mean squared errors for the particle localisation on the X- and Y-axes and for the orientation detection.
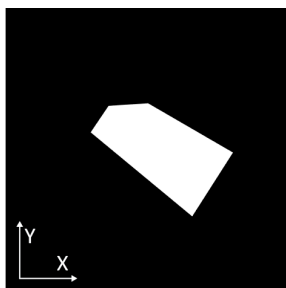
Reference Name	RMSE$_X$ (μm)	RMSE$_Y$ (μm)	RMSE$_\alpha$ (deg)
10xLowSNR	0.02	0.02	-
10xHighSNR	0.01	0.004	-
40xLowSNR	-	-	0.22

Figure 4.15: Left hand side: Synthetic particle image of a polygon with five edges. Right hand side: Calculated root mean squared errors for the particle localisation on the X- and Y-axes and for the orientation detection.

4.6 Summary

In this section, we introduced our optical imaging system to analyse the particle manipulation in solution. The system consists of a purpose-built transmission microscope that monitors the particle with a camera. We have described how the acquired videos are analysed with our own image analysis code written in Matlab to extract the particle size, position and orientation. We introduced methods to evaluate the minimum measurable particle size and the errors in the particle localisation and orientation detection. The results of this analysis are summarized in Table 4.4. The localisation and orientation detection errors are at least one order of magnitude smaller than the range of linear and angular displacements in our experiments.

Uncertainty type	Uncertainty value
Orientation detection error in Chapter 5	0.2°
Localisation error in Chapter 6	0.02 μm
Localisation error in Chapter 7	0.03 μm

Table 4.4: Summary of uncertainties for the image-based particle analysis in this thesis.

Chapter 5

Magneto-electric orientation of HOPG microparticles

5.1 Introduction

Graphitic materials such as HOPG or graphene have anisotropic electrical, magnetic, optical and mechanical properties as mentioned earlier in Chapter 2. Because of these properties, particles made of such materials can be oriented with external fields. This feature opens up possibilities for innovative applications including the generation of artificial materials with enhanced electrical or thermal properties [44–46], electric and magnetic switching of liquid crystal displays [47, 48, 12, 49, 11, 13] and the improvement of batteries [50, 14, 15].

To align a large array of particles, e.g. a sheet of aligned graphene microparticles, studies have used techniques such as vacuum filtration [44] and chemical vapour deposition [51]. Those techniques, however, are costly and do not allow full control over the orientation of the particles. To date, only few studies have looked into the alignment of graphitic particles in solution with electric and magnetic fields. The orientation with AC electric fields has been demonstrated for graphene flakes in a nematic liquid crystal medium [48, 49] and for graphene oxide liquid crystals [12]. The orientation with magnetic fields has been demonstrated for graphene oxide [47, 46] and for graphite [52, 50]. All studies reviewed lack of full control of the particle orientation as particles in single orienting fields (either electric or magnetic) can still rotate freely around an axis parallel to the field direction.

In this chapter, we demonstrate the alignment and full orientational confinement of HOPG microparticles in solution with a combination of an AC electric field operating at MHz frequencies and a static magnetic field. We analyse the rotational motion of individual particles in solution and evaluate the potential of our HOPG rotational trapping method as a tool

for torque application and sensing. Our HOPG microparticles are coated with a layer of the phospholipid POPC and dispersed in a 20 mM NaCl aqueous solution. We first present the specific theoretical framework that follows from Chapter 3 to highlight the criteria for electric and magnetic orientation. In the subsequent section, we describe our experimental setup and the methods to acquire our data. We then present our results demonstrating full confinement of the HOPG microparticle orientation to a plane of our choice. We conclude this chapter by outlining potential applications and future developments.

5.2 Principles of magnetic and electrical orientation

In this section, we present the theoretical framework for electric and magnetic torques on lipid-coated HOPG microparticles in solution. The theory describing the electric and magnetic orientation of such particles is not necessarily intuitive as it depends on many factors such as the particle shape and the electrical and magnetic properties of the particle, the lipid layer and the solution.

In our experiment, we first apply a vertical static magnetic field, $\mathbf{B}_0$, to orientate the graphene planes in the HOPG particle in the vertical direction (see Figure 5.1a). Once oriented, the particle can rotate freely around the vertical axis (here: y-axis). We then turn on an AC electric field, $\mathbf{E}_0(t)$, in the horizontal direction, which causes the particle to rotate around the vertical axis until the graphene planes are parallel to the electric field direction (see Figure 5.1b).

For the theoretical description, we apply the effective moment method described in Chapter 3. We use the same particle frame of reference, where the x-y plane is parallel to the graphene planes in the particle and the z-axis is normal to the plane. Additionally, we introduce a laboratory frame of reference with the axes X, Y and Z as shown in Figure 5.1a. Without loss of generality, we set $\mathbf{B}_0$ along the Z direction and $\mathbf{E}_0(t)$ along the X direction.
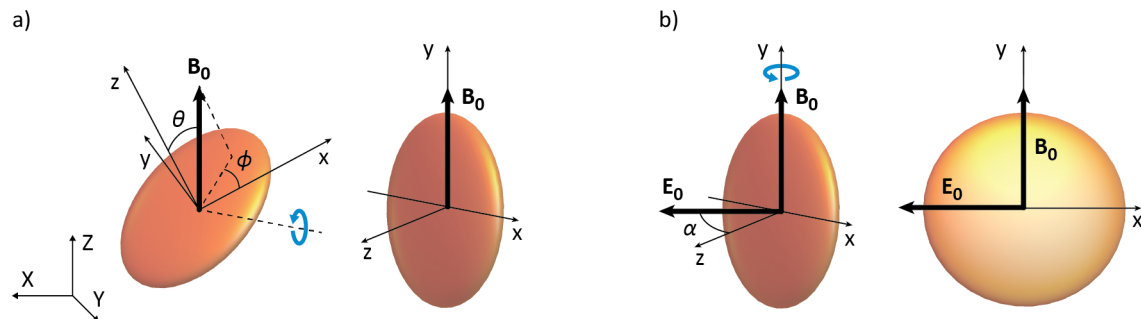
Figure 5.1: Illustration of the magneto-electric orientation of lipid-coated HOPG microparticles modelled as an ellipsoid. a) Vertical alignment of the HOPG microparticle upon exposure to a magnetic field $\mathbf{B}_0$ along the Z direction. b) Horizontal alignment of the HOPG microparticle upon additional application of a horizontal electric field $\mathbf{E}_0$ in the X direction.

5.2.1 Magnetic orientation of lipid-coated HOPG microparticles

For the description of the magnetic torque on the particle, we assume a constant magnetic field with magnitude B_0. To account for the orientation of the particle with respect to the magnetic field we introduce spherical polar coordinates (θ, ϕ) as shown in Figure 5.1a. This allows us to express the magnetic field as:

$$\mathbf{B}_0 = B_{0,x}\hat{\mathbf{x}} + B_{0,y}\hat{\mathbf{y}} + B_{0,z}\hat{\mathbf{z}} = B_0\left(\sin\theta\cos\phi\,\hat{\mathbf{x}} + \sin\theta\sin\phi\,\hat{\mathbf{y}} + \cos\theta\,\hat{\mathbf{z}}\right), \tag{5.1}$$

where $B_{0,x}$, $B_{0,y}$ and $B_{0,z}$ are the magnetic field components and $\hat{\mathbf{x}}$, $\hat{\mathbf{y}}$ and $\hat{\mathbf{z}}$ are the unit vectors along the x-, y- and z-axes in the particle frame of reference. To calculate the magnetic torque $\boldsymbol{\mathcal{T}}_{mag} = \mathbf{m}_{eff} \times \mathbf{B}_0$, we use Equation (5.1) and the expression for $\mathbf{m}_{eff}$ from Equation (3.14), which results in:

$$\mathbf{m}_{eff} = \frac{V_1}{\mu_0}\begin{pmatrix} \left(\chi_\parallel - \chi_1\right)B_{0,x} \\ \left(\chi_\parallel - \chi_1\right)B_{0,y} \\ \left(\chi_\perp - \chi_1\right)B_{0,z} \end{pmatrix}, \tag{5.2}$$

where V_1 is the volume of the lipid-coated HOPG microparticle, χ_1 is the magnetic susceptibility of the solution and $\chi_\parallel$ and $\chi_\perp$ are the magnetic susceptibilities of HOPG in the in-plane and out-of-plane directions, respectively. In the resulting expression for the magnetic torque, the only non-zero components are the ones along the x direction $(\mathcal{T}_{mag,x})$ and the y direction $(\mathcal{T}_{mag,y})$. This implies that for a fixed magnetic field direction, the induced torque vector is always parallel to the graphene planes. Consequently, the particle will always rotate around an axis on the x-y plane until it reaches orientational equilibrium. The magnitude of the torque is given by:

$$|\boldsymbol{\mathcal{T}}_{mag}| = \frac{V_1}{2\mu_0}\left(\chi_\parallel - \chi_\perp\right)\sin\left(2\theta\right)B_0^2. \tag{5.3}$$

From Equation (5.3), we can see that the magnetic torque on the particle depends on the anisotropic magnetic properties of HOPG, i.e. $\left(\chi_\parallel - \chi_\perp\right) \neq 0$, but not on the magnetic susceptibility of the solution. Furthermore, the magnetic torque depends on the applied field and on the particle volume but it is independent of the particle shape. The magnitude of the torque reaches its maximum value, $\mathcal{T}_{mag,max} = \frac{V_1}{2\mu_0}\left(\chi_\parallel - \chi_\perp\right)B_0^2$, for $\theta = \pm 45°$.

In a constant magnetic field, the magnetic potential energy, U_{mag}, of the particle is:

$$\begin{aligned}
U_{mag} &= -\int_0^{B_0}\mathbf{m}_{eff}\left(B\right)\cdot\mathrm{d}\mathbf{B} \\
&= -\frac{V_1 B_0^2}{2\mu_0}\left[\left(\chi_\parallel - \chi_1\right) + \left(\chi_\perp - \chi_\parallel\right)\cos^2\theta\right],
\end{aligned} \tag{5.4}$$

where $d\mathbf{B} = dB \begin{pmatrix} \sin\theta\cos\phi \\ \sin\theta\sin\phi \\ \cos\theta \end{pmatrix}$. The integration over B accounts for the work required to

generate the magnetic dipole in the particle. The orientations of stable equilibrium, θ_0, are those where the potential energy is minimized, i.e. they must satisfy $\frac{\partial U_{\text{mag}}}{\partial\theta} = 0$ and $\frac{\partial^2 U_{\text{mag}}}{\partial\theta^2} > 0$ at $\theta = \theta_0$. By applying both conditions, we find that θ_0 depends on the sign of $\left(\chi_\perp - \chi_\parallel\right)$. For HOPG, this difference is negative because $\chi_\perp < \chi_\parallel < 0$, which implies a stable equilibrium at $\theta_0 = \pm 90°$ so that the graphene planes align parallel to the magnetic field direction.

5.2.2 Electric orientation of lipid-coated HOPG particles

We now focus on the electric orientation of lipid-coated HOPG particles in solution in the presence of an AC electric field at MHz frequencies. In comparison to the magnetic case, the electric one is more complex because the contributions of the lipid layer and the solution cannot be neglected and the electrical conductivity of all components introduces a dependency on the electric field frequency. We derive the electric torque on a lipid-coated HOPG microparticle with induced effective electric dipole moment $\mathbf{p}_{\text{eff}}\left(t\right)$ exerted by a linearly polarised AC electric field $\mathbf{E}\left(t\right)$. As described in Section 3.1, we use the complex permittivity to account for the relative permittivity and electrical conductivity of the HOPG core, the lipid layer and the solution. It is given by $\epsilon = \varepsilon - i\frac{\sigma}{\varepsilon_0\omega}$, where $\omega = 2\pi f$ is the angular frequency of the AC electric field. Following the complex notation, we express the electric field as $\mathbf{E}\left(t\right) = \mathbf{E}_0 e^{i\omega t}$ where $\mathbf{E}_0$ is the complex and time-independent electric field vector. Similarly, $\mathbf{p}_{\text{eff}}\left(t\right) = \mathbf{p}_{\text{eff},0} e^{i\omega t}$ is the induced complex effective electric dipole moment of the layered ellipsoid, where $\mathbf{p}_{\text{eff},0}$ is the corresponding complex and time-independent vector. As described in [53], the instantaneous electric torque acting on the particle in solution is then given by:

$$\mathcal{T}_{\text{el}} = \text{Re}[\mathbf{p}_{\text{eff}}\left(t\right)] \times \text{Re}[\mathbf{E}\left(t\right)]. \tag{5.5}$$

Equation (5.5) results in two terms: one constant average term and one that oscillates at twice the angular frequency. For micron-sized particles, the rotational motion is strongly damped by the dominant viscosity of the solution. As a result, the latter term in Equation (5.5) can be neglected and only the time-averaged electric torque is relevant, expressed as:

$$\langle\mathcal{T}_{\text{el}}\rangle = \frac{1}{2}\text{Re}\left[\mathbf{p}_{\text{eff},0} \times \mathbf{E}_0^*\right], \tag{5.6}$$

where $\mathbf{E}_0^*$ is the complex conjugate of $\mathbf{E}_0$. To calculate the electric torque on lipid-coated HOPG particles, we use the effective electric dipole moment in Equation (3.6) with the com-

ponents $p_{\text{eff},0,\text{k}} = V_1 \varepsilon_1 \varepsilon_0 K_k E_{0,\text{k}}$ and substitute the expression into Equation (5.6). Then, the components of the time-averaged electric torque take the form:

$$\langle \mathcal{T}_{\text{el},\text{x}} \rangle = \frac{1}{2} \text{Re} \left[p_{\text{eff},0,\text{y}} E_{0,\text{z}}^* - p_{\text{eff},0,\text{z}} E_{0,\text{y}}^* \right]$$
$$= \frac{1}{2} V_1 \varepsilon_1 \varepsilon_0 \text{Re} \left[K_\text{y} E_{0,\text{y}} E_{0,\text{z}}^* - K_\text{z} E_{0,\text{z}} E_{0,\text{y}}^* \right] ,$$

(5.7)

$$\langle \mathcal{T}_{\text{el},\text{y}} \rangle = \frac{1}{2} \text{Re} \left[p_{\text{eff},0,\text{z}} E_{0,\text{x}}^* - p_{\text{eff},0,\text{x}} E_{0,\text{z}}^* \right]$$
$$= \frac{1}{2} V_1 \varepsilon_1 \varepsilon_0 \text{Re} \left[K_\text{z} E_{0,\text{z}} E_{0,\text{x}}^* - K_\text{x} E_{0,\text{x}} E_{0,\text{z}}^* \right] ,$$

(5.8)

$$\langle \mathcal{T}_{\text{el},\text{z}} \rangle = \frac{1}{2} \text{Re} \left[p_{\text{eff},0,\text{x}} E_{0,\text{y}}^* - p_{\text{eff},0,\text{y}} E_{0,\text{x}}^* \right]$$
$$= \frac{1}{2} V_1 \varepsilon_1 \varepsilon_0 \text{Re} \left[K_\text{x} E_{0,\text{x}} E_{0,\text{y}}^* - K_\text{y} E_{0,\text{y}} E_{0,\text{x}}^* \right] ,$$

(5.9)

where K_x, K_y and K_z are the components of the complex effective polarisation factor in Equation (3.7) that account for the electric field frequency, the particle shape and the electrical properties of the particle, lipid-coating and solution. This amount of dependencies is in contrast to the magnetic case where the magnetic anisotropy of the HOPG core is the only relevant factor for the magnetic orientation (see Equation (5.3)).

With respect to our experiment, we can further simplify Equations (5.7) to (5.9) as we apply the horizontal AC electric field once the lipid-coated HOPG microparticle has been vertically aligned with the static magnetic field (see Figure 5.1b). For the description, we set the electric field along the X-axis as shown in Figure 5.1b and fix the phase of the electric field. Then, we can express the electric field in the particle frame of reference as a real vector given by $\mathbf{E}_0 = E_0 \left(\sin\alpha\, \hat{\mathbf{x}} + \cos\alpha\, \hat{\mathbf{z}} \right)$, where $E_0 = |\mathbf{E}_0|$ is the electric field amplitude and α is the angle between the z-axis and the electric field direction. By substituting $\mathbf{E}_0$ into Equations (5.7) to (5.9), the electric torque components in the x and z directions vanish and the component in the y direction is given as:

$$\langle \mathcal{T}_\parallel \rangle = \frac{1}{4} V_1 \varepsilon_1 \varepsilon_0 E_0^2 \sin(2\alpha) \, \text{Re} \left[K_\perp - K_\parallel \right]$$
$$= -\mathcal{T}_{\text{el,max}} \sin(2\alpha) ,$$

(5.10)

where we use $\langle \mathcal{T}_\text{y} \rangle = \langle \mathcal{T}_\parallel \rangle$, $K_\text{x} = K_\parallel$ and $K_\text{z} = K_\perp$ to highlight that the x and y directions are parallel ($\parallel$) to the HOPG particle planes and the z direction is perpendicular ($\perp$) to these planes. We have also defined:

$$\mathcal{T}_{\text{el,max}} = \frac{1}{4} V_1 \varepsilon_1 \varepsilon_0 E_0^2 \text{Re} \left[K_\parallel - K_\perp \right] ,$$

(5.11)

which is the maximum amplitude of the electric torque at $\alpha = \pm 45°$. Consequently, in the

presence of a horizontal AC electric field, the vertically aligned particle will rotate around the vertical axis (Z-axis) until it reaches orientational equilibrium.

To illustrate the frequency dependency of the maximum electric torque, we calculate $\mathcal{T}_{\text{el,max}}$, $\text{Re}\left[K_{\parallel}\right]$ and $\text{Re}\left[K_{\perp}\right]$ for a lipid-coated HOPG microparticle in a 20 mM NaCl aqueous solution. We use the typical particle size in our experiments: $a_1 = 3.3\,\mu\text{m}$, $b_1 = 1.85\,\mu\text{m}$, $c_1 = 0.7\,\mu\text{m}$. Furthermore, we chose $\delta = 0.17\,\mu\text{m}^2$ so that the thickness of the lipid-coating over the entire particle is between 4 nm and 20 nm. The values for the electrical properties are taken from the literature: for the solution, we use $\varepsilon_1 = 80$ and $\sigma_1 = 0.2\,\text{S/m}$ as reported in [54]; for the lipid layer, we use $\varepsilon_2 = 11$ and $\sigma_2 = 10^{-7}\,\text{S/m}$ as reported in [37]; and for the HOPG core, we chose the average values from Table 2.1: $\epsilon_{\parallel} = 2.54$, $\sigma_{\parallel} = 2.1 \times 10^6\,\text{S/m}$, $\epsilon_{\perp} = 1.85$ and $\sigma_{\perp} = 550\,\text{S/m}$. The electric field amplitude is set to $1.5 \times 10^{-2}\,\text{V}/\mu\text{m}$ which is a typical value in our experiments. Figure 5.2a shows a plot of the maximum electric torque as a function of the electric field frequency. The corresponding plots of $\text{Re}\left[K_{\parallel}\right]$ and $\text{Re}\left[K_{\perp}\right]$ are presented in Figure 5.2b. In both figures, we can see a low plateau at frequencies below 10^6 Hz and a high plateau at frequencies above 10^7 Hz. In the frequency range between 10^6 Hz and 10^7 Hz, all three quantities increase monotonically with frequency. This characteristic frequency dependency is caused by the phospholipid bilayer shell which is electrically insulating and polarises in the presence of an electric field. The electric polarisation gives rise to a large capacitive impedance that decreases with increasing field frequency. Because of this effect, at frequencies below 10^6 Hz the lipid-shell reduces the effective electric dipole moment to the point where $\mathcal{T}_{\text{el,max}}$, $\text{Re}\left[K_{\parallel}\right]$ and $\text{Re}\left[K_{\perp}\right]$ are reduced. As the frequency increases, the capacitive impedance decreases and the lipid-coated particle becomes electrically transparent to the field so that $\mathcal{T}_{\text{el,max}}$, $\text{Re}\left[K_{\parallel}\right]$ and $\text{Re}\left[K_{\perp}\right]$ increase with frequency as shown in the plots. At electric field frequencies above 10^7 Hz, all quantities reach a higher plateau which is caused by the resistance of the HOPG core and the solution.

The electric potential energy for a vertically aligned lipid-coated HOPG microparticle can be expressed as:

$$
\begin{aligned}
U_{\text{el}} &= -\int_0^{E_0} \text{Re}\left[\mathbf{p}_{\text{eff,0}}e^{i\omega t}\right] \cdot \text{Re}\left[e^{-i\omega t}\text{d}\mathbf{E}\right] \\
&= -\frac{V_1\varepsilon_1\varepsilon_0 E_0^2}{4}\text{Re}\left[K_{\parallel} + \left(K_{\perp} - K_{\parallel}\right)\cos^2\alpha\right],
\end{aligned}
\tag{5.12}
$$

where $\text{d}\mathbf{E} = \text{d}E\begin{pmatrix}\sin\alpha \\ 0 \\ \cos\alpha\end{pmatrix}$. Similar to Equation (5.4), the integration accounts for the work required to generate the electric dipole inside the particle.

As we can see from Figure 5.2, the relationships between the complex effective polarisation factors for lipid-coated HOPG microparticles are $\mathrm{Re}\left[K_\perp - K_\parallel\right] < 0$ and $0 < \mathrm{Re}\left[K_\perp\right] < \mathrm{Re}\left[K_\parallel\right]$. Hence, the stable equilibrium orientation that minimises the potential energy of the particle is $\alpha_0 = \pm 90°$, so that the graphene planes align parallel to the electric field direction.

Consequently, by using $\mathbf{B}_0$ and $\mathbf{E}_0(t)$ that are perpendicular to each other, the graphene planes in the HOPG microparticle are aligned in the plane spanned by both external fields. Later on, we will explain how this can be exploited for controlled orientation, rotational trapping and torque sensing in solution.
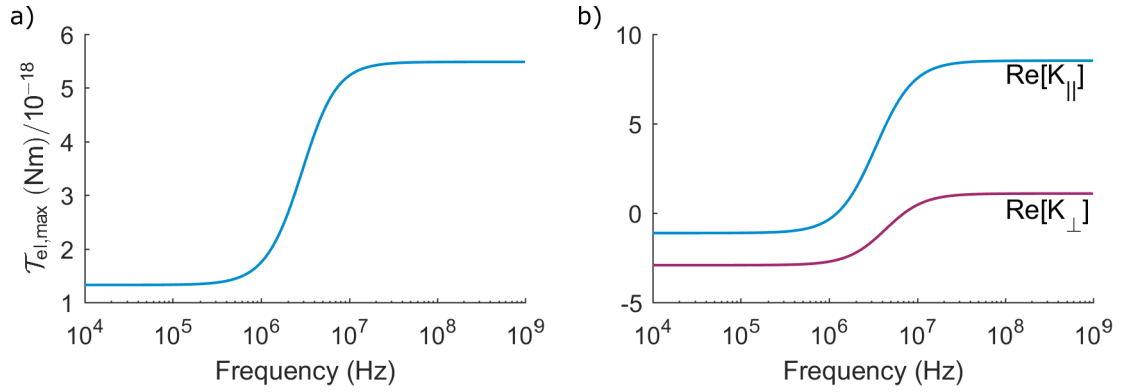
Figure 5.2: Plots of $\mathcal{T}_{\mathrm{el,max}}$, $\mathrm{Re}\left[K_\parallel\right]$ and $\mathrm{Re}\left[K_\perp\right]$ as a function of electric field frequency for lipid-coated HOPG microparticles in $20\,\mathrm{mM}$ NaCl aqueous solution. a) Plot of $\mathcal{T}_{\mathrm{el,max}}$. b) Plots of $\mathrm{Re}\left[K_\parallel\right]$ and $\mathrm{Re}\left[K_\perp\right]$. The calculations are made for a particle with size $a_1 = 3.3\,\mu\mathrm{m}$, $b_1 = 1.85\,\mu\mathrm{m}$, $c_1 = 0.7\,\mu\mathrm{m}$ and $\delta = 0.17\,\mu\mathrm{m}$.

5.3 Experimental demonstration

We study the magneto-electric orientation of individual lipid-coated HOPG microparticles in a $20\,\mathrm{mM}$ NaCl aqueous solution. To avoid particle interactions, we use a sample with a low particle concentration. The lipid-coated HOPG microparticles are produced as described in Section 2.4.1. They are fabricated from a bulk HOPG sample with a mosaic spread of $3.5° \pm 1.5°$.

5.3.1 Experimental setup

In this subsection, we describe our experimental setup to record the rotational motion of HOPG microparticles in solution and to expose them to a vertical static magnetic field and a horizontal AC electric field. Figures 5.3a and b show a photograph and a schematic of the setup, respectively. The upper part of our setup is the purpose-built upright microscope described in Chapter 4 which we use to record the rotational motion of the particle. A LED illuminates our sample from below as shown in Figure 5.3b. We image the particle with the
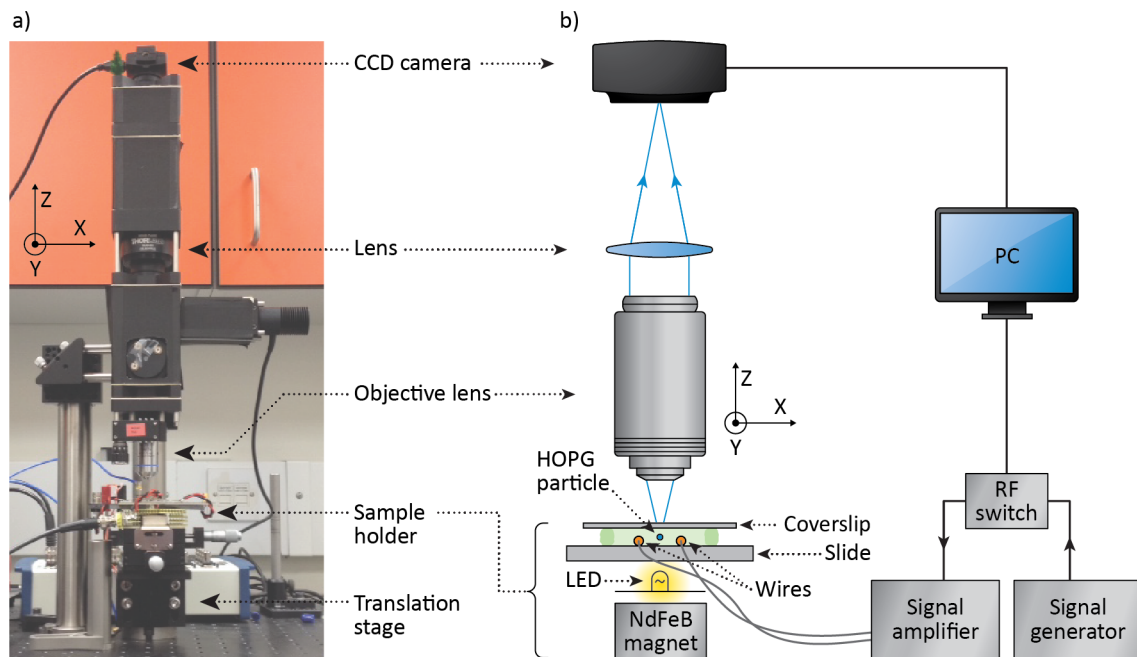
Figure 5.3: Experimental setup to study the magneto-electric orientation of lipid-coated HOPG microparticles in solution. a) Photograph of the setup. b) Schematic of the setup. The particle motion is recorded with an upright microscope that is connected to the computer. To generate the magnetic field, a NdFeB magnet is placed below the sample. To generate the electric field, a voltage from a radio frequency signal generator is applied between the wires.
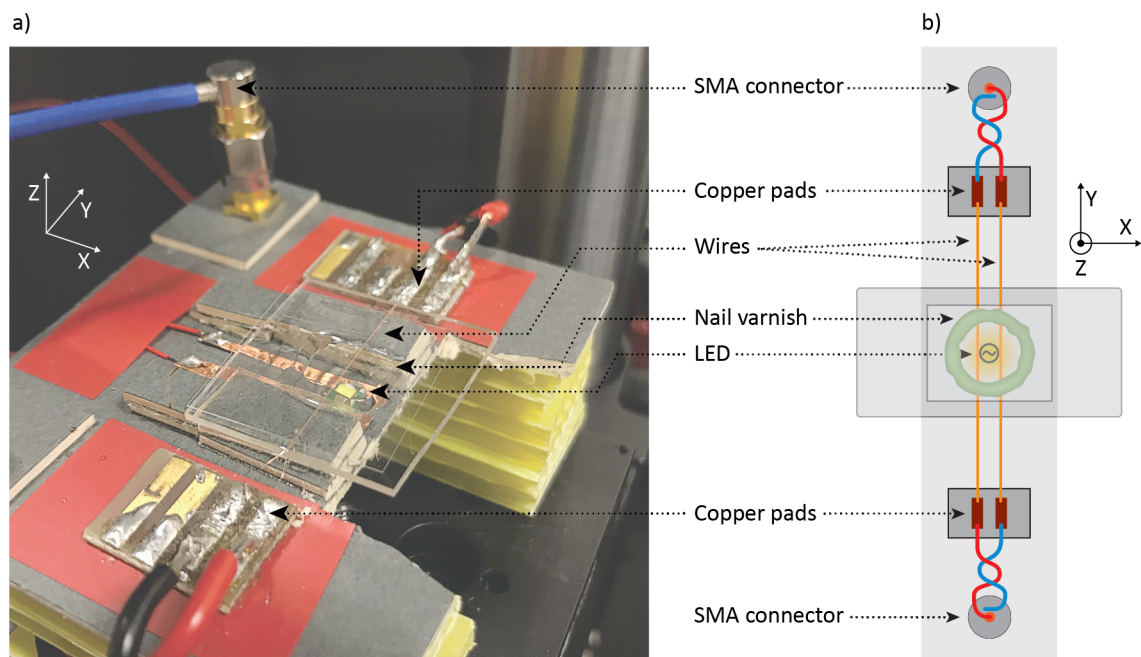
Figure 5.4: Customised sample holder for the application of a vertical static magnetic field and a horizontal AC electric field on lipid-coated HOPG microparticles in solution. a) Photograph of the sample holder. b) Schematic of the sample holder (top view). For the experiment, a slide with two parallel wires is placed on the sample holder. The wire ends are soldered onto copper pads to generate an electric field in the sample region.

40× objective (from Table 4.1) above the sample onto a CMOS camera at acquisition rates up to 150 frames per second (fps) in a 100×100 pixel wide region. By using the conversion factors from Table 4.2, we find that the reduced region covers a $12 \times 12\,\mu m$ wide area within the sample region. The lower part in the setup consists of a customized sample holder which is needed to expose the HOPG microparticles to the electric and magnetic field. The sample holder is mounted onto two translation stages allowing us to move the sample along the X and Y directions.

Figure 5.4a shows a close-up photograph of the sample holder with the corresponding schematic viewed from the top in Figure 5.4b. It is made out of cardboard and plastic pieces to avoid interferences with the applied magnetic and electric fields. On top of the sample holder there are two SMA connectors that are connected to two copper pads with twisted wires.

To generate the magnetic field, we place NdFeB magnet (Magnet Sales, part no. NIBL 01483) of size $25\,mm \times 25\,mm \times 10\,mm$ below the sample with one of its magnetic poles facing the sample. The magnet has a grade N50 which describes the maximum magnetic field strength that can be generated with it (current highest grade is N52). The vertical magnetic field component in the sample region is measured at different distances from the top surface of the magnet with a Gaussmeter. The measurement is shown in Figure 5.5. Throughout the experiment, the distance from the top surface of the magnet to the sample region is $\sim 6\,mm$, so that the magnetic field strength is $\sim 0.24\,T$ and the field gradient in the Z direction is $\sim 3 \times 10^{-5}\,T/\mu m$. Since we only select particles that are on average $\sim 7\,\mu m$ wide, the magnetic field variations over the particle volume are negligible.
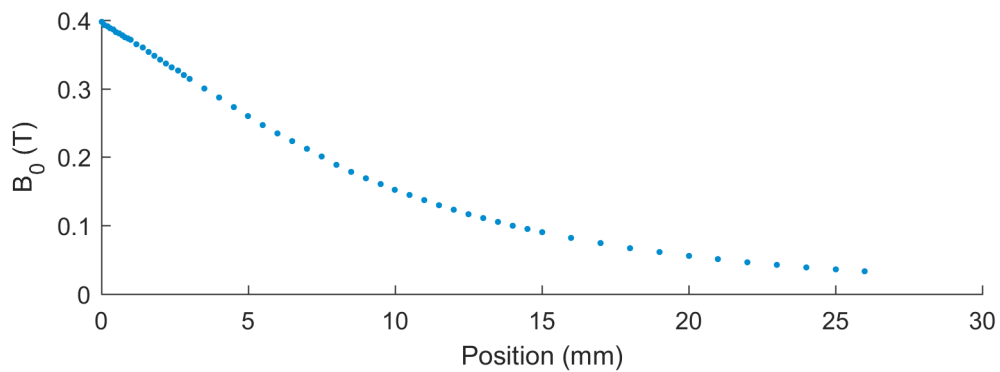
Figure 5.5: Measured vertical component of the magnetic field as a function of distance from the surface of the magnetic pole. The magnetic field is generated by a grade N50 NdFeB magnet of size $25\,mm \times 25\,mm \times 10\,mm$.

The horizontal AC electric field is generated with two parallel insulated copper wires that have a diameter of $50\,\mu m$ and an insulation thickness of $6\,\mu m$ (Brocott). We fix the wires at a centre-to-centre distance of $\sim 150\,\mu m$ onto a glass slide using nail varnish as shown in

Figure 5.4b. The ends of the wires are soldered onto the copper pads. The voltage signal is generated by a radio frequency (RF) signal generator which passes through an amplifier. In order to turn the AC electric field in the sample region on and off, we set up a RF switch (Mini Circuits, part no. MSP2TA-18-12+) between the signal generator and the amplifier as shown in Figure 5.3b. The switch is controlled with our Labview software and allows us to turn on the AC electric field and the video acquisition at the same time (see Chapter 4). We set the applied voltage amplitude to $2.3\,\text{V}$ and use frequencies in the range $1-70\,\text{MHz}$. To assess the electric field strength at the sample region we simulate our setup with the software 'Finite Element Method Magnetics' (FEMM). The result of the simulation is shown in Figure 5.6, where the electric field strength between the wires and on the glass surface is $1.5 \times 10^{-2}\,\text{V}/\text{μm}$.

For the acquisition, we place $20\,\text{μl}$ of our solution between the wires and put a cover-slip on top. We chose eight individual HOPG microparticles and measure their motion at different electric field frequencies. The average size and standard deviation of those eight particles is $(6.6 \pm 0.5)\,\text{μm} \times (3.9 \pm 1.3)\,\text{μm} \times (1.4 \pm 0.3)\,\text{μm}$ which we determined from images on the microscope as explained later in Section 5.3.3.
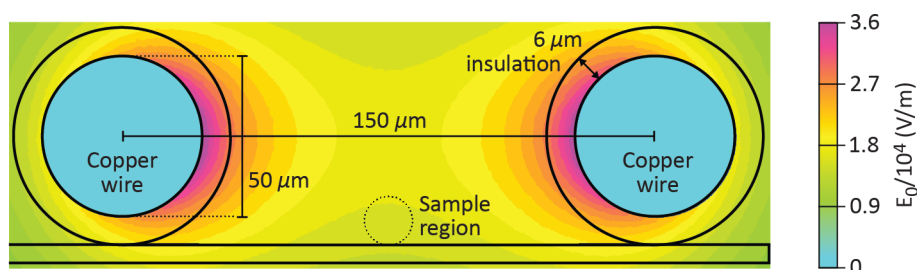
Figure 5.6: Calculated electric field strength for two insulated copper wires placed at a centre-to-centre distance of $150\,\text{μm}$ onto a glass slide.

5.3.2 Measurement sequence

In the absence of any fields, the HOPG microparticles tend to lie with their graphene planes parallel to the glass surface. This is shown in Figure 5.7a where the HOPG microparticles are imaged from above. By placing the magnet below the sample, we expose the HOPG microparticles to a vertical magnetic field that points in the Z direction. Following the principles explained in Section 5.2.1, the graphene planes in the HOPG microparticle align vertically as shown in Figure 5.7b. At this point, the HOPG microparticles can still rotate freely around the Z-axis. When in addition, we turn on the AC electric field in the X direction, the HOPG microparticles start to align parallel to the electric field direction as shown in the time-sequence in Figure 5.7c. The sequence shows the rotational motion of the HOPG microparticle from the moment the AC electric field is turned on at $t = 0$ to the moment at $t = 1.7\,\text{s}$. For our

analysis, we focus on the rotational motion of the HOPG microparticle after the AC electric field is turned on. We distinguish between two rotational motions. The first motion is the time-evolution of the particle orientation from the moment the AC electric field is turned on to the moment the particle reaches its final equilibrium orientation. The second motion takes place right after the first one and consists of orientational Brownian fluctuations of the particle around its equilibrium orientation while the AC electric field is turned on. As we will see in Section 5.4.2, the analysis of this motion allows us to measure the strength of the rotational trap. No heating effects are observed over the course of the acquisition.
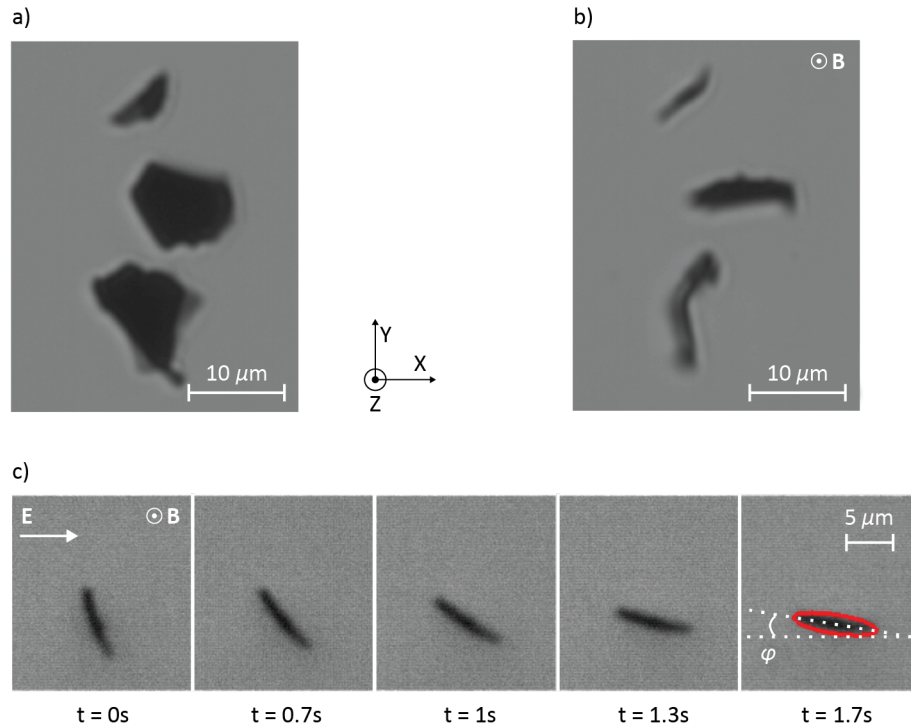
Figure 5.7: Orientation and rotational trapping of HOPG microparticles in solution with external electric and magnetic fields. a) HOPG microparticles in absence of any external fields. b) Vertically aligned HOPG microparticles in a vertical static magnetic field. c) Time-sequence of the rotational motion of vertically aligned HOPG microparticles once a horizontal AC electric field is turned on at time $t = 0$.

5.3.3 Tracking the rotational motion and determining the particle size

The use of a strong vertical magnetic field allows us to restrict our analysis of the electric-field-induced rotational motion to particle rotations around the Z-axis. From Figure 5.7c, we see that vertically aligned HOPG microparticles appear as elongated objects. We define the particle orientation as the angle, φ, between the longest particle dimension and the negative X-axis (see Figure 5.7c). By comparing this angle with α in Figure 5.1b, we get $\varphi = 90° - \alpha$

and the electric torque in Equation (5.10) becomes:

$$\langle \mathcal{T}_{\text{el}} \rangle = -\mathcal{T}_{\text{el,max}} \sin\left(2\alpha\right) = -\mathcal{T}_{\text{el,max}} \sin\left(2\varphi\right). \tag{5.13}$$

The stable equilibrium orientation of the particle is at $\varphi_0 = 90° - \alpha_0 = 0°$. To extract the orientation from the videos we use our image analysis code as described in Section 4.4.

To determine the particle size, use particle images before and after exposing them to the vertical magnetic field (see Figures 5.7a and b). These images are fitted to an ellipse to extract the major and minor axis length. The length corresponding to each of the three semi-axes of the particle are then manually selected from the fit results.

5.3.4 Variation of the electric field amplitude with frequency

Since the electric torque on HOPG microparticles depends on the electric field amplitude, it is important to quantify the actual electric field amplitude in the sample region. In practice, the amplitude varies with frequency due to impedance mismatch effects and output voltage variations from our RF signal generator and amplifier. The first effect occurs at higher frequencies and describes a phenomenon where the signal is partially transmitted and reflected at connection interfaces with different impedances. This can lead to cavity build-up effects that vary the field amplitude with frequency in the sample region. In our experimental setup, all circuit components leading up to the wires (signal generator, amplifier, BNC cables, switches) have an impedance of $50\,\Omega$. For the twisted wires and the parallel copper wires (see Figure 5.4b), the impedance Z is given by [55]:

$$Z = \frac{Z_0}{\pi\sqrt{\varepsilon_{\text{gap}}}}\text{arcosh}\left(\frac{D}{d}\right) \approx \frac{120}{\sqrt{\varepsilon_{\text{gap}}}}\ln\left(\frac{2D}{d}\right), \tag{5.14}$$

where $Z_0 = \mu_0 c_0$ is the impedance of free space, c_0 is the speed of light, ε_{gap} is the relative permittivity of the material between the wires, D is the distance between the wire centres and d is the diameter of a single wire. Our twisted wires are made from a pair of insulated wires with an internal diameter of $d = 0.8\,\text{mm}$ and a $0.35\,\text{mm}$ thick coating of Teflon ($\varepsilon_{\text{gap}} = 2.1$). For $D = 1.5\,\text{mm}$, which is the minimum distance between the wires, we get an impedance of $109\,\Omega$. For our parallel copper wires, we have $d = 0.05\,\text{mm}$ and $D = 0.15\,\text{mm}$. Assuming that the medium between the wires is air $\varepsilon_{\text{space}} = 1$, we get an impedance of $215\,\Omega$. This calculation shows that impedance mismatch is unavoidable due to the geometrical constrains of our experiment.
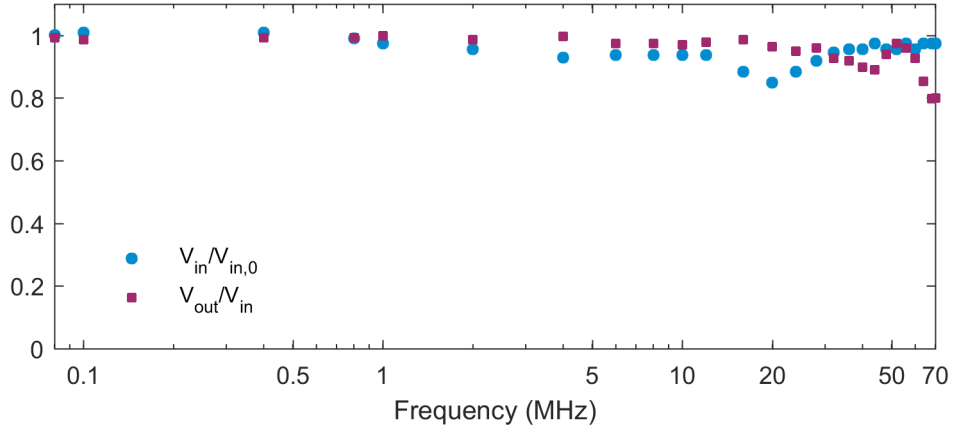
Figure 5.8: Voltage measurements in our experimental setup. V_{in}: input voltage, that comes from the voltage source. $V_{in,0}$: input voltage at zero frequency (here: $V_{in,0} = 2.3\,V$). V_{out}: measured voltage of the signal after passing through the twisted wires and parallel copper wires on the sample.

As an assessment of the signal losses in the sample region, we use an oscilloscope (Keysight DSO1072B) to measure the input voltage amplitude V_{in} after amplification and the output voltage amplitude V_{out} after the voltage signal is fed through the twisted wires and parallel copper wires (see Figure 5.4b). The measurements are presented in Figure 5.8. We normalise the input voltage at all frequencies to the input voltage at zero frequency, i.e. $V_{in,0} = 2.3\,V$ to analyse the variations of the signal amplitude produced by the RF source and the amplifier. In the measured data, we find variations of the amplified voltage signal mostly below 10 % that goes up to 15 % at around 20 MHz. This measurement shows that our RF source and signal amplifier produce a varying voltage signal with frequency. To analyse the output voltage we divide its value at each frequency by the corresponding input voltage. The ratio V_{out}/V_{in}, as presented in Figure 5.8, shows that the transmission losses are mainly less than 10 % and go up to 20 % around 70 MHz. This implies that the signal losses in the frequency range 1 MHz to 70 MHz are not zero but they are relatively low. Note, that while we can measure the transmission voltage an estimation of the actual voltage between the wires is not trivial. However, from the measurement of V_{out} we expect this correction to be small and thus it is omitted. Therefore, we only apply a small correction to our raw torque data to account for the voltage variation with frequency from our RF source and signal amplifier. Since the electric torque is proportional to the square of the electric field amplitude and since $E_0 \propto V$, it follows that the torque is proportional to the square of the input voltage, i.e. $\mathcal{T}_{el} \propto V^2$. Therefore, to scale the torque to a constant electric field and to account for the measured source voltage variations with frequency, we multiply our measurements of the electric torque by $(V_0/V_{in})^2$. This ensures that all measured electric torque data points correspond to the same electric field amplitude and that the observed variations are only due to changes in the electric field frequency. For this analysis, we set the value of V_0 to 2.3 V.

5.4 Results and discussion

Our analysis is divided into two parts. First, we analyse the rotation of an individual particle upon exposing it to an AC electric field and compare the rotational motion to the solution of the rotational equation of motion, neglecting thermal fluctuations. In the second part, we focus on rotationally trapped particles and analyse their orientational Brownian fluctuations around the equilibrium orientation. The analysis of this motion allows us to extract the maximum electric torque, $\mathcal{T}_{el,max}$, and the rotational trap stiffness, k_{tot}.

As mentioned before, all measurements are carried out on HOPG microparticles that are vertically aligned with a static magnetic field $B_0 = 0.24\,\text{T}$. For a HOPG microparticle with average size of $6.6\,\mu\text{m} \times 3.9\,\mu\text{m} \times 1.4\,\mu\text{m}$, we can calculate the maximum magnetic torque with Equation (5.3) using the measured magnetic susceptibility values for $\chi_{\parallel}$ and $\chi_{\perp}$ in Table 2.3. This gives us a maximum magnetic torque of $1.7 \times 10^{-15}\,\text{Nm}$ which is sufficiently large as all our selected particles align vertically in solution. All experiments are conducted at $23\,°\text{C}$. The results have already been published in [56]

5.4.1 Electric rotation of HOPG microparticles

Figure 5.9 shows the time-evolution of the orientation angle φ for a single HOPG microparticle in an AC electric field for three frequencies, namely, $20\,\text{MHz}$, $40\,\text{MHz}$ and $60\,\text{MHz}$. In all three datasets, the electric field is turned on at $t = 0$ and the initial orientation angle of the particle is between $70°$ and $80°$. Small variations of the initial angle occur because we move the magnet below the sample to rotate it back to its initial orientation. Our measurements show an immediate response of the particle to the field which starts rotating until it reaches its equilibrium orientation at $\varphi \approx 0°$. From the principles explained in Section 5.2.2, it follows that at the equilibrium orientation the graphene planes are aligned parallel to the applied AC electric field. As the electric field frequency increases from $20\,\text{MHz}$ to $60\,\text{MHz}$, the rotation towards equilibrium is visibly faster which implies an increase in the electric torque with frequency.

The rotational equation of motion for particles in solution is given by the balance of torques:

$$I\underbrace{\frac{d^2\varphi(t)}{dt^2}}_{\text{inertia}} = \underbrace{-c\frac{d\varphi(t)}{dt}}_{\text{rotational viscous drag}} + \underbrace{\langle\mathcal{T}_{el}\rangle}_{\text{el. torque}} + \underbrace{\sqrt{2k_B T c}\,W(t)}_{\text{random Brownian fluctuations}} \quad, \tag{5.15}$$

where I is the moment of inertia, c is the rotational friction coefficient, T is the temperature, k_B is the Boltzmann constant and $W(t)$ is a Gaussian noise term with zero mean and unity variance [53]. Note, that since $\langle\mathcal{T}_{el}\rangle$ is given by Equation (5.10), it is proportional to $\sin(2\varphi)$. As mentioned in Section 5.2.2, the rotational motion of the particle is strongly damped by the
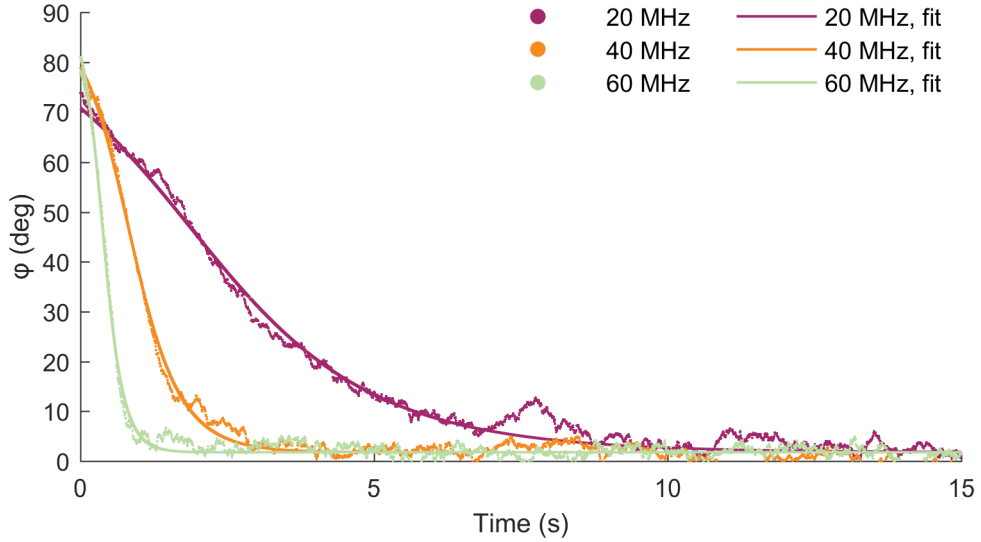
Figure 5.9: Time-evolution of the orientation of a HOPG microparticle in an AC electric field at three different frequencies: 20 MHz, 40 MHz, 60 MHz. In the measurement, the particle is vertically aligned with a vertical static magnetic field $\mathbf{B}_0$.

viscosity of the solution. This means that the viscous term is much larger than the inertial term. Therefore, Equation (5.15) describes an overdamped oscillator with characteristic time $\tau_{\mathrm{c}} = \frac{I}{c}$. The latter quantity describes the timescale it takes for a particle to reach its terminal angular velocity once a torque is applied on the particle. The characteristic time for micron-sized particles is of order 10^{-6} s which is much shorter than the acquisition rate of our camera (10^{-3} s). As a result, we can assume that as we apply a torque on the particle it immediately rotates at terminal angular velocity. This assumption is equivalent to neglecting the inertial term in Equation (5.15). The rotational motion of the particle is therefore described by the torques that act on the particle at that moment. Additionally, we exclude the random Brownian fluctuation term as a first approximation for the rotational motion. Both assumptions allow us to solve Equation (5.15) analytically and express the particle orientation as:

$$\varphi\left(t\right) = \arctan\left[\tan\left(\varphi_0\right)\exp\left(-2\frac{\mathcal{T}_{\mathrm{el,max}}}{c}t\right)\right], \tag{5.16}$$

where φ_0 is the initial orientation at $t = 0$ and $\mathcal{T}_{\mathrm{el,max}}$ is given in Equation (5.11). The fits of the data to Equation (5.16) can be appreciated in Figure 5.9 which show good agreement with the data. Note that in principle, we can use the fits to determine the maximum electric torque by approximating the particle shape as an ellipsoid and calculating the theoretical rotational friction coefficient c with existing theories [57]. In the next subsection, however, we use a more accurate method that does not rely on theoretical calculations and instead, determines $\mathcal{T}_{\mathrm{el,max}}$ and c directly from the data.

5.4.2 Rotational fluctuations of electrically aligned HOPG microparticles

Once particles are aligned and rotationally trapped by the combination of $\mathbf{B}_0$ and $\mathbf{E}_0$, they are still subject to orientational Brownian fluctuations around their equilibrium orientation. For example, we can see these orientational Brownian fluctuations in Figure 5.9 for the data corresponding to the electric field frequency 60 MHz. In this data, the particle reaches its equilibrium orientation in less than 3 s and starts fluctuating around its equilibrium orientation after that. These orientational Brownian fluctuations arise from collisions at the particle surface with the molecules of the solution.

To describe the rotational motion of the rotationally trapped microparticle, we must account for the Brownian fluctuation term in Equation (5.15). Equation (5.13) shows that the electric torque is proportional to $\sin(2\varphi)$. For small angular fluctuations around the equilibrium orientation, we can use $\sin(2\varphi) \approx 2\varphi$ and the electric torque in Equation (5.13) becomes $\langle \mathcal{T}_{\text{el}} \rangle \approx -2\mathcal{T}_{\text{el,max}}\varphi = -k_{\text{el}}\varphi$, where $k_{\text{el}} = 2\mathcal{T}_{\text{el,max}}$ is the electrical rotational trap stiffness. In this approximation, the rotational equation of motion can be expressed as:

$$-c\frac{\mathrm{d}\varphi(t)}{\mathrm{d}t} - k_{\text{el}}\varphi + \sqrt{2k_{\text{B}}Tc}\,W(t) = 0, \tag{5.17}$$

which describes the rotational motion of a microparticle in a rotational harmonic trap. The form of this equation is identical to the linear motion of a particle in a harmonic trap for which there exists a theory in the literature [58, 53]. Therefore, we can translate these theories to our case and determine $\mathcal{T}_{\text{el,max}}$ and k_{el} by analysing the orientational Brownian fluctuations of the particles around its equilibrium orientation.

In order to measure $\mathcal{T}_{\text{el,max}}$ and k_{el} from the orientational Brownian fluctuations, we monitor the particle as it stays aligned in the electric field for $20 - 30\,$s. We then turn off the electric field and monitor the free orientational fluctuations for another $20 - 30\,$s to analyse additional motion restrictions due to potential interactions of the particle with the glass surface. Figure 5.10 shows the free orientational fluctuations ('E-field off') together with the orientational Brownian fluctuations around the equilibrium orientation in the AC electric field with the frequencies 20 MHz, 40 MHz and 60 MHz. On the left hand side of Figure 5.10, the orientational Brownian fluctuations are plotted as a function of time for all four datasets. On the right hand side, we can see the corresponding histograms of explored orientations. The data shows clearly that as the field frequency increases, the amplitude of the angular fluctuations becomes smaller as evidenced by a narrower distribution in the histograms. This agrees with our previous observation in Figure 5.9 that the strength of the rotational trapping increases with electric field frequency. Furthermore, the angular fluctuations around the equilibrium
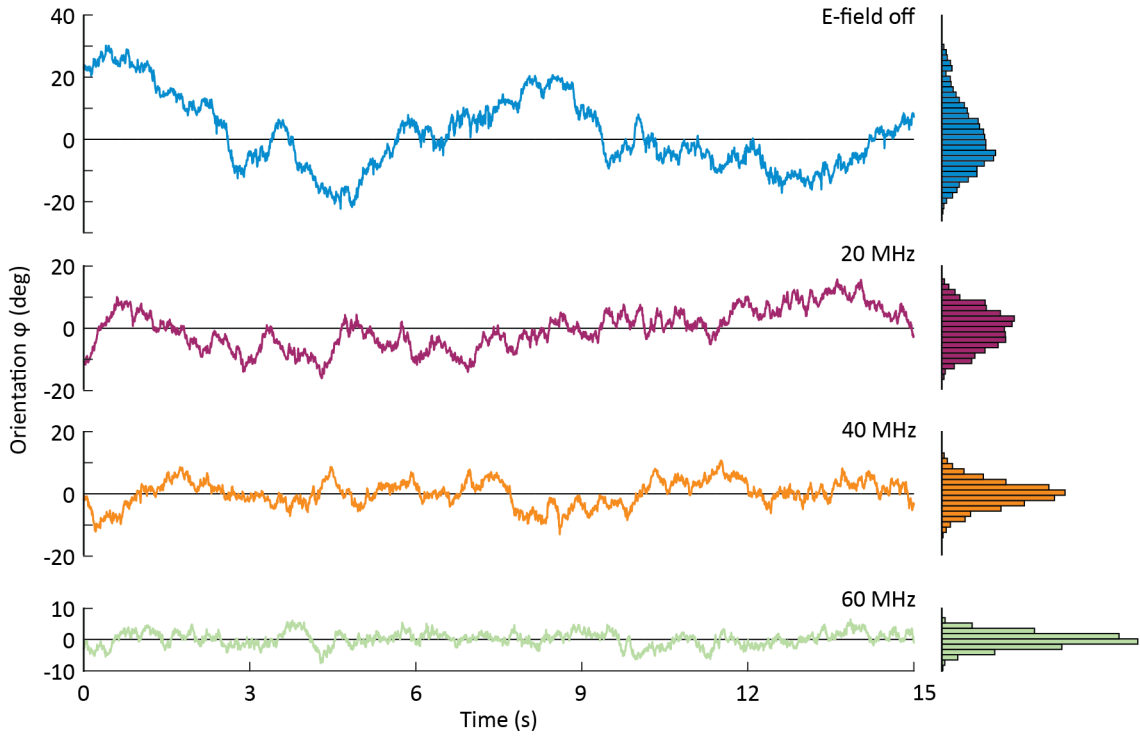
Figure 5.10: Orientational Brownian fluctuations for a single HOPG microparticle that is vertically aligned with a static magnetic field $B_0 = 0.24\,\mathrm{T}$ and then additionally exposed to a horizontal AC electric field E_0. The data corresponding to 'E-field off' describes the free orientational fluctuations as a function of time when the electric field is turned off. The other three datasets below describe the orientational Brownian fluctuations around the equilibrium orientation in an electric field with frequencies $20\,\mathrm{MHz}$, $40\,\mathrm{MHz}$ and $60\,\mathrm{MHz}$. A histogram of the fluctuations is shown on the right hand side.

orientation in the presence of the electric field are normally distributed. This confirms that our rotational trap is harmonic for the small angular fluctuations measured. We can therefore characterize our trap with the electrical rotational trap stiffness.

To analyse the angular fluctuations we can calculate the angular mean squared displacement (aMSD) which is defined as:

$$\mathrm{aMSD}\,(\tau) = \langle [\varphi\,(t_0 + \tau) - \varphi\,(t_0)]^2 \rangle, \tag{5.18}$$

where t_0 is the initial time and τ is the lag time. The angle brackets in Equation (5.18) indicate the averaging over all t_0 with lag time τ. Theoretically, the aMSD of the rotational motion described by Equation (5.17) can be expressed as [53]:

$$\mathrm{aMSD}\,(\tau) = \frac{2 k_\mathrm{B} T}{k_\mathrm{el}} \left[1 - \exp\left(-\frac{k_\mathrm{el}}{c} \tau \right) \right]. \tag{5.19}$$

For free orientational fluctuations, i.e. in the absence of any trap ($k_\mathrm{el} = 0$), the aMSD increases linearly with τ as $\mathrm{aMSD}\,(\tau) = \frac{2 k_\mathrm{B} T}{k_\mathrm{el}} \left[1 - \left(1 - \frac{k_\mathrm{el}}{c} \tau + \dots \right) \right] \approx 2 D_\varphi \tau$, where $D_\varphi = \frac{k_\mathrm{B} T}{c}$ is the rotational diffusion coefficient as defined by F. Perrin in [57]. As we turn on the electric field,

i.e. $k_{el} \neq 0$, the aMSD deviates from this behaviour and converges towards $\frac{2k_B T}{k_{el}}$.

Figure 5.11 shows the aMSD calculated from the data in Figure 5.10. The error bars account for the fact that for a finite data set the amount of data points for a given lag time decreases with increasing lag time. To calculate this error, we use the formula provided by Qian *et al.* in [59]. In the datasets corresponding to the electric field frequencies 20 MHz, 40 MHz and 60 MHz, the aMSD converges towards a constant value as the lag time increases. The decrease of the constant value with increasing frequency is caused by an increase of the electrical rotational trap stiffness as shown in Equation (5.19)
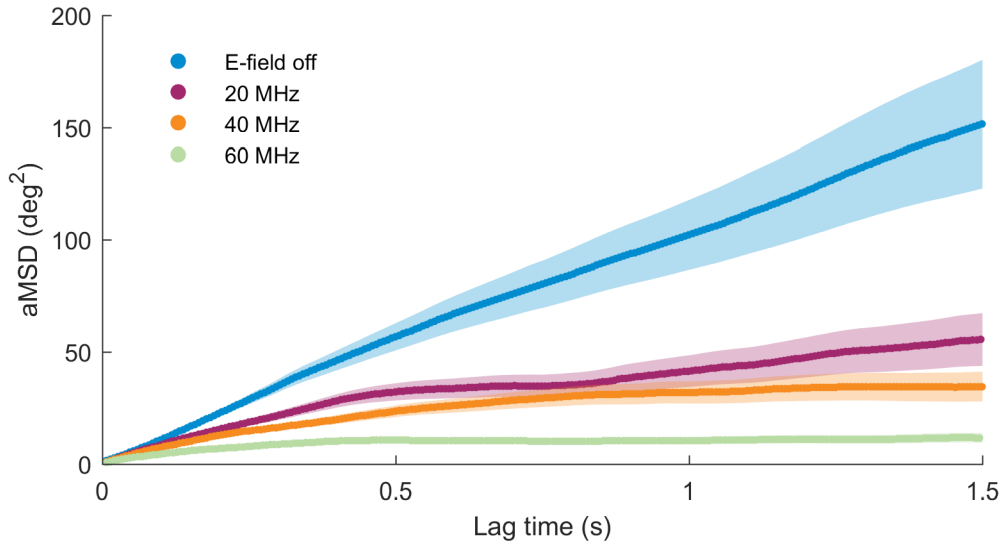
Figure 5.11: Calculated angular mean square displacement (aMSD) from the orientational Brownian fluctuation data presented in Figure 5.10. The envelopes are the calculated error bars which account for the fact that for a finite dataset the number of instances to calculate the aMSD decreases with increasing lag time.

Figure 5.11 also shows a slight non-linearity in the aMSD calculated for the free orientational fluctuations (E-field off). The small effect could arise due to the fact that the particle falls under gravity and inevitably interacts with the nearby glass surface. We interpret the surface interaction as an additional harmonic trap with rotational trap stiffness k_{glass}. This additional constant accounts for effects that are not related to the electric field, such as sticking effects due to interactions of the lipid-coating with the glass surface or effects due to charges on the glass surface. By accounting for this additional effect, the rotational equation of motion in Equation (5.15) becomes:

$$-c\frac{d\varphi(t)}{dt} - k_{tot}\varphi(t) + \sqrt{2k_B T c}\,W(t) = 0, \tag{5.20}$$

where $k_{tot} = k_{el} + k_{glass}$ is the total rotational trap stiffness that includes the electrical rotational

trap stiffness k_{el} and the rotational trap stiffness due to surface interactions k_{glass}. The aMSD in Equation (5.19) then becomes:

$$\text{aMSD}\,(\tau) = \frac{2k_B T}{k_{total}} \left[1 - \exp\left(-\frac{k_{total}}{c}\tau \right) \right].$$ (5.21)

Alternatively, we can calculate the auto-correlation from the data defined as [53]:

$$R(\tau) = \langle \varphi\,(t_0)\,\varphi\,(t_0 + \tau) \rangle = \frac{k_B T}{k_{tot}} \exp\left(-\frac{k_{tot}}{c}\tau \right).$$ (5.22)

The calculated auto-correlation corresponding to the data in Figure 5.10 and the fit result are presented in Figure 5.12. Similar to the aMSD, the auto-correlation shows a clear dependency on the electric field frequency as evidenced by a slower exponential decay (note log scale) and a decreasing value at $t = 0$ as the frequency increases. Both observations indicate an increasing electrical rotational trap stiffness with increasing electric field frequency in agreement with the results from our aMSD analysis.
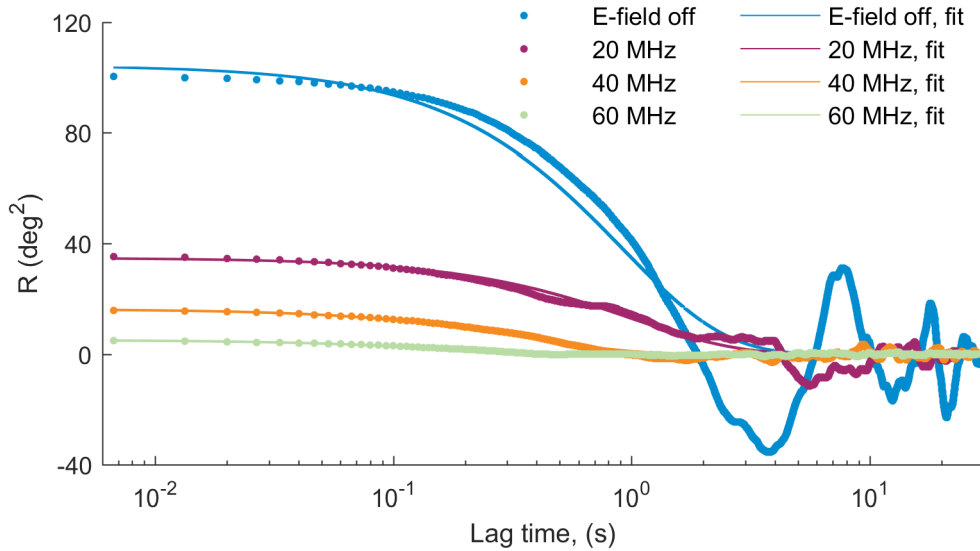
Figure 5.12: Calculated autocorrelation, R, from the orientational Brownian fluctuation data presented in Figure 5.10. The fit is calculated by fitting the autocorrelation data to Equation (5.22).

5.4.3 Frequency dependency of the maximum electric torque and rotational trap stiffness

The maximum electric torque and the rotational trap stiffness can be determined from the orientational Brownian fluctuations by calculating the aMSD or the auto-correlation and fit them to the expressions in Equation (5.21) or Equation (5.22). In general, both methods are equivalent and yield the same results. For that reason, we analyse our data with the auto-

correlation method and extract k_{tot} and $\mathcal{T}_{el,max}$ from the auto-correlation value at zero lag time $R\left(\tau = 0\right)$. For each frequency, we obtain k_{tot} from the orientational Brownian fluctuations measured with the electric field turned on and k_{glass} from the free orientational fluctuations measured with the electric field turned off. The electrical rotational trap stiffness k_{el} is determined as $k_{el} = k_{tot} - k_{glass}$ and the maximum electric torque is obtained as $\mathcal{T}_{el,max} = \frac{k_{el}}{2}$.

To investigate the frequency dependency of k_{el} and $\mathcal{T}_{el,max}$, we analyse the orientational Brownian fluctuations at different frequencies in the range $1 - 70\,\mathrm{MHz}$. The values are then corrected for variations in the voltage amplitude from the signal amplifier as described in Section 5.3.4. For each particle, we take up to five measurements at a given frequency. Due to variations in the particle shape, we look at the individual particles rather than at the average value of all of them together. Table 5.1 summarizes the particle size and the type of surface they were measured on (see Section 5.4.4). Figures 5.13 to 5.15 show the average values for k_{el}, k_{glass} and $\mathcal{T}_{el,max}$ as a function of electric field frequency for a total number of eight particles. The error bars correspond to the standard deviations of the measurements (no error bar is plotted if there is only one measurement). We group the plots by the type of glass surface: Figure 5.13 contains two particles on untreated glass, Figure 5.14 contains four particles on plasma-cleaned glass and Figure 5.15 contains two particles on PEGylated glass (details on PEGylation will be given later). For all particles, we see that k_{el} and $\mathcal{T}_{el,max}$ increase with electric field frequency. On the other hand, the k_{glass} values are frequency-independent and their low standard deviations imply small variations over the course of the measurement (further details in Section 5.4.4). Few data points for k_{el} at low frequencies are negative since the applied electric torques are weak and can lead to an overestimation of k_{glass}.

Particle Name	a (μm)	b (μm)	c (μm)	Glass surface
2105_p2	3.5	3.3	0.9	untreated
2406_p1	3.1	0.9	0.7	untreated
2105_p4	3.7	2	0.7	plasma-cleaned
0106_p2	3.4	2.1	0.6	plasma-cleaned
0806_p6	2.9	1.5	0.5	plasma-cleaned
0906_p4	3	1.8	0.6	plasma-cleaned
1106_p3	3.3	2.2	0.6	PEGylated
1206_p1	3.5	1.8	0.8	PEGylated

Table 5.1: Table of measured particle size and type of glass surface treatment used in the magneto-electric orientation. The particle is approximated as an ellipsoid with semi-axes a, b and c. Three types of glass surfaces are used in the experiment: untreated glass surface (untreated); plasma-cleaned glass surface (plasma-cleaned); and PEG-silane passivated glass surfaces (PEGylated).

Figure 5.16 combines all data into a single plot highlighting the reproducibility of the overall trend with frequency. Below $10\,\mathrm{MHz}$, we see no electric-field-induced particle rotation

even if we increase the field amplitude. As the electric field frequency exceeds 10 MHz, we can see that k_{el} and $\mathcal{T}_{el,max}$ increase with frequency. In the frequency range $10 - 70$ MHz the electric field produces a rotational trap with an electrical rotational trap stiffness k_{el} as high as 3.3×10^{-18} Nm/rad. This corresponds to a maximum electrical torque of 1.7×10^{-18} Nm.

The variations of k_{el} and $\mathcal{T}_{el,max}$ with frequency, are caused by the lipid-coating around the HOPG core as described in Section 5.2.2. A comparison with the theoretical prediction in Figure 5.2a reveals that we should see a low plateau level at frequencies below 10^6 Hz. Its absence can be caused by the insulating effect of the lipid layer (see Section 5.2.2) and the surface interaction such as friction between the particle and the glass surface. The absence of the higher plateau as predicted in Figure 5.2 suggests that field frequencies in excess of 70 MHz are required to reach it. However, such frequencies are beyond the capacity of our experiment and can be subject for further research.
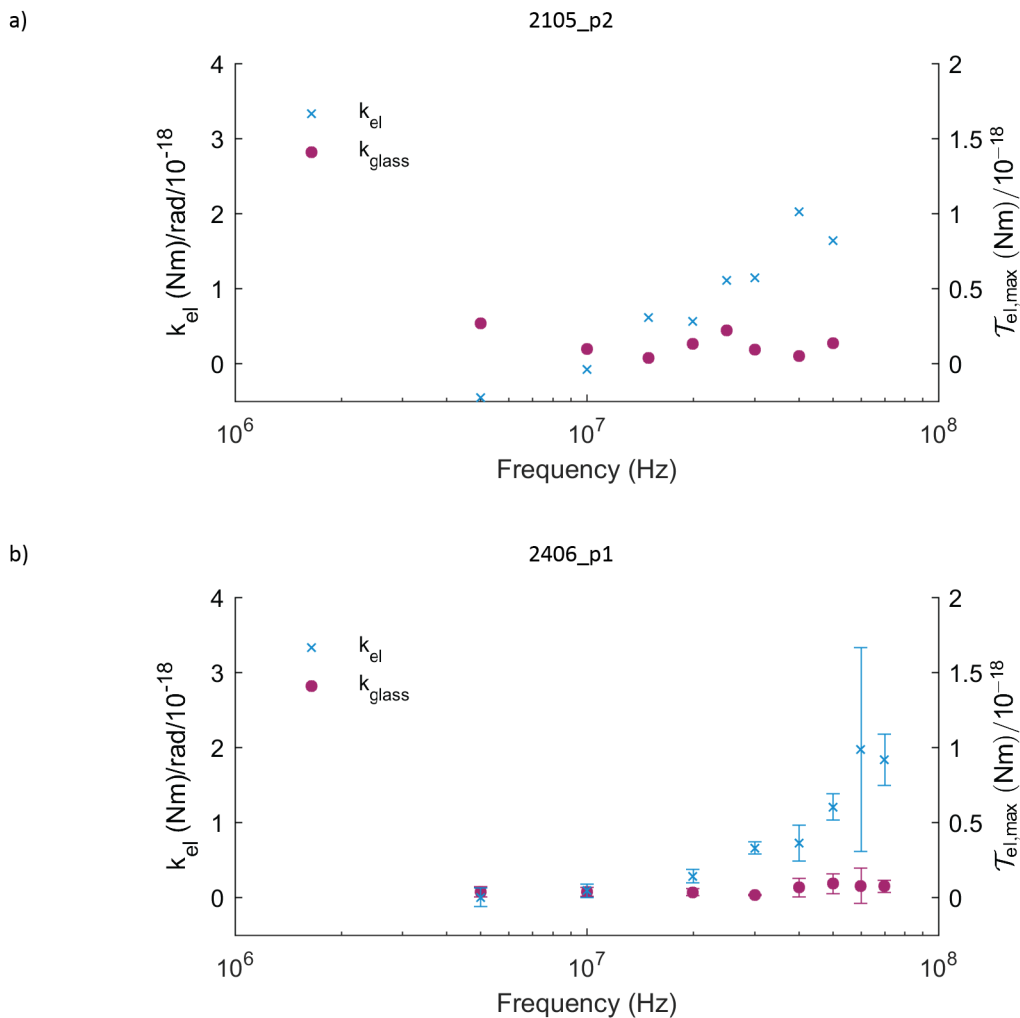
Figure 5.13: Measured values of k_{el} (left hand side) and $\mathcal{T}_{el,max}$ (right hand side) at different electric field frequencies for two single lipid-coated HOPG particles on untreated glass surfaces. k_{glass} is a quantity to describe the particle interaction with the glass surface.
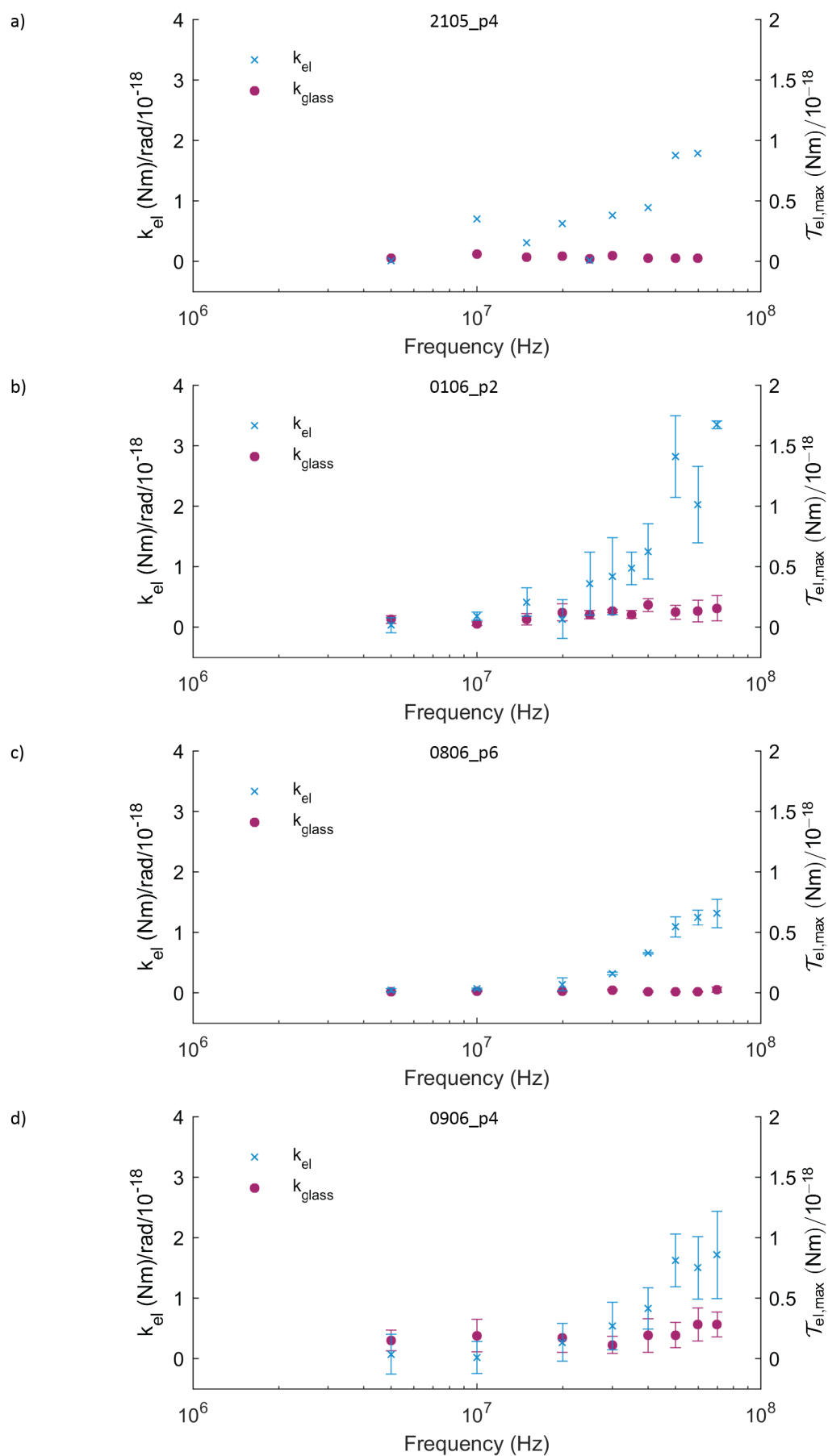
Figure 5.14: Measured values of k_{el} (left hand side) and $\mathcal{T}_{el,max}$ (right hand side) at different electric field frequencies for four single lipid-coated HOPG particles on plasma-cleaned glass surfaces. k_{glass} is a quantity to describe the particle interaction with the glass surface.
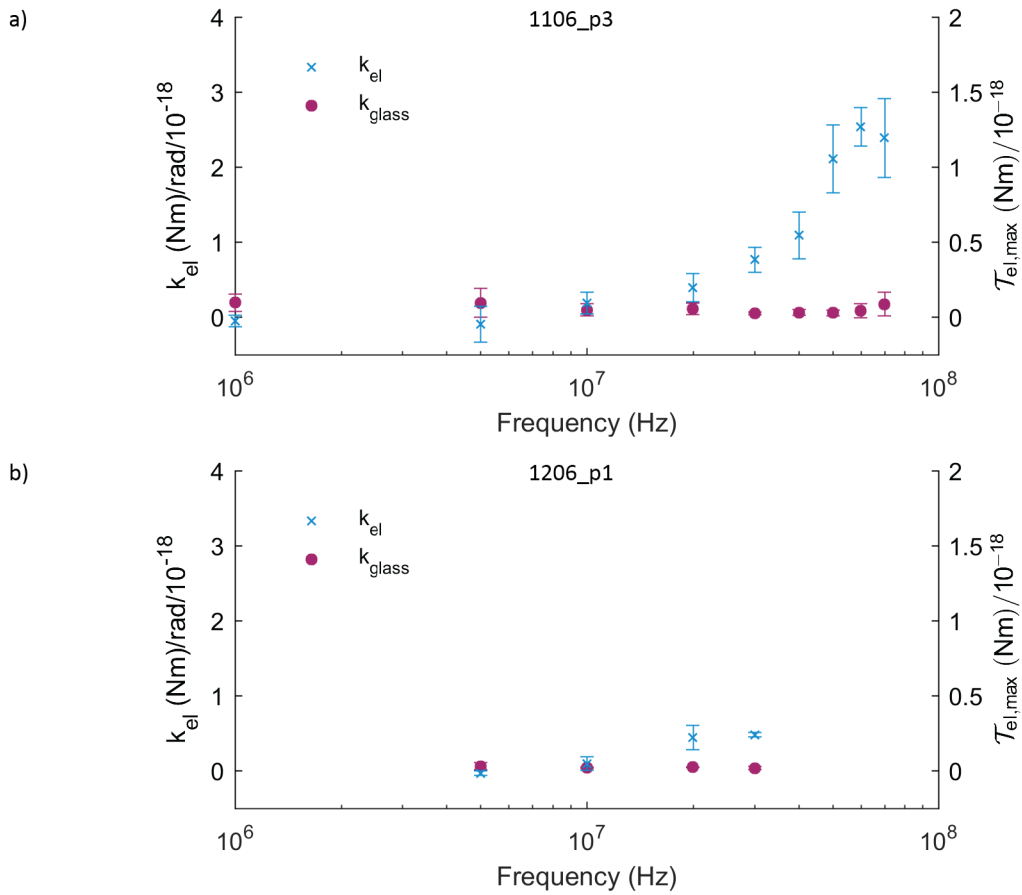
Figure 5.15: Measured values of k_{el} (left hand side) and $\mathcal{T}_{el,max}$ (right hand side) at different electric field frequencies for two single lipid-coated HOPG particles on PEG-silane passivated surfaces. k_{glass} is a quantity to describe the particle interaction with the glass surface.
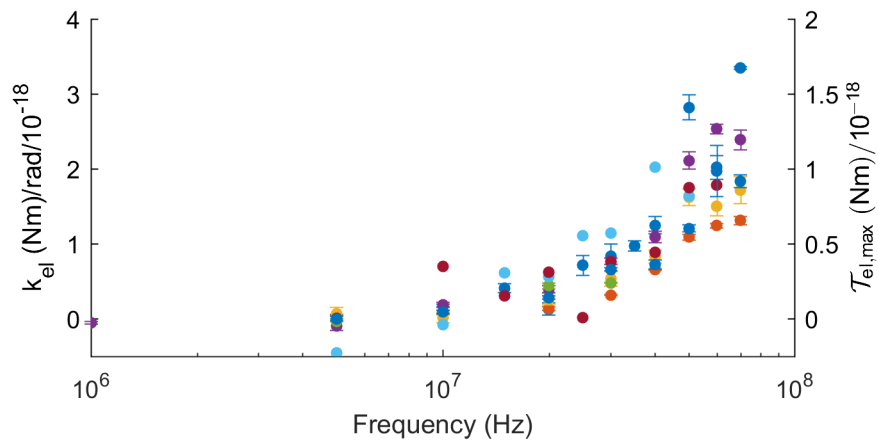
Figure 5.16: Superposition of measured k_{el} and $\mathcal{T}_{el,max}$ values at different electric field frequencies for all eight particles measured on different surfaces.

5.4.4 Interactions with the glass surface

Since our HOPG microparticles fall under gravity, we can only conduct our experiments on particles near the glass surface. As part of the analysis, we characterise the particle-surface interactions on three differently treated glass surfaces: an untreated surface, a plasma-cleaned surface and a PEG-silane passivated surface. Prior to any treatment, all surfaces are sonicated in acetone for 5 min (including the untreated glass) to remove potential contaminations. To prepare the plasma-cleaned glass, we place it for 10 min in a plasma cleaner (Diener Zepto) using air as the gas and set the power to 50 W and the pressure to 0.35 mbar. To passivate the glass surface, we use the polymer PEG-silane where the silane groups attach to the glass surface and the PEG molecules form a dense brush that sterically blocks any adhesion [60]. The process of coating a surface with a brush of PEG molecules is commonly referred to as PEGylation. For the passivation, we prepare a fresh PEG stock solution in the concentration range $10 - 50$ mg/ml by dissolving PEG-silane in a freshly prepared solution of ethanol and water with volume fractions 95 % and 5 %, respectively. Then, we cover a plasma-cleaned surface with the solution and let it incubate overnight in a dark environment at room temperature. Finally, we rinse the surface with ultrapure water and dry it with N_2 gas.

For the characterisation of the different glass surfaces, we use the extracted k_{glass} values which are calculated from fits of free orientational fluctuation data to the auto-correlation function in Equation (5.22) as mentioned in Section 5.4.3. The distributions of the extracted k_{glass} values for each surface are shown in Figure 5.17. These consist of 48, 113 and 67 measurements from all eight particles on untreated glass, plasma-cleaned glass and PEGylated glass, respectively. The histograms show some differences between the three surface treatments. PEGylated glass surfaces have the distribution with the lowest mean and standard deviation value. Therefore, such a treatment can minimize the particle-surface interaction. The widest distribution is observed for plasma-cleaned glass surfaces. Such a treatment can negatively charge the glass surface. As mentioned in Chapter 3, the lipid-layer of the particle could be charged positively by absorbing the Na^+ ions in the NaCl solution. Consequently, the broad distribution observed for particles on plasma-cleaned glass surfaces may be the result of electrical interactions between the negatively charged glass surface and the positively charged lipid-shell around the HOPG microparticle. Another possible contribution in all cases could be friction at the interface between the particle and the glass surface. Since HOPG microparticles fabricated by means of sonication have irregular shapes, the friction between the particles could vary and contribute to a broad distribution of the k_{glass} values.
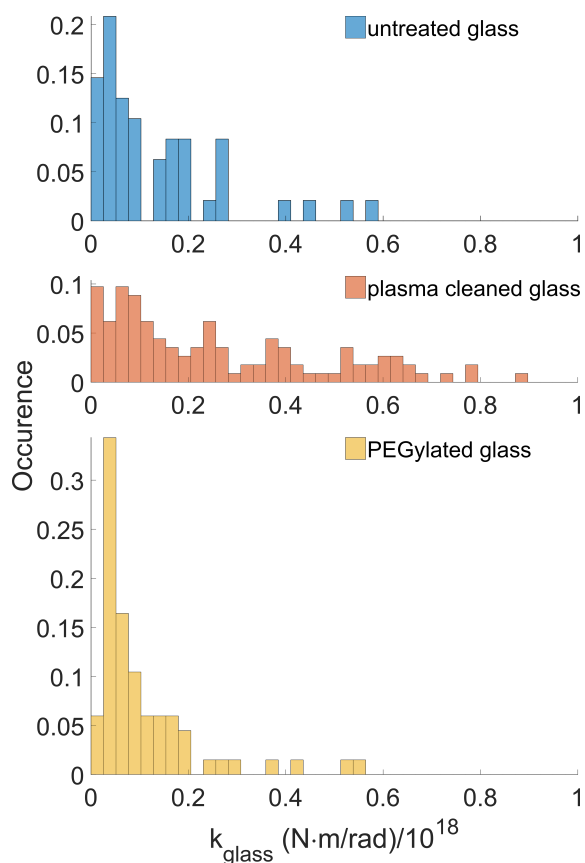
Figure 5.17: Histograms of k_{glass} measured for untreated glass surfaces, plasma-cleaned glass surfaces and PEG-silane passivated (PEGylated) glass surfaces. The values are extracted by calculating the auto-correlation of the free orientational fluctuations data and fit it to Equation (5.22).

5.5 Conclusion

We have presented the first study of the magneto-electric orientation of lipid-coated HOPG microparticles in aqueous solution, including a theoretical framework and quantitative experimental results. To confine the orientation of the particle to a well-defined plane of our choice, we took advantage of the anisotropic electrical and magnetic properties of HOPG. We demonstrated the rotational trapping by using a vertical static magnetic field and a horizontal AC electric field to confine the particle orientation to a vertical plane. This allowed us to investigate the electrical rotational trap stiffness and the maximum electric torque on the lipid-coated HOPG microparticle for different electric field frequencies. We found that the field frequency is the main factor to apply electric torques on lipid-coated particles close to the glass surface: particle rotations were only observed after exceeding 10 MHz. This behaviour is caused by the insulating property of the lipid-coating and non-electric interactions between the particle and the glass surface. Additionally, we found that by evaluating the free orientational fluctuations of the particles on various substrates we can discriminate between glass surfaces with differ-

ent treatments. This can be useful to probe glass surfaces for their stickiness which can be undesirable for certain applications, e.g. microfluidic experiments close to the surface.

Our experiments are particularly relevant for biological applications. Lipid-coated HOPG microparticles can be functionalised by using modified lipids that have additional molecules attached to them. The use of such lipids makes it possible to specifically bind the particles to biomolecules such as antibodies, enzymes or cell receptors. By attaching the particles onto biomolecules, we could apply and sense biologically relevant torques which are typically in the range $0.01 - 1 \times 10^{-18}$ Nm. For example, Palanisami et $al.$ used a magnetic nanorod to analyse the rotational motion of the rotating enzyme F_1-ATPase and reported torques in the range $0.02 - 0.08 \times 10^{-18}$ Nm. The enzyme is a subunit of the enzyme ATP synthase which is responsible for the synthesis of adenosine triphosphate (ATP) that provides energy for all biological processes [61]. Lipfert et $al.$ conducted torque measurements with a magnetic tweezer on the enzyme RNA polymerase which unwinds the DNA for the synthesis of RNA [62]. They reported torques of about 0.01×10^{-18} Nm. In our experiment, we achieved trap stiffness values up to 3.3×10^{-18} Nm/rad which are within the range of those in magnetic tweezer experiments with superparamagnetic particles tethered to a surface [63]. The resolution for torque sensing depends on the uncertainties in the particle orientation detection via particle tracking. In our experiments, this uncertainty is around 0.2° or 0.004 rad (see Table 4.4) which is twice as large than the uncertainty reported for techniques used in biological studies [64]. Further improvements in the orientation detection can be achieved by using elongated particles with a smooth shape as discussed in Section 4.5.4.

The magneto-electrical orientation of lipid-coated HOPG microparticles is in particular interesting for the development of novel tools for simultaneous force and torque sensing. Since HOPG is a diamagnetic material, it is in principle possible to trap HOPG microparticles with static magnetic fields. The principle of our experimental setup could be used to apply torques on the magnetically trapped particle which has never been done before. The three-dimensional magnetic trapping of HOPG microparticles will be the subject of Chapter 7.

5.6 Developments towards full particle rotation experiments

Our experimental setup can be extended to more complex experiments by using two pairs of electrodes. In a wire arrangement where both pairs are perpendicular to each other, it is possible to generate rotating electric fields by applying an AC voltage on each pair with a phase shift between the voltage signals. This would allow us to generate full particle rotations which is not possible with a single pair of electrodes.

To start working in this direction for the future, we developed a wire chip with microfabricated gold electrodes in collaboration with the David Bullett Nanofabrication Facility at the University of Bath. A realisation of the wire chip is shown in Figure 5.18a where the gold wires are patterned on a $0.13 - 0.16\,$mm thick cover slip. The wires are attached onto the glass surface by first applying a $30 - 40\,$nm adhesion layer of chromium followed by a $200\,$nm layer of gold (Au). Since the experiments are conducted in solution, a $30\,$nm thick insulating layer of hydrogen silsesquioxane (HSQ) is applied on top of the wires to prevent electrochemical reactions at the electrode-solution interface. On the left and right hand side in Figure 5.18a there are rectangular gold pads that can be connected to the voltage source to generate the electric field in the sample region. In the centre of the pattern, there are four sample regions where two pairs of electrodes are arranged in a cross shape as shown in Figure 5.18b. Each electrode in the sample region is $10\,\mu$m wide and the size of the gap between two opposing electrodes is either $20\,\mu$m, $30\,\mu$m, $40\,\mu$m or $50\,\mu$m.
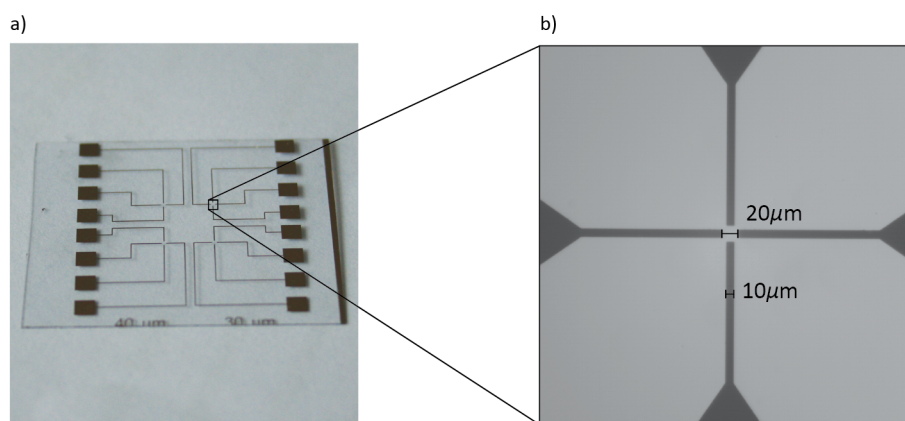
Figure 5.18: Photographs of the wire chip prototype. a) Photograph of the entire wire chip. The wires are patterned on a $0.13 - 0.16\,$mm thick cover slip. b) Image of the wire chip in the sample region. Each electrode is $10\,\mu$m wide. The distance between two opposing electrodes is either $20\,\mu$m, $30\,\mu$m, $40\,\mu$m or $50\,\mu$m (here: $20\,\mu$m).

In order to use the wire chip for particle rotation experiments, we must use a different experimental design than the one used in this chapter. A potential design for the study of particle rotations in rotating electric fields is presented in Figure 5.19. In order to confine the particle solution to the sample region, a channel slide (i.e. a slide with an engraved micronsized cavity on the surface) can be placed on top of the wires as shown in Figure 5.19a. The channel slide is sufficiently long to cover two sample regions as shown in Figure 5.19b. To place the particles in the sample region, the solution can be injected into one of the channel ends. In order to monitor the particle rotations with high magnification objectives,

an inverted microscope is needed to image the particle from below as shown in Figure 5.19c. This adjustment is necessary because the distance between the sample and the top wall of the channel is too large to fit microscope objectives with large magnifications which operate at short working distances. To vertically align the particle with a static magnetic field a magnet can be placed on top instead of below the sample.
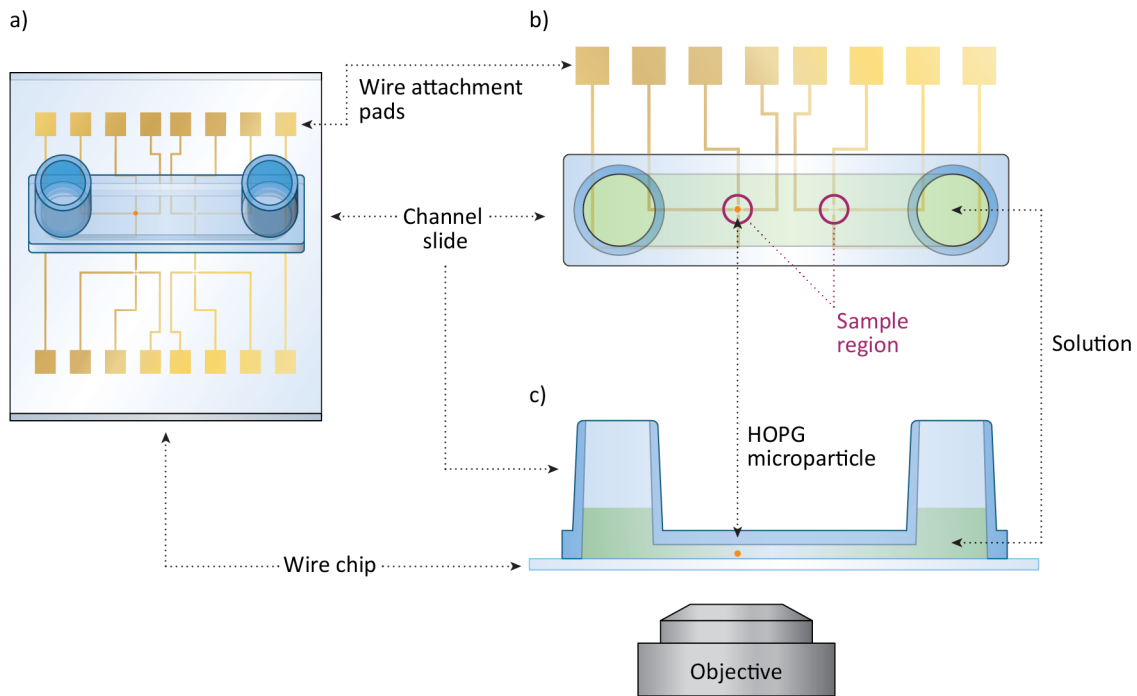
Figure 5.19: Schematic of a potential experimental setup to study magneto-electric orientations of HOPG microparticles with a wire chip. a) Diagonal view of the wire chip with a channel slide attached on top. b) Top view of the wire pattern and the channel slide. The channel covers two sample regions on the wire chip. c) Side view of the experimental setup. To monitor the rotational motion of the particle with a large magnification objective, the particle must be imaged from below due to the short working distance of the objective.

Chapter 6

Magnetophoresis of HOPG microparticles

6.1 Introduction

Magnetophoresis describes the directed motion of an object through a fluid in an inhomogeneous magnetic field. The force on the particle, often termed as magnetophoretic force, depends on the magnetic properties of the particle and the fluid, the particle volume and shape, the fluid viscosity, the magnetic field strength and the magnetic field gradient. Since magnetic fields interact with all materials by inducing a magnetisation inside them (diamagnetism is a property of all matter), particles made from any material can express magnetophoresis. Magnetophoresis is therefore attractive for particle manipulation as it offers a contactless method to move microparticles in solution.

Nowadays, magnetophoresis has found a widespread use in many lab-on-a-chip applications to move magnetic microparticles in microfluidic devices. Magnetic fields can be used to separate a continuously flowing mixture of magnetic microparticles and to sort them by their sizes and magnetic properties as shown in ref. [65, 66]. Various experiments show that magnetophoresis is also useful to functionalise the surface of magnetic microparticles (e.g. for specific binding to biomolecules) in a single microfluidic setup with minimal user intervention. In such applications, the microparticles are pumped into a microchannel and a magnetic field is used to manoeuvre the particle through multiple streams of different solutions [67–70]. This has the advantage that all reaction and washing steps are integrated in a single device and the use of expensive solutions is drastically minimised. In terms of biological applications, magnetic microparticles can be used to move biological structures such as cells. This can be realized by either attaching magnetic microparticles to the cell surface [71, 72] or through cellular

uptake of magnetic nanoparticles [65, 73]. That way, individual cells can be separated from cell mixtures and sorted using different magnetic labels as demonstrated by Pamme *et al.* [65]. The magnetic labelling of cells can also be used to hold the cells within the microfluidic channels which can enhance the efficiency of biological assays as shown in a cell toxicity study by García-Alonso *et al.* [74]. Especially attractive in this field is the integration of magnetophoresis into full-analysis experiments on a single microfluidic device. Liu *et al.* [75] and Hopwood *et al.* [76], for example, designed a system for DNA analysis that integrates extraction, reaction, separation and detection steps in a single microfluidic device.

In this chapter, we focus on the magnetophoresis of diamagnetic particles in solution. Such particles are attracted towards the magnetic field minimum as opposed to commonly used superparamagnetic or ferromagnetic particles which are attracted towards the magnetic field maximum. One of the main contributing factors to the magnetophoretic force is the magnetic susceptibility of the particle. We chose particles made from HOPG as it is the strongest diamagnetic material known to date and therefore the most suitable material as for this experiment. The magnitude of the magnetophoretic force can be increased by using a paramagnetic solution and/or a strong magnetic field with a large field gradient. Since the natural environment of living systems is diamagnetic and paramagnetic solutions are in general toxic, we study the magnetophoresis of HOPG particles in a diamagnetic solution. In this chapter, we show that an arrangement of permanent magnets and focussing steel components generates a magnetic field suitable to transport HOPG particles. First, we present the theoretical background on magnetophoresis for HOPG microparticles and the experimental design. We then proceed to describe how the data is taken and our methods to evaluate the data. In the results, we show evidence for the magnetophoretic transport of HOPG microparticles in a diamagnetic solution and compare the transport rate of HOPG microparticles from different samples. To show that the setup can also transport other diamagnetic particles, we present the results for the directed transport of polystyrene beads in a paramagnetic solution, too.

6.2   Forces on HOPG microparticles in solution

Particles in solution that are exposed to an external magnetic field are subject to several forces, namely the inertial force, the viscous drag force, the buoyancy, the gravitational force, the magnetophoretic force and the random forces that cause Brownian motion. For micron-sized objects, the Reynolds number (ratio of the inertial force to the viscous drag force) is very low (Re $\ll$ 1) and hence the inertial force can be neglected. As a result, the particle energy is immediately absorbed by the fluid and particles move instantaneously at terminal velocity,

v, once an external force acts upon them. The Brownian motion is caused by collisions with the molecules of the solution. To estimate if the magnetophoretic force is much stronger than the random forces, we calculate the Péclet number which is defined as the ratio of the advective transport rate to the diffusive transport rate. The advective transport describes the transport of a physical quantity (e.g. mass, thermal energy) by the surrounding fluid motion. For example, this can be the transport of mass due to fluid flow. Diffusive transport describes the transport of a physical quantity as a result of random collisions on the molecular scale. The magnetophoresis of HOPG microparticles corresponds to a transport of masses for which the Péclet number is defined as [77]:

$$\text{Pe} = \frac{Lv}{D} = \frac{Lv\gamma}{k_\text{B}T},$$

(6.1)

where L is the characteristic length of transport, v is the particle velocity, $D = \frac{k_\text{B}T}{\gamma}$ is the diffusion coefficient and γ is the viscous drag coefficient. If the particle motion is mainly driven by the advective transport, the Péclet number is larger than 1, i.e. $\text{Pe} > 1$. In our experiments, the HOPG microparticles migrate over distances between $25 - 170\,\mu\text{m}$ with velocities in the range $0.7 - 10\,\mu\text{m/s}$. The viscous drag coefficient values are between $0.3 \times 10^{-7}\,\text{kg/s}$ and $10^{-7}\,\text{kg/s}$. For $L = 25\,\mu\text{m}$, $v = 0.7\,\mu\text{m/s}$, $\gamma = 0.3 \times 10^{-7}\,\text{kg/s}$ and $T = 295\,\text{K}$ (temperature in the experiment) the minimum Péclet number value is $\text{Pe} \approx 156$ and thus the random forces are negligible. We also exclude the influence of the gravitational force and buoyancy as we focus on the horizontal particle motion perpendicular to the direction of gravitation. Consequently, the particle motion is described by the magnetophoretic force, $\mathbf{F}_\text{mag}$, and the viscous drag force, $\mathbf{F}_\text{d}$ and the equation of motion is expressed as:

$$\mathbf{F}_\text{mag} + \mathbf{F}_\text{d} = 0.$$

(6.2)

6.2.1 Magnetophoretic force on HOPG microparticles

For the description of the magnetophoretic force on a HOPG microparticle in solution, we apply the effective moment method introduced in Chapter 3 and use the expressions derived for an ellipsoid-shaped HOPG particle with semi-axes a_1, b_1 and c_1 (see Figure 3.1). Let us consider a HOPG microparticle with volume V_1 that is submerged in an isotropic solution with magnetic susceptibility χ_1. The particle is subject to an external magnetic field, $\mathbf{B}_0$, which can be expressed as:

$$\mathbf{B}_0 = B_0 \begin{pmatrix} \sin\theta\cos\phi \\ \sin\theta\sin\phi \\ \cos\theta \end{pmatrix},$$

(6.3)

in which $B_0 = |\mathbf{B}_0|$ is the magnetic field strength and θ and ϕ are the polar angles as defined in Chapter 5.

By substituting the expression for the magnetic moment in Equation (3.14) into Equation (3.3), the magnetophoretic force becomes:

$$\mathbf{F}_{\mathrm{mag}} = \frac{V_1}{\mu_0} \left[\left(\chi_\perp - \chi_\parallel \right) \cos^2\theta + \chi_\parallel - \chi_1 \right] B_0 \nabla B_0. \tag{6.4}$$

In Chapter 5, we saw that particles align their graphene planes parallel to the magnetic field direction when the field is sufficiently strong. Therefore, we can set $\theta = 90°$ for aligned particles and write Equation (6.4) as:

$$\mathbf{F}_{\mathrm{mag}} = \frac{V_1}{\mu_0} \left(\chi_\parallel - \chi_1 \right) B_0 \nabla B_0. \tag{6.5}$$

From Equation (6.5), we can see that the direction of the force depends on the difference between the magnetic susceptibility of the particle and the solution. This means that the direction of the particle motion can be controlled by choosing a solution with suitable magnetic susceptibility: if $\left(\chi_\parallel - \chi_1 \right) < 0$, particles move towards the magnetic field minimum, whereas if $\left(\chi_\parallel - \chi_1 \right) > 0$ they move towards the field maximum. Our experiment fulfils the condition $\left(\chi_\parallel - \chi_1 \right) < 0$ so that particles move towards the field minimum.

6.2.2 Viscous drag force on an ellipsoidal particle

Particles in motion in solution experience a viscous drag force, $\mathbf{F}_d$, as a result of the interaction between the particle surface and the solution. The viscous drag force, $F_{d,i}$, for a smooth ellipsoid was derived by F. Perrin [57, 78]. Along each of the ellipsoid's principal axes with $i = x$, y, z, it is given by:

$$F_{d,i} = -\gamma_i v_i, \tag{6.6}$$

where v_i is the velocity of the ellipsoid in the x, y and z directions and γ_i is the corresponding viscous drag coefficient. For movements in solution with viscosity η, the viscous drag coefficients along the x, y and z directions are given as:

$$\gamma_x = \frac{16\pi\eta}{S + a_2{}^2 P\left(a_2\right)}, \tag{6.7}$$

$$\gamma_y = \frac{16\pi\eta}{S + b_2{}^2 P\left(b_2\right)}, \tag{6.8}$$

$$\gamma_z = \frac{16\pi\eta}{S + c_2{}^2 P\left(c_2\right)},\tag{6.9}$$

with

$$S = \int_0^\infty \frac{\mathrm{d}s}{\sqrt{\left(a_2{}^2 + s\right)\left(b_2{}^2 + s\right)\left(c_2{}^2 + s\right)}}\tag{6.10}$$

and

$$P\left(\lambda\right) = \int_0^\infty \frac{\mathrm{d}s}{\left(\lambda^2 + s\right)\sqrt{\left(a_2{}^2 + s\right)\left(b_2{}^2 + s\right)\left(c_2{}^2 + s\right)}},\tag{6.11}$$

where λ can be a_2, b_2 or c_2.

6.2.3 Magnetophoretic velocity for HOPG microparticles

The components of the horizontal magnetophoretic velocity, $v_{\text{theo,i}}$, for a HOPG microparticle can be calculated by substituting the magnetophoretic force in Equation (6.5) and the viscous drag force in Equation (6.6) into the equation of motion in Equation (6.2). We define $v_{\text{theo,i}}$ as v_i and get:

$$v_{\text{theo,i}} \equiv v_i = \frac{V_1}{\mu_0 \gamma_i}\left(\chi_\parallel - \chi_1\right)B_0\left(\nabla B_0\right)_i,\tag{6.12}$$

for $\theta = 90°$. Equation (6.12) shows that the velocity depends on the particle volume and shape (through γ_i), the magnetic susceptibility of the particle and of the solution, and the external magnetic field strength and gradient.

6.3 Experimental setup

This section describes the experimental setup designed to achieve and analyse magnetophoresis of HOPG microparticles in solution. The main challenge revolves around the generation of a strong magnetic field with a steep gradient as required by the factor $B_0 \nabla B_0$ in Equations (6.5) and (6.12).

Figure 6.1a shows a photograph of the experimental setup. The HOPG microparticle is imaged from above using the microscope (total magnification: $10\times$) as described in Chapter 4. The videos of the particle motion are acquired at 13 fps. Figure 6.1b shows a close-up view of the magnetic arrangement in our setup. To generate the magnetic field for the magnetophoretic transport, we focus the magnetic field lines of two opposing block magnets by means of two steel wedges. To hold and expose the HOPG microparticles to the magnetic field in the gap between the steel wedges, we use glass capillaries with square cross section (CM Scientific, part no. 8510). The internal width and the wall thickness of the capillaries are 100 μm
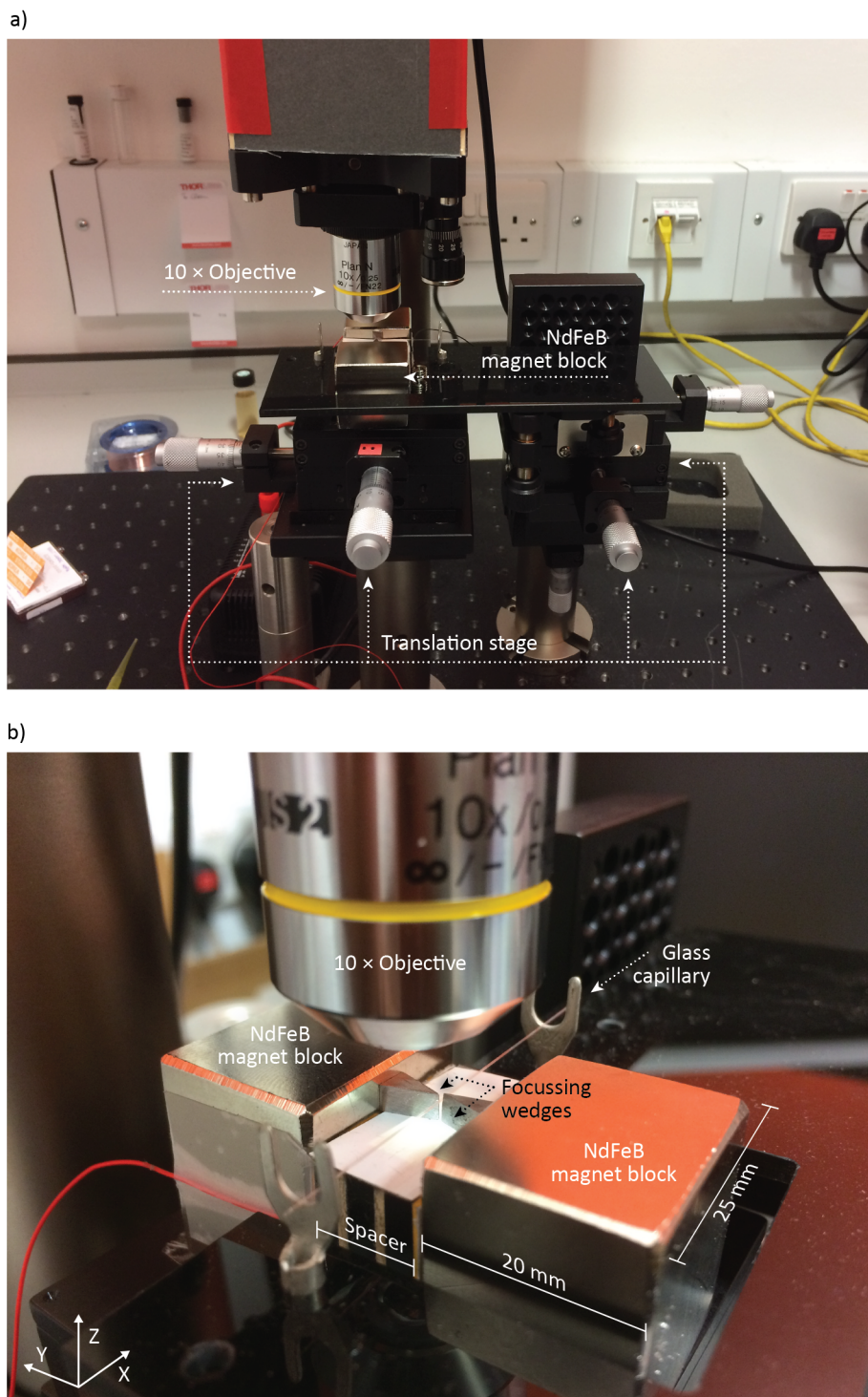
Figure 6.1: Photographs of the experimental setup to study the magnetophoretic transport of HOPG microparticles. a) Photograph of the entire experimental setup. b) Close-up view of the setup in the sample region. The magnetic field is generated with two NdFeB block magnets (size: $25 \times 20 \times 25$ mm) and two focussing wedges made from steel. The HOPG microparticles in solution are contained in a glass capillary which is placed in the magnetic field between the steel wedges.

and 50 μm, respectively. Each capillary is cleaned in an ultrasonic bath with acetone for 15 minutes and then dried on a hot stove for at least one hour before use. The microparticles are introduced into the capillary by dipping it into a dilute particle dispersion. The capillary ends are then sealed with quick-drying nail varnish to prevent fluid flow or evaporation during the experiments. To place the capillary in the magnetic field, we designed a sample holder which was cut out of a sheet of acrylic glass by our mechanical workshop. We adjust the positions of the capillary and the magnets under the microscope by means of five translation stages (Thorlabs, Part. No. MT1B) with micrometre precision as shown in Figure 6.1a.

6.3.1   Generating the magnetic field

NdFeB magnets are permanent magnets that can generate strong magnetic fields at the surface and hence are suitable for this experiment. In our setup, we use grade N50M NdFeB magnets (Magnet Sales Ltd., Part. No. NIBL 01483) that have a block shape with size 25 mm × 20 mm × 25 mm in the X, Y and Z directions (see Figure 6.1b). The magnetisation direction of the magnets is parallel to the Y-axis. Figure 6.2 shows Gaussmeter measurements of the magnetic field in the Y direction for a single magnet as a function of distance to the surface. We can see that the maximum value of the magnetic field and corresponding gradient at the surface are $\sim 0.5\,\mathrm{T}$ and $\sim 40\,\mathrm{T/m}$, respectively. Therefore, the largest $B_0 \nabla B_0$ value in the Y direction is around $20\,\mathrm{T^2/m}$. In our earlier tests, we have placed the HOPG microparticles in solution as close as possible to the magnet and could not observe any magnetic field induced particle migration. Consequently, stronger magnetic fields and field gradients are necessary to move HOPG microparticles in solution.
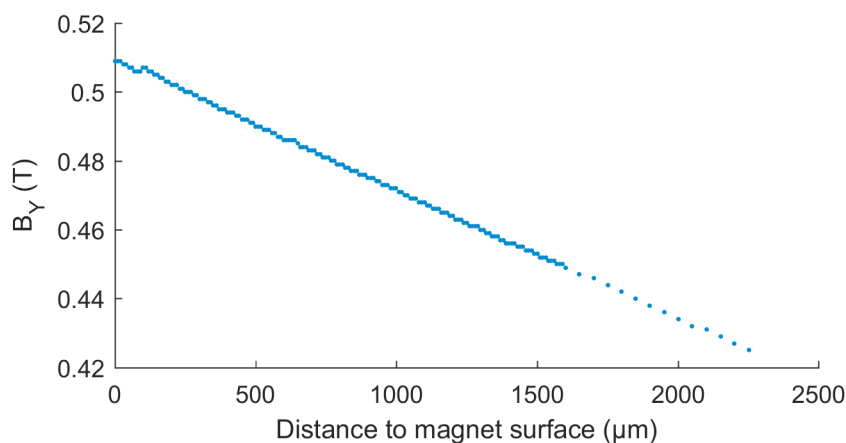
Figure 6.2: Measured magnetic field strength in the Y direction as a function of distance to the magnet's surface. The measurements correspond to a grade N50M NdFeB block magnet with size 25 mm × 20 mm × 25 mm in the X, Y and Z directions.

To generate a larger $B_0 \nabla B_0$ value, we use steel wedges which increase the field line density (magnetic flux) towards the tip where it generates a local field with large B_0 and ∇B_0. Each wedge has a base width of 4 μm, a height of 6 μm and a thickness of 3 μm. Since an increase of ∇B_0 implies a fast drop in B_0 with distance from the tip, it is important to place the wedges as close as possible to the HOPG microparticles. Here, we set the gap distance between the tip of the wedges to ~ 250 μm. Since the magnets are attracted to each other, we use spacers made of fitted acrylic glass pieces and paper sheets to keep them separated (see Figure 6.1b).

6.3.2   Simulating and measuring the magnetic field

Since the distance between the tips of the wedges is smaller than the thickness of the Gaussmeter probe (1 mm), it is impossible to measure the magnetic field in the sample region directly. Instead, we use the Mathematica package Radia [79] to generate a 3D model of our setup and simulate the magnetic field.

Figure 6.3a shows a 3D model of a single NdFeB magnet with a steel wedge placed onto the magnet. The magnet is modelled with a remanent magnetisation of 1.4 T (as reported by the manufacturer). For the modelling of the wedge, we use the sizes presented in the previous subsection and use microscope images of the wedge tip. The latter accounts for the irregular shape of the tip as a result of the machining process. Since steel is a non-linear magnetic material, the magnetisation inside the wedge is not uniform. Therefore, we subdivide the wedge into 25 sections along the X, Y and Z directions. This number has been determined empirically by increasing the subdivisions until the calculated field values stop to fluctuate.

The magnetic susceptibility and the saturation magnetisation of steel are also needed as inputs to the simulation. We optimize both values until the simulation agrees with the Gaussmeter measurements of the magnetic field in the Y direction generated by a single NdFeB magnet with a steel wedge placed in the centre of the magnet's north pole (see Figure 6.3b). A superposition of the simulated magnetic field with the optimized parameters and the measured magnetic field is shown in Figure 6.3c, evidencing good agreement. This corresponds to a (volume) magnetic susceptibility and the saturation magnetisation of 34 and 2 T, respectively. Both values are within the range reported in the literature [80]. We use these parameter values to simulate the magnetic field in the gap between two NdFeB magnets with two wedges as shown in Figure 6.4a. Figure 6.4b shows the calculated magnetic field map on the X-Y plane at $Z = Z_0$ which is at half the thickness of the wedge as indicated in Figure 6.4a. In the gap, we find magnetic field values around 1.5 T at the centre ($Y = 0$) which can increase up to 2 T closer to the wedges. Following Equation (6.5), we can determine the direction of the magnetophoretic force by calculating the components of $B_0 \nabla B_0$. The corresponding values
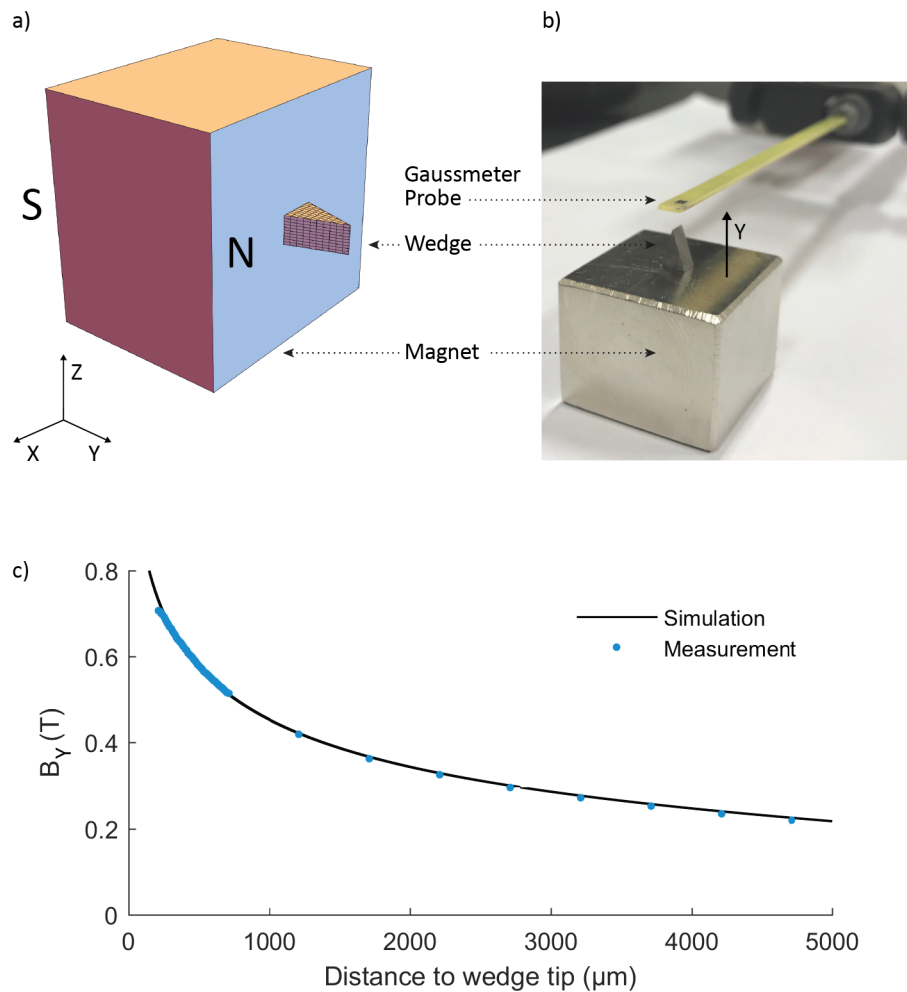
Figure 6.3: Magnetic field of a single NdFeB magnet with a steel wedge placed on the magnet's north pole. a) 3D model for the magnetic field simulation with Radia (N=North pole, S=South pole). b) Photograph of the setup to measure the Y component of the magnetic field. c) Superposition of the measured data and the simulation (with optimized material parameters for the wedge) as a function of distance from the wedge tip along the Y direction.

in the X and Y directions can be appreciated in Figure 6.4c and d, respectively. In the Y direction, we see the forces directed towards the centre between the wedges whereas in the X direction, they are pointing away from the wedges. The largest $B_0 \nabla B_0$ value in the X direction is about $3000 \, T^2/m$ which is two orders of magnitude larger than the value found for a single magnet. Figure 6.4e shows the magnetic field strength along the red dotted line (Y $= 0$) in Figure 6.4b over a distance of $1000 \, \mu m$. We can see that the magnetic field strength and the field gradient decrease as we move further away from the wedges along the X direction. With respect to Figure 6.4d, this shows clearly that particles move towards the magnetic field minimum. Figure 6.4f shows the calculated magnetic potential energy (divided by the thermal energy $k_B T$) and the theoretical magnetophoretic force along the red dotted line for a HOPG microparticle with representative volume ($34 \, \mu m^3$) in a $20 \, mM$ NaCl aqueous solution. For the calculation, we assume the graphene planes to be aligned in the magnetic field direction and

set the temperature to $T = 295\,\mathrm{K}$. Both plots show that particles placed on the red dotted line and exposed to the magnetic field move along the X direction away from $X = 0$.
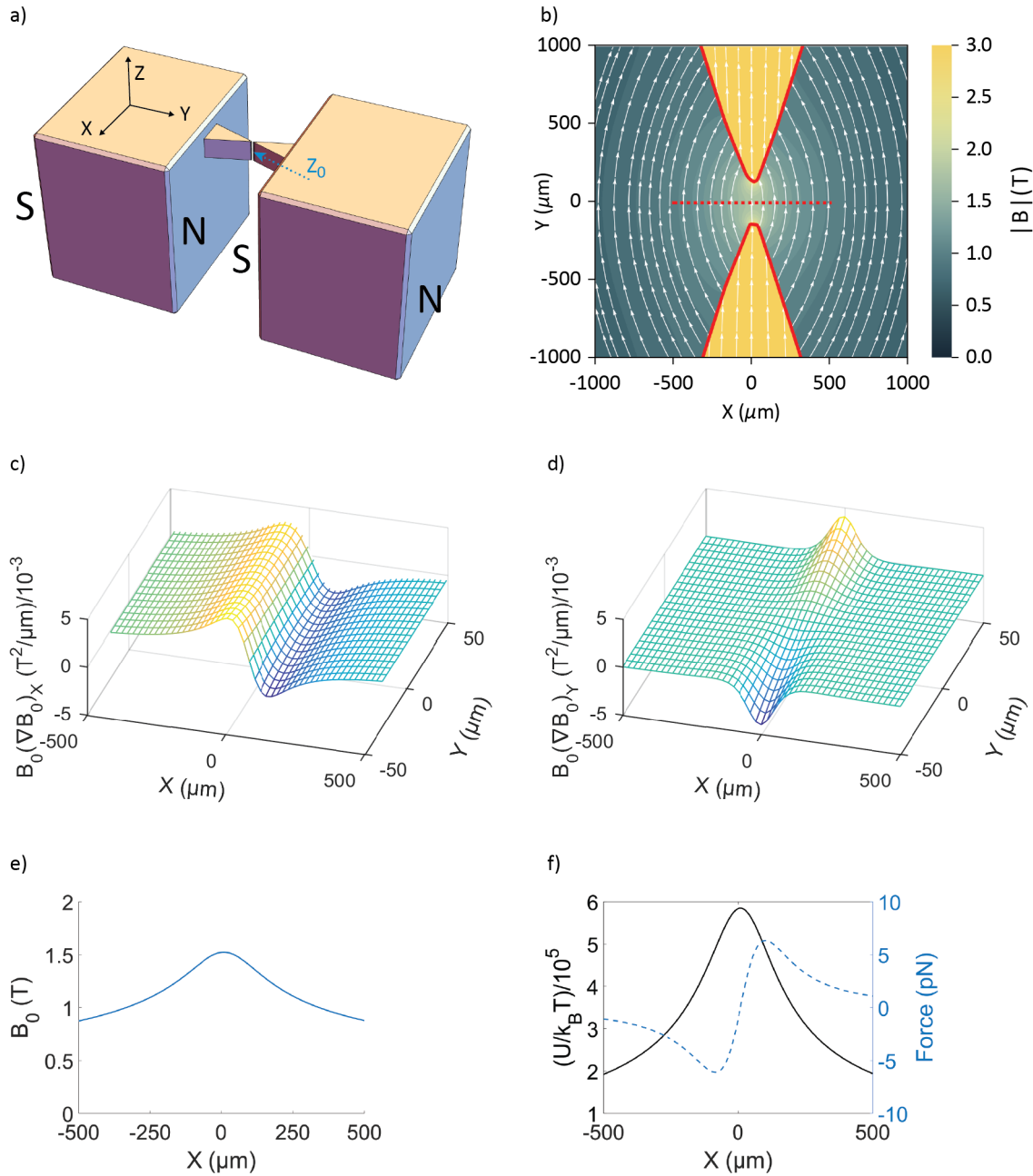
Figure 6.4: Magnetic field simulation of the magnetic arrangement to study the magnetophoretic transport of HOPG microparticles. a) The 3D model for the magnetic field simulation with Radia (N=North pole, S=South pole). b) Simulated magnetic field map on the X-Y plane at Z_0. c) 3D map of $B_0 \left(\nabla B_0 \right)_\mathrm{X}$. d) 3D map of $B_0 \left(\nabla B_0 \right)_\mathrm{Y}$. e) Magnetic field profile along the red dotted line in b). f) Magnetic potential energy divided by $k_\mathrm{B} T$ (solid black line) and magnetophoretic force (dashed blue line) along the same red dotted line in b) for a HOPG particle with volume $34\,\mathrm{\mu m}^3$ in a $20\,\mathrm{mM}$ NaCl aqueous solution. The graphene planes of the HOPG microparticle are assumed to be aligned in the magnetic field direction and the temperature is set to $T = 295\,\mathrm{K}$.

6.4 Data acquisition and analysis

We study the magnetophoretic transport of an individual HOPG microparticle by monitoring its velocity in the capillary under the microscope. Interactions with other particles are neglected as we use low particle concentrations in the solution. We investigate how the transport can be influenced by the lipid-coating, the mosaic spread of HOPG and the sonication duration set to break large HOPG flakes into micron-sized HOPG particles in the particle-fabrication protocol. For this purpose, we prepare seven different HOPG samples that are summarized in Table 6.1. The lipid-coated HOPG microparticles in a 20 mM NaCl aqueous solution are prepared as described in Section 2.4.1. We fabricate those particles from HOPG with a mosaic spread of 0.4° (HOPG-0.4) and set the sonication duration in the particle-production protocol to one hour. The uncoated HOPG microparticles in a mixture of acetone and water with volume fractions 40% and 60% (AceWater) are produced as described in Section 2.4.2. Those particles are fabricated from HOPG with a mosaic spread of either 0.4° or 3.5° (HOPG-3.5). The sonication duration is set to one, two or four hours. For every sample, we capture the motion of five to nine particles with shapes that resemble flat ellipsoids ($c_2 < a_2, b_2$).

Sample Name	HOPG Mosaic Spread	Solution	Coating	Soni. Time	Protocol
HOPG-0.4C-1h	$0.4° \pm 0.1°$	NaCl, 20 mM in water	POPC	1 h	Section 2.4.1
HOPG-0.4-1h	$0.4° \pm 0.1°$	AceWater	-	1 h	Section 2.4.2
HOPG-0.4-2h	$0.4° \pm 0.1°$	AceWater	-	2 h	Section 2.4.2
HOPG-0.4-4h	$0.4° \pm 0.1°$	AceWater	-	4 h	Section 2.4.2
HOPG-3.5-1h	$3.5° \pm 1.5°$	AceWater	-	1 h	Section 2.4.2
HOPG-3.5-2h	$3.5° \pm 1.5°$	AceWater	-	2 h	Section 2.4.2
HOPG-3.5-4h	$3.5° \pm 1.5°$	AceWater	-	4 h	Section 2.4.2

Table 6.1: List of samples prepared for the analysis of magnetophoresis with HOPG microparticles in solution. Soni. time: Sonication time. AceWater: Acetone and water mixture with volume fractions 40% and 60%.

6.4.1 Tracking the HOPG microparticle in the videos

The particle localisation process in this experiment involves applying our particle localisation code on a selected region of the video. We extract the particle position (on the X- and Y-axes) as a function of time by determining the particle centre of mass in each frame as detailed in Chapter 4. Occasional tracking errors, usually due to the interference of nearby microparticles, are identified and removed manually.

6.4.2 Quantifying the magnetophoretic velocity of HOPG microparticles

To determine the particle velocity, we fit the extracted particle position data on the X- and Y-axes (see Section 6.4.1) to a polynomial function and take its derivative. The fit minimises the noise that would be present when calculating the velocity between two consecutive positional datapoints.

The particle velocity depends on several variables namely the particle volume, the magnetic susceptibility of the particle and the solution, the viscous drag coefficient, the magnetic field strength and the field gradient (see Equation (6.12)). For our analysis, we evaluate the particle velocity along the X direction as it is the main direction of motion (see Figures 6.4d − e). Since we acquire the position data from HOPG microparticles with different sizes in different solutions and magnetic fields, we cannot simply compare the measured velocities, $v_{exp,x}$, in the X direction with each other. Instead, we use Equation (6.12) to calculate the theoretical velocity, $v_{theo,x}$, along the X direction for all particles at each position and take the ratio of $v_{exp,x}$ to $v_{theo,x}$. By evaluating this ratio, we can exclude the influence of the particle volume, the magnetic field strength and field gradient (see Equation (6.12)). That way, the comparison of the velocity ratios between the different samples reflects changes in the magnetic susceptibility and the viscous drag coefficient of the HOPG microparticles in the corresponding sample.

The variables to calculate $v_{theo,x}$ are determined as follows. To determine the particle size and volume, we use the same method as described in Section 5.3.3. The viscous drag coefficient is calculated with Equation (6.7), where we use the viscosity of water [81] for particles in a 20 mM NaCl aqueous solution ($\eta = 8.9 \times 10^{-4}$Pa s) and the value reported by Noda *et al.* for the viscosity of AceWater ($\eta = 1.5 \times 10^{-4}$Pa s) [82]. The magnetic field strength and the field gradient at each position on the X-Y plane are obtained from simulations with Radia. The simulated fields are loaded into Matlab where we use interpolation to calculate the values of B_0 and ∇B_0 corresponding to a given position of the particle. All particles are assumed to have a magnetic susceptibility equal to that of the bulk material in Table 2.3. For HOPG-0.4 and HOPG-3.5 the magnetic susceptibilities in the in-plane direction are -8.16×10^{-5} and -7.81×10^{-5}, respectively. For the solutions in Table 6.1, the magnetic susceptibility of the 20 mM NaCl aqueous solution is assumed to be equal to that of water ($\chi_1 = -9 \times 10^{-6}$), whereas the magnetic susceptibility of AceWater, χ_{mix}, is calculated with the formula [83, 84]:

$$\chi_{mix} = \alpha_{acetone}\, \chi_{acetone} + \alpha_{H_2O}\, \chi_{H_2O}, \tag{6.13}$$

where $\alpha_{\text{acetone}} = 0.34$ and $\alpha_{\text{H}_2\text{O}} = 0.66$ are the molar fractions of acetone and water in the 40% acetone and 60% water volume mixture and $\chi_{\text{H}_2\text{O}} = -9 \times 10^{-6}$ and $\chi_{\text{acetone}} = -5.8 \times 10^{-6}$ are the respective magnetic susceptibilities from ref. [85]. By applying the formula, we get $\chi_{\text{mix}} = -7.9 \times 10^{-6}$. For mixtures of acetone and water this additive law is valid as shown by Smith *et al.* [86].

6.5 Results and discussion

We evaluate the data from a total of 48 HOPG microparticles from the samples in Table 6.1. The distributions of measured semi-axis lengths a_2, b_2 and c_2 for each particle are presented in Figures $6.5a - c$. Their mean values and standard deviations are summarized in Figure 6.5d.

We begin this section by showing evidence for the magnetophoretic transport of individual HOPG microparticles in solution followed by a comparison of the magnetophoretic transport in the HOPG samples in Table 6.1. Finally, as an additional demonstration we show results for the magnetophoretic transport of polystyrene beads in solution.
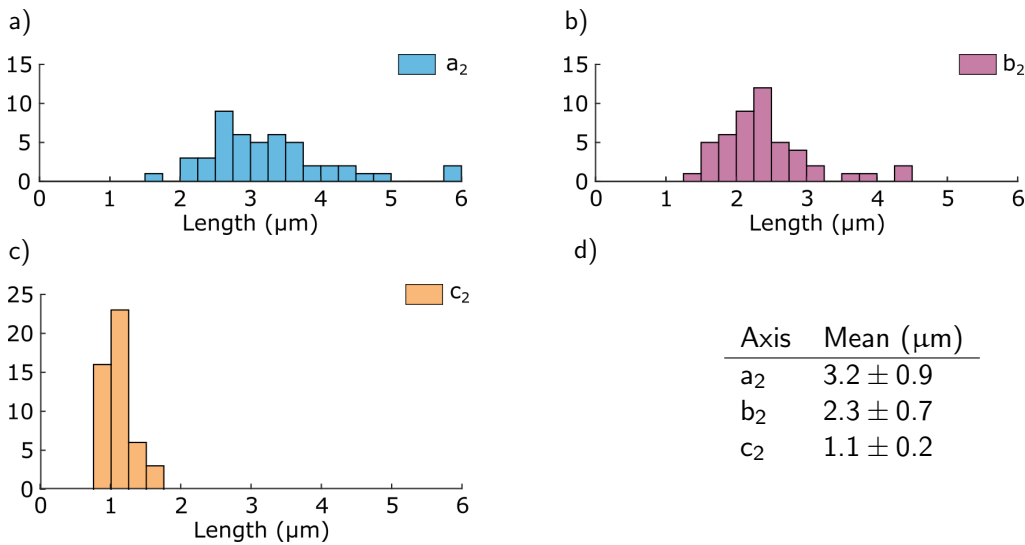
Figure 6.5: Measured semi-axis lengths for all 48 particles. a-c): Distributions of semi-axis lengths: a) a_2, b) b_2, c) c_2. d): Calculated mean value and standard deviation.

6.5.1 Magnetophoretic transport of single HOPG microparticles

Upon exposure, all HOPG microparticles immediately align their planes parallel to the Y-axis which is the direction of the magnetic field lines in the capillary (see Figure 6.4b). Once oriented, they can freely rotate around the Y-axis as shown in Figure 6.6. The alignment and rotational motion around the Y-axis are the result of the minimisation of the magnetic potential energy as described in Chapter 5.
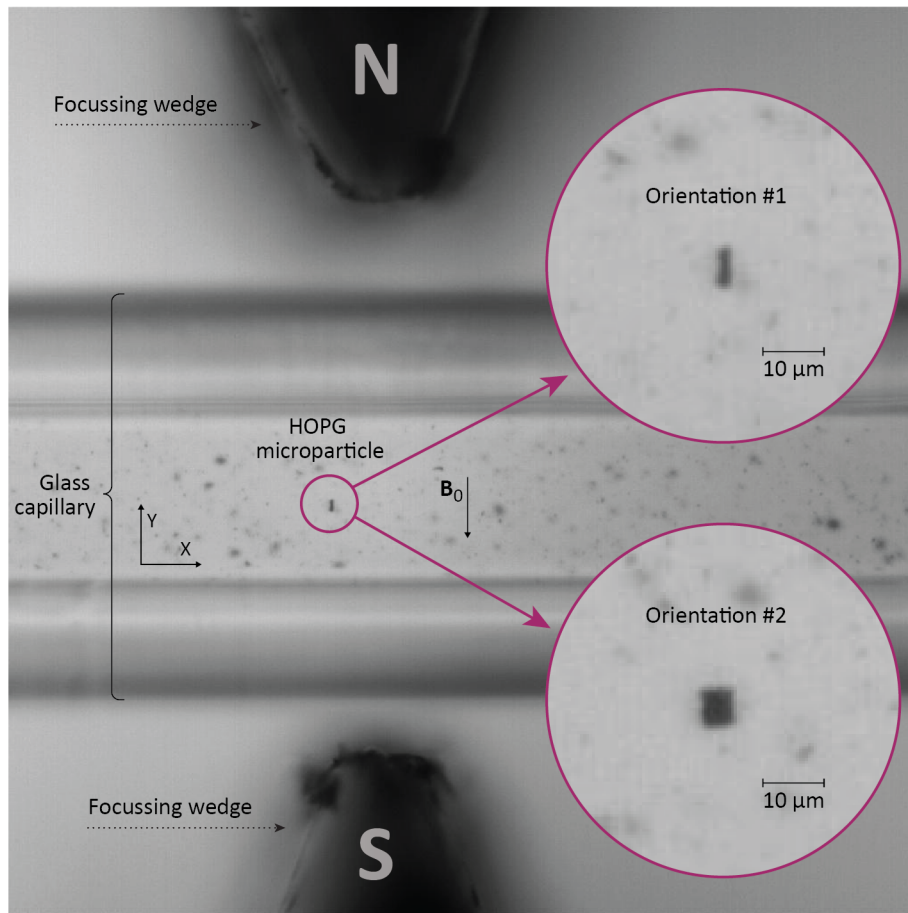
Figure 6.6: Image of a HOPG microparticle between two NdFeB magnets and two focussing steel wedges. The particle confined in a capillary is exposed to a magnetic field $\mathbf{B}_0$ that is parallel to the Y-axis. The graphene planes of the particle are aligned parallel to $\mathbf{B}_0$ and can rotate around the Y-axis as shown in orientation #1 and orientation #2. N: North pole. S: South pole.

Figure 6.7 illustrates the motion of a HOPG microparticle in the magnetic field. It shows a time sequence for a particle (from sample HOPG-3.5-1h in Table 6.1) which moves towards the magnetic field minimum (from right to left). The corresponding trajectory on the X-Y plane extracted from Figure 6.7 is shown in Figure 6.8a. We see a stable motion in the X direction over a distance of $\sim 170\,\mu m$ while there is hardly any motion in the Y direction. This clearly demonstrates, for the first time, the controlled directional transport of submerged HOPG microparticles. Figure 6.8b shows the particle positions (X and Y) as a function of time. As explained in Section 6.4.2, we use this data to determine the particle velocity components. We found that the fit results corresponding to the start and the end of the particle motion deviate slightly from the data due to the use of polynomial functions. To accommodate for this observation we remove the first and last 15 % from the fitted velocity data. The velocity components as a function of position X are presented in Figure 6.8c. The variation of the velocity along the X direction reflects the change in $B_0\,(\nabla B_0)_X$ in the magnetic landscape (see Equation (6.12)). We can see that the Y component of the particle velocity is practically zero, while the X component reaches a maximum absolute value of $\sim 6\,\mu m/s$.
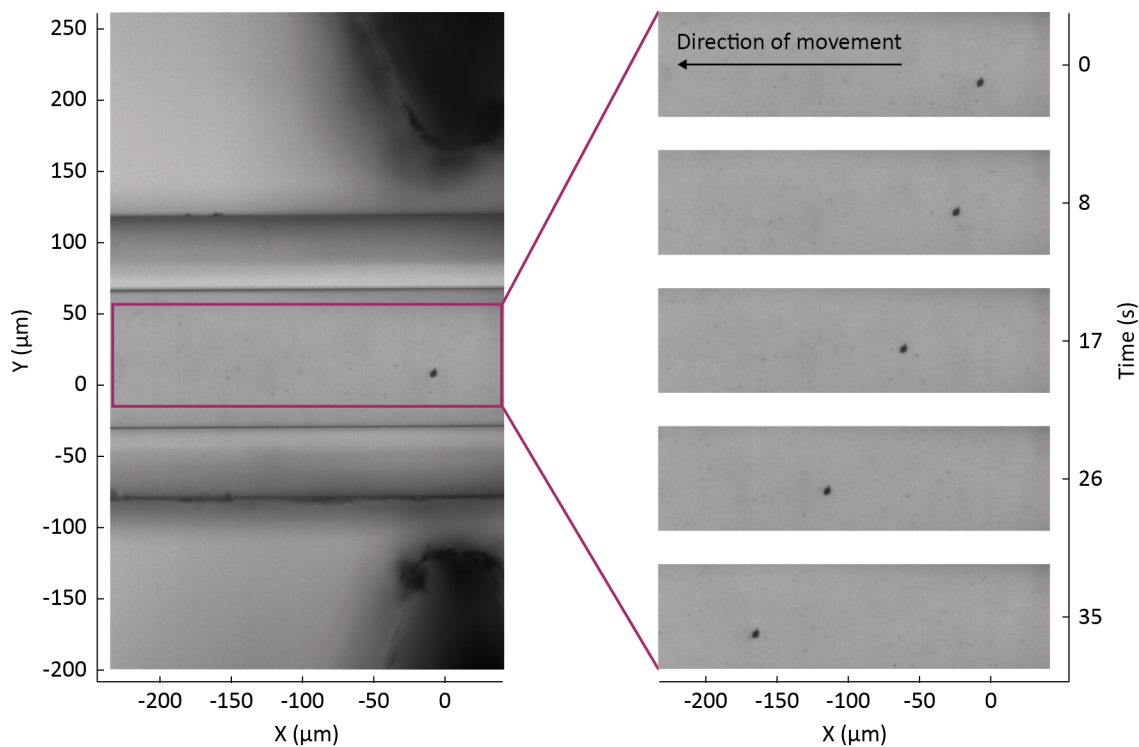
Figure 6.7: Magnetophoresis of a HOPG microparticle in AceWater. Left hand side: Image of the particle in the capillary. Right hand side: Image sequence of the particle position as a function of time.
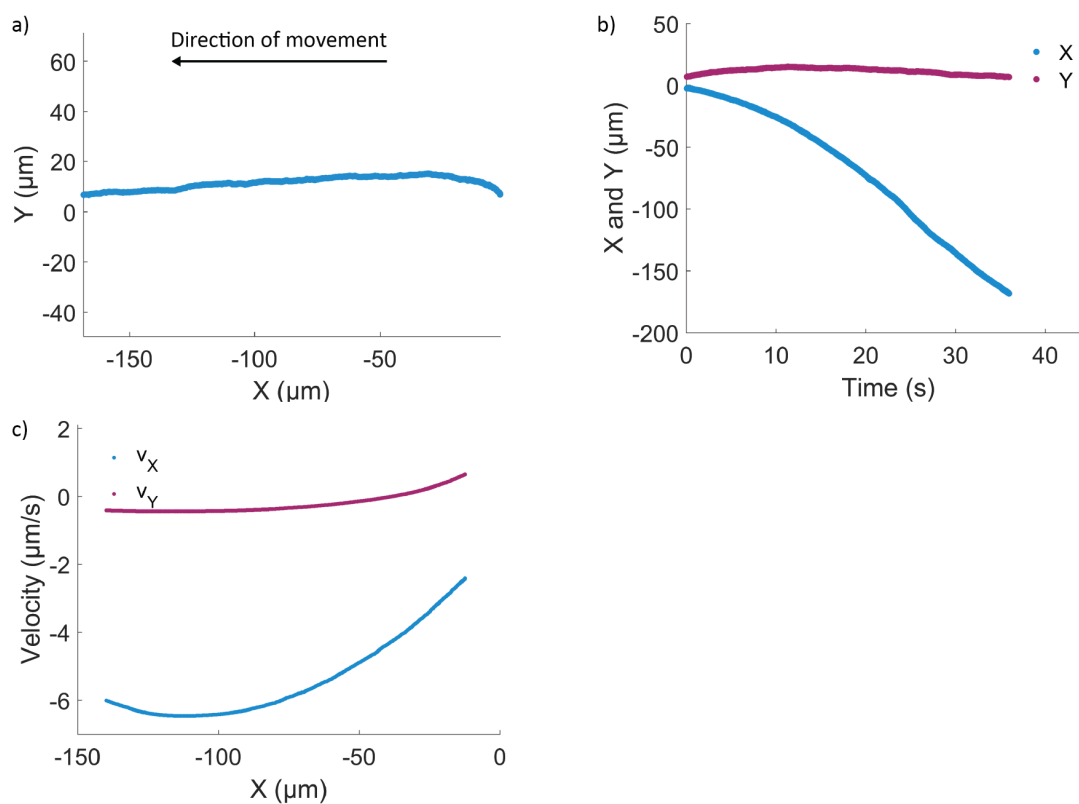
Figure 6.8: Extracted position and velocity for the HOPG microparticle in Figure 6.7. a) Trajectory on the X-Y plane. b) Position vs. time. c) Velocity components vs. position along the X direction. The velocity is calculated by fitting the data in b) to a polynomial function and then taking the derivative.

6.5.2   Magnetophoretic transport of HOPG microparticles in different samples

The HOPG microparticles fabricated by means of sonication have irregular shapes and sizes. As a result, the magnetophoretic transport of individual microparticles from the same sample can be different and hence the individual velocity ratio curves can differ in shape and distribution. Therefore, to analyse the magnetophoretic transport of individual HOPG microparticles from the same sample, we look at the velocity ratio curves as a function of position along the X direction. Figures 6.9 to 6.11 show the velocity ratios of the HOPG microparticle samples divided into three groups. Figure 6.9 shows the data for lipid-coated HOPG microparticles in a 20 mM NaCl aqueous solution. Figures 6.10a-c show the velocity ratio curves for uncoated HOPG microparticles made from a bulk piece of HOPG-3.5. The individual plots correspond to HOPG microparticles fabricated by means of sonication for one, two or four hours. Figure 6.11 shows similar plots to Figure 6.10 but for HOPG microparticles made from a bulk piece of HOPG-0.4. The velocity curves take values in the range $0.01 - 0.09$ implying a significant discrepancy between the theory and the experimental data. HOPG is about twice as dense as the surrounding solution and settles to the bottom within a few seconds. Since this time-scale is much larger than the sample preparation time, the effects due to the proximity of the particle to the wall are likely to be present. One well-documented effect is the wall-effect which describes an increased viscous drag due to different fluid velocities on the particle surface away and towards the wall [87]. For plate-like structures such as our HOPG microparticles, this effect can slow down the particle transport well beyond a factor of three [88]. The latter factor is the maximum value derived for the transport of a sphere parallel to a planar wall [87]. Another possible contribution to the low velocities can also be particle surface interactions that can lead to an increased surface friction as shown in Section 5.4.4. For the majority of the velocity ratio curves, we observe little variations of the velocity ratio over the length scale of the magnetophoretic transport. Furthermore, we see no difference in the velocity ratios along the positive and negative X directions which suggests that the forces on the particle (e.g. magnetophoretic force, drag force, friction) are consistent in both directions.

Table 6.2 summarises the average velocity ratio with the corresponding standard deviation, the number of analysed particles per sample ($N_{\text{particles}}$), the total number of data points (N_{points}) and the number of particle tracks (N_{tracks}) for each sample. The variations of the average velocity ratios between the samples indicate possible influences of the particle-fabrication protocol on the magnetophoretic transport of HOPG microparticles.

Sample	$\langle v_{exp,x}/v_{theo,x} \rangle$	$N_{particles}$	N_{points}	N_{tracks}
HOPG-0.4C-1h	0.04 ± 0.02	9	12427	22
HOPG-0.4-1h	0.06 ± 0.02	5	3991	17
HOPG-0.4-2h	0.03 ± 0.01	6	4184	16
HOPG-0.4-4h	0.02 ± 0.01	6	10723	20
HOPG-3.5-1h	0.03 ± 0.01	8	7032	24
HOPG-3.5-2h	0.03 ± 0.01	9	6697	23
HOPG-3.5-4h	0.03 ± 0.01	5	8148	19

Table 6.2: Calculated average velocity value and standard deviation for the HOPG microparticle samples in Table 6.1. $N_{particles}$: Number of particles measured in each sample. N_{points}: Number of data points in each sample. N_{tracks}: Number of particle tracks acquired for each sample. The velocity ratio is defined as the measured X component of the particle velocity, $v_{exp,X}$, to the corresponding theoretical velocity, $v_{theo,X}$.
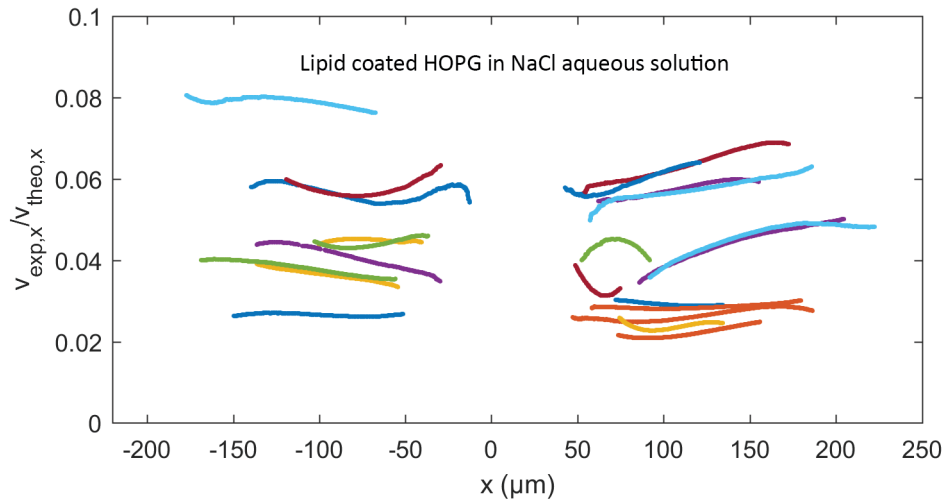
Figure 6.9: Velocity ratio as a function of position in the X direction for lipid-coated HOPG microparticles in a 20 mM NaCl aqueous solution. The HOPG microparticles are fabricated by means of sonication for one hour. The velocity ratio is defined as the measured X component of the particle velocity, $v_{exp,X}$, to the corresponding theoretical velocity, $v_{theo,X}$.
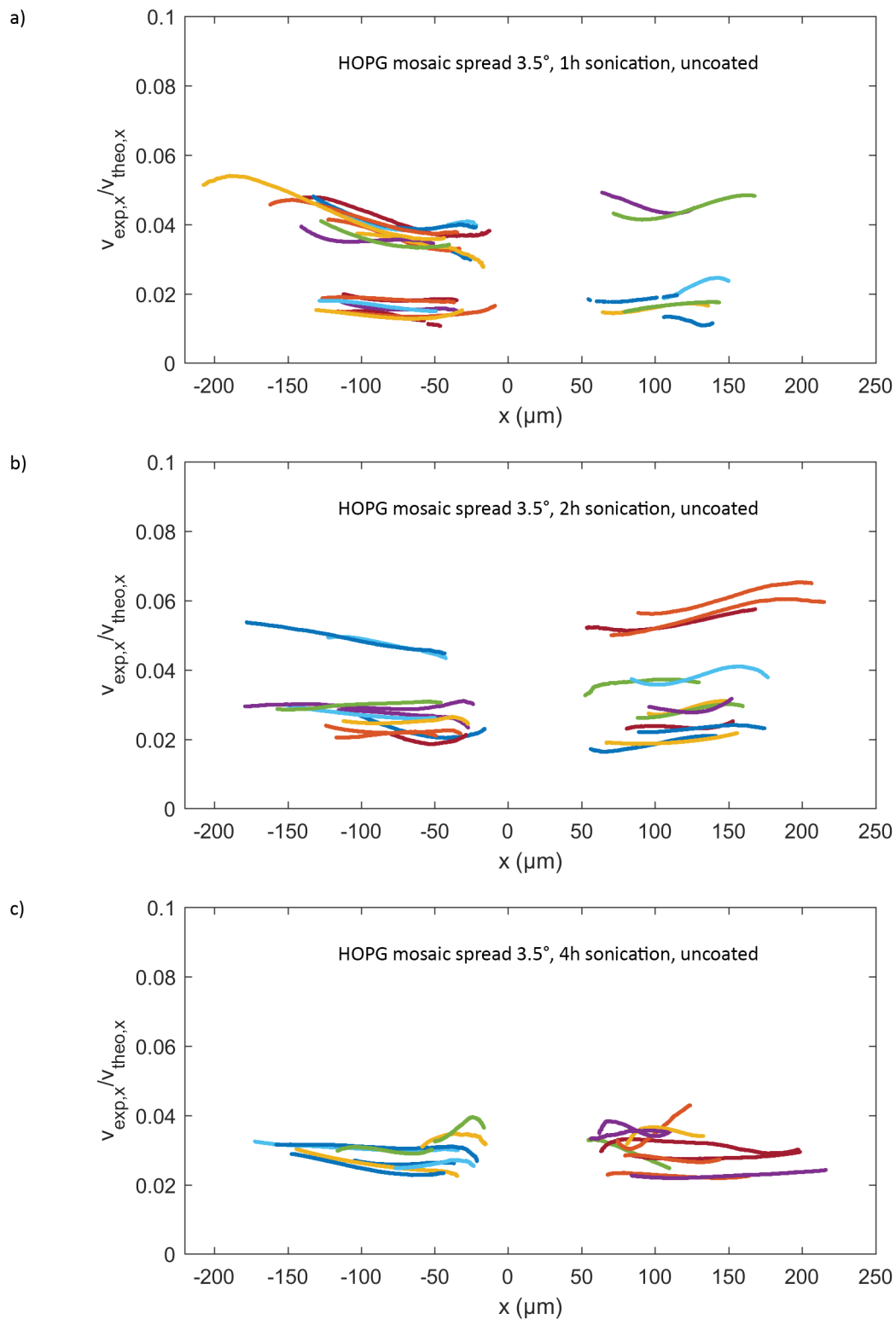
Figure 6.10: Velocity ratio as a function of position in the X direction for uncoated HOPG microparticles in AceWater. The HOPG microparticles are produced from a bulk HOPG sample with mosaic spread 3.5°. a) Curves of HOPG microparticles sonicated for one hour. b) Curves of HOPG microparticles sonicated for two hours. c) Curves of HOPG microparticles sonicated for four hours. The velocity ratio is defined as the measured X component of the particle velocity, $v_{exp,X}$, to the corresponding theoretical velocity, $v_{theo,X}$.
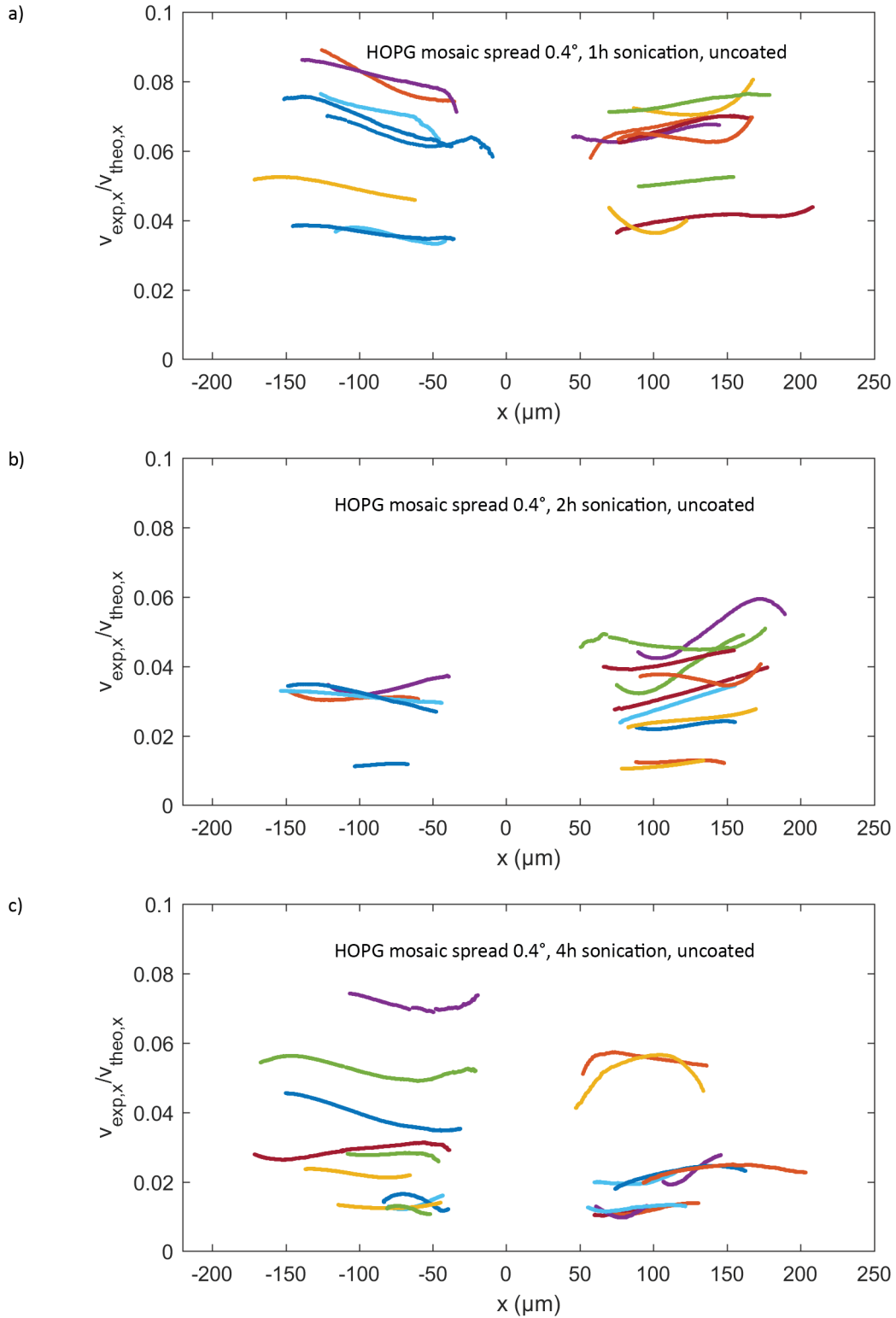
Figure 6.11: Velocity ratio as a function of position in the X direction for uncoated HOPG microparticles in AceWater. The HOPG microparticles are produced from a bulk HOPG sample with mosaic spread 0.4°. a) Curves of HOPG microparticles sonicated for one hour. b) Curves of HOPG microparticles sonicated for two hours. c) Curves of HOPG microparticles sonicated for four hours. The velocity ratio is defined as the measured X component of the particle velocity, $v_{exp,X}$, to the corresponding theoretical velocity, $v_{theo,X}$.

Influence of the lipid-layer on the magnetophoretic transport of HOPG microparticles

We evaluate the potential influence of lipid-coatings on the magnetophoretic transport by comparing the velocity ratios corresponding to the lipid-coated HOPG microparticles in a 20 mM NaCl aqueous solution (HOPG-0.4C-1h) and to the uncoated HOPG microparticles in AceWater (HOPG-0.4-1h). Both samples were prepared from HOPG-0.4 and sonicated for one hour.

Figure 6.12 shows the distribution of the velocity ratio for uncoated (Figure 6.12a) and lipid-coated HOPG microparticles (Figure 6.12b). While the distributions are broad, we find indications that for uncoated particles higher velocity ratios are more frequent than for coated ones. Consequently, lipid-coated HOPG microparticles tend to move slightly more slowly compared to uncoated HOPG microparticles. The average velocity ratios for lipid-coated and uncoated HOPG microparticles are 0.04 ± 0.02 and 0.06 ± 0.02, respectively. Therefore, the lipid-coating amounts to a potential drop in average magnetophoretic velocity by about 30 %.

Knecht *et al.* showed that lipid layers could absorb ions from the surrounding fluid [89]. In our case, these ions would be the Na^+ ions in the NaCl aqueous solution, meaning that the outer lipid layer would then be positively charged and interact with the negatively charged glass surface. However, the exact nature of this velocity reduction requires more research.

Figure 6.12: Calculated velocity ratio distribution of different HOPG microparticle samples: a) Uncoated HOPG microparticles in AceWater. b) Lipid-coated HOPG microparticles in 20 mM NaCl. In both samples, the HOPG microparticles are prepared from HOPG with a mosaic spread of 0.4° and are fabricated by means of sonication for one hour. The velocity ratio is defined as the measured X component of the particle velocity, $v_{exp,X}$, to the corresponding theoretical velocity, $v_{theo,X}$.

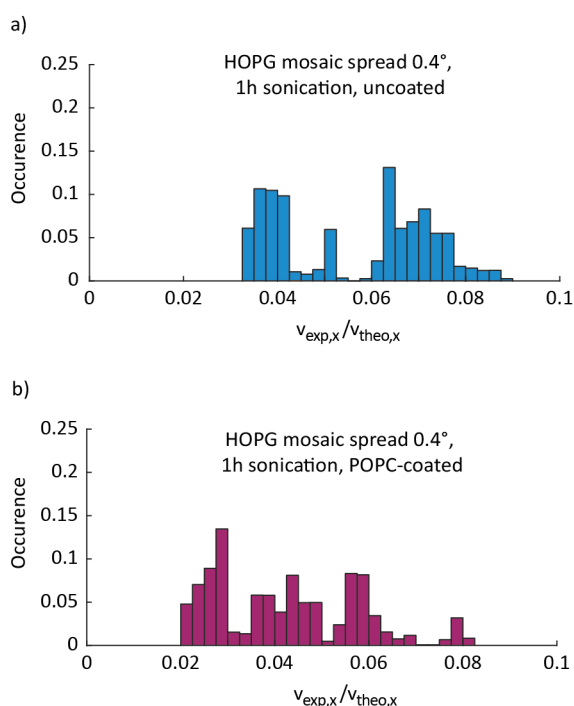**Influence of the mosaic spread and the sonication time**

We investigate whether the mosaic spread of the HOPG bulk samples could influence the magnetophoretic force by examining the data for microparticles made from HOPG-0.4 and HOPG-3.5. Additionally, we look at the effect of sonication time by comparing our results for HOPG-0.4 and HOPG-3.5 in AceWater, for sonication times of one, two and four hours.

Figures 6.13a − c show the measured velocity ratio distributions for HOPG-0.4 and Figures 6.13d − f show the same for HOPG-3.5. Each figure corresponds to a different sonication time.

Our data reveals no clear evidence that the mosaic spread could affect the magnetophoretic transport. In Section 2.3, we found that the bulk magnetic susceptibility values of HOPG-0.4 and HOPG-3.5 are similar to each other. Therefore, it is likely that the mosaic spread does not have an influence on the magnetic-field-induced particle motion.

On the other hand, it appears that the sonication duration in the particle-fabrication process does have an impact on the magnetophoretic transport. In the velocity ratio distributions for HOPG microparticles prepared from HOPG-0.4 (Figure 6.13a - c), we can see that higher velocity ratios are more frequent for HOPG microparticles sonicated for one hour (Figure 6.13a). As the sonication time increases to two and four hours, we can see that the low velocity ratios become more frequent. From Table 6.2, we can see that the average velocity ratio for HOPG microparticles made from HOPG-0.4 and sonicated for one hour is 0.06 ± 0.02. The velocity ratio decreases further to 0.03 ± 0.01 and 0.02 ± 0.01 when the sonication duration increases to two and four hours, respectively. For HOPG-3.5 (Figure 6.13d-f), this behaviour is less clear although we do observe that the distribution becomes more narrow with increasing sonication time. In the next subsection, we investigate potential effects of the sonication process on the HOPG microparticle that could lead to the observed decrease in the magnetophoretic velocity.

6.5.3 Characterizing the surface and magnetic properties of sonicated HOPG microparticles

During the sonication process, high frequency sound waves (usually above $20\,\text{kHz}$) generate microbubbles in solution that collapse and can generate high local temperatures above $5000\,\text{K}$ [90]. As the sonication time increases, these local implosions tear up millimetre-sized HOPG flakes into thin micron-sized flakes. This process can introduce changes on the particle surface and generate vacancies and edge defects on HOPG along with increased surface roughness. The latter can be observed from the SEM measurements in Figure 2.4. Additionally,
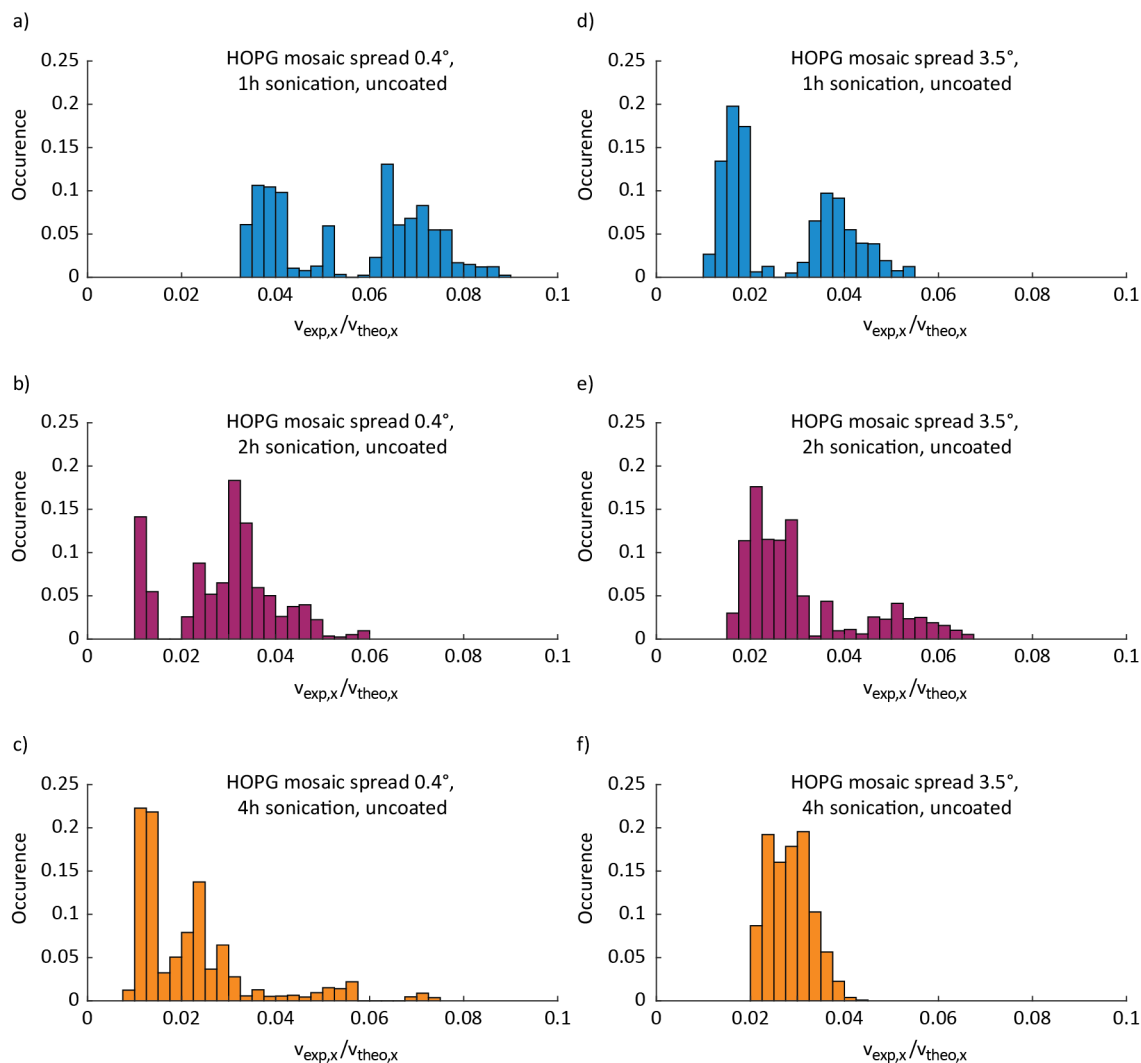
Figure 6.13: Calculated velocity ratio distribution of uncoated HOPG microparticles in AceWater. a-c) Histograms of the velocity ratios for HOPG microparticles prepared from HOPG-0.4. The different figures correspond to the different sonication times set in the particle-fabrication protocol: a) One hour, b) Two hours, c) Four hours. d-f) Histograms of the velocity ratios for HOPG microparticles prepared from HOPG-3.5. The different figures correspond to the different sonication times set in the particle-fabrication protocol: d) One hour, e) Two hours, f) Four hours. The velocity ratio is defined as the measured X component of the particle velocity, $v_{exp,X}$, to the corresponding theoretical velocity, $v_{theo,X}$.

this was demonstrated in an atomic force microscopy study on sonicated graphite particles by Xia *et al.* [91]. As they increased the sonication time from one to five hours, the root mean squared surface roughness increased from 5 nm to 30 nm. An increase in the surface roughness can lead to larger viscous drag forces on the particle in solution as it causes friction between the particle surface and the solution. As a result, it can reduce the measured magnetophoretic velocity as observed in this experiment.

It is also possible that the sonication-induced vacancies and edge defects in HOPG could cause a reduction in the diamagnetism of the particle. Theoretical studies show that isolated vacancies in the molecular structure of graphite and certain molecular structures ('zig-zag'

structures) at the particle edges are paramagnetic with a magnetic moment equivalent to that of an ion with spin $1/2$ [92–94]. This was experimentally verified through SQUID measurements with graphene sheets where vacancies were introduced by irradiating them with protons in the energy range $350-400$ keV [95]. A study by Milev *et al.* [96] also revealed that HOPG can become paramagnetic at room temperature after an extended ball milling period of 30 hours. Although, this does not apply to our experiment since our particles are still diamagnetic, it illustrates that the particle processing method can affect the magnetic properties of the particle. Based on these studies, it is possible that sonication-induced defects could change the volume magnetic susceptibility compared to that of pristine bulk HOPG. This would imply that the decline in migration velocity in comparison to the theoretical prediction is partly the consequence of sonication-induced surface roughness and defects in the particle.

To clarify the presence of vacancies and edge defects in our particles, we conduct measurements with a Raman spectrometer on an individual HOPG microparticle and on a bulk piece of pristine HOPG. Additionally, we use a SQUID magnetometer to determine the volume magnetic susceptibility of an aggregate of HOPG microparticles from measurements of the sample magnetisation at different magnetic field strengths. The HOPG microparticles and the bulk HOPG sample are prepared from HOPG-0.4. To prepare the bulk HOPG sample, we use a cleaned razor blade and cut out a piece from the pristine HOPG sample. The HOPG microparticle aggregate is prepared from a concentrated suspension of HOPG microparticles sonicated for four hours in AceWater. To prepare a dried aggregate of microparticles, we centrifuge 100 µl of the solution for 30 min at 10000 rpm to accumulate the particles at the bottom of the centrifuge tube and remove the solution at the top. This process is repeated several times until a sufficient amount of HOPG microparticles is accumulated at the bottom. Finally, we leave the sample on a hot stove for three days to make sure that the residual fluids on the particle are completely evaporated.

Analysing the HOPG microparticle surface with Raman spectroscopy

The presence of vacancies and edge defects in the HOPG sample can be identified by analysing two specific peaks in the Raman spectrum of HOPG: the G-peak at $1582\,\mathrm{cm}^{-1}$ and the D-peak at $1350\,\mathrm{cm}^{-1}$. The D-peak arises in the presence of molecular disorder in the graphene planes and can therefore be used as an indicator for defects in the molecular structure of HOPG [97–99]. A common practice for the analysis of defects in HOPG is to look at the ratio of the D-peak intensity to the G-peak intensity (D/G ratio) [97, 100]. If the D/G ratio is close to 0, the molecular structure of HOPG is intact.

The Raman spectrometer uses a $50\times$ objective and a 488 nm laser with a Gaussian intensity

profile and a full-width-half-maximum of 3 μm at the sample. It operates at 2.5 mW in order to prevent laser-induced damages in the sample. We take 36 Raman spectra over a $10 \times 10\,\mu m^2$ area with a grid size of 2 μm. Particular care is taken to choose visually smooth surfaces. This reduces contributions of particle edges to the spectrum which always appear as defects in the spectrum even if the molecular structure is intact [98]. All measurements are taken in collaboration with Dr. Chris Howard from the department of physics and astronomy at UCL.

Figure 6.14a shows a superposition of all 36 acquired Raman spectra from the scanned surface area of one pristine bulk piece of HOPG. In all spectra, the D-peak is absent and the distribution of the G-peak is narrow which is typical for HOPG with an intact molecular structure. Figure 6.14b shows the map of D/G ratios on top of a microscope image of the scanned surface. The entire grey area corresponds to the surface of the bulk HOPG sample which shows no surface roughness. Hence, the G/D ratios are very low with values in the range $0.008 - 0.013$. This confirms that the molecular structure in bulk HOPG is free from defects before it is processed to produce microparticles.

In Figure 6.15a we can see the 36 different Raman spectra acquired over a scanned area of an individual HOPG microparticle. All spectra have a D-peak at $1350\,cm^{-1}$ which was absent in the spectra of the bulk HOPG sample. Figure 6.15b shows the map of calculated D/G ratios on top of an image of the particle surface. The D/G ratio values are now in the range $0.05 - 0.17$ which is a clear increase compared to the results in Figure 6.14. Since the D-peak emerges only in the Raman spectra of sonicated particles, this could imply that sonication induces defects (e.g. vacancies) in the graphene planes of HOPG. As a result, it is possible that the magnetic susceptibilities of the microparticle are lower in absolute value to those of bulk HOPG. However, Figure 6.15b also shows a clear increase in surface roughness. In that case, the lower magnetophoretic velocities are the result of a larger viscous drag force on the particle. To investigate the contribution of defects to the magnetic properties of sonicated HOPG microparticles, we conduct measurements with a SQUID magnetometer in the following section.

Evaluating the magnetic contribution of sonication-induced defects with SQUID

As mentioned in the beginning of this subsection, sonication-induced defects in HOPG microparticles have been reported to be paramagnetic. At room temperature (295 K), the magnetic moments carried by the sonication-induced defects are agitated by thermal motion and require large magnetic field strengths to be aligned to the field and reach the maximum sample magnetisation (saturation magnetisation M_s). At low temperatures, the thermal agitation is reduced which makes it possible to align the magnetic moments with a weaker magnetic field.
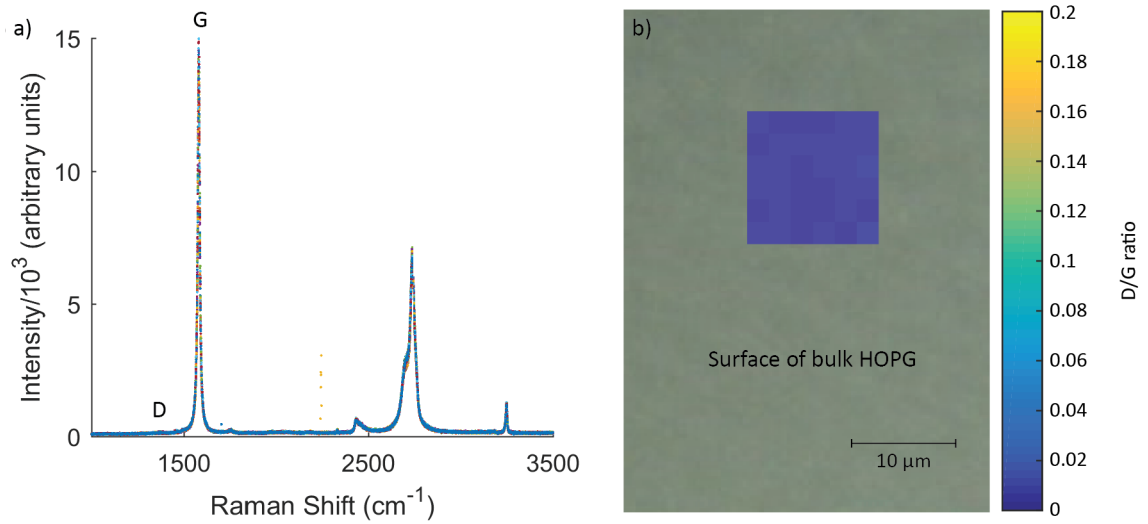
Figure 6.14: Raman spectroscopy measurements on a piece of bulk HOPG with a mosaic spread of 0.4°. a) Superimposed Raman spectra of pristine bulk HOPG. b) D/G ratio on a scanned surface of pristine bulk HOPG.
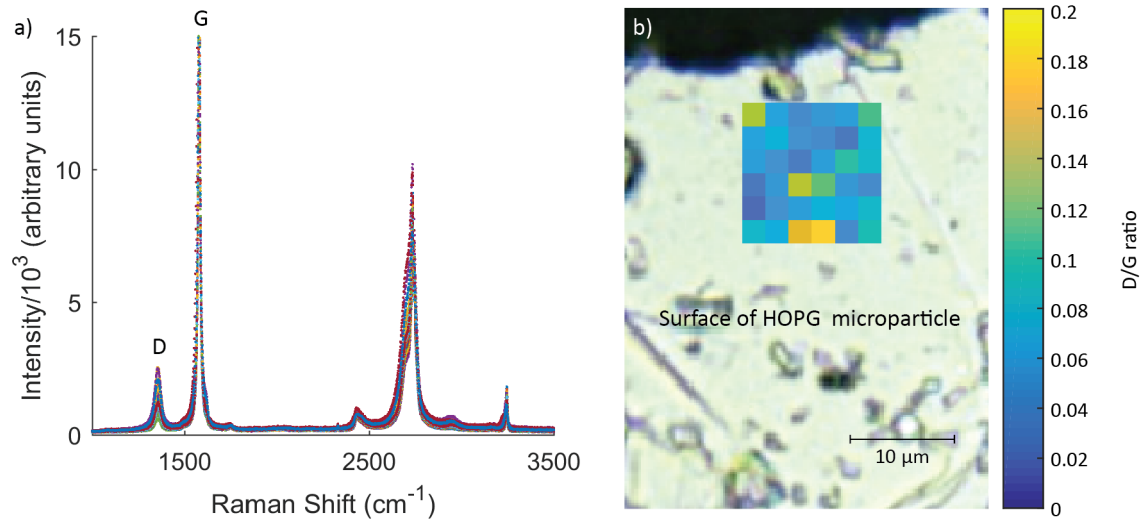
Figure 6.15: Raman spectroscopy measurements on a HOPG microparticle fabricated by means of sonication for four hours. a) Superimposed Raman spectra of a HOPG microparticle. b) D/G ratio on a scanned surface of a HOPG microparticle.

To illustrate the temperature behaviour, in Figure 6.16 we show the theoretical magnetisation curve of a paramagnet, $M_{para}(H)$, at different temperatures which we calculate with the formula [101]:

$$M_{para}(H) = M_s \tanh\left(\frac{\mu_0 \mu_B g}{k_B T} H\right),\tag{6.14}$$

where μ_B is the Bohr magneton and g is the g-factor of an electron. The plots show clearly that at low temperatures, the paramagnetic response (i.e. the linear increase of the sample magnetisation with the magnetic field strength and the saturation magnetisation) can be appreciated at relatively weak magnetic fields. Note that, in theory, the saturation magnetisation is temperature independent.
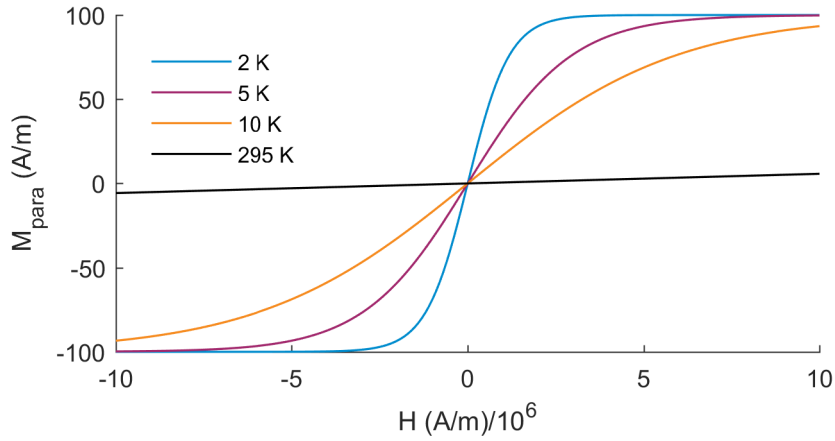
Figure 6.16: Illustration of the sample magnetisation of a paramagnet as a function of magnetic field strength at 2 K, 5 K, 10 K and 295 K. The magnetisation curves are calculated with a theoretical formula for paramagnets in an external magnetic field.
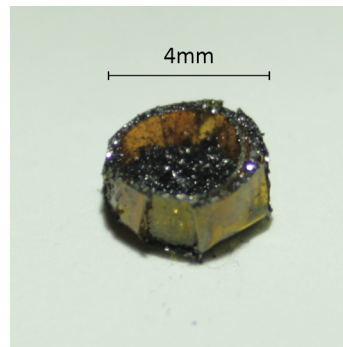
Figure 6.17: Sample of dried HOPG microparticles sonicated for four hours for examination with a SQUID magnetometer.

To measure the magnetic properties of HOPG microparticles with a SQUID magnetometer, we place 7.1 ± 0.1 mg of an aggregate of HOPG microparticles in a container as shown in Figure 6.17. The latter is constructed as described in Chapter 2. Because of the temperature dependency of paramagnets, we conduct the measurements at 295 K and at 2 K and set the sequence of the magnetic field to individual steps from 2.4×10^6 A/m to -2.4×10^6 A/m which is equivalent to 3 T to -3 T in air. For the measurements at 2 K, we include more steps at low magnetic fields than at 295 K to analyse the paramagnetic contribution from the sonication-induced defects. Figure 6.18 shows the sample magnetisation of the aggregate at 295 K and 2 K. At 2 K, the magnetisation of the aggregate becomes nonlinear at low magnetic fields between -0.8×10^6 A/m and 0.8×10^6 A/m. This behaviour could indicate two contributions to the sample magnetisation, namely, the main diamagnetic contribution of HOPG, $M_{\text{dia}}(H) = \chi_{\text{dia}} H$ (χ_{dia} is the magnetic susceptibility of HOPG), and the paramagnetic contribution from sonication-induced defects. Therefore, we assume the total sample magnetisation, $M_{\text{tot}}(H)$,

to be expressed as:

$$M_{\text{tot}}(H) = M_{\text{para}}(H) + M_{\text{dia}}(H) = M_{\text{para}}(H) + \chi_{\text{dia}}H. \qquad (6.15)$$

To extract the paramagnetic contribution from the total sample magnetisation data at $2\,\text{K}$, we need to determine χ_{dia}. For this purpose, we account for the fact that the paramagnetic term reaches saturation magnetisation when the absolute magnetic field strength is sufficiently high. Once the paramagnetic term is constant, the total sample magnetisation is linear to the magnetic field strength with a slope equal to χ_{dia}. From the total sample magnetisation data at $2\,\text{K}$ in Figure 6.18, it appears that the paramagnetic term reaches saturation magnetisation when the absolute magnetic field strength exceeds $0.8 \times 10^6\,\text{A/m}$, i.e. $M_{\text{para}}(H) = M_{\text{s}}$ for $|H| > 0.8 \times 10^6\,\text{A/m}$. To determine χ_{dia}, we fit the two data points below $-0.8 \times 10^6\,\text{A/m}$ to a linear function and the two data points above $0.8 \times 10^6\,\text{A/m}$ to another linear function. We then extract the slope from both fit results and calculate the average value and standard deviation of χ_{dia}. From this procedure, we get $\chi_{\text{dia}} = (-1.5 \pm 0.2) \times 10^{-4}$ which is between the measured values $\chi_{\parallel}$ and $\chi_{\perp}$ in Table 2.3. Such a value can be explained by the fact that the particles in the aggregate are randomly oriented.
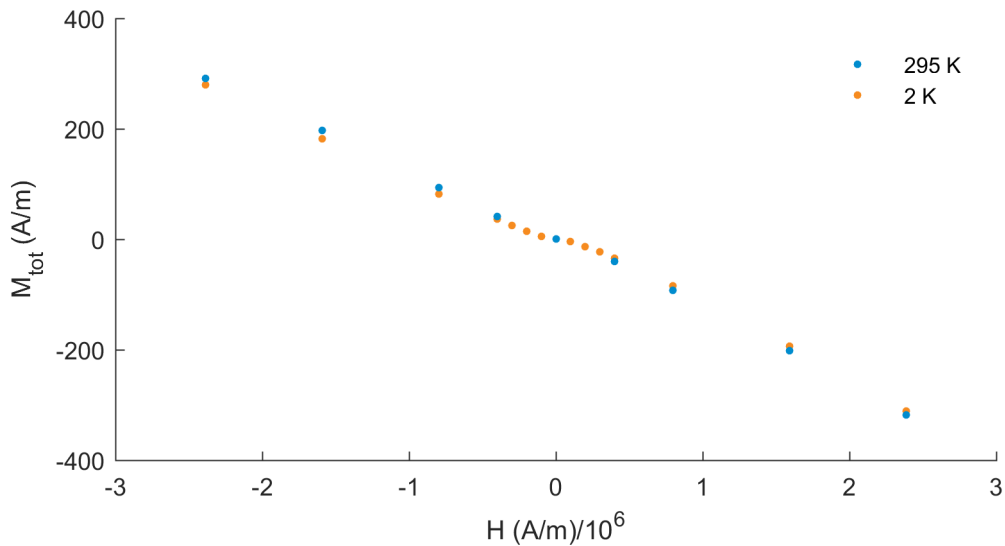
Figure 6.18: Sample magnetisation as a function of the external magnetic field strength at $295\,\text{K}$ (blue) and $2\,\text{K}$ (yellow). The data is measured for an aggregate of HOPG microparticles that was sonicated for four hours in the particle-fabrication process.

Figure 6.19 shows a superposition of M_{tot}, M_{dia} and M_{para} (obtained by subtracting M_{dia} from M_{tot}) for the aggregate at $2\,\text{K}$. At low magnetic fields, M_{para} is proportional to the magnetic field strength with a positive slope which is a typical behaviour for paramagnets. The saturation magnetisation of the paramagnetic term has a value in the range $20 - 50\,\text{A/m}$. At low magnetic fields, the temperature behaviour of the slope of M_{para} is described by Curie's law
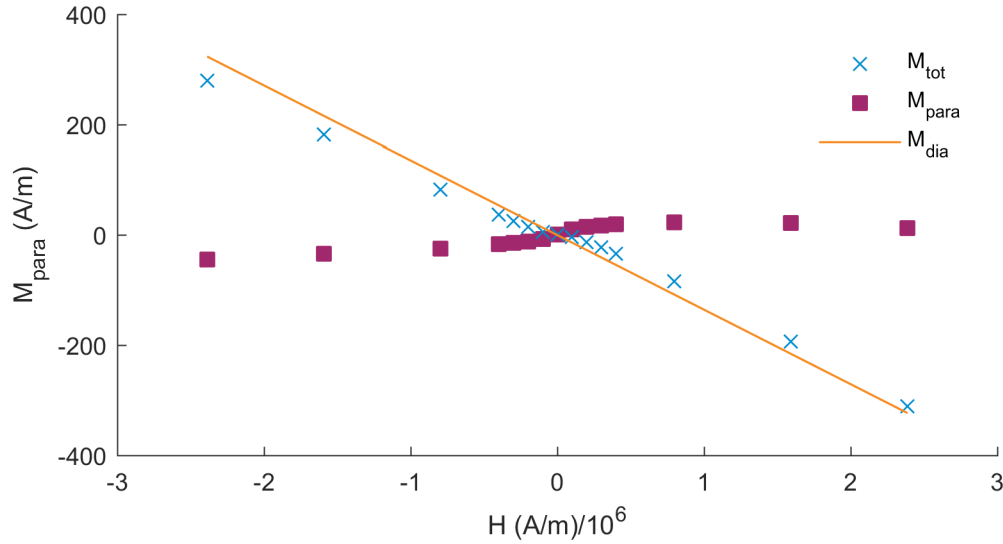
Figure 6.19: Calculated diamagnetic (M_{dia}) and paramagnetic (M_{para}) contribution to the measured total sample magnetisation (M_{tot}) of an aggregate of HOPG microparticles at 2 K.

which states that the slope is inversely proportional to the temperature T. It follows that, at 295 K the slope is reduced by a factor of 2/295 compared to the one at 2 K. By applying Curie's law on the paramagnetic data in Figure 6.19, we can expect the paramagnetic contribution to be negligible at 295 K. Therefore, while there is some contribution from the vacancies and edge defects, we can rule out sonication-induced defects inside the HOPG microparticles as a source for a strong reduction of the diamagnetism of HOPG microparticles fabricated by means of sonication. Another contributing source can be ferromagnetic impurities such as iron oxide in the bulk HOPG sample as reported by Nair *et al.* [95]. Following our measurements, however, this contribution is possibly negligible in our experiment as well. Note, that measurements with a SQUID can only clarify the general presence of defects and impurities in the sample. The magnetic properties of individual particles, on the other hand, cannot be measured since magnetisation is too weak to measure with a SQUID. To date, however, a magnetometer technique for the analysis of individual microparticles is not known.

6.5.4 Magnetophoretic transport of polystyrene beads

As mentioned in the beginning, we also conduct the magnetophoresis experiments with 5 μm-diameter polystyrene (PS) beads (Kisker Biotech, Part. No. PPS-5.0) in a 0.6 M MnCl$_2$ aqueous solution. To prevent the beads from sticking to the capillary walls, we add 2 μl of the non-ionic surfactant TritonX-100 (Sigma Aldrich, part no. X100-500ML) to 1 ml of the solution. PS beads are diamagnetic with a magnetic susceptibility of $\chi_{\mathrm{PS}} = -8.21 \times 10^{-6}$ while the 0.6 M MnCl$_2$ solution is paramagnetic with a magnetic susceptibility of $\chi_{\mathrm{MnCl_2}} = 1.036 \times 10^{-4}$ [102]. As a result, we get $\chi_{\mathrm{PS}} - \chi_{\mathrm{MnCl_2}} = -1.11 \times 10^{-4}$ and thus, PS beads in

the MnCl$_2$ solution move towards the magnetic field minimum (see Equation (6.12)). We can formulate the velocity similarly to Equation (6.12) as:

$$\mathbf{v}_{\text{PS,theo}} = \frac{V_{\text{PS}}}{\mu_0 \gamma_{\text{PS}}} \left(\chi_{\text{PS}} - \chi_{\text{MnCl}_2} \right) B_0 \nabla B_0, \qquad (6.16)$$

where V_{PS} is the volume of the PS bead and $\gamma_{\text{PS}} = 6\eta\pi R$ is the viscous drag coefficient for a sphere with radius R and smooth surface. For our calculation, we assume the viscosity of the solution to be equal to that of water.

We analyse the magnetophoretic transport of a PS bead from a total of 10 videos where in half of them, the bead moves in the negative X direction whereas in the other half it moves in the positive X direction. Each video is about $5 - 7\,$s long and contains the particle motion over a distance of $170 - 220\,\mu$m.

The measurements of the PS bead motion are similar to those in Section 6.5.1. Figure 6.20 shows a time sequence of the magnetophoretic transport of a PS bead, where the motion is directed towards the positive X direction.
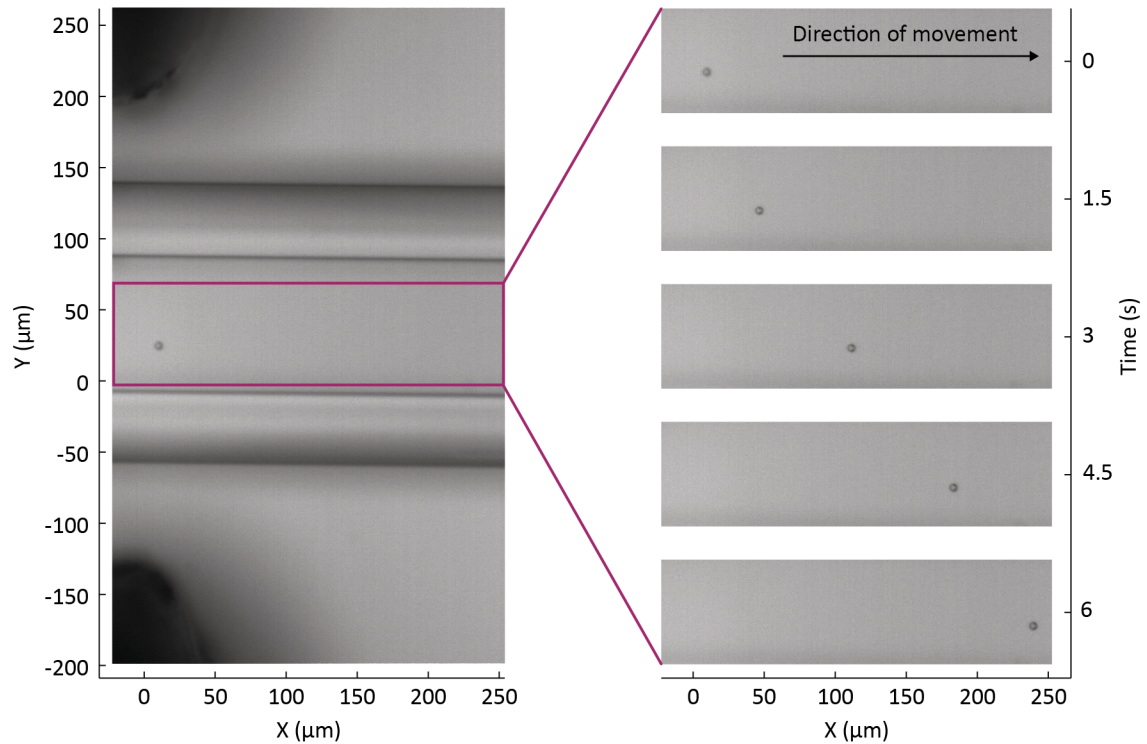
Figure 6.20: Magnetophoresis of a 5 μm-diameter polystyrene bead in a 0.6 M MnCl$_2$ aqueous solution. Left hand side: Image of the particle in the capillary. Right hand side: Image sequence of the particle position as a function of time.
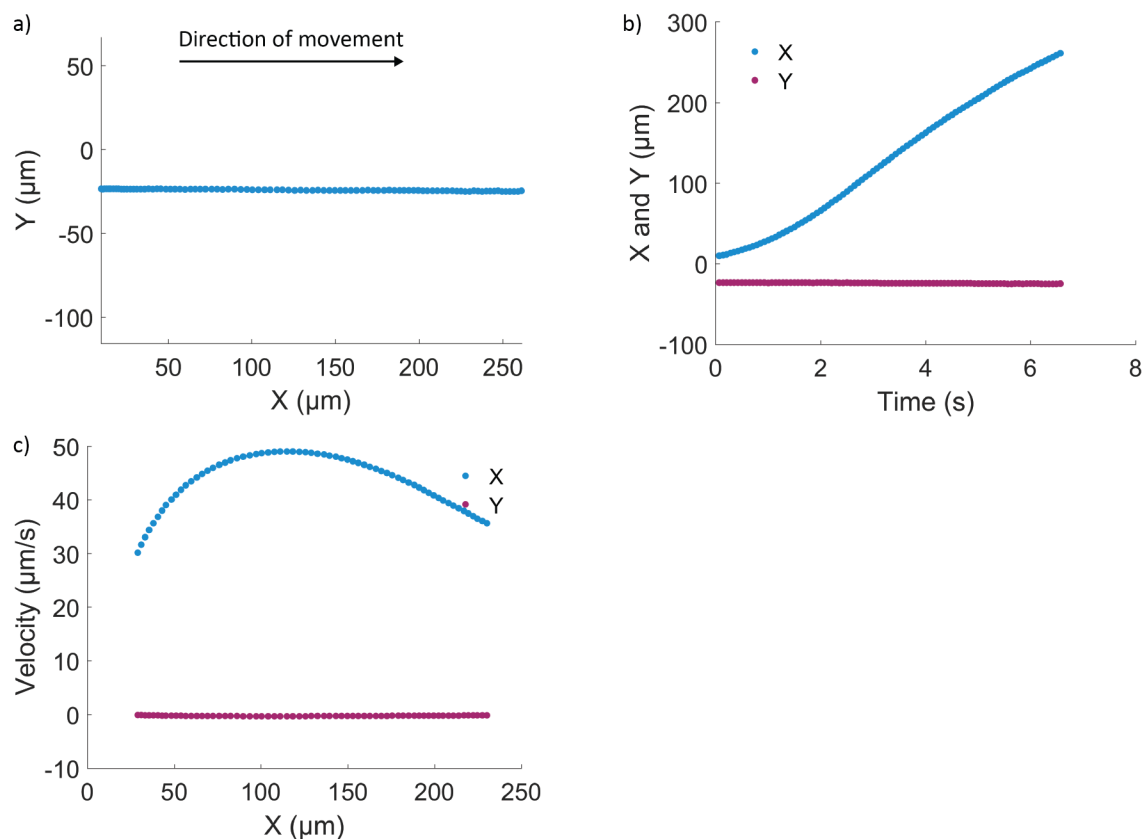
Figure 6.21: Extracted position and velocity for the polystyrene bead in Figure 6.20. a) Trajectory on the X-Y plane. b) Position vs. time. c) Velocity components vs. position along the X direction. The velocity is calculated by fitting the data in b) to a polynomial function and then taking the derivative.

Figure 6.21a shows the trajectory of the PS bead in Figure 6.20 on the X-Y plane which demonstrates the magnetophoretic transport of a single particle along a straight line over a transport length of 230 µm. Figure 6.21b shows a plot of the particle position (in X and Y) as a function of time. The corresponding calculated velocities are presented in Figure 6.21c where the particle velocities are between 30 µm/s and 50 µm/s. These values are about an order of magnitude larger than measured for HOPG and are due to the increased bead volume and the susceptibility difference $\chi_3 - \chi_1$ (see Equation (6.12)). To reduce the particle velocities, the concentration of $MnCl_2$ can be lowered as this reduces the magnetic susceptibility of the solution.

Figure 6.22a shows a plot of the velocity ratios as a function of position along the X direction for all 10 data sets. The low spread of the velocity ratio curves shows the reproducibility of our acquired data. This is due to the fact that the beads have regular shapes as opposed to sonicated HOPG microparticles which have irregular shapes. Furthermore, the similarity of the curves in the positive and negative X directions suggests that the forces on the bead in both directions are identical. Figure 6.22b shows the calculated average velocity ratio and standard deviation for each velocity ratio curve in Figure 6.22a. We can see that the average

velocity ratios are consistently around 0.18 ± 0.01. The distribution of the velocity ratios from all the data in Figure 6.22a is presented in Figure 6.22c. From the histogram, we can see that the velocity ratios for PS beads in our experiment are in the range between 0.17 and 0.19. It follows that the measured magnetophoretic velocity is about five times less than predicted by our theory. This reduction is possibly due to interactions between the particle and the capillary walls which can lead to surface friction and sticking effects. For example, the viscous drag force can increase by up to a factor of three for movements parallel and at close distance to a planar wall as discussed in [87]. A summary of the average velocity ratio with the corresponding standard deviation, the number of analysed particles per sample ($N_{particles}$), the total number of data points (N_{points}) and the number of particle tracks (N_{tracks}) for each sample is presented in Table 6.3.

Sample	$\langle v_{exp,x}/v_{theo,x} \rangle$	$N_{particles}$	N_{points}	N_{tracks}
PS Beads	0.18 ± 0.01	1	904	10

Table 6.3: Calculated average velocity ratio and standard deviation for the magnetophoretic transport of 5 μm-diameter PS beads in a 0.6 M $MnCl_2$ aqueous solution. $N_{particles}$: Number of particles measured in each sample. N_{points}: Number of data points in each sample. N_{tracks}: Number of particle tracks acquired for each sample. The velocity ratio is defined as the measured X component of the particle velocity, $v_{exp,X}$, to the corresponding theoretical velocity, $v_{theo,X}$.
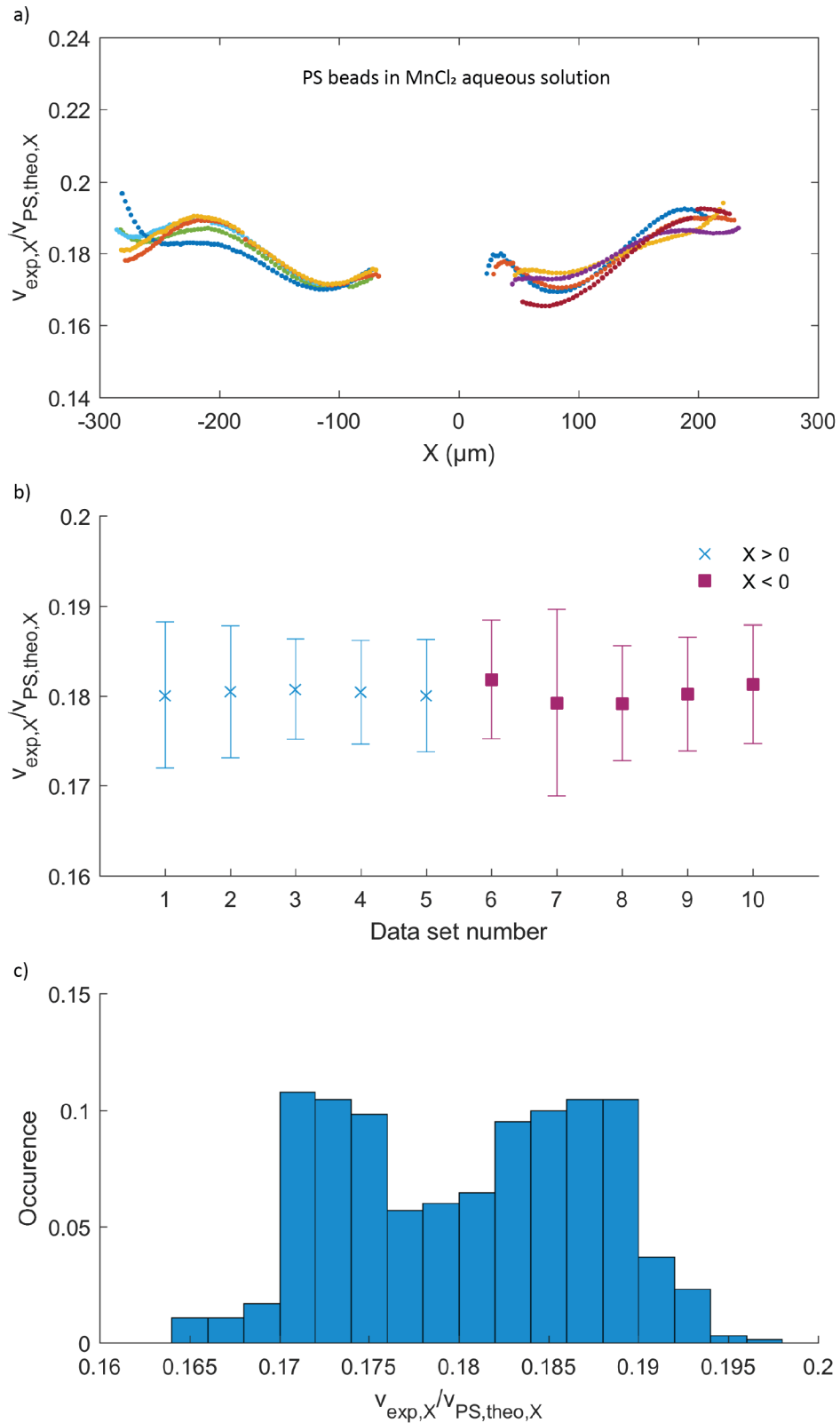
Figure 6.22: Calculated ratio of the measured experimental velocity along the X direction ($v_{exp,X}$) to the corresponding theoretical velocity ($v_{PS,theo,X}$). a) Velocity ratio as a function of position along the X direction for all 10 data sets. b) Average ratio and standard deviation for each velocity ratio curve in a). c) Histogram of all velocity ratio values in a).

6.6 Conclusion and outlook

In this chapter, we have demonstrated the magnetophoretic transport of HOPG microparticles in a diamagnetic solution which, to our knowledge, has never been done before. We show that directional transport of HOPG microparticles in solution is possible by means of an arrangement of two NdFeB magnets and two steel wedges. The magnetic field strength and the field gradient are sufficiently large to transport HOPG microparticles over distances of hundreds of micrometres with velocities between $\sim 1\,\mu m/s$ and $10\,\mu m/s$. We have also showed that PS beads can be transported in a paramagnetic solution with velocities between $\sim 30\,\mu m/s$ and $50\,\mu m/s$. The results demonstrate that our setup is capable of transporting diamagnetic particles in solution.

Our setup proves to be an easy to use and quick tool to analyse the magnetophoretic transport of HOPG microparticles from different samples. Based on the analysis of the magnetophoretic velocities, we found indications that the lipid-coating on the particle can slow down the particle transport in solution. Furthermore, we observed that an increase of the sonication duration in the particle-fabrication process could produce microparticles that move slower. The analysis of the HOPG microparticles with a Raman spectrometer and SQUID showed that the sonication produces particles with rough surfaces and defects such as vacancies. However, it turns out that the contribution of the defects to the magnetophoretic velocity is likely to be negligible.

An additional contribution to the lower magnetophoretic transport rate could be particle interactions with the inner capillary wall. To avoid this interaction, it would be necessary to guide the particle along a line that is centred inside the capillary and away from its walls. However, to our knowledge such a technique has not been developed yet.

To improve the magnetophoretic transport rate of HOPG microparticles, the sonication process in the particle production protocol should be omitted. For example, Chen *et al.* used photolithography to fabricate well defined pillars on a piece of HOPG [103]. These pillars can be detached from the surface by pouring *Polydimethylsiloxane* (PDMS) on it and removing the compound once dried. This is possible because the ordered planar structure of HOPG makes it relatively easy to mechanically remove thin sheets from the surface. To remove the pillars from PDMS, one can use chloroform which causes PDMS to swell [104] and pushes out the pillars from the PDMS layer. To further develop this idea, we started a collaboration with the David Bullett Nanofabrication Facility at the University of Bath. Figure 6.23, shows an electron microscope image of round HOPG pillars that were directly etched onto a smooth surface of HOPG using photolithography. Each pillar has a diameter of 5 μm and is 1 μm high.
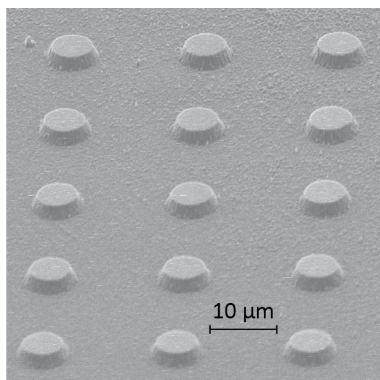
Figure 6.23: Electron microscope image of HOPG pillars on a sheet of HOPG. The pillars are fabricated using photolithography in collaboration with David Bullett Nanofabrication Facility at the University of Bath.

The magnetophoresis of lipid-coated HOPG microparticles in a saline aqueous solution is relevant for biological applications. In the future, we could functionalise the lipids in order to attach lipid-coated HOPG microparticles onto biomolecules on the cell membrane. Since HOPG is diamagnetic, it is repelled by the magnetic field as opposed to paramagnets which are attracted towards the field. Therefore, the use of lipid-coated HOPG microparticles opens up new opportunities to navigate cells through a medium. For example, in microfluidic experiments cells labelled with HOPG can be focussed in the microchannel by using the same magnetic arrangement as presented in this chapter. Such a manipulation technique would be impossible, if cells are labelled with commonly used superparamagnetic and ferromagnetic particles as they would move towards the magnetic field maximum.

Chapter 7

Magnetic trapping of HOPG microparticles

Particle trapping is a manipulation method in which the particle is spatially confined in its environment (e.g. solution or gas). For sufficiently small displacements from the trap centre, the particle experiences a restoring force towards the trap centre. If the force magnitude as a function of distance from the trap centre is known, the particle position can be tracked (e.g. with a camera) and associated to a force that acts on the particle at any moment. Based on this principle, it is possible to use an individual trapped particle as a probe to apply and measure forces on microscopic systems.

Force spectroscopy techniques are of particular interest for the study of biological interactions where forces are on the piconewton-scale. To date, there are three common tools that are used for force spectroscopy on biological systems: optical tweezers, magnetic tweezers and atomic force microscopy. Amongst them, only optical tweezers can trap particles in three dimensions and hence it is the only tool that can apply and sense forces in all directions simultaneously. Optical tweezers rely on the use of focussed laser beams which could induce sample heating and thermal exchange with the environment which raises concerns over the functionality of the studied living system [105, 106]. Therefore, new techniques for particle trapping in living systems are desirable.

Static magnetic fields are a possible alternative as they do not influence the functionality of cells [107] and sample heating is non-existent. Such fields are commonly used in combination with superparamagnetic particles to apply pulling forces and torques on biological structures such as DNA [108]. However, since superparamagnetic particles are attracted towards the field maximum, they cannot be trapped as Earnshaw's theorem states that it is fundamentally impossible to generate a three-dimensional local maximum with static magnetic fields. On the

other hand, three-dimensional magnetic minima can be generated with static magnetic fields. As a result, only diamagnetic particles can be trapped as they are attracted towards the field minimum (see Chapter 6).

So far, diamagnetic trapping for force spectroscopy in living systems has remained widely unexplored. There have been two studies that demonstrate magnetic trapping of diamagnetic particles in solution. Winkleman *et al.* successfully trapped polystyrene beads in a paramagnetic solution with a magnetic field generated by two identical and opposing cone-shaped magnets [109]. However, it is difficult to assess the potential of their setup for force spectroscopy experiments as they did not quantify the strength of their trap. Timonen *et al.* designed a magnetic micropen consisting of a non-magnetic core and a ferromagnetic shell surrounded by an electromagnet [110]. By turning on the latter, a magnetic field in the shell is induced that can pick up objects below the non-magnetic core and drop them in other locations. With respect to three-dimensional force probing, however, their setup is not suitable because there is no restoring force on the particle in the direction of gravitation. Despite the successful demonstration of particle trapping, both studies are not applicable to living systems since paramagnetic solutions were used which are in general toxic for living organisms.

The purpose of this chapter is to close this gap by investigating magnetic trapping with static magnetic fields in diamagnetic solutions. Since the magnetic interaction of diamagnetic materials is in general weak, it is necessary to use diamagnetic particles with a large negative volume magnetic susceptibility for the magnetic trapping. In this context, microparticles made specifically from HOPG are ideal candidates as the material has the largest negative magnetic susceptibility ($\sim -10^{-4}$) known to date.

We separate this chapter into two parts. The first part focusses on the magnetic trapping of HOPG microparticles in a diamagnetic solution using permanent magnets. We start with the fundamentals which cover the conditions for magnetic trapping and the basics needed to evaluate the magnetic trap. Then, we describe our experimental setup and our procedure to measure the data. In the results, we present our findings on magnetic trapping of HOPG microparticles in a diamagnetic solution and discuss the potential for force sensing with static magnetic fields. In the second part, we study the potential of magnetic trapping with current-carrying microfabricated wires. For this purpose, we simulate the magnetic field of two wire setups that could potentially be used for magnetic trapping in two and three dimensions.

7.1 Principles for magnetic trapping

7.1.1 Condition for magnetic trapping with static magnetic fields

Let us consider a HOPG microparticle of volume V_1 in solution located at $\mathbf{r}$ and subject to an external non-homogeneous magnetic field, $\mathbf{B}_0(\mathbf{r})$. The magnetic force, $\mathbf{F}_{\text{mag}}(\mathbf{r})$, on the particle has already been derived in Equation (6.4) and is given as:

$$
\begin{aligned}
\mathbf{F}_{\text{mag}}(\mathbf{r}) &= \frac{V_1}{\mu_0}\left[(\chi_\perp - \chi_\parallel)\cos^2\theta + \chi_\parallel - \chi_1\right] B_0(\mathbf{r})\nabla B_0(\mathbf{r}) \\
&= \frac{V_1}{\mu_0}\Delta\chi(\theta) B_0(\mathbf{r})\nabla B_0(\mathbf{r}).
\end{aligned}
\tag{7.1}
$$

where $B_0(\mathbf{r}) = |\mathbf{B}_0(\mathbf{r})|$, $\Delta\chi(\theta) = \left[(\chi_\parallel - \chi_1) + (\chi_\perp - \chi_\parallel)\cos^2\theta\right]$, $\chi_\parallel$ and $\chi_\perp$ are the in-plane and out-of-plane magnetic susceptibilities of HOPG, χ_1 is the magnetic susceptibility of the solution and θ is the angle between the graphene planes in the particle and the magnetic field direction.

We assume that the magnetic field strength and field gradient are sufficiently large to overcome the thermal fluctuations. As discussed in Section 6.2.1, particles migrate towards the magnetic field minimum only if the magnetic susceptibility of the particle is lower than that of the solution. With respect to Equation (7.1), this means that the factor $\Delta\chi(\theta)$ must fulfil the condition:

$$
\Delta\chi(\theta) < 0,
\tag{7.2}
$$

for all values of θ. For HOPG microparticles in a 20 mM NaCl aqueous solution or in an acetone and water mixture this condition is fulfilled as discussed in Section 6.2.1 and hence, HOPG microparticles can be magnetically trapped in any orientation to the magnetic field.

7.1.2 From trapping to force measurements

We describe the particle motion in the laboratory frame of reference (with the axes X, Y and Z) as defined in Figure 5.1. For simplicity, we limit our theoretical description to particle motions along the X direction.

For sufficiently small displacements from the magnetic field minimum at X_{eq}, the potential associated with a magnetic trap can be described in the harmonic approximation:

$$
U_{\text{mag,X}}(X) = \frac{1}{2}\kappa_{\text{X}}(X - X_{\text{eq}})^2,
\tag{7.3}
$$

where X is the particle position and κ_{X} is the trap stiffness in the X direction. The latter quantifies the trap's capability to confine the particle in the trap: a large κ_{X} value implies a

steep magnetic potential and thus, a strong magnetic trap. From Equation (7.3), it follows that the force on the particle in the trap is given by:

$$F_{mag,X}(X) = -\frac{\partial U_{mag,X}(X)}{\partial X} = -\kappa_X (X - X_{eq}),$$
(7.4)

and the trap stiffness can be formulated as:

$$\kappa_X = -\frac{\partial F_{mag,X}}{\partial X} = \frac{\partial^2 U_{mag,X}}{\partial X^2}.$$
(7.5)

For a system at thermodynamic equilibrium, we can derive an analytical expression for κ_X by applying the equipartition theorem, which states that the average energy per degree of freedom is equal to $\frac{1}{2}k_B T$. Then, the average potential can be expressed as:

$$\langle U_{mag,X}(X) \rangle = \frac{1}{2}\kappa_X \langle (X - X_{eq})^2 \rangle = \frac{1}{2}k_B T,$$
(7.6)

and thus, the trap stiffness is:

$$\kappa_X = \frac{k_B T}{\langle (X - X_{eq})^2 \rangle} = \frac{k_B T}{\sigma_X^2},$$
(7.7)

where $\sigma_X^2 = \langle (X - X_{eq})^2 \rangle$ is the position variance in the X direction. Consequently, for harmonic potentials, we can obtain the trap stiffness by simply tracking the particle position in the trap over a sufficiently long period of time and calculating the position variance from the data.

7.2   Experimental setup

We study the magnetic trapping for HOPG microparticles in a 40 % acetone and 60 % water mixture that we introduced in Chapter 6 as 'AceWater'. We focus on the generation of a strong static magnetic field with large field gradient that is capable of trapping HOPG microparticles with a typical size of 6 μm × 6 μm × 2 μm. Static magnetic fields can be generated with permanent magnets or current-carrying wires. For this experiment, we use cone-shaped NdFeB magnets (grade N52, first4magnets) that were manufactured according to our design. Each magnet has a base diameter of 4 mm and a height of 12 mm.

Figure 7.1a shows a photograph of our experimental setup. The magnetic field is generated with two opposing cone-shaped NdFeB magnets that have the same magnetic poles at the tip and base. To increase the magnetic field gradient, both magnets are supplemented by two cone-shaped steel pieces that sit perpendicular to them. To reduce the stray magnetic fields

which could weaken the magnetic trap, we add steel blocks to each of the steel cones to guide the field lines to the base of one of the magnets. We designed all steel pieces and have them machined in the departmental mechanical workshop. The motion of the particle is imaged with the upright microscope (total magnification: $10 \times$) described in Chapter 4.
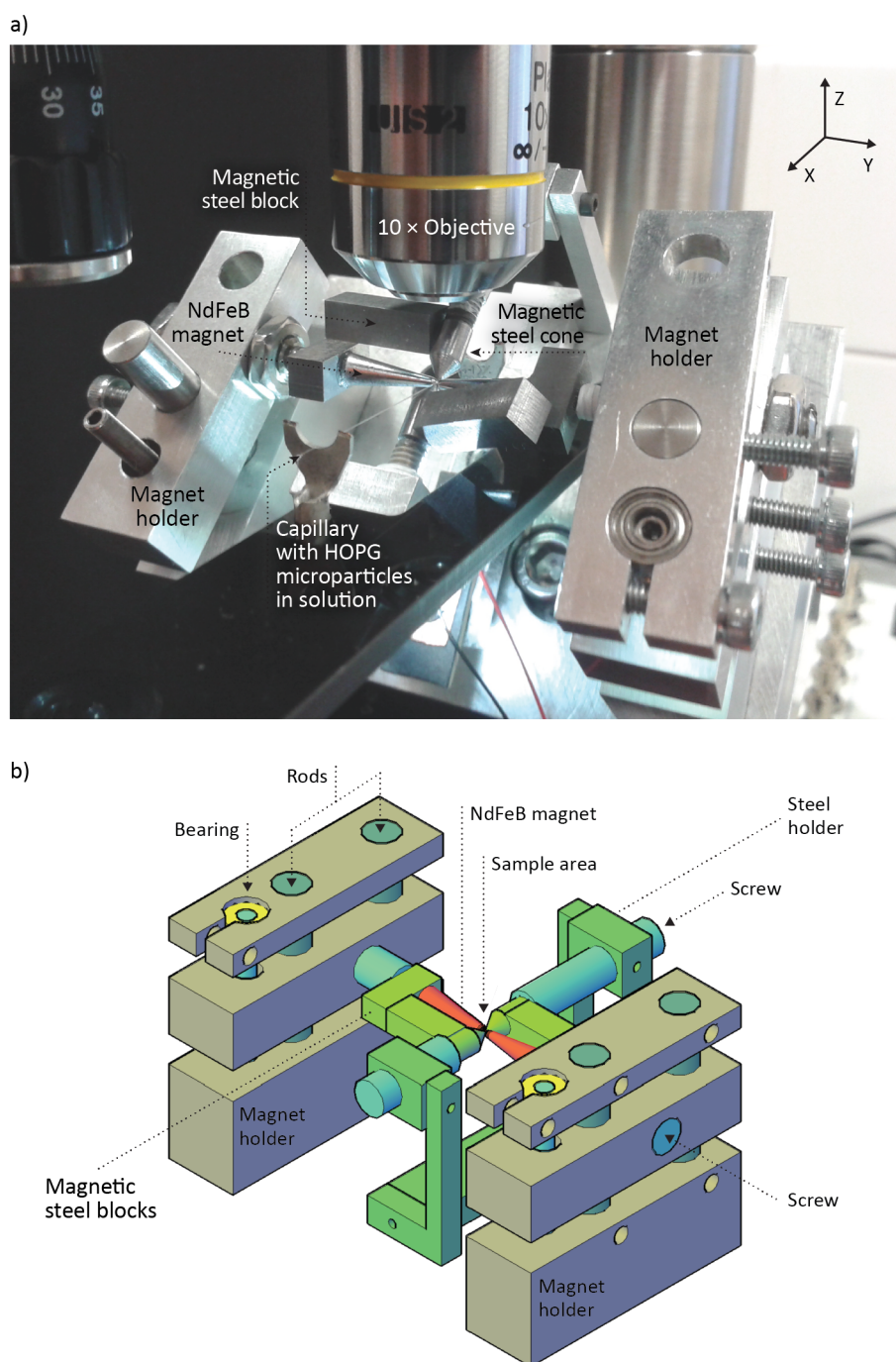
Figure 7.1: Experimental setup for magnetic trapping. The magnetic field is generated with two opposing cone-shaped NdFeB magnets and two steel cones that sit perpendicular to the magnets. a) Photograph of the experimental setup. To expose the HOPG microparticles to the magnetic field, a capillary with the HOPG sample is introduced into the sample region. b) CAD drawing of the custom-made holder designed to adjust and fix the positions of the magnets and the steel cones.

The magnets and the steel components are subject to magnetic forces and either attract or repel each other when placed in close proximity. Because of this, we use superglue and mount them in a custom-made holder made of aluminium. A CAD drawing of our construction is shown in Figure 7.1b. The schematic highlights the rods, screws and bearings that are used to precisely adjust the positions of the magnets and steel cones in our setup.

To expose the particle to the magnetic field, we introduce the particle solution into a glass capillary with a square-shaped cross section. We use glass capillaries of two different sizes: one that have a channel width of 50 µm and a wall thickness of 25 µm (CM Scientific, part no.: 8505); and one that have a channel width and wall thickness of 100 µm and 50 µm, respectively (CM Scientific, part no.: 8510). Once the capillary is filled with the fluid, its ends are sealed with quick drying nail varnish to avoid potential fluid motion in the experiment. In order to place the capillary between the magnets, we tilt the entire magnetic setup in Figure 7.1b by 45° as shown in Figure 7.1a. This creates a small gap to insert the capillary and hold it in a horizontal position with a customized holder that has been cut out from a sheet of acrylic glass by our mechanical workshop.

7.2.1   Generating a magnetic trap with two cone-shaped permanent magnets

Our magnets are chrome-plated which protects them from corrosion but also sets a minimum distance between the particle and the surface of the magnet. To assess the thickness of the plating, we take off the plating from one magnet and measure its thickness with a calliper. It follows that the plating is 100 µm thick which we include in all subsequent calculations.

In our experiments, we set the gap size between the magnet tips without the chrome-plating, d_{cone}, in the range $350 - 600 \, \mu\mathrm{m}$. Since the small gap size makes it impossible to measure the magnetic field strength with our Gaussmeter, we use simulations to calculate the magnetic field as we did before in Chapter 6. In the following, we focus on magnetic traps generated with only cone-shaped permanent magnets. Such setups are axissymmetric so that it is not necessary to create a three-dimensional model with Radia for the simulations. Instead, we model the setup in two dimensions and simulate the magnetic field with the software Finite Element Method Magnetics (FEMM) which is optimized for simulating axissymmetric models. To verify the simulations with FEMM, we measure the magnetic field of a single cone-shaped NdFeB magnet with a Gaussmeter at different distances d_{single} from the tip and parallel to the cone's axis of symmetry as shown in Figure 7.2a and compare the data with the results of the simulation. Figure 7.2b shows a superposition of the measured field and the corresponding simulation evidencing good agreement. The superposition accounts for the thickness of the chrome-plating ($100 \, \mu\mathrm{m}$) and the Gaussmeter probe ($\approx 0.6 \, \mathrm{mm}$) which results in a shift of the

experimental data in the x direction.
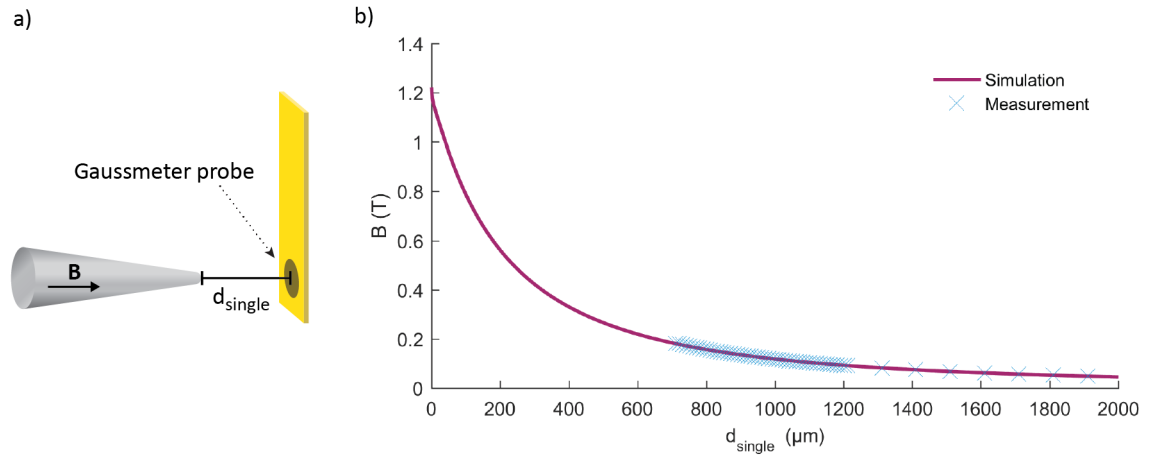
Figure 7.2: a) Schematic of the setup to measure the magnetic field at the tip of a cone-shaped NdFeB magnet with a Gaussmeter. b) Superposition of simulated and measured magnetic field of a cone-shaped NdFeB magnet as a function of distance from the magnet tip and parallel to the cone's axis of symmetry. The measured data is shifted to account for the thickness of the chrome-plating (100 μm) and the Gaussmeter probe (≈ 0.6 mm).

Figure 7.3 shows a contour map of the simulated magnetic field of two cone-shaped magnets separated by $d_{cone} = 350$ μm on the X-Y plane. We can see that the shape of the contours around the magnetic field minimum (blue enclosed contour) are elliptical and the corresponding major axes are aligned in the X direction. The magnetic field strength is roughly in the range $0 - 0.75$ T and the field gradient is of order 10^{-3} T/μm. The field gradient in the Y direction is stronger than in the X direction which implies a stronger trapping force in the Y direction than in the X and Z directions (see Equation (7.1)).

Because of the gravitational force and buoyancy, the trap centre is not located at the magnetic field minimum but at X_0, Y_0 and Z_0 where the magnetic force balances the other two forces. To determine the trap position in the Z direction, we use the magnetic field simulation and calculate the position where the Z component of the magnetic force, $F_{mag,Z}$ (from Equation (7.1)), balances the gravitational force, $F_{grav} = -V_2\rho_{HOPG}g$, and buoyancy, $F_{buoy} = V_2\rho_{Mix}g$:

$$F_{mag,Z}(\mathbf{r_0}) = F_{grav} + F_{buoy}$$
$$\frac{V_2}{\mu_0}\Delta\chi(\theta) B_0(\mathbf{r_0}) \left.\frac{dB_0}{dZ}\right|_{\mathbf{r=r_0}} = V_2(-\rho_{HOPG} + \rho_{Mix})g, \tag{7.8}$$

where $\mathbf{r_0}$ is the trap centre position, g is the gravitational acceleration, and $\rho_{HOPG} = 2.26$ g/cm^3 and $\rho_{Mix} = 0.94$ g/cm^3 (from ref. [82]) are the densities of HOPG and AceWater, respectively. For a HOPG microparticle with a volume of 72 μm^3 (size 6 μm $\times$ 6 μm $\times$ 2 μm), the total force on the particle due to buoyancy and gravitational force is 0.9 pN in the direction of
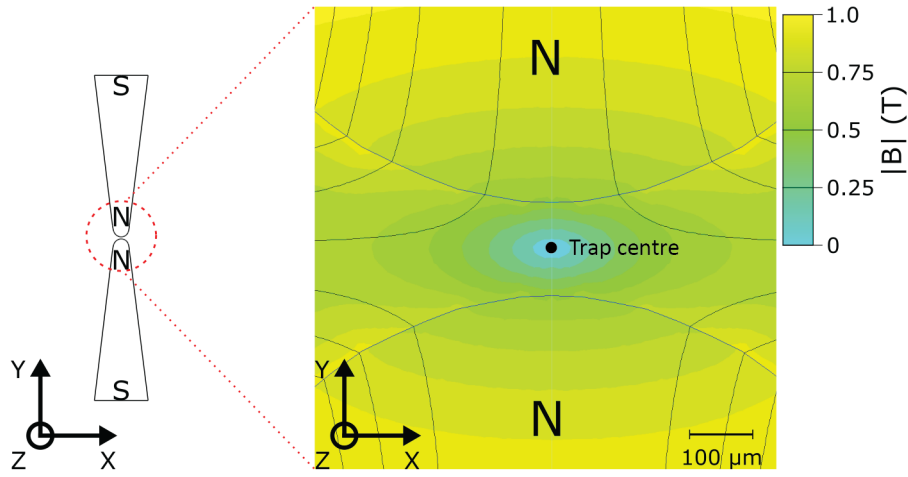
Figure 7.3: Simulated magnetic field of two opposing cone-shaped magnets separated by $d_{cone} = 350\mu m$. Left hand side: Model used in the simulation. Right hand side: Simulated magnetic field in FEMM.

gravity. Because of the anisotropy of HOPG, the magnetic force on the particle is the lowest when the graphene planes in the HOPG microparticle are aligned parallel to the magnetic field direction ($\theta = 90°$). In this particle orientation, the trap centre is shifted by $60\,\mu m$ from the magnetic field minimum in the direction of gravity for the setup in Figure 7.3. Figure 7.4 shows a plot of the corresponding forces on a HOPG microparticle ($V_2 = 72\,\mu m^3$) in AceWater for displacements from the trap centre in the X, Y and Z directions. We can see a linear increase of the force with increasing distance from the trap centre which implies that the magnetic potential of the particle around the trap centre is harmonic. This allows us to calculate the trap stiffness by applying Equation (7.5) which gives us $\kappa_X = 0.015\,pN/\mu m$, $\kappa_Y = 0.067\,pN/\mu m$ and $\kappa_Z = 0.012\,pN/\mu m$ in the X, Y and Z directions, respectively.
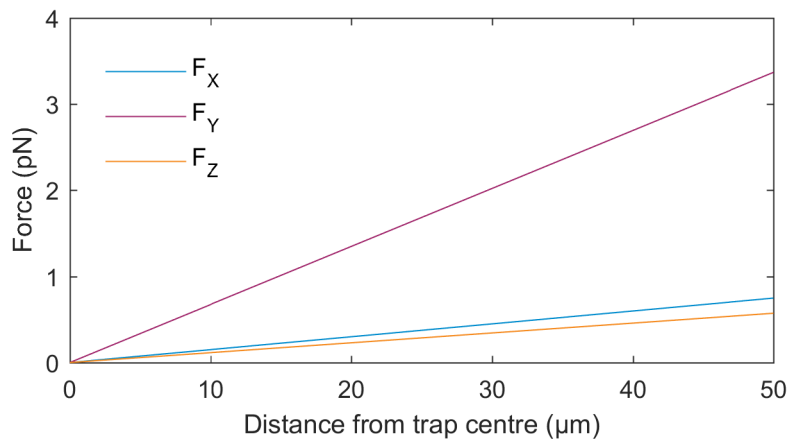
Figure 7.4: Magnetic force on a HOPG microparticle in the X, Y and Z directions for displacements from the trap centre in the magnetic field in Figure 7.3. The force is calculated for a HOPG microparticle of size $6\,\mu m \times 6\,\mu m \times 2\,\mu m$ in AceWater.

7.3 Data acquisition

For each trapped particle, we take multiple videos at 400 fps in a manually defined image region. To extract the particle trajectory from the videos, we use two different tools depending on the particle shape. If the particle shape is spherical, e.g. for polystyrene beads, we use the image processing software ImageJ with the MosaicSuite plug-in which incorporates the particle tracking algorithm described in ref. [111]. For irregularly shaped particles, which is the typical case for HOPG microparticles, we use our image analysis code described in Section 4.4.

7.4 Results and discussion

We divide our analysis into two parts. In the first part, we evaluate the trap stiffness in the X and Y directions for different magnetic trap setups by means of polystyrene beads in a paramagnetic solution. In the second part, we show our results of the magnetic trapping of HOPG microparticles in AceWater. All experiments are conducted at room temperature (295 K). During our measurements we keep the particle in the centre of the capillary in order to avoid particle interactions with the inner wall of the capillary (see Chapter 6).

7.4.1 Trap stiffness of magnetic trap setups with permanent magnets

We analyse the three magnetic setups that are illustrated in Figure 7.5. Setup A consists of two opposing cone-shaped magnets with equal magnetic poles facing each other. The distance between the cone tips without the chrome-plating is given by d_{cone}. In setup B, we add two steel cones to setup A where the tips are separated by d_{steel}. In setup C, we use steel blocks as backing elements to guide the magnetic field lines to the base of the cone-shaped magnets (see also Figure 7.1). To determine the trap stiffness, we use 5 μm-diameter polystyrene (PS) beads (Kisker Biotech, PPS-5.0) in a 0.6 M $MnCl_2$ aqueous paramagnetic solution because of their regular shape and well-defined volume. The magnetic force on a PS bead in solution located at $\mathbf{r}$ can be formulated similar to Equation (7.1):

$$\mathbf{F}_{\mathrm{PS}} = \frac{V_{\mathrm{PS}}}{\mu_0}\left(\chi_3 - \chi_1\right) B_0\left(\mathbf{r}\right)\nabla B_0\left(\mathbf{r}\right), \qquad (7.9)$$

where V_{PS} is the volume of the PS bead, $\chi_3 = -0.8 \times 10^{-5}$ is the magnetic susceptibility of polystyrene and $\chi_1 = 10.4 \times 10^{-5}$ is the magnetic susceptibility of the solution. The difference of the magnetic susceptibilities is $\chi_3 - \chi_1 = -11.2 \times 10^{-5}$ which fulfils the condition for magnetic trapping in Equation (7.2). To prevent the beads from sticking to the capillary surface, we add 2 μl of the non-ionic surfactant Triton X-100 (Sigma Aldrich, part no. X100-
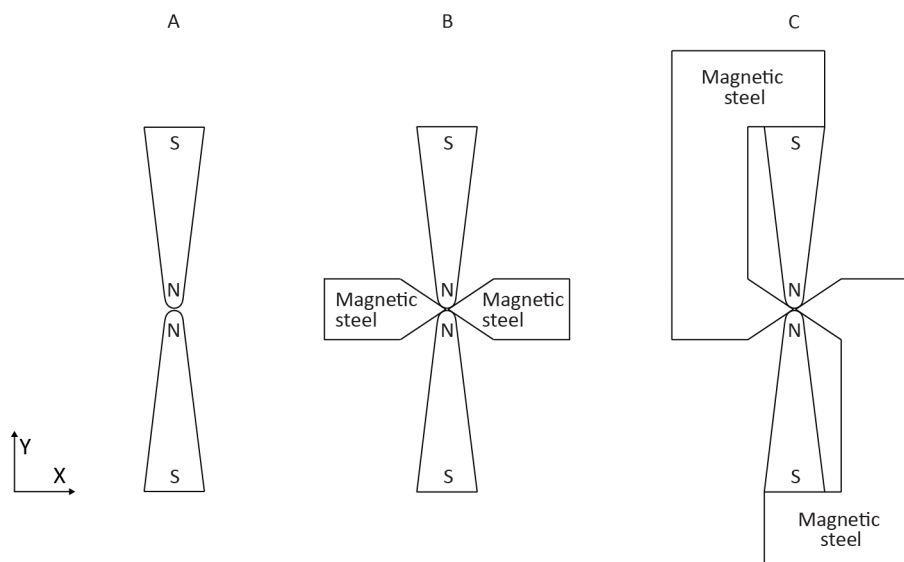
Figure 7.5: Illustration of different setups used for magnetic trapping. Setup A consists of two opposing cone-shaped magnets that have the same magnetic poles at the cone tips. In setup B, two steel cones are added to setup A. In setup C, we use steel blocks to guide the magnetic field lines to the base of the magnet.

500ML) to 1 ml of the particle solution.

Setup A: Magnetic trapping with two opposing cone-shaped magnets

Upon exposure to the magnetic field, particles migrate immediately towards the field minimum between the magnets. By moving the magnets while holding the capillary still, we can move the particles inside the capillary as they follow the location of the magnetic field minimum. Figure 7.6 illustrates the magnetic trapping of 5 μm-diameter PS beads with setup A for two different concentrations of PS beads. Figures 7.6a and b show microscope images of a trapped PS bead in the capillary where the magnets are separated by $d_{cone} = 393$ μm. From Figure 7.6a to b, we displace the two magnets in the negative Y direction which causes the PS bead to follow the displaced location of the trap centre. Figures 7.6c and d show the magnetic trapping of a cluster of PS beads with $d_{cone} = 475$ μm. We can see that the shape of the cluster is elongated which reflects the asymmetric magnetic field contours from our simulations in Figure 7.3. As we move both magnets to the right (from Figure 7.6c to d), the bead cluster follows the trap centre.

Figure 7.7a shows the trajectory on the X-Y plane of a trapped PS bead in setup A with $d_{cone} = 428$ μm. The trap centre is located at $X = 0$ and $Y = 0$. The trajectory consists of over 10^6 data points which are extracted from a five minute-long video of the particle motion. We can clearly see from the trajectory that the particle movement on the Y-axis is more confined than on the X-axis. This is expected since the magnetic forces in the direction
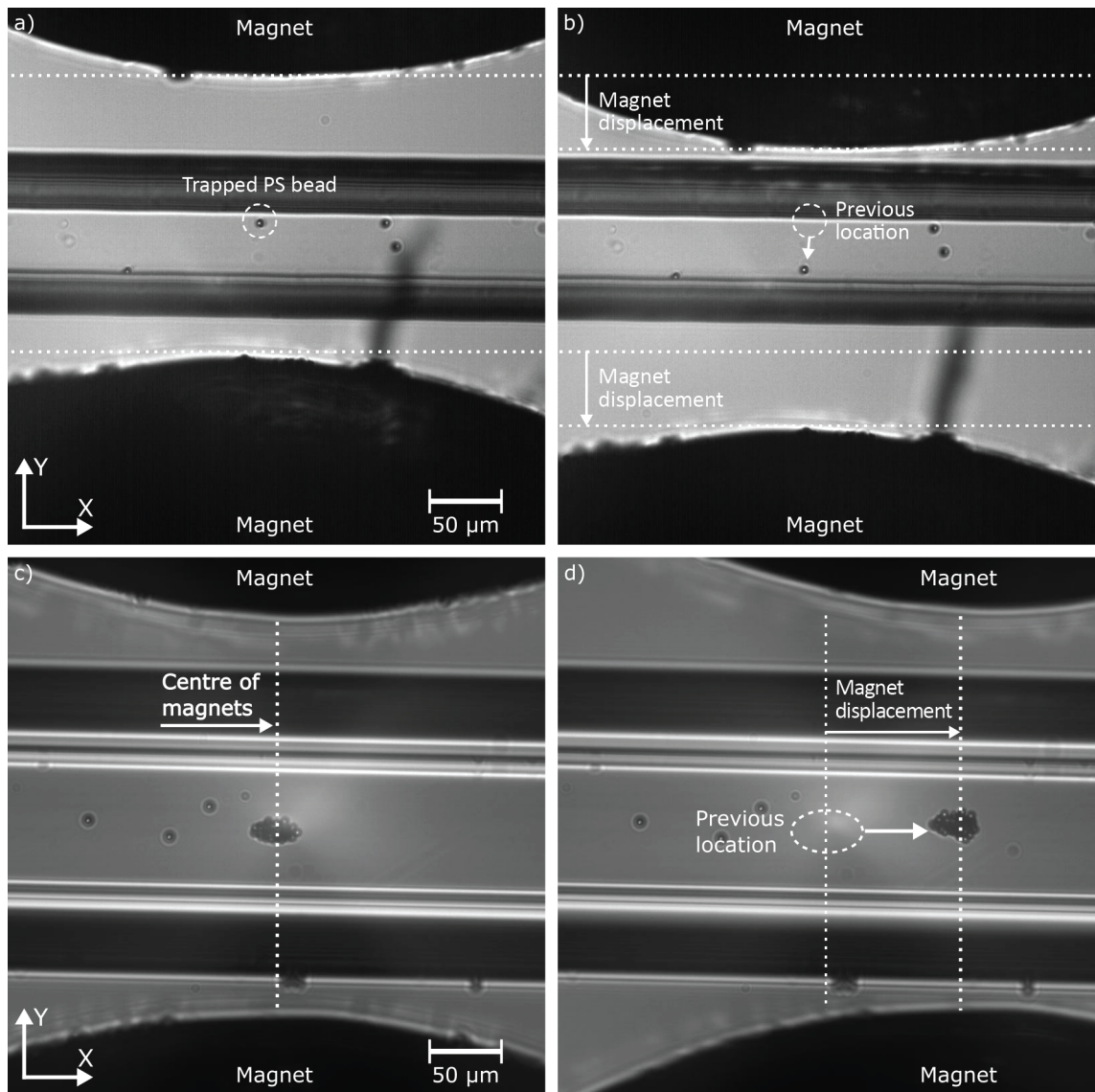
Figure 7.6: Magnetic trapping of $5\,\mu\text{m}$-diameter PS beads in a $0.6\,\text{M}$ $MnCl_2$ aqueous solution with setup A. a) and b) Displacement of a PS bead in the negative Y direction. The distance between the magnet tips, excluding the $100\,\mu\text{m}$-thick chrome-plating, is $d_{cone} = 393\,\mu\text{m}$. c) and d) Displacement of a cluster of PS beads in the X direction. The distance between the magnet tips is $d_{cone} = 475\,\mu\text{m}$.
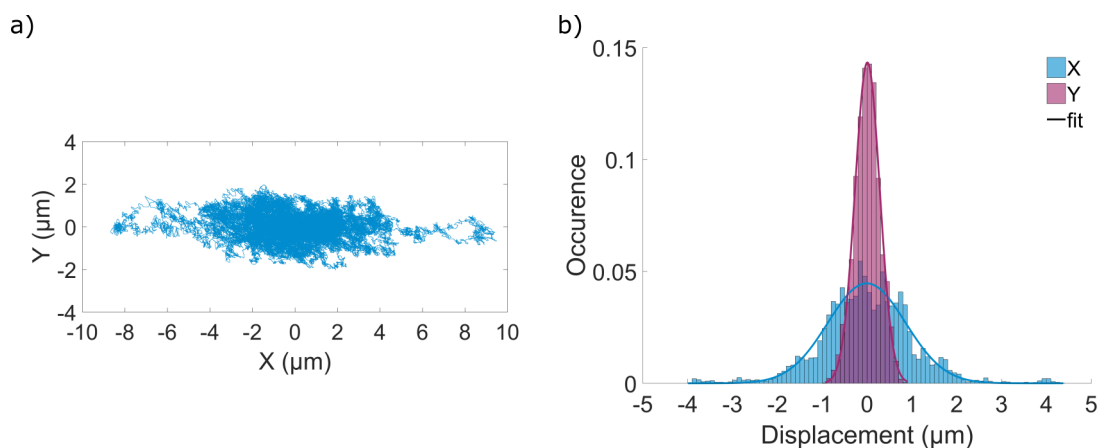
Figure 7.7: Tracked position of a PS bead in a $0.6\,\text{M}$ $MnCl_2$ aqueous solution in setup A with $d_{cone} = 428\,\mu\text{m}$. a) Particle trajectory on the X-Y plane. b) Position distributions on the X- and Y-axes for the data in a).

perpendicular to the magnets (X direction) are weaker (see also Figure 7.3). Figure 7.7b shows the position distributions in Figure 7.7a in the X and Y directions. Both distributions are normally distributed as we can see from a fit of the data to Gaussian functions (solid lines in Figure 7.7b). This confirms that we can extract the trap stiffness in the X and Y directions from the position data using Equation (7.7). For the PS bead in Figure 7.7, we get a trap stiffness of $\kappa_X = 0.0038 \pm 0.0002\,\mathrm{pN/\mu m}$ and $\kappa_Y = 0.05 \pm 0.01\mathrm{pN/\mu m}$ in the X and Y directions, respectively. The uncertainties of the trap stiffness values are calculated from the localisation error of our particle localisation code. This source of error is more pronounced when the displacement length of the particle from the trap centre are comparable to the localisation error. As a result, we can see that the uncertainty of the trap stiffness is larger in the Y direction than in the X direction.

To measure the trap stiffness in the X and Y directions for different d_{cone} values, we take two to seven minute-long videos from at most four individual beads for each value of d_{cone}. For each setup, we also calculate the theoretical trap stiffness using a similar method to the one described in Section 7.2.1. First, we simulate the magnetic field for each setup with FEMM. Then, we use the simulated field to calculate the location of the trap centre on the Z-axis from the balance of forces, given by:

$$F_{\mathrm{PS,Z}}\left(\mathbf{r}_0\right) = F_{\mathrm{grav}} + F_{\mathrm{buoy}}$$
$$\frac{V_{\mathrm{PS}}}{\mu_0}\left(\chi_1 - \chi_3\right) B_0\left(\mathbf{r}_0\right) \left.\frac{\mathrm{d}B_0}{\mathrm{d}Z}\right|_{\mathbf{r}=\mathbf{r}_0} = V_{\mathrm{PS}}\left(-\rho_{\mathrm{PS}} + \rho_{\mathrm{MnCl}}\right)g,$$

(7.10)

where $\rho_{\mathrm{PS}} = 1.04\,\mathrm{g/cm^3}$ is the density of polystyrene and $\rho_{\mathrm{MnCl}} = 1\,\mathrm{g/cm^3}$ is the density of the $0.6\,\mathrm{M}$ $\mathrm{MnCl_2}$ solution which we assume to be equal to the density of water. Finally, we calculate the force on the particle for displacements from the trap centre with Equation (7.9) and fit the data to a linear function to extract the trap stiffness in the X and Y directions (see Equation (7.5)).

Figure 7.8 shows the measured and the theoretical trap stiffness in the X and Y directions as a function of d_{cone}. The measured values present the trap stiffness averaged over all data corresponding to a given value of d_{cone}. The error bars are the corresponding calculated standard deviations. Both data show that the trap stiffness decreases with increasing value of d_{cone}. Table 7.1 summarises the measured and calculated values in Figure 7.8. In both directions, our experimental results are close to the theoretical predictions but for the majority there is no agreement within the error bars. Possible explanations for this are uncertainties in the cone alignment, the cone shape and the distance d_{cone}.
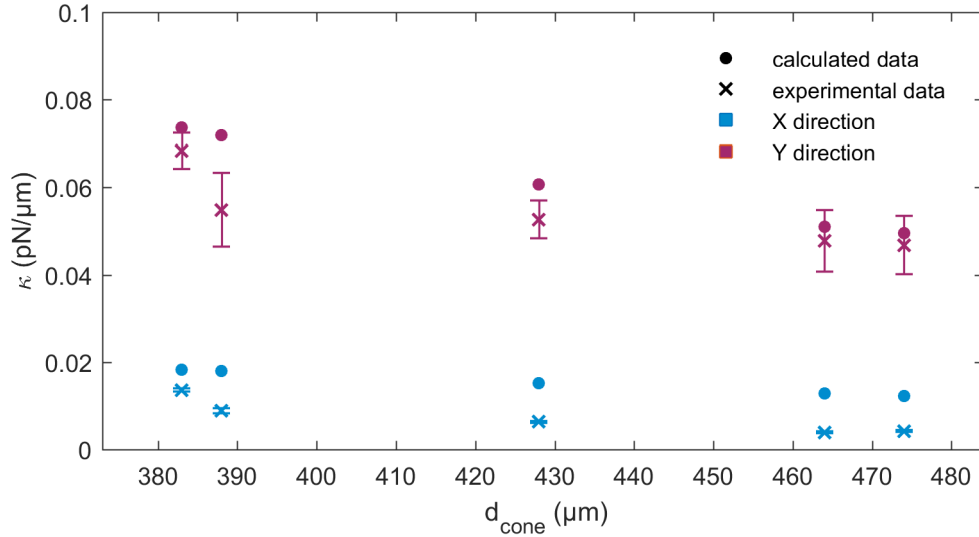
Figure 7.8: Measured trap stiffness in the X and Y directions for a magnetic trap generated with setup A as a function of d_{cone}. The trap stiffness values correspond to a PS bead in a 0.6 M MnCl solution. The plot shows the measured data (marked as $\times$) and the theoretical data from magnetic field simulations with FEMM (marked as $\bullet$).

d_{cone} (μm)	κ_X (pN/μm)	$\kappa_{theo,X}$ (pN/μm)	κ_Y (pN/μm)	$\kappa_{theo,Y}$ (pN/μm)	N_{vid}
383	0.0136 ± 0.0004	0.018	0.068 ± 0.004	0.074	7
388	0.0089 ± 0.0006	0.018	0.055 ± 0.009	0.072	2
428	0.0063 ± 0.0002	0.015	0.053 ± 0.004	0.061	7
464	0.0039 ± 0.0002	0.013	0.048 ± 0.007	0.051	2
474	0.0042 ± 0.0002	0.012	0.047 ± 0.007	0.050	2

Table 7.1: Trap stiffness in the X and Y directions for setup A with different values for d_{cone}. The values are measured for 5 μm-diameter PS beads in a 0.6 M MnCl$_2$ aqueous solution. κ: Average trap stiffness and corresponding standard deviation measured from the particle trajectory. κ_{theo}: Trap stiffness calculated from simulations of the setup with FEMM. N_{vid}: Number of videos acquired for each value of d_{cone}.

Setups B and C: Improving the magnetic field with steel components

We now evaluate the potential increase of the trap stiffness by adding steel components to the setup. To compare all three setups in Figure 7.5, we set the distance between the tips of the magnets to $d_{cone} = 428\,\mu$m and the distance between the cone-shaped steel pieces to $d_{steel} = 243\,\mu$m. For each setup, we take $6 - 20$ videos that are two to seven minutes long each.

In setup B and C, we observe magnetic trapping of PS beads in solution, too. To illustrate this, in Figures 7.9a and b we show a trapped PS bead in setup B. As we move the setup in
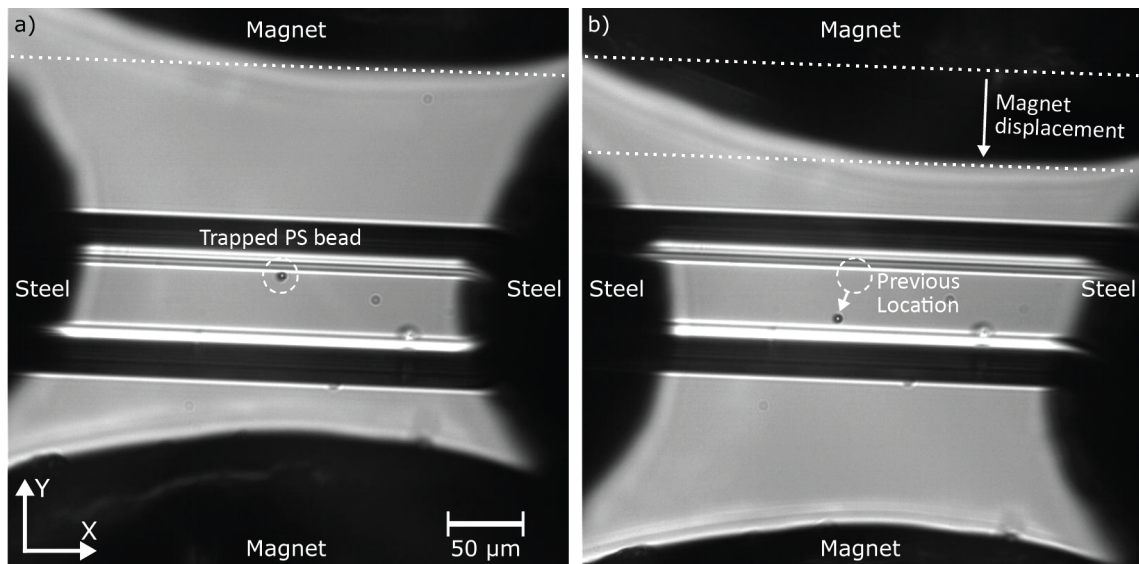
Figure 7.9: Magnetic trapping of an individual 5 μm-diameter PS bead with setup B in a 0.6 M MnCl$_2$ aqueous solution. a) Initial position of the PS bead between the cone-shaped magnets. b) Position of the PS bead after moving the setup in the negative Y direction while holding the capillary still.

the negative Y direction while holding the capillary still, we can see that the PS bead follows the trap centre.

Table 7.2 presents the measured average trap stiffness and standard deviation for each setup. In comparison to setup A, we see that the addition of steel cones in setup B increases the trap stiffness in both directions by at least a factor of two: κ_X increases from 0.006 pN/μm to 0.017 pN/μm and κ_Y increases from 0.05 pN/μm to 0.11 pN/μm. The improvement is due to an increase of the magnetic flux at the tips of the magnetic steel cones as we have seen in Section 6.3.2. It follows that setup B is capable of trapping particles with smaller volumes or lower magnetic susceptibilities as shown in Equations (7.1) and (7.9). For the analysis of setup C, we acquired more videos compared to the other two setups as we observed fluctuations for the trap stiffness value. From our evaluation, it appears that the addition of steel blocks in setup C does not improve the trap stiffness. Therefore, further studies, including magnetic field simulations with a three-dimensional model, are necessary in order to optimize the steel block dimensions and potentially generate a stronger magnetic trap.

Setup	κ_X (pN/μm)	κ_Y (pN/μm)	N_{vid}
A	0.0063 ± 0.0002	0.053 ± 0.004	7
B	0.017 ± 0.001	0.11 ± 0.01	6
C	0.0071 ± 0.0001	0.085 ± 0.005	20

Table 7.2: Measured average trap stiffness in the X and Y directions for setup A, B and C in Figure 7.5. κ: Measured average trap stiffness. $\Delta\kappa$: Standard deviation of the trap stiffness. N_{vid}: Number of videos acquired for each setup. For all setups, the distance between the tips of the magnets is $d_{cone} = 428$ μm and the distance between the cone-shaped steel pieces is $d_{steel} = 243$ μm

7.4.2 Magnetic trapping of HOPG microparticles in AceWater

For the magnetic trapping of uncoated HOPG microparticles, we use setup A and B where the distance between the tips of the magnets is $d_{\text{cone}} = 428\,\mu\text{m}$ and the gap between the cone-shaped steel cones is $d_{\text{steel}} = 243\,\mu\text{m}$ (for setup B). The particle sample is prepared from bulk HOPG with a mosaic spread of 0.4° and are fabricated by means of sonication for one hour. We choose particles with volumes up to $86\,\mu\text{m}^3$.

In both setups, we see that particles migrate towards the magnetic field minimum on the X-Y plane but they cannot be lifted against gravity or they align their graphene planes to the field but do not migrate at all. This implies that the magnetic trapping forces are insufficient to compensate for the gravitational force and buoyancy on the particle. As we can see in Equation (7.1), the magnetic force on the particle depends, amongst other factors, on the magnetic susceptibility of the particle, the magnetic field strength and field gradient. To clarify their contribution to the magnetic force, we conduct the magnetic trapping on graphite microparticles from a graphite powder (Sigma Aldrich, part no. 282863). Those particles have the same density as HOPG ($2.26\,\text{g/cm}^3$) and hence the gravitational force and buoyancy on the particle are the same as on HOPG microparticles. However, graphite powder microparticles are fabricated differently and may have a different magnetic susceptibility to HOPG microparticles. Therefore, if graphite powder microparticles can be trapped, its magnetic susceptibility can be extracted and related to HOPG microparticles fabricated by means of sonication. To compare the experimental outcome with our observations for HOPG microparticles, we disperse the graphite powder microparticles in AceWater and trap them in setup A with $d_{\text{cone}} = 428\,\mu\text{m}$. We specifically pick particles with volumes similar to those chosen for HOPG microparticles (i.e. volumes up to $86\,\mu\text{m}^3$).

The typical behaviour of the particles in the magnetic field is shown in Figure 7.10. In Figures 7.10a and b, we see graphite powder microparticles in various shapes that migrate towards the trap centre. After 78 seconds (Figure 7.10b), they accumulate around the magnetic field minimum and can be moved in the capillary volume by moving the magnets.

We can see the formation of a cluster which can be displaced over the entire capillary volume. By reducing the particle concentration in the solution, we can trap an individual particle in solution as shown in Figures 7.10c and d. As we move the magnets in all three directions, the graphite powder particle follows the trap centre. This confirms that we have achieved magnetic trapping of graphite powder microparticles in a diamagnetic solution.

Figure 7.11 shows the measured trap stiffness in the X and Y directions as a function of particle volume of four different graphite powder microparticles. Each trap stiffness value is
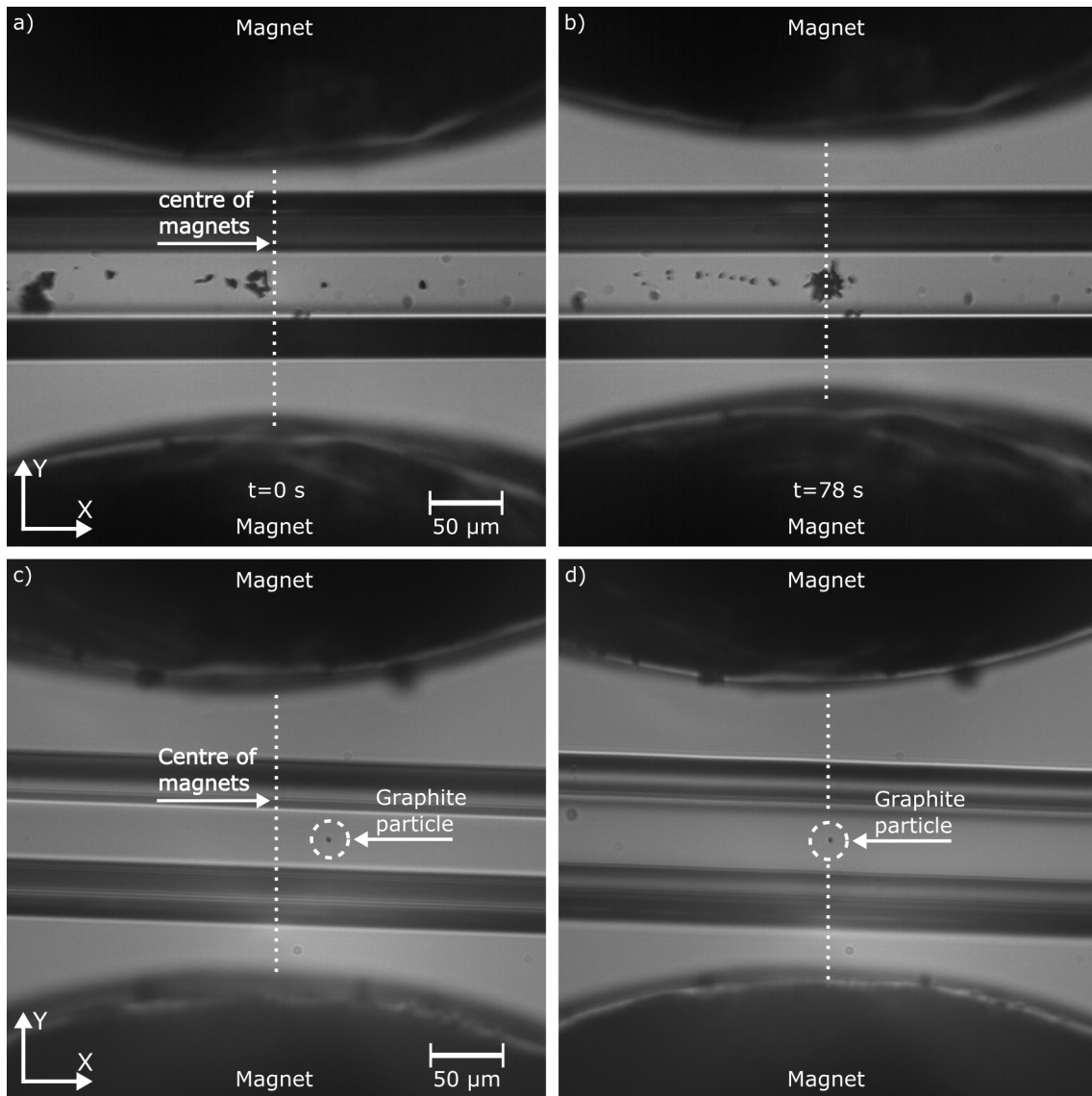
Figure 7.10: Magnetic trapping of graphite powder microparticles from a factory-made graphite powder in setup A with $d_{cone} = 428\,\mu m$. a) and b) Migration of graphite powder particles over an observation duration of 78 s. c) and d) Migration of an individual graphite powder microparticle towards the trap centre.
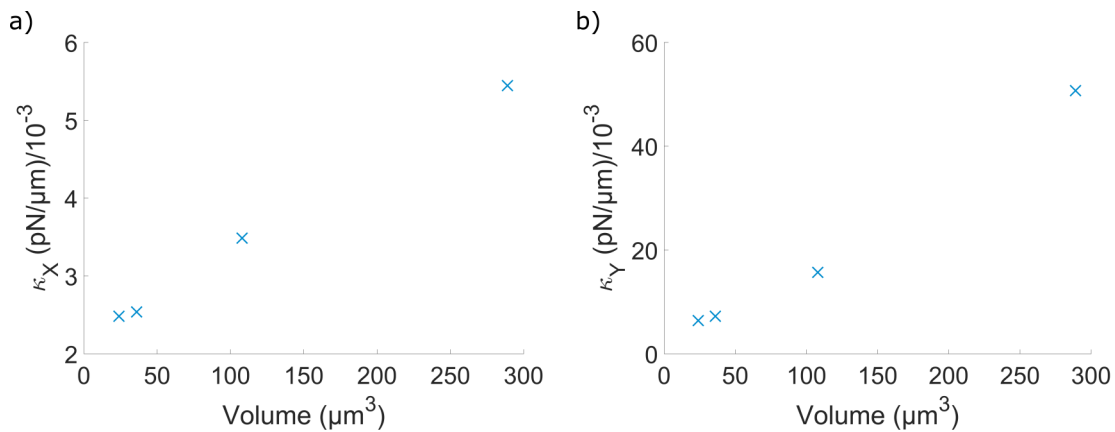
Figure 7.11: Measured trap stiffness of graphite powder particles in AceWater for setup A with $d_{cone} = 428\,\mu m$. a) Trap stiffness in the X direction. b) Trap stiffness in the Y direction.

determined from two to seven minute-long videos of the particle motion in the trap. In both directions, we can see a linear increase of the trap stiffness with particle volume which is in accordance to Equations (7.1) and (7.5). The trap stiffness values and the corresponding standard deviations due to the particle tracking error are presented in Table 7.3.

We can calculate the magnetic susceptibility of the graphite powder microparticles in Table 7.3 by rearranging Equation (7.5):

$$\chi_i = \frac{2\mu_0 \kappa_i}{V} \left(\frac{\partial^2}{\partial i^2} B_0^2 (\mathbf{r}) \Big|_{\mathbf{r}=\mathbf{r}_0} \right)^{-1} + \chi_1, \tag{7.11}$$

where $i = X, Y$ and $\mathbf{r}_0$ is the trap centre position determined from the simulations. Table 7.4 summarises the calculated magnetic susceptibility values which are between -7×10^{-5} and -2×10^{-5}. These values are lower (in absolute value) than the measured in-plane magnetic susceptibility of HOPG with a mosaic spread of 0.4° which is given by -8.2×10^{-5} (from Table 2.3). Since sonicated HOPG microparticles with similar volumes cannot be trapped with the same setup, the magnetic susceptibility of sonicated HOPG microparticles is probably lower than that of pristine, bulk HOPG and of the graphite powder microparticles. It follows that the absence of magnetic trapping of HOPG microparticles in the Z direction could be due to a reduced magnetic susceptibility of the particle.

Particle Volume (μm^3)	κ_X (pN/μm)	κ_Y (pN/μm)
24	0.0024 ± 0.0001	0.0064 ± 0.0004
36	0.0025 ± 0.0001	0.0072 ± 0.0006
108	0.0035 ± 0.0002	0.016 ± 0.002
289	0.0054 ± 0.0004	0.05 ± 0.01

Table 7.3: Measured trap stiffness and standard deviation of individual graphite powder particles with different volumes in AceWater.

Particle Volume (μm^3)	$\chi_X / 10^{-5}$	$\chi_Y / 10^{-5}$
24	-6.9 ± 0.2	-3.7 ± 0.3
36	-5 ± 0.2	-3 ± 0.2
108	-2.7 ± 0.2	-2.4 ± 0.3
289	-1.9 ± 0.1	-2.7 ± 0.6

Table 7.4: Volume magnetic susceptibility of graphite powder particles with different volumes calculated from the measured trap stiffness in the X and Y directions.

7.5 Conclusion and outlook for permanent magnet traps

The results of this part of the study constitutes the first demonstration of the magnetic trapping of graphitic microparticles in a diamagnetic solution. We achieved this by using two opposing cone-shaped and made-to-order NdFeB magnets with the same magnetic poles at their tips. We conducted trapping experiments with sonicated HOPG microparticles and factory-made graphite powder microparticles. In the outcome, we magnetically trapped graphite powder particles while no trapping was achieved for sonicated HOPG microparticles. The results could imply that the magnetic properties of graphite microparticles could be influenced by the fabrication process. This shows that our setup is useful to probe the magnetic properties of the particle.

The trap stiffness of the magnetic trap can be increased by adding two opposing steel cones close to the particle. Such improvements of the magnetic trap are of great benefit for particle manipulation, as they make it possible to apply magnetic trapping on microparticles with smaller volumes. A further increase of the trap stiffness can be achieved by increasing the sharpness of the tips of the cone-shaped magnets and the steel cones. As for now, it is difficult to find manufacturers that are capable of producing magnets and steel pieces to such specifications. Other improvements could be achieved by reducing the thickness of the protective plating on the magnet to get the particle closer to the surface of the magnet; by replacing steel with a material with higher permeability, e.g. supermalloy, as this could increase the magnetic flux at the tips; and by optimizing the dimensions of the cone-shaped magnets and steel pieces through simulations.

For the evaluation of the trapping strength, we focused on the particle motion on the plane perpendicular to the direction of gravity. In order to use three-dimensional magnetic traps to carry out force-sensing experiments in three-dimensions, one would need to detect particle position in all three dimensions. The position recognition via imaging along the vertical direction can be complex because traditional methods for precise particle detection along the imaging axis, such as back focal plane interferometry using a quadrant photodiode (QPD) [112], require transparent and spherical particles while our graphitic microparticles are opaque and irregularly shaped. One possible method involves taking particle images at different heights while keeping the microscope objective at a fixed position. The acquired diffraction images can be used to generate a lookup table that can later be used to find the particle position via interpolation. Such a method, which is routinely used in magnetic tweezer experiments for spherical particles [113], could be extended to irregular particle shapes that would require the generation of an individual table for every particle considered.

Our setup can be integrated into potential flow experiments. For example, Kabir *et al.* used a flow experiment to study the viscous drag on trapped PS beads in optical tweezers [114]. They calculated the drag coefficient by evaluating the particle motion inside the trap and keeping the flow of the fluid constant. By using magnetic trapping, flow experiments can be conducted on irregular shaped micron-sized objects as the technique does not depend on the particle shape. If the electrical and magnetic properties of the object are anisotropic, we could additionally expose the particle to an AC electric field to align the particle with respect to the fluid flow. Such an addition would allow the measurement of the viscous drag force on irregular shaped micron-sized particles for different particle orientations.

The results for the three-dimensional magnetic trapping in a diamagnetic solution are in particular relevant for biological experiments as the natural environment of living systems is diamagnetic. In order to measure the forces in biological interactions with a trapped graphitic microparticle, our setup must be capable of measuring forces on the piconewton scale (10^{-12} N). With our current setup, we were capable of generating a magnetic trap with a trap stiffness of order $10^{-2} - 10^{-3}$ pN/μm. Consequently, in order to measure piconewton-forces the particle has to be displaced from the trap centre by several hundreds of micrometres. Such displacement distances are impractical because the relationship between the particle displacement and the force may not be linear for such long distances. Additionally, our current setup has a limited space for the sample since the magnets and the steel cones must to be as close as possible to the particle. Both issues could potentially be improved by optimizing the dimensions of the magnets and the steel components. A handful of studies demonstrate that micron-sized permanent magnets can be generated on a chip using lithography [115–118]. Such magnets can produce field gradients up to 1 T/μm [115] which is three orders of magnitude larger than the ones generated in this experiment. A possible setup has been presented by Kauffmann *et al.* who used an array of microfabricated magnets to trap cells in a paramagnetic buffer[116]. Alternatively, we could use current-carrying microfabricated wires which can generate stronger magnetic field gradients and offer better sample access. The latter idea will be extended in the following section.

7.6 Beyond permanent magnets: Magnetic trapping with current-carrying wires

Static magnetic fields generated by means of current-carrying wires have the advantage that the magnetic field can be switched on and off. The magnetic field strength of an infinitely long and thin wire is given by:

$$\mathbf{B}_{\text{wire}} = \frac{\mu_0 I}{2\pi r}\mathbf{e}_\phi, \tag{7.12}$$

where I is the electric current, r is the radial distance to the centre of the wire and $\mathbf{e}_\phi$ is the polar coordinate unit vector. From the equation, we can see that the magnetic field strength and field gradient increases with decreasing distance to the surface of the wire. Therefore, current-carrying wires with small cross sections can generate strong magnetic fields and gradients at the close vicinity of the wire surface. Advances in microfabrication have made it possible to fabricate micrometre-thick wires that are capable of handling current densities over $10^7\,\text{A/cm}^2$ [119] and allowed the generation of strong magnetic field gradients. Today, microfabricated wires are used in atom optics, where complex wire patterns on centimetre-sized chips allow the fabrication of atom guides and atom traps as demonstrated by Denschlag *et al.* in ref. [120]. In this section, we take these ideas as a starting point to investigate theoretically if three-dimensional magnetic traps for HOPG microparticles in solution could be generated in this way.

7.6.1 Physical principle of generating magnetic field minima with current-carrying wires

We illustrate the principle of magnetic trapping with current-carrying wires for the case of magnetic trapping in two dimensions, i.e. the trapping of particles along a line of magnetic field minima. Let us consider an infinitely thin and straight wire that extends along the X-axis. The wire carries an electric current, I, in the positive direction of X and generates a circular magnetic field perpendicular to the X-axis as illustrated in Figure 7.12a. To generate a magnetic field minimum at a distance r_0 away from the wire centre, we need a constant magnetic field (the bias field), $\mathbf{B}_{\text{bias}}$, in the direction perpendicular to the wire (Figure 7.12b). The superposition of both magnetic fields generates a magnetic field minimum on the Y-Z plane that extends infinitely along the X direction as shown in Figure 7.12c. Mathematically, the magnitude of the superimposed magnetic field, $\mathbf{B}_{\text{tot}}$, can be expressed as:

$$|\mathbf{B}_{\text{tot}}| = |\mathbf{B}_{\text{wire}} + \mathbf{B}_{\text{bias}}| = |\frac{\mu_0 I}{2\pi r}\mathbf{e}_\phi + \mathbf{B}_{\text{bias}}|. \tag{7.13}$$
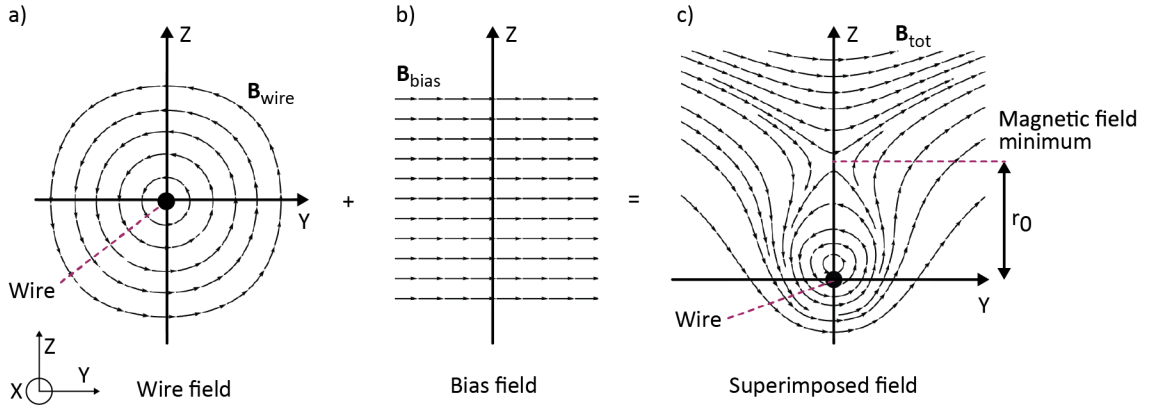
Figure 7.12: Principle of the generation of a line minima above an infinitely long and thin current-carrying wire that extends in the X direction. a) Magnetic field of a current-carrying wire on the Y-Z plane. b) Bias field on the Y-Z plane. c) Superposition of the magnetic fields in a) and b) which generates a magnetic field minimum at a given distance from the wire centre on the Y-Z plane.

At the position of the magnetic field minimum ($r = r_0$), both fields cancel each other out:

$$|\mathbf{B}_{\text{wire}} + \mathbf{B}_{\text{bias}}| = 0 \qquad \text{at } r = r_0. \tag{7.14}$$

Therefore, we can solve Equation (7.14) for r_0 which gives:

$$r_0 = \frac{\mu_0 I}{2\pi |\mathbf{B}_{\text{bias}}|}. \tag{7.15}$$

Equation (7.15) shows that the distance between the magnetic field minimum and the wire centre (on the Y-Z plane) is determined by the electric current in the wire and the strength of the bias field.

7.6.2 Magnetic trapping of HOPG microparticles with current-carrying wires

We investigate two different setups of wires that corresponds to the magnetic trapping of HOPG microparticles in AceWater in two and three dimensions. To calculate the magnetic field, we use the Mathematica package Radia. In our simulation, each wire is 10 cm long with a rectangular cross section of size $5 \times 5\,\mu$m. The current in the wire is set to 3 A which gives us a current density of $1.2 \times 10^{-7}\,\text{A/cm}^2$ and has been shown to be a realistic value for trapping atoms in vacuum [119]. The bias field strength and direction are adjusted to generate the magnetic field minimum $5\,\mu$m above the wire surface.

In order to compare our model with the simulations of magnetic traps generated by permanent magnets, we calculate the magnetic forces on a point-like HOPG microparticle with a volume of $72\,\mu\text{m}^3$ (same value used in Section 7.2.1). The implications of the finite particle size on magnetic trapping will be addressed during the discussion of our results. To account

for the magnetic anisotropy of HOPG, we evaluate the trap for the cases where the graphene planes and the magnetic field are parallel and perpendicular to each other.

HOPG microparticles in a two-dimensional magnetic trap

Figure 7.13a shows our model for the magnetic trapping in two dimensions. It consists of a single wire that is positioned along the X-axis and a bias field in the positive Y direction. In order to generate a magnetic field minimum at $5\,\mu m$ above the wire surface, we set the bias field strength to 0.08 T. The contour map of the superimposed magnetic field on the Y-Z plane is presented in Figure 7.13b. The magnetic field minimum is indicated by the closed contours at $Y = 0\,\mu m$ and $Z = 5\,\mu m$. In the X direction, this magnetic field produces a line of field minima parallel to the wire surface.

a)

b)
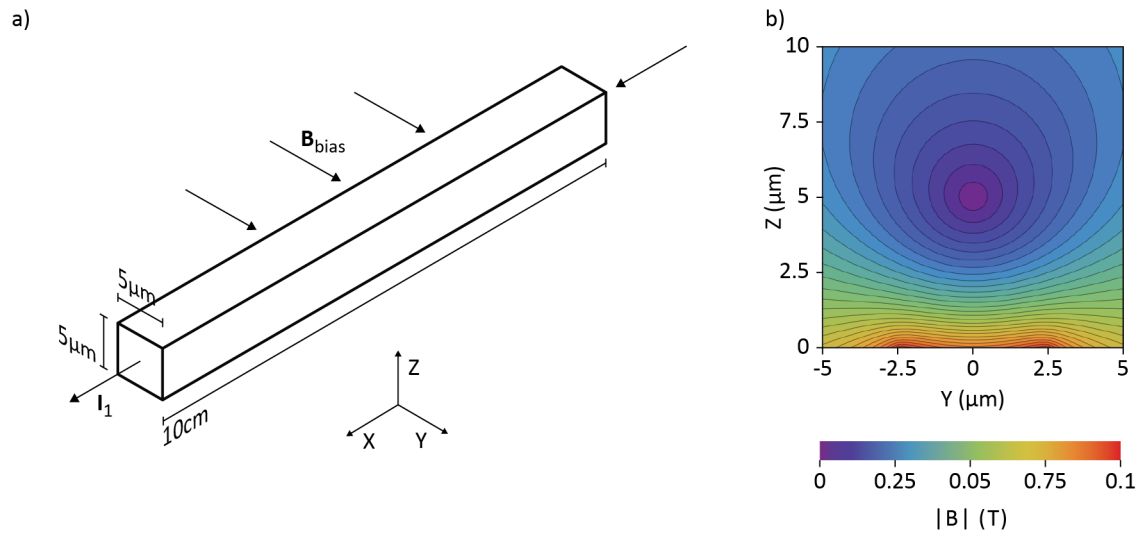
Figure 7.13: a) Model of a rectangular wire aligned on the X-axis with current I_1 and a bias field B_{bias}. b) Contour map of a magnetic field generated with a current-carrying rectangular wire with $I_1 = 3\,A$ and a bias field $B_{bias} = 0.08\,T\,(0, 1, 0)$. The wire surface is at $Z = 0$.

To calculate the magnetic force on the particle, we apply Equation (7.1). Due to the balance of magnetic force, gravitational force and buoyancy (see Section 7.2.1), the trap centre on the Z-axis is at $Z_0 = 3.8\,\mu m$ if the graphene planes are parallel to the superimposed magnetic field $\mathbf{B}_{tot}$, and $Z_0 = 4.8\,\mu m$ if they are aligned perpendicular to $\mathbf{B}_{tot}$. The different values are expected because the magnetic force in the direction parallel to the planes is lower than in the direction perpendicular to the planes. On the Y-axis, the trap centre is located at $Y_0 = 0$. Figure 7.14 shows the magnetic forces on the HOPG microparticle for displacements from the trap centre. The plots in Figures 7.14a and b correspond to the forces in the Y and Z directions when the graphene planes are aligned parallel to the magnetic field. In Figure 7.14b, we see that for displacements towards the wires $(Z - Z_0 < 0)$, the force increases whereas for
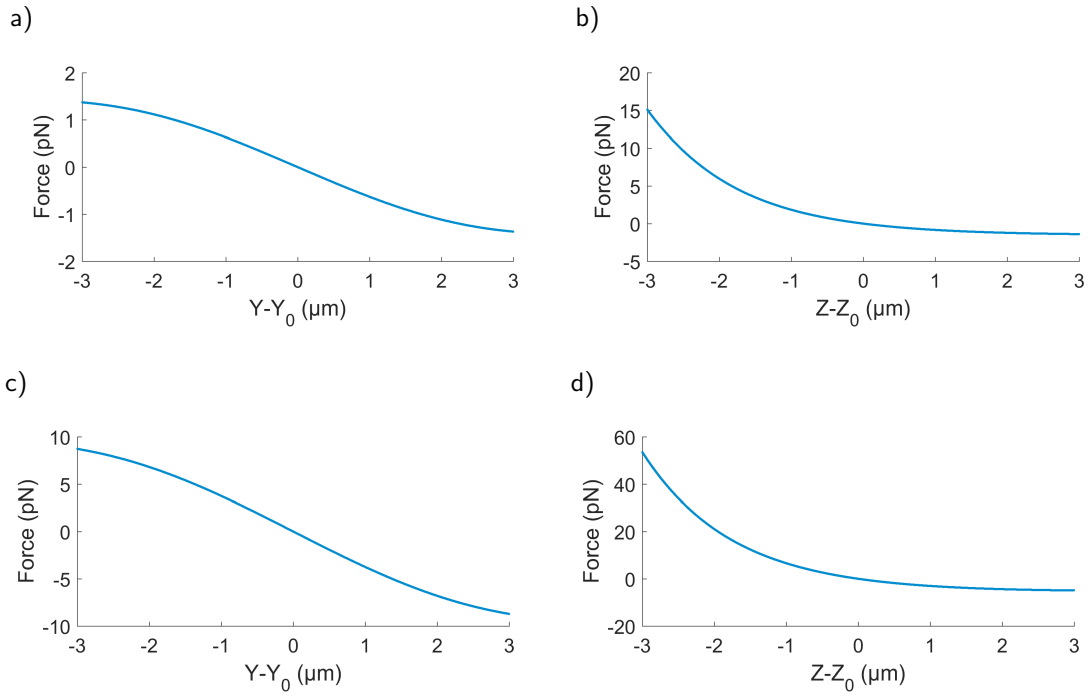
Figure 7.14: Magnetic force on a HOPG microparticle of volume 72 µm³ in AceWater for displacements from the trap centre. The magnetic field is generated by a single current-carrying wire with a rectangular cross section and a bias field $\mathbf{B}_{\text{bias}} = 0.08\,\text{T}(0, 1, 0)$. The plots show the forces in the Y and Z directions for two different particle orientations. a) and b) The graphene planes are aligned parallel to the superimposed magnetic field $\mathbf{B}_{\text{tot}}$. The trap centre is at $Y_0 = 0$ and $Z_0 = 3.8\,\mu\text{m}$. c) and d) The graphene planes are aligned perpendicular to $\mathbf{B}_{\text{tot}}$. The trap centre is at $Y_0 = 0$ and $Z_0 = 4.8\,\mu\text{m}$.

displacements away from the wires ($Z - Z_0 > 0$) the force eventually reaches a value around $-1.4\,\text{pN}$. This implies that the particle escapes the trap if a force in excess of $1.4\,\text{pN}$ is applied on the particle in the positive Z direction.

Figures 7.14c and d present the forces on the HOPG microparticle when the graphene planes are aligned perpendicular to the field. The main differences compared to the previous case are the larger magnetic forces on the particle due to the particle orientation. For displacements away from the wires ($Z - Z_0 > 0$) the force on the particle reaches a value of around $-5\,\text{pN}$.

From the data in Figure 7.14, we can calculate the range of particle positions in which the force increases linearly with displacement from the trap centre. We define the linear regime as the displacement range over which the trap stiffness measured at the trap centre changes by at most 10 %. In the Y direction, the displacement range is $\pm 1\,\mu\text{m}$ for both particle orientations. As for the Z direction, the range is $\pm 0.1\,\mu\text{m}$ if the graphene planes are parallel to the field and $-0.2\,\mu\text{m}$ to $0.1\,\mu\text{m}$ if the planes are perpendicular to the field. The linear regime is of particular interest for force experiments because it guarantees a simple association between the force and displacement as long as the particle volume is confined in this range. In our case, the particles are larger than the linear regime. Therefore, it is necessary for the future to re-evaluate the force profile by integrating the force over the entire particle volume. Such a procedure can be complex as the particle shapes are irregular.

137

Table 7.5 summarizes the calculated trap stiffness values in the Y and Z directions in the trap centre. We can see that the values are in the range $0.7 - 4.4 \, \mathrm{pN/\mu m}$ which are one order of magnitude larger than those calculated in Section 7.2.1 for HOPG microparticles in AceWater between two cone-shaped magnets that are separated by $350 \, \mu m$. Note, that the trap stiffness has been calculated specifically for HOPG in AceWater at $5 \, \mu m$ above the surface of rectangular shaped wires. In addition to the orientation of HOPG to B_{tot}, the trap stiffness depends on all factors that can influence the magnetic force (Equation (7.1)), the trapping height, the wire dimensions and the applied current.

Orientation	κ_Y (pN/μm)	κ_Z (pN/μm)
Parallel	0.7	1.2
Perpendicular	3.9	4.4

Table 7.5: Trap stiffness values in the Y and Z directions for a HOPG microparticle of volume $72 \, \mu m^3$ in AceWater. The magnetic trap is generated with a single current-carrying wire with rectangular cross section and a bias field $\mathbf{B}_{\mathrm{bias}} = 0.08 \, \mathrm{T}(0,1,0)$. Parallel: the graphene planes are aligned parallel to $\mathbf{B}_0$. Perpendicular: the graphene planes are aligned perpendicular to $\mathbf{B}_0$.

Extension to three-dimensional magnetic trapping

Three-dimensional magnetic traps can be constructed by generating a magnetic field with multiple current-carrying wires and superimposing it with a bias field. Several wire configurations for magnetic trapping of neutral atoms have already been studied, including Z-shaped wire patterns [120] and chip designs with intersecting wires [121]. Here, we analyse the magnetic field generated by two current-carrying wires that intersect at a right angle as shown in Figure 7.15. We align one wire in the direction $(-1, -1, 0)$ and the other wire in the direction $(1, -1, 0)$. Each wire carries a current in the direction specified by I_1 or I_2.
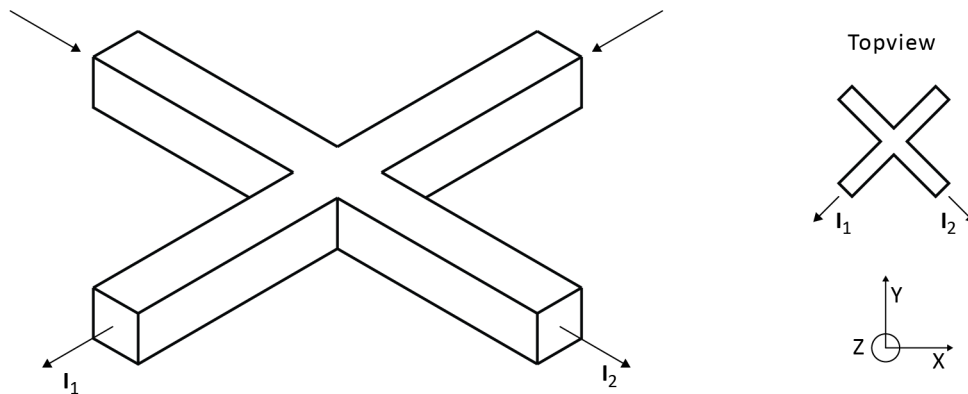
Figure 7.15: Three-dimensional model of two intersecting wires with a rectangular cross section for the generation of a three-dimensional magnetic trap. The wire carrying the current I_1 is aligned in the direction $(-1, -1, 0)$ and the wire carrying the current I_2 is aligned in the $(1, -1, 0)$ direction.
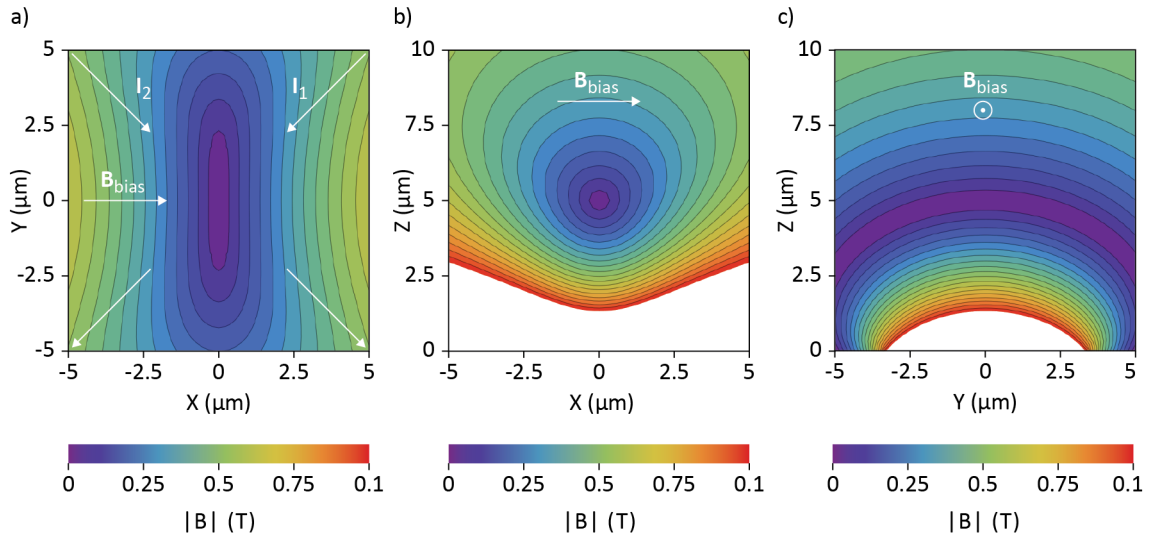
Figure 7.16: Contour maps for the magnetic field generated by two current-carrying wires and a bias field $\mathbf{B}_{bias} = 0.11\,\mathrm{T}(1,0,0)$. The plots show the magnetic field strength on different planes: a) X-Y plane at 5 μm above the wire surface, b) X-Z plane at $Y = 0$, c) Y-Z plane at $X = 0$. The surface of the wires is at $Z = 0$.

Our simulation shows that in the present wire configuration any bias field on the X-Y plane, i.e. $\mathbf{B}_{bias,Z} = 0$, cannot generate a local three-dimensional magnetic field minimum appropriate for trapping. This is illustrated in Figure 7.16, which shows contour maps of the magnetic field strength on three different planes for the wire setup with the bias field $\mathbf{B}_{bias} = 0.11\,\mathrm{T}\,(1,0,0)$. Figure 7.16a shows the contour map on the X-Y plane at the height of the trap centre, i.e. 5 μm above the surface of the wires. If we look at the magnetic field strength on the X-Z plane at $Y = 0$ as shown in Figure 7.16b, we find a minimum (purple closed contour in figure) which may give us the impression that we generated a trap above the wires. However, on the Y-Z plane at $X = 0$, we get a contour map as shown in Figure 7.16c. We find a bent shape of the trap where particles could displace by large distances in the Z and Y direction which is not useful for particle trapping and potential force sensing.

If, instead, we use the bias field $\mathbf{B}_{bias} = 0.11\,\mathrm{T}\,(1,0,-1)$, we generate a magnetic field as shown in Figure 7.17. In contrast to the contour maps in Figure 7.16, we find closed contours around the magnetic field minimum in all planes. Therefore, the magnetic field generated with a combination of two intersecting current-carrying wires and the bias field $\mathbf{B}_{bias} = 0.11\,\mathrm{T}\,(1,0,-1)$ is suitable for particle trapping. As before, the magnetic field minimum is located 5 μm above the surface of the wires. A contour map of the magnetic field at this height on the X-Y plane is shown in Figure 7.17a. We can see that the magnetic field minimum is not located above the intersection of the wires but instead is at $X = 5.3$ μm and $Y = 0$. Figure 7.17b shows the contour map of the magnetic field on the X-Z plane at $Y = 0$. We can see that the shape of the contours around the field minimum is slightly tilted by $\sim 15°$
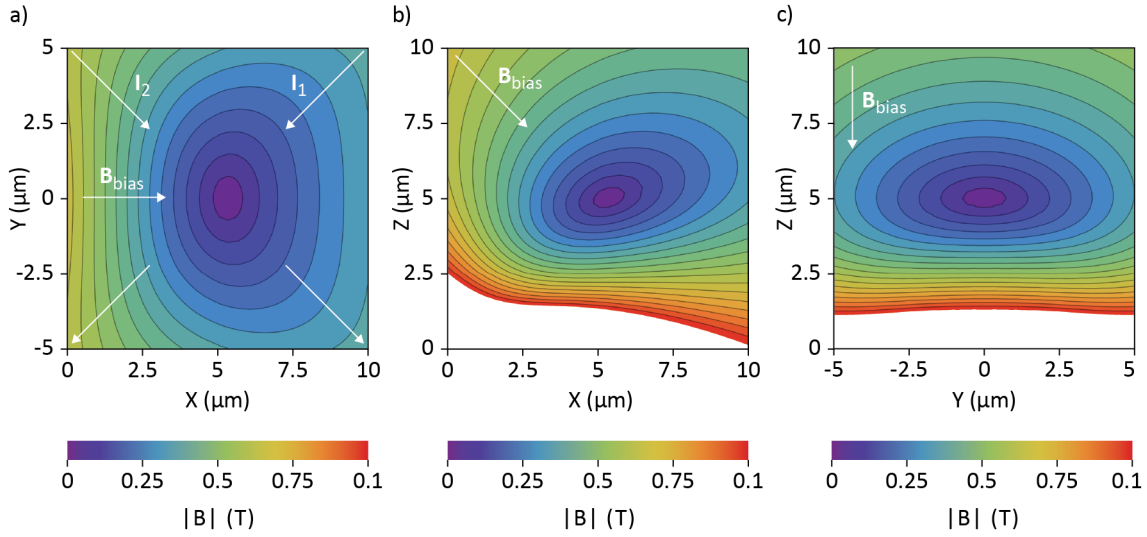
Figure 7.17: Contour maps of the magnetic field generated by two current-carrying wires and the bias field $\mathbf{B}_{bias} = 0.11\,\text{T}(1, 0, -1)$. a) Map on the X-Y plane at $5\,\mu\text{m}$ above the wire surface, b) Map on the X-Z plane at $Y = 0$ c) Map on the Y-Z plane at $X = 5.3\,\mu\text{m}$. The wire surface is at $Z = 0$.

away from the X-axis. In this analysis, we neglect this tilt and evaluate the magnetic field in the direction parallel to the X- and Z-axes instead. Figure 7.17c shows the contour map of the magnetic field on the Y-Z plane at $X = 5.3\,\mu\text{m}$.

In the following, we analyse the magnetic potential and forces for HOPG microparticles in the magnetic field presented in Figure 7.17. Figures 7.18a-c show the contour maps of the magnetic potential on the X-Y, X-Z and Y-Z planes for a particle with its graphene planes aligned in the direction of $\mathbf{B}_{tot}$. The trap centre is located at $X_0 = 5\,\mu\text{m}$, $Y_0 = 0$ and $Z_0 = 4.3\,\mu\text{m}$ which is marked accordingly on each contour map. The closed contours around the trap centre on each plane show clearly that HOPG microparticles can be trapped in three dimensions. Figures 7.18d-f show the magnetic forces on the particle for displacements from the trap centre in the X, Y and Z directions. Similar to the results in Section 7.6.2, we can see that the restoring forces decrease with distance from the wires: in Figure 7.18d, the restoring forces for $X - X_0 > 0$ are at most $-0.8\,\text{pN}$; and in Figure 7.18f the forces for $Z - Z_0 > 0$ reach a maximum value of $\sim -2\,\text{pN}$. The particle can therefore escape the trap if the force on the particle exceeds the limit in the corresponding direction.

Figure 7.19 shows similar plots to Figure 7.18 but for a HOPG microparticle with its graphene planes aligned perpendicular to $\mathbf{B}_{tot}$. The alignment results in larger values for the magnetic potential (Figures 7.19a-c) and the magnetic forces (Figures 7.19d-f). The trap centre is located at $X_0 = 5.3\,\mu\text{m}$, $Y_0 = 0$ and $Z_0 = 4.9\,\mu\text{m}$ which is marked accordingly in Figures 7.19a-c. As before, the restoring forces decrease with distance from the wires: the restoring forces for $X - X_0 > 0$ are at most $-5.5\,\text{pN}$ (Figure 7.19d); and for $Z - Z_0 > 0$ the forces reach a maximum value of $-9.8\,\text{pN}$ (Figure 7.19f).
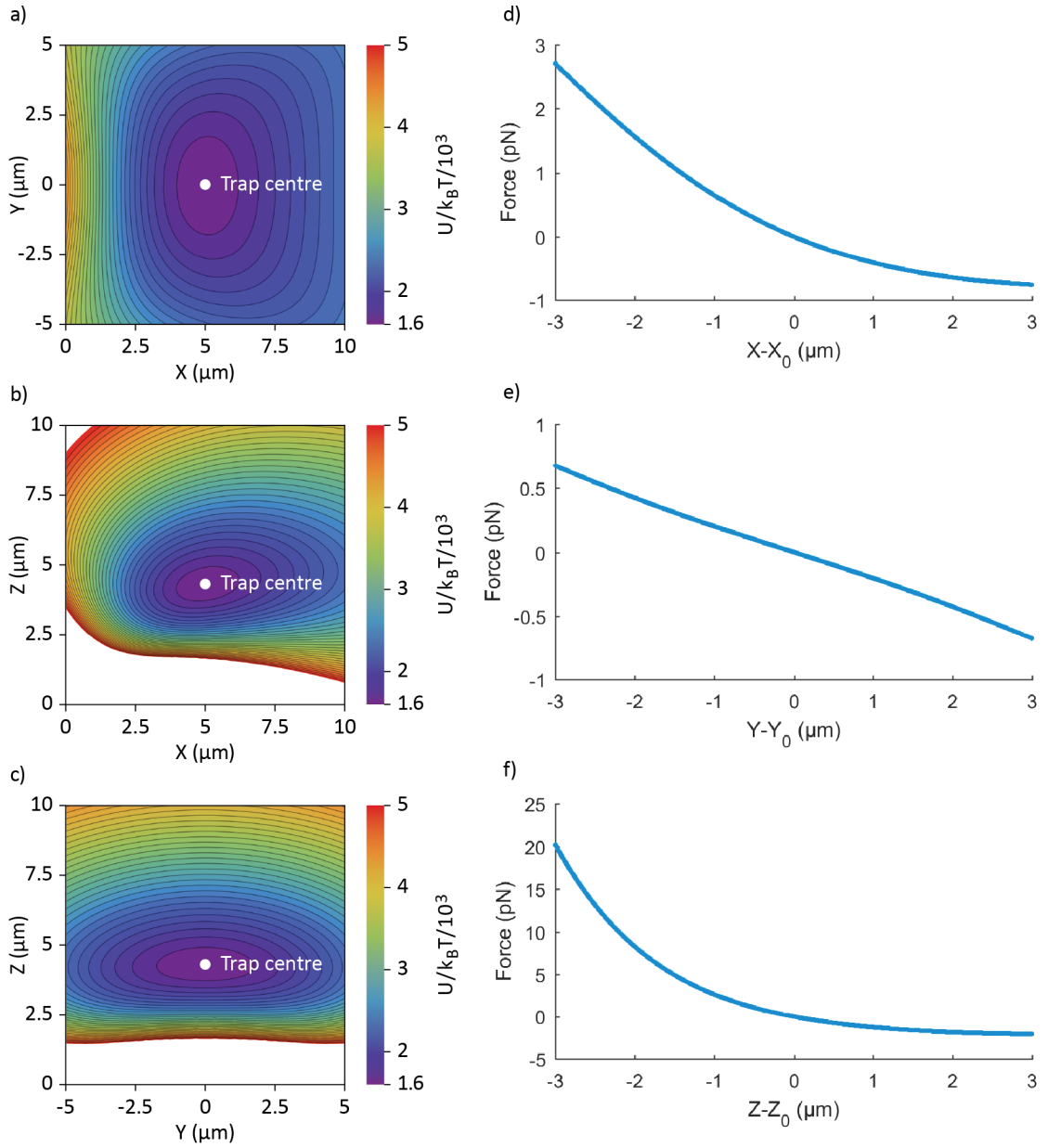
Figure 7.18: Magnetic potential and magnetic force for a HOPG microparticle in a magnetic trap generated by two intersecting current-carrying wires and a bias field $\mathbf{B}_{bias} = 0.11\,\text{T}(1, 0, -1)$. The calculations are made for a HOPG microparticle of volume $72\,\mu\text{m}^3$ in AceWater with its graphene planes aligned parallel to the magnetic field direction. The location of the magnetic trap is at $X_0 = 5\,\mu\text{m}$, $Y_0 = 0$ and $Z_0 = 4.3\,\mu\text{m}$ (wire surface at $Z = 0$). a-c) Maps of magnetic potential on individual planes: a) X-Y plane at $Z = 4.3\,\mu\text{m}$, b) X-Z plane at $Y = 0$, c) Y-Z plane at $X = 5\,\mu\text{m}$. d-f) Magnetic force for displacements from the trap centre on different axes: d) X-axis, e) Y-axis, f) Z-axis.
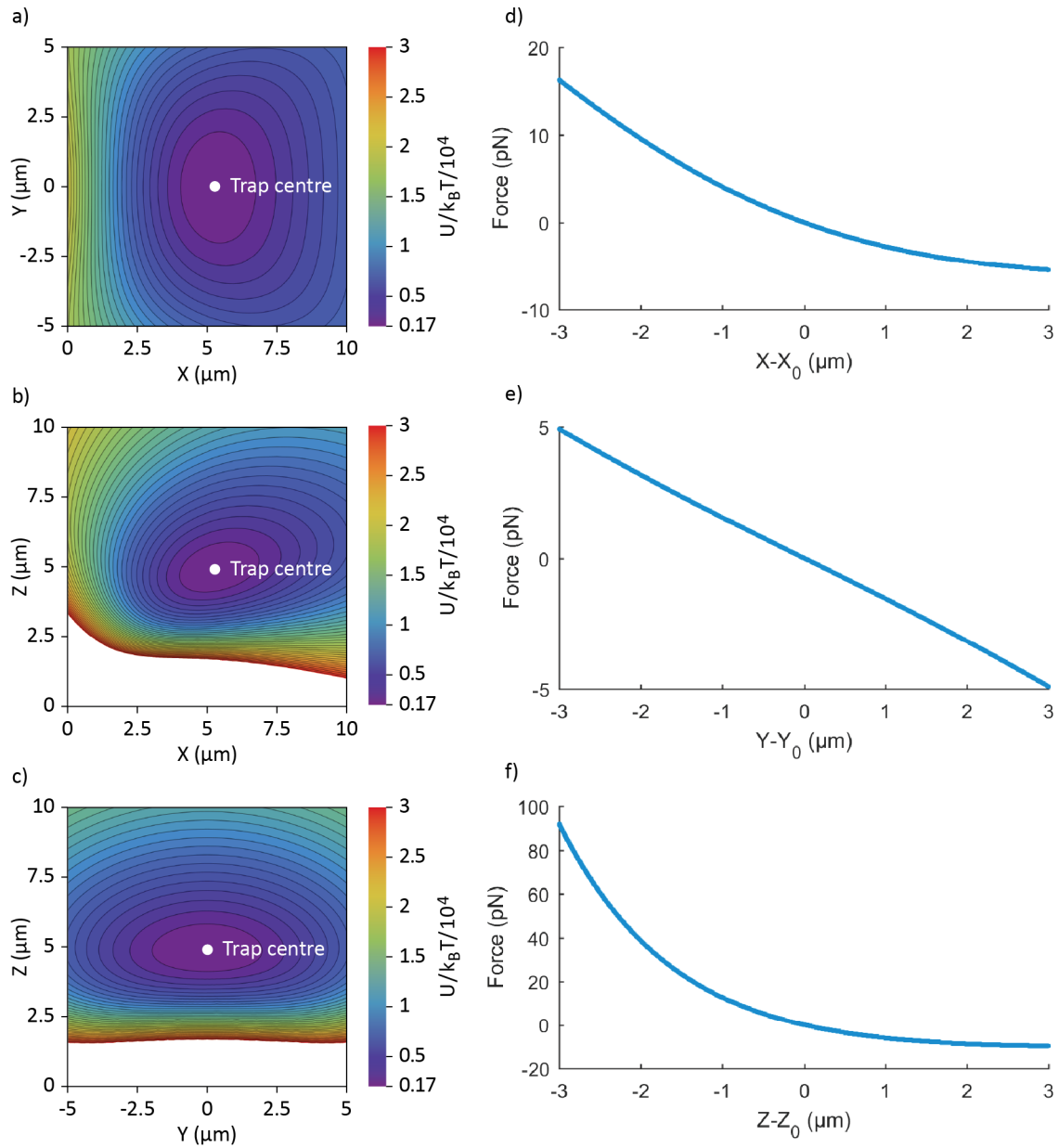
Figure 7.19: Magnetic potential and magnetic force for a HOPG microparticle in a magnetic trap generated by two intersecting current-carrying wires and a bias field $\mathbf{B}_{bias} = 0.11\,\mathrm{T}(1, 0, -1)$. The calculations are made for a HOPG microparticle of volume $72\,\mu\mathrm{m}^3$ in AceWater with its graphene planes aligned perpendicular to the magnetic field direction. The location of the magnetic trap is at $X_0 = 5.3\,\mu\mathrm{m}$, $Y_0 = 0$ and $Z_0 = 4.9\,\mu\mathrm{m}$ (wire surface at $Z = 0$). a-c) Maps of magnetic potential on individual planes: a) X-Y plane at $Z = 4.9\,\mu\mathrm{m}$, b) X-Z plane at $Y = 0$, c) Y-Z plane at $X = 5.3\,\mu\mathrm{m}$. d-f) Magnetic force for displacements from the trap centre on different axes: d) X-axis, e) Y-axis, f) Z-axis.

Table 7.6 presents the trap stiffness values evaluated at the trap centre. Similar to two-dimensional wire traps, we see values that are one order of magnitude larger than those calculated for a permanent magnet trap in Section 7.2.1. This proves that current-carrying wires can generate magnetic traps that are stronger than those generated with permanent magnets. An optimisation of the bias field direction could possibly generate larger trap stiffness values in all three directions. The range in which the force increases linearly with displacement from the trap centre are summarized in Table 7.7. These values are less than the typical sizes of HOPG microparticles in our samples which are 6 μm × 6 μm × 2 μm. Consequently, it is necessary to re-evaluate the magnetic forces along each direction by integrating over the entire particle volume.

Orientation	κ_X pN/μm	κ_Y pN/μm	κ_Z pN/μm
Parallel	0.5	0.2	1.8
Perpendicular	3.4	1.5	8.6

Table 7.6: Trap stiffness along the X, Y and Z directions for a HOPG microparticle of volume 72 μm^3 in AceWater. The particle is in a magnetic trap generated by two intersecting wires with a rectangular cross section and a bias field $\mathbf{B}_{bias} = 0.11 \, T(1, 0, -1)$. Parallel: the graphene planes are aligned parallel to $\mathbf{B}_0$. Perpendicular: the graphene planes are aligned perpendicular to $\mathbf{B}_0$.

Orientation	Range X (μm)	Range Y (μm)	Range Z (μm)
Parallel	±0.2	±1.4	±0.1
Perpendicular	±0.3	±2	±0.2

Table 7.7: Calculated displacement range on the X-, Y- and Z-axes over which the trap stiffness measured at the trap centre changes by at most 10 % for HOPG microparticle of volume 72 μm^3 in AceWater. The magnetic trap is generated by two intersecting current-carrying wires with a rectangular cross section and a bias field $\mathbf{B}_{bias} = 0.11 \, T(1, 0, -1)$. Parallel: the graphene planes are aligned parallel to $\mathbf{B}_0$. Perpendicular: the graphene planes are aligned perpendicular to $\mathbf{B}_0$.

### 7.6.3 Discussion on microfabricated wires for force spectroscopy

In this section, we used simulations to analyse the magnetic trapping of HOPG microparticles (assuming that its magnetic properties are identical to the bulk) in AceWater with current-carrying microfabricated wires. We found that microfabricated wires can generate a magnetic trap with trap stiffness values of order $0.1 - 1\,\mathrm{pN/\mu m}$. These values are at least one order of magnitude larger than the ones measured for two opposing cone-shaped permanent magnets as shown in the first part of this chapter.

To analyse the use of microfabricated wires for force spectroscopy, we evaluated the forces on the HOPG microparticle relative to its distance from the trap centre. We found that the range in which displacements from the trap centre are proportional to the magnetic force is small ($0.1 - 2\,\mathrm{\mu m}$) compared to the typical sizes of our HOPG microparticles ($2 - 10\,\mathrm{\mu m}$). Because of this, the magnetic trapping of HOPG microparticles is possible but the relationship between displacements from the trap centre and the magnetic force could be non-linear. For that reason, the magnetic trap must be re-evaluated with respect to the size of the HOPG microparticles by integrating the magnetic force over the entire particle volume as a function of displacement from the trap centre. This procedure would then allow us to associate particle displacements with the force and to extract the trap stiffness value. In practice, this process may be impractical due to the irregular shapes of our HOPG microparticles. Instead, it may be better to track the particle inside the magnetic trap and analyse the distributions of the particle positions which are directly related the magnetic potential and the force.

An additional aspect for force applications is the limited restoring force on the particle for displacements away from the wires. This property must be included in the experimental design as particles can escape the trap if the forces away from the wires are too large.

To use current-carrying microfabricated wires for magnetic trapping, the heat generation due to the large current densities must be accounted for as this could affect the solution above the wires and/or eventually break the thin wires. This is in particular relevant for biological applications since the heat development could influence the functionality of the studied system. To address this issue, the wires would ideally be patterned on an electrically insulating material with high thermal conductivity to dissipate the heat downwards as illustrated in Figure 7.20. One potential material that could fulfil this requirement is aluminium nitrate [122]. Such a wire chip could then be attached to a block of copper which serves as a heat reservoir. On top of the wires, an electrically insulating layer must be applied in order to avoid electro-chemical effects at the wire-solution interface. Such a layer needs to be as thin as possible because strong magnetic traps can only be generated close to the wire surface.
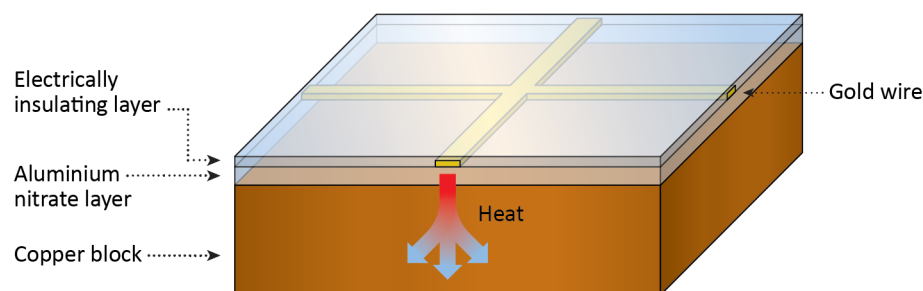
Figure 7.20: Illustration of a potential method to dissipate the heat in current-carrying wires away from the sample region. The wires are fabricated on aluminium nitrate which is electrically insulating and has a high thermal conductivity. This layer is mounted on top of a copper block that acts as a heat reservoir. The experiments are conducted in solution on top of the wires. This makes it necessary to coat the wires with an electrically insulating layer to prevent electro-chemical reactions at the wire-solution interface.

7.7   Conclusion

In this chapter, we investigated the three-dimensional magnetic trapping of graphitic microparticles in a diamagnetic solution with static magnetic fields. We analysed the magnetic trapping with permanent magnets and with current-carrying microfabricated wires. In each part, we provided the theoretical framework for magnetic trapping and showed clear evidences that graphitic microparticles in solution can be trapped with static magnetic fields.

One of the key results of this chapter is the first experimental demonstration of magnetic trapping of an individual graphitic microparticle in a diamagnetic solution with a static magnetic field. This result is interesting with respect to our results in Chapter 5 where we showed that HOPG microparticles in solution can be rotated with an AC electric field. Therefore, we can integrate this principle into our magnetic trapping setup which could lead to the first integrated trapping system that is capable of confining the linear and rotational motion of a microparticle in solution. The particles could be used as a transducer to measure and apply forces and torques simultaneously on a microscopic system of interest (e.g. a cell). This shows that graphitic microparticles with anisotropic electrical and magnetic properties can be used for novel force and torque applications.

Chapter 8

Summary and conclusion

In this thesis, we presented the first study on the manipulation of diamagnetic graphitic microparticles in solution with AC electric fields and static magnetic fields. The particle manipulation experiments were conducted with microparticles made from HOPG which we chose as a representative graphitic material. We focussed on contactless particle manipulation methods that allow the control of the particle position and orientation in solution. Accordingly, we designed three distinct experiments: the orientation and rotational trapping of HOPG microparticles with a horizontal AC electric field and a vertical static magnetic field; the magnetophoretic transport of HOPG microparticles with static magnetic fields and, lastly, the three-dimensional particle trapping of HOPG microparticles with static magnetic fields. To the best of our knowledge, this is the first time that the manipulation of individual graphitic microparticles in solution has been researched.

In Chapter 5, we took advantage of the anisotropic electrical and magnetic properties of HOPG to manipulate the orientation of lipid-coated HOPG microparticles in solution. We showed that the graphene planes in HOPG align in the direction of the orientating field (electric or magnetic). This makes it possible to rotationally trap HOPG microparticles on any plane spanned by an AC electric field and a static magnetic field. The orientational confinement was used to study the electrical alignment of HOPG microparticles as a function of the electric field frequency. For this purpose, we aligned the graphene planes of the particle vertically with a static magnetic field and then additionally applied a horizontal AC electric field. The combination of the two fields confined the particle planes to a vertical plane, which allowed us to monitor the particle orientation with an upright microscope. Our experiment reveals that the lipid-layer on HOPG microparticles has a substantial influence on the particle alignment to the AC electric field. At low electric field frequencies ($< 10\,\text{MHz}$), we observed no particle alignment as the lipid layer effectively isolates the HOPG core from the external field. As

the electric field frequency increases, particle alignment can be observed. Since this is a characteristic behaviour caused by the lipid layer, it can serve as a criteria to distinguish lipid-coated HOPG microparticles from uncoated ones. We also analysed the orientational random fluctuations of rotationally trapped lipid-coated HOPG microparticles to measure the strength of the rotational trap and the maximum electric torque that can be applied on the particle. In the electric frequency range between $10 - 70\,\mathrm{MHz}$, the largest electric rotational trap stiffness and electric torque were $3.3 \times 10^{-18}\,\mathrm{Nm/rad}$ and $1.7 \times 10^{-18}\,\mathrm{Nm}$, respectively. This is in particular attractive for applications in biology as lipid-coated microparticles can be used as a transducer to measure and apply torques on biomolecules which are typically in the range $0.01 - 1 \times 10^{-18}\,\mathrm{Nm}$.

In Chapter 6, we focussed on the magnetophoretic transport of HOPG microparticles in a diamagnetic solution. For that purpose, we built a setup with two permanent magnets and two magnetic steel wedges to generate a strong magnetic field with a large field gradient. In the experiment, we showed that HOPG microparticles can be moved along a straight line over hundreds of micrometres with transport velocities of up to $10\,\mathrm{\mu m/s}$. We also studied the magnetophoretic transport of HOPG microparticles with respect to the application of lipid coatings, the mosaic spread in the particle and the sonication time that was used in the particle-fabrication protocol. By comparing the measured magnetophoretic velocities between the different samples, we found that HOPG microparticles tend to move slower with increasing sonication time. To explain this, we looked into two potential explanations: first, the increase in the hydrodynamic drag due to sonication-induced surface roughness; and second, the change in the magnetic properties due to sonication-induced defects in HOPG. In subsequent measurements of the HOPG microparticles with a Raman spectrometer and a SQUID, we found evidence that both sonication-induced changes are present in the HOPG microparticles. However, based on our measurements with SQUID, the magnetic contribution of sonication-induced defects is likely to be negligible.

In Chapter 7, we investigated the two- and three-dimensional magnetic trapping of HOPG microparticles in a diamagnetic solution with static magnetic fields. We addressed the magnetic trapping with permanent magnets and current-carrying wires separately. In the first part, we generated a magnetic trap with two opposing cone-shaped NdFeB magnets that have the same magnetic poles at their tips. We used polystyrene beads in a $0.6\,\mathrm{M}$ $MnCl_2$ aqueous solution to measure the magnetic trap stiffness of the magnetic trap for different distances between the cone tips. Furthermore, we demonstrated that the addition of steel cones to the magnetic field can enhance the trap stiffness by at least a factor of two. From our measurements we found a trap stiffness of order $10^{-3} - 10^{-2}\,\mathrm{pN/\mu m}$. We showed clear evidence that factory-

made graphite powder microparticles can be trapped with our setup as opposed to HOPG microparticles fabricated by means of sonication.

In the second part of Chapter 7, we used simulations to evaluate the potential use of current-carrying microfabricated wires for magnetic trapping of HOPG microparticles in solution. In comparison to magnetic traps generated with permanent magnets, the use of current-carrying microfabricated wires has the huge advantage that the magnetic trap can be turned on and off. We considered wires with rectangular cross section (5 µm × 5 µm) and a current density of $1.2 \times 10^{-7} \, \text{A/cm}^2$. The magnetic field minimum was generated by superimposing the magnetic field of the current-carrying wires with a constant unidirectional magnetic field, i.e. a bias field. We showed evidence that two- or three-dimensional trapping can be achieved with a single wire or two wires intersecting at a right angle, respectively. Our evaluation showed that the combination of current-carrying wires and a bias field generates a magnetic field suitable for magnetic trapping of HOPG microparticles in solution. The calculated magnetic trap stiffness values of the wire trap were one order of magnitude larger than the ones calculated for permanent magnet traps. Therefore, current-carrying microfabricated wires can generate stronger magnetic fields that can potentially trap smaller particles in solution. This is in particular interesting for biomedical applications where three-dimensional magnetic trapping with static magnetic fields can lead towards the development of novel three-dimensional force sensing techniques. Interestingly, the combination with HOPG microparticles adds the capability to apply and sense torques with AC electric fields because of its anisotropic electrical properties. Such a combination would lead to a unique technique that is capable of applying or measuring forces and torques, simultaneously. This shows that three-dimensional magnetic trapping with current-carrying wires has a huge potential that is worth pursuing in the future. To enable its application to biological experiments, the heat generation in the wires, that comes with the use of high current densities, has to be addressed. A potential solution to this would involve the use of materials that divert the heat towards a heat reservoir and thus, prevent heat transfer with the solution.

In conclusion, we demonstrated throughout this thesis that HOPG microparticles can be manipulated in solution by using AC electric fields and static magnetic fields. The developed techniques and results gained from our research show that the electrical and magnetic properties of graphitic materials offer unique opportunities for versatile particle manipulation. This opens up novel application prospects for graphitic microparticles in a broad number of research fields, including material and electrical engineering, and especially in the biomedical research on living systems.

Acknowledgements

 First of all, I would like to express my deepest gratitude to my supervisor, Dr. Isabel Llorente-García, for her guidance, engagement and infinite patience throughout this journey. I thank my second supervisor Prof. Phil Jones for his support and expertise throughout the years. Furthermore, I thank Prof. Sonia Contera for allowing me to use her lab, Dr. Laura Bovo and Dr. Chris Howard for their expertise and especially Prof. Tania Monteiro and Dr. Carla Figueira de Morisson Faria for their help in the hottest phase of my PhD. Special thanks go to the MVPs in the entire physics department, Rafid Jawad and John Dumper, who did exceptional work for my experiments.

The materialisation of this thesis would not be as enjoyable without the many people I met throughout the years. From the Llorente-García crew, I thank Dario for his expertise at times when the laws of physics turned against me and for being passionate enough to hunt for seafood at three in the morning (one day, that lobster will be ours!), Johannes for being a good friend and my happy pill when I needed it. To the original office boys Chris, Tom, Nick and Tom Selleck: Best of luck to all of you! Of course, the existence of this page would not be justified if I would not honor my moderate gang and friends: Michela Adventurelli, Chris Perrmeister, Raffa, Oxford Johnson, Robi, OMG-Ilhan, Luca (thanks for all the spare parts), Pik and family, plasma-woman Alice, Elly, Lia, Dr. Alexandros Gerakis. Special thanks goes to Advait for his generosity in the first weeks, Alex Honor Harris for brightening up the day (I mentioned you in my acknowledgements...do I get four Serrano Hams now?) and Maggy because I can.

From the family side, I thank Pe for her support and professional coaching leading to the start of this long journey, my supportive mami for believing in me, Dr. Tobi for his encouragement from the continent and Leon for his Linsensuppe.

As we are approaching slightly slower towards the end, I thank my girlfriend/fiance Nori for allowing me to stay for free in my entitled flat. This work would not be possible without her endless support, crisis management and expertise. Your spaghetti vongole are not slimy.

♔

Bibliography

[1] R. W. Cole, T. Jinadasa, and C. M. Brown, "Measuring and interpreting point spread functions to determine confocal microscope resolution and ensure quality control," *Nature Protocols*, vol. 6, pp. 1929–1941, nov 2011.

[2] R. Shinar, G. Liu, and M. D. Porter, "Graphite Microparticles as Coatings for Quartz Crystal Microbalance-Based Gas Sensors," *Analytical Chemistry*, vol. 72, pp. 5981–5987, dec 2000.

[3] D. Cosgrove, "Ultrasound contrast agents: An overview," *European Journal of Radiology*, vol. 60, no. 3, pp. 324–330, 2006.

[4] C. C. Ahrens, Z. Dong, and W. Li, "Engineering cell aggregates through incorporated polymeric microparticles," *Acta Biomaterialia*, vol. 62, pp. 64–81, oct 2017.

[5] D. S. Kohane, "Microparticles and nanoparticles for drug delivery," *Biotechnology and Bioengineering*, vol. 96, pp. 203–209, feb 2007.

[6] R. L. Macdonald, "Nanoparticles and Microparticles," *Neurosurgery*, vol. 62, pp. 152–159, aug 2015.

[7] J. R. Moffitt, Y. R. Chemla, S. B. Smith, and C. Bustamante, "Recent Advances in Optical Tweezers," *Annual Review of Biochemistry*, vol. 77, pp. 205–228, jun 2008.

[8] R. Sengupta, M. Bhattacharya, S. Bandyopadhyay, and A. K. Bhowmick, "A review on the mechanical and electrical properties of graphite and modified graphite reinforced polymer composites," *Progress in Polymer Science*, vol. 36, pp. 638–670, may 2011.

[9] A. Yasmin and I. M. Daniel, "Mechanical and thermal properties of graphite platelet/epoxy composites," *Polymer*, vol. 45, pp. 8211–8219, nov 2004.

[10] D. Ponnamma, Q. Guo, I. Krupa, M. A. S. A. Al-Maadeed, V. K. T., S. Thomas, and K. K. Sadasivuni, "Graphene and graphitic derivative filled polymer composites as

potential sensors," *Physical Chemistry Chemical Physics*, vol. 17, no. 6, pp. 3954–3981, 2015.

[11] R. Narayan, J. E. Kim, J. Y. Kim, K. E. Lee, and S. O. Kim, "Graphene Oxide Liquid Crystals: Discovery, Evolution and Applications," *Advanced Materials*, vol. 28, pp. 3045–3068, apr 2016.

[12] T.-Z. Shen, S.-H. Hong, and J.-K. Song, "Electro-optical switching of graphene oxide liquid crystals with an extremely large Kerr coefficient," *Nature Materials*, vol. 13, pp. 394–399, mar 2014.

[13] C. Niu, F. Lin, Z. M. Wang, J. Bao, and J. Hu, "Graphene levitation and orientation control using a magnetic field," *Journal of Applied Physics*, vol. 123, p. 044302, jan 2018.

[14] J. Billaud, F. Bouville, T. Magrini, C. Villevieille, and A. R. Studart, "Magnetically aligned graphite electrodes for high-rate performance Li-ion batteries," *Nature Energy*, vol. 1, p. 16097, jul 2016.

[15] S. Wang, K. V. Kravchyk, F. Krumeich, and M. V. Kovalenko, "Kish Graphite Flakes as a Cathode Material for an Aluminum Chloride–Graphite Battery," *ACS Applied Materials & Interfaces*, vol. 9, pp. 28478–28485, aug 2017.

[16] M. Pumera, "Graphene in biosensing," *Materials Today*, vol. 14, pp. 308–315, jul 2011.

[17] A. Servant, A. Bianco, M. Prato, and K. Kostarelos, "Graphene for multi-functional synthetic biology: The last 'zeitgeist' in nanomedicine," *Bioorganic & Medicinal Chemistry Letters*, vol. 24, pp. 1638–1649, apr 2014.

[18] X. Sun, Z. Liu, K. Welsher, J. T. Robinson, A. Goodwin, S. Zaric, and H. Dai, "Nano-graphene oxide for cellular imaging and drug delivery," *Nano Research*, vol. 1, pp. 203–212, sep 2008.

[19] J. Liu, L. Cui, and D. Losic, "Graphene and graphene oxide as new nanocarriers for drug delivery applications," *Acta Biomaterialia*, vol. 9, pp. 9243–9257, dec 2013.

[20] H. S. Jung, W. H. Kong, D. K. Sung, M.-Y. Lee, S. E. Beack, D. H. Keum, K. S. Kim, S. H. Yun, and S. K. Hahn, "Nanographene Oxide–Hyaluronic Acid Conjugate for Photothermal Ablation Therapy of Skin Cancer," *ACS Nano*, vol. 8, pp. 260–268, jan 2014.

[21] K. A. Vincent, X. Li, C. F. Blanford, N. A. Belsey, J. H. Weiner, and F. A. Armstrong, "Enzymatic catalysis on conducting graphite particles," *Nature Chemical Biology*, vol. 3, pp. 761–762, dec 2007.

[22] Y. Yoshimi, Y. Yagisawa, R. Yamaguchi, and M. Seki, "Blood heparin sensor made from a paste electrode of graphite particles grafted with molecularly imprinted polymer," *Sensors and Actuators B: Chemical*, vol. 259, pp. 455–462, apr 2018.

[23] G. E. Jellison, J. D. Hunn, and H. N. Lee, "Measurement of optical functions of highly oriented pyrolytic graphite in the visible," *Physical Review B*, vol. 76, p. 085125, aug 2007.

[24] K. Matsubara, K. Sugihara, and T. Tsuzuku, "Electrical resistance in the c direction of graphite," *Physical Review B*, vol. 41, pp. 969–974, jan 1990.

[25] J. Heremans, C. H. Olk, and D. T. Morelli, "Magnetic susceptibility of carbon structures," *Physical Review B*, vol. 49, pp. 15122–15125, jun 1994.

[26] M. D. Simon, L. O. Heflinger, and A. K. Geim, "Diamagnetically stabilized magnet levitation," *American Journal of Physics*, vol. 69, p. 702, 2001.

[27] P. Esquinazi and R. Höhne, "Magnetism in carbon structures," *Journal of Magnetism and Magnetic Materials*, vol. 290-291, pp. 20–27, apr 2005.

[28] M. Sepioni, R. R. Nair, S. Rablen, J. Narayanan, F. Tuna, R. Winpenny, A. K. Geim, and I. V. Grigorieva, "Limits on intrinsic magnetism in graphene," *Physical Review Letters*, vol. 105, no. 20, pp. 1–4, 2010.

[29] H. O. Pierson, *Handbook of Carbon, Graphite, Diamonds and Fullerenes*. 1993.

[30] A. V. Titov, P. Král, and R. Pearson, "Sandwiched graphene-membrane superstructures," *ACS Nano*, vol. 4, pp. 229–234, jan 2010.

[31] R. Frost, G. E. Jönsson, D. Chakarov, S. Svedhem, and B. Kasemo, "Graphene Oxide and Lipid Membranes: Interactions and Nanocomposite Structures," *Nano Letters*, vol. 12, pp. 3356–3362, jul 2012.

[32] Y. Okamoto, T. Motegi, S. Iwasa, A. Sandhu, and R. Tero, "Fluidity evaluation of cell membrane model formed on graphene oxide with single particle tracking using quantum dot," *Japanese Journal of Applied Physics*, vol. 54, p. 04DL09, apr 2015.

[33] J. Liu, S. Guo, L. Han, T. Wang, W. Hong, Y. Liu, and E. Wang, "Synthesis of phospholipid monolayer membrane functionalized graphene for drug delivery," *Journal of Materials Chemistry*, vol. 22, no. 38, p. 20634, 2012.

[34] M. Sepioni, *Magnetic properties of graphene*. PhD thesis, University of Manchester, 2013.

[35] Y. Nonomura, Y. Morita, S. Deguchi, and S.-a. Mukai, "Anomalously stable dispersions of graphite in water/acetone mixtures," *Journal of Colloid and Interface Science*, vol. 346, pp. 96–99, jun 2010.

[36] J. Nguyen, J. G. Underwood, and I. Llorente García, "Orienting lipid-coated graphitic micro-particles in solution using AC electric fields: A new theoretical dual-ellipsoid Laplace model for electro-orientation," *Colloids and Surfaces A: Physicochemical and Engineering Aspects*, vol. 549, pp. 237–251, jul 2018.

[37] T. B. Jones, *Electromechanics of Particles*. Cambridge: Cambridge University Press, 1995.

[38] J. D. Jackson, *Classical Electrodynamics*. 3rd ed., 1998.

[39] V. Knecht, B. Klasczyk, and R. Dimova, "Macro- versus Microscopic View on the Electrokinetics of a Water–Membrane Interface," *Langmuir*, vol. 29, pp. 7939–7948, jun 2013.

[40] V. Sukhorukov and U. Zimmermann, "Electrorotation of Erythrocytes Treated with Dipicrylamine: Mobile Charges within the Membrane Show their "Signature' in Rotational Spectra," *Journal of Membrane Biology*, vol. 153, pp. 161–169, sep 1996.

[41] K. Asami, T. Hanai, and N. Koizumi, "Dielectric Approach to Suspensions of Ellipsoidal Particles Covered with a Shell in Particular Reference to Biological Cells," *Japanese Journal of Applied Physics*, vol. 19, pp. 359–365, feb 1980.

[42] M. Azanza, B. Blott, A. del Moral, and M. Peg, "Measurement of the red blood cell membrane magnetic susceptibility," *Bioelectrochemistry and Bioenergetics*, vol. 30, pp. 43–53, mar 1993.

[43] N. Otsu, "A Threshold Selection Method from Gray-Level Histograms," *IEEE Transactions on Systems, Man, and Cybernetics*, vol. 9, pp. 62–66, jan 1979.

[44] Q. Liang, X. Yao, W. Wang, Y. Liu, and C. P. Wong, "A Three-Dimensional Vertically Aligned Functionalized Multilayer Graphene Architecture: An Approach for Graphene-Based Thermal Interfacial Materials," *ACS Nano*, vol. 5, pp. 2392–2401, mar 2011.

[45] R. M. Erb, R. Libanori, N. Rothfuchs, and A. R. Studart, "Composites Reinforced in Three Dimensions by Using Low Magnetic Fields," *Science*, vol. 335, pp. 199–204, jan 2012.

[46] L. Wu, M. Ohtani, M. Takata, A. Saeki, S. Seki, Y. Ishida, and T. Aida, "Magnetically Induced Anisotropic Orientation of Graphene Oxide Locked by in Situ Hydrogelation," *ACS Nano*, vol. 8, pp. 4640–4649, may 2014.

[47] J. E. Kim, T. H. Han, S. H. Lee, J. Y. Kim, C. W. Ahn, J. M. Yun, and S. O. Kim, "Graphene Oxide Liquid Crystals," *Angewandte Chemie International Edition*, vol. 50, pp. 3043–3047, mar 2011.

[48] W. Tie, S. S. Bhattacharyya, Y. J. Lim, S. W. Lee, T. H. Lee, Y. H. Lee, and S. H. Lee, "Dynamic electro-optic response of graphene/graphitic flakes in nematic liquid crystals," *Optics Express*, vol. 21, p. 19867, aug 2013.

[49] R. Basu, D. Kinnamon, and A. Garvey, "Nano-electromechanical rotation of graphene and giant enhancement in dielectric anisotropy in a liquid crystal," *Applied Physics Letters*, vol. 106, p. 201909, may 2015.

[50] M. Sung, K. Hattori, and S. Asai, "Crystal alignment of graphite as a negative electrode material of the lithium-ion secondary batteries," *Materials & Design*, vol. 30, pp. 387–390, feb 2009.

[51] S. C. Youn, D. W. Kim, S. B. Yang, H. M. Cho, J. H. Lee, and H.-T. Jung, "Vertical alignment of reduced graphene oxide/Fe-oxide hybrids using the magneto-evaporation method," *Chemical Communications*, vol. 47, no. 18, p. 5211, 2011.

[52] H. Chihara, C. Uyeda, A. Tsuchiyama, and T. Yamanaka, "The Magnetic Ordering of Graphite Grains and an Experimental Application to Grain Alignment," *Publications of the Astronomical Society of Japan*, vol. 50, pp. 149–154, feb 1998.

[53] P. Jones, O. Marago, and G. Volpe, *Optical Tweezers*. Cambridge: Cambridge University Press, 2015.

[54] A. Peyman, C. Gabriel, and E. Grant, "Complex permittivity of sodium chloride solutions at microwave frequencies," *Bioelectromagnetics*, vol. 28, pp. 264–274, may 2007.

[55] R. A. Chipman, *Transmission Lines*. McGraw-Hill, 1 ed., 1968.

[56] J. Nguyen, S. Contera, and I. Llorente García, "Magneto-electrical orientation of lipid-coated graphitic micro-particles in solution," *RSC Advances*, vol. 6, no. 52, pp. 46643–46653, 2016.

[57] F. Perrin, "Mouvement brownien d'un ellipsoide - I. Dispersion diélectrique pour des molécules ellipsoidales," *Journal de Physique et le Radium*, vol. 5, pp. 497–511, 1934.

[58] M. C. Wang and G. E. Uhlenbeck, "On the Theory of the Brownian Motion II," *Rev. Mod. Phys.*, vol. 17, pp. 323–342, apr 1945.

[59] H. Qian, M. Sheetz, and E. Elson, "Single particle tracking. Analysis of diffusion and flow in two-dimensional systems," *Biophysical Journal*, vol. 60, pp. 910–921, oct 1991.

[60] N. D. Winblade, H. Schmökel, M. Baumann, A. S. Hoffman, and J. A. Hubbell, "Sterically blocking adhesion of cells to biological surfaces with a surface-active copolymer containing poly(ethylene glycol) and phenylboronic acid," *Journal of Biomedical Materials Research*, vol. 59, pp. 618–631, mar 2002.

[61] A. Palanisami and T. Okamoto, "Torque-Induced Slip of the Rotary Motor F 1 -ATPase," *Nano Letters*, vol. 10, pp. 4146–4149, oct 2010.

[62] J. Lipfert, M. M. van Oene, M. Lee, F. Pedaci, and N. H. Dekker, "Torque Spectroscopy for the Study of Rotary Motion in Biological Systems," *Chemical Reviews*, vol. 115, pp. 1449–1474, feb 2015.

[63] M. M. van Oene, L. E. Dickinson, F. Pedaci, M. Köber, D. Dulin, J. Lipfert, and N. H. Dekker, "Biological Magnetometry: Torque on Superparamagnetic Beads in Magnetic Fields," *Physical Review Letters*, vol. 114, p. 218301, may 2015.

[64] J. Lipfert, J. W. J. Kerssemakers, T. Jager, and N. H. Dekker, "Magnetic torque tweezers: measuring torsional stiffness in DNA and RecA-DNA filaments," *Nature Methods*, vol. 7, pp. 977–980, dec 2010.

[65] N. Pamme and C. Wilhelm, "Continuous sorting of magnetic cells via on-chip free-flow magnetophoresis," *Lab on a Chip*, vol. 6, no. 8, p. 974, 2006.

[66] M. D. Tarn, N. Hirota, A. Iles, and N. Pamme, "On-chip diamagnetic repulsion in continuous flow," *Science and Technology of Advanced Materials*, vol. 10, p. 014611, jan 2009.

[67] S. A. Peyman, E. Y. Kwan, O. Margarson, A. Iles, and N. Pamme, "Diamagnetic repulsion—A versatile tool for label-free particle handling in microfluidic devices," *Journal of Chromatography A*, vol. 1216, pp. 9055–9062, dec 2009.

[68] C. Phurimsak, E. Yildirim, M. D. Tarn, S. J. Trietsch, T. Hankemeier, N. Pamme, and P. Vulto, "Phaseguide assisted liquid lamination for magnetic particle-based assays," *Lab on a Chip*, vol. 14, no. 13, p. 2334, 2014.

[69] M. Karle, J. Miwa, G. Czilwik, V. Auwärter, G. Roth, R. Zengerle, and F. von Stetten, "Continuous microfluidic DNA extraction using phase-transfer magnetophoresis," *Lab on a Chip*, vol. 10, no. 23, p. 3284, 2010.

[70] L. A. Sasso, A. Ündar, and J. D. Zahn, "Autonomous magnetically actuated continuous flow microimmunofluorocytometry assay," *Microfluidics and Nanofluidics*, vol. 9, pp. 253–265, aug 2010.

[71] T. Schneider, S. Karl, L. R. Moore, J. J. Chalmers, P. S. Williams, and M. Zborowski, "Sequential CD34 cell fractionation by magnetophoresis in a magnetic dipole flow sorter," *The Analyst*, vol. 135, no. 1, pp. 62–70, 2010.

[72] M. D. Tarn, L. T. Elders, S. A. Peyman, and N. Pamme, "Diamagnetic repulsion of particles for multilaminar flow assays," *RSC Adv.*, vol. 5, no. 126, pp. 103776–103781, 2015.

[73] D. Robert, N. Pamme, H. Conjeaud, F. Gazeau, A. Iles, and C. Wilhelm, "Cell sorting by endocytotic capacity in a microfluidic magnetophoresis device," *Lab on a Chip*, vol. 11, no. 11, p. 1902, 2011.

[74] J. García-Alonso, R. F. Fakhrullin, V. N. Paunov, Z. Shen, J. D. Hardege, N. Pamme, S. J. Haswell, and G. M. Greenway, "Microscreening toxicity system based on living magnetic yeast and gradient chips," *Analytical and Bioanalytical Chemistry*, vol. 400, pp. 1009–1013, may 2011.

[75] P. Liu, X. Li, S. A. Greenspoon, J. R. Scherer, and R. A. Mathies, "Integrated DNA purification, PCR, sample cleanup, and capillary electrophoresis microchip for forensic human identification," *Lab on a Chip*, vol. 11, no. 6, p. 1041, 2011.

[76] A. J. Hopwood, C. Hurth, J. Yang, Z. Cai, N. Moran, J. G. Lee-Edghill, A. Nordquist, R. Lenigk, M. D. Estes, J. P. Haley, C. R. McAlister, X. Chen, C. Brooks, S. Smith, K. Elliott, P. Koumi, F. Zenhausern, and G. Tully, "Integrated Microfluidic System for

Rapid Forensic DNA Analysis: Sample Collection to DNA Profile," *Analytical Chemistry*, vol. 82, pp. 6991–6999, aug 2010.

[77] B. E. Rapp, *Microfluidics: Modelling, Mechanics and Mathematics*. Elsevier, 1st ed., 2017.

[78] F. Perrin, "Mouvement Brownien d'un ellipsoide (II). Rotation libre et dépolarisation des fluorescences. Translation et diffusion de molécules ellipsoidales," 1936.

[79] P. Elleaume, O. Chubar, and J. Chavanne, "Computing 3D magnetic fields from insertion devices," in *Proceedings of the 1997 Particle Accelerator Conference (Cat. No.97CH36167)*, vol. 3, pp. 3509–3511, IEEE.

[80] "www.kayelaby.npl.co.uk."

[81] J. Kestin, M. Sokolov, and W. a. Wakeham, "Viscosity of liquid water in the range of -8C to 150C," 1978.

[82] K. Noda, M. Ohashi, and K. Ishida, "Viscosities and densities at 298.15 K for mixtures of methanol, acetone, and water," *Journal of Chemical & Engineering Data*, vol. 27, pp. 326–328, jul 1982.

[83] W. R. Angus and D. V. Tilston, "Magnetochemical investigations. Part V. The diamagnetism of binary liquid mixtures," *Transactions of the Faraday Society*, vol. 43, p. 221, 1947.

[84] M. Zborowski, *Magnetic Cell Separation*, vol. 32. 2007.

[85] "www.wilmad-labglass.com."

[86] A. W. Smith and A. W. Smith, "Magnetic susceptibility of mixtures of liquids," *Journal of the American Chemical Society*, vol. 40, pp. 1218–1224, aug 1918.

[87] J. Happel and H. Brenner, *Low Reynolds number hydrodynamics*, vol. 1 of *Mechanics of fluids and transport processes*. Dordrecht: Springer Netherlands, 1981.

[88] M.-U. Kim, K. W. Kim, Y.-H. Cho, and B. M. Kwak, "Hydrodynamic force on a plate near the plane wall. Part I: plate in sliding motion," *Fluid Dynamics Research*, vol. 29, pp. 137–170, sep 2001.

[89] V. Knecht, B. Klasczyk, and R. Dimova, "Macro- versus Microscopic View on the Electrokinetics of a Water–Membrane Interface," *Langmuir*, vol. 29, pp. 7939–7948, jun 2013.

[90] T. Y. Wu, N. Guo, C. Y. Teh, and J. X. W. Hay, "Theory and Fundamentals of Ultrasound," pp. 5–12, 2013.

[91] Z. Y. Xia, S. Pezzini, E. Treossi, G. Giambastiani, F. Corticelli, V. Morandi, A. Zanelli, V. Bellani, and V. Palermo, "The Exfoliation of Graphene in Liquids by Electrochemical, Chemical, and Sonication-Assisted Techniques: A Nanoscale Study," *Advanced Functional Materials*, vol. 23, no. 37, pp. 4684–4693, 2013.

[92] O. V. Yazyev and L. Helm, "Defect-induced magnetism in graphene," *Physical Review B*, vol. 75, p. 125408, mar 2007.

[93] R. Singh and P. Kroll, "Magnetism in graphene due to single-atom defects: dependence on the concentration and packing geometry of defects," *Journal of Physics: Condensed Matter*, vol. 21, p. 196002, may 2009.

[94] O. V. Yazyev, "Emergence of magnetism in graphene materials and nanostructures," *Reports on Progress in Physics*, vol. 73, p. 056501, may 2010.

[95] R. R. Nair, M. Sepioni, I.-L. Tsai, O. Lehtinen, J. Keinonen, a. V. Krasheninnikov, T. Thomson, a. K. Geim, and I. V. Grigorieva, "Spin-half paramagnetism in graphene induced by point defects," *Nature Physics*, vol. 8, no. 3, pp. 199–202, 2012.

[96] A. Milev, D. M. a. S. Dissanayake, G. S. K. Kannangara, and a. R. Kumarasinghe, "Defect induced electronic states and magnetism in ball-milled graphite.," *Physical chemistry chemical physics : PCCP*, vol. 15, no. 38, pp. 16294–302, 2013.

[97] F. Tuinstra, "Raman Spectrum of Graphite," *The Journal of Chemical Physics*, vol. 53, no. 3, p. 1126, 1970.

[98] A. C. Ferrari, "Raman spectroscopy of graphene and graphite: Disorder, electron–phonon coupling, doping and nonadiabatic effects," *Solid State Communications*, vol. 143, pp. 47–57, jul 2007.

[99] P. Tan, Y. Deng, and Q. Zhao, "Temperature-dependent Raman spectra and anomalous Raman phenomenon of highly oriented pyrolytic graphite," *Physical Review B*, vol. 58, pp. 5435–5439, sep 1998.

[100] L. G. Cancado, A. Jorio, E. H. M. Ferreira, F. Stavale, C. A. Achete, R. B. Capaz, M. V. O. Moutinho, A. Lombardo, T. S. Kulmala, and A. C. Ferrari, "Quantifying Defects in Graphene via Raman Spectroscopy at Different Excitation Energies," *Nano Letters*, vol. 11, pp. 3190–3196, aug 2011.

[101] M. Getzlaff, *Fundamentals of Magnetism*. Berlin, Heidelberg: Springer Berlin Heidelberg, 2006.

[102] H. Watarai and M. Namba, "Capillary magnetophoresis of human blood cells and their magnetophoretic trapping in a flow system," *Journal of Chromatography A*, vol. 961, no. 1, pp. 3–8, 2002.

[103] C.-H. Chen, K. M. Reddy, and N. P. Padture, "Site-specific stamping of graphene micro-patterns over large areas using flexible stamps," *Nanotechnology*, vol. 23, p. 235603, jun 2012.

[104] J. N. Lee, C. Park, and G. M. Whitesides, "Solvent Compatibility of Poly(dimethylsiloxane)-Based Microfluidic Devices," *Analytical Chemistry*, vol. 75, pp. 6544–6554, dec 2003.

[105] Y. Liu, D. Cheng, G. Sonek, M. Berns, C. Chapman, and B. Tromberg, "Evidence for localized cell heating induced by infrared optical tweezers," *Biophysical Journal*, vol. 68, pp. 2137–2144, may 1995.

[106] E. J. Peterman, F. Gittes, and C. F. Schmidt, "Laser-Induced Heating in Optical Traps," *Biophysical Journal*, vol. 84, pp. 1308–1316, feb 2003.

[107] J. Miyakoshi, "The review of cellular effects of a static magnetic field," *Science and Technology of Advanced Materials*, vol. 7, pp. 305–307, jan 2006.

[108] S. Smith, L. Finzi, and C. Bustamante, "Direct mechanical measurements of the elasticity of single DNA molecules by using magnetic beads," *Science*, vol. 258, no. 5085, pp. 1122–1126, 1992.

[109] A. Winkleman, K. L. Gudiksen, D. Ryan, G. M. Whitesides, D. Greenfield, and M. Prentiss, "A magnetic trap for living cells suspended in a paramagnetic buffer," *Applied Physics Letters*, vol. 85, pp. 2411–2413, sep 2004.

[110] J. V. I. Timonen, A. F. Demirörs, and B. A. Grzybowski, "Magnetofluidic Tweezing of Nonmagnetic Colloids," *Advanced Materials*, vol. 28, pp. 3453–3459, may 2016.

[111] I. Sbalzarini and P. Koumoutsakos, "Feature point tracking and trajectory analysis for video imaging in cell biology," *Journal of Structural Biology*, vol. 151, pp. 182–195, aug 2005.

[112] F. Gittes and C. F. Schmidt, "Interference model for back-focal-plane displacement detection in optical tweezers," *Optics Letters*, vol. 23, p. 7, jan 1998.

[113] C. Gosse and V. Croquette, "Magnetic Tweezers: Micromanipulation and Force Measurement at the Molecular Level," *Biophysical Journal*, vol. 82, pp. 3314–3329, jun 2002.

[114] A. M. R. Kabir, D. Inoue, Y. Kishimoto, J.-i. Hotta, K. Sasaki, N. Kitamura, J. P. Gong, H. Mayama, and A. Kakugo, "Drag force on micron-sized objects with different surface morphologies in a flow with a small Reynolds number," *Polymer Journal*, vol. 47, pp. 564–570, aug 2015.

[115] M. Kustov, P. Laczkowski, D. Hykel, K. Hasselbach, F. Dumas-Bouchiat, D. O'Brien, P. Kauffmann, R. Grechishkin, D. Givord, G. Reyne, O. Cugat, and N. M. Dempsey, "Magnetic characterization of micropatterned Nd–Fe–B hard magnetic films using scanning Hall probe microscopy," *Journal of Applied Physics*, vol. 108, p. 063914, sep 2010.

[116] P. Kauffmann, A. Ith, D. O'Brien, V. Gaude, F. Boué, S. Combe, F. Bruckert, B. Schaack, N. M. Dempsey, V. Haguet, and G. Reyne, "Diamagnetically trapped arrays of living cells above micromagnets," *Lab on a Chip*, vol. 11, no. 18, p. 3153, 2011.

[117] T. Fujita, S. Miki, T. Kotoge, M. Uehara, K. Kanda, K. Higuchi, and K. Maenaka, "Batch Fabrication Technique of NdFeB for MEMS based Electromagnetic Energy Harvester," *Procedia Engineering*, vol. 47, pp. 639–642, 2012.

[118] O. D. Oniku and D. P. Arnold, "Microfabrication of High-Performance Thick Co80Pt20 Permanent Magnets for Microsystems Applications," *ECS Transactions*, vol. 50, pp. 167–174, mar 2013.

[119] S. Groth, P. Krüger, S. Wildermuth, R. Folman, T. Fernholz, J. Schmiedmayer, D. Mahalu, and I. Bar-Joseph, "Atom chips: Fabrication and thermal properties," *Applied Physics Letters*, vol. 85, no. 14, pp. 2980–2982, 2004.

[120] J. Denschlag, D. Cassettari, A. Chenet, S. Schneider, and J. Schmiedmayer, "A neutral atom and a wire: towards mesoscopic atom optics," *Applied Physics B*, vol. 69, pp. 291–301, oct 1999.

[121] J. Reichel, W. Hänsel, P. Hommelhoff, and T. Hänsch, "Applications of integrated magnetic microtraps," *Applied Physics B*, vol. 72, pp. 81–89, jan 2001.

[122] J. Armijo, C. L. Garrido Alzar, and I. Bouchoule, "Thermal properties of AlN-based atom chips," *The European Physical Journal D*, vol. 56, pp. 33–39, jan 2010.